Spintronics Physics of Thin-film Interfaces

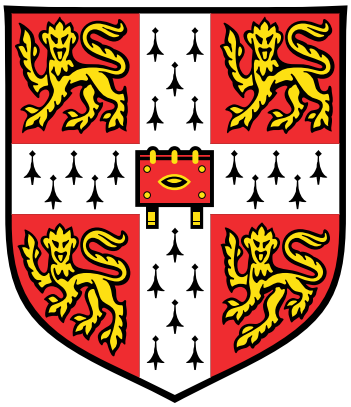

Razan Omar M Aboljadayel

Department of Physics
University of Cambridge

This dissertation is submitted for the degree of
Doctor of Philosophy

Homerton College

September 2018

To my beloved parents.

Abstract

Magnetic heterostructures may exhibit new features at the interface while leaving the bulk properties of the films unaltered, which make them ideal for technological applications. Here, I explore the interfaces of EuO(001)/$LaAlO_3$(001), EuO/NiO(111) and graphene/metal heterostructures.

Published DFT calculations postulated the formation of a spin polarised two-dimensional electron gas (2DEG) in the EuO film at $\sim$1.5 nm away from the EuO(001)/$LaAlO_3$(001) interface, due to the polar catastrophe which would also enhance the T_C of the EuO. Magnetisation depth profiles of the interface with the LaO^+- and mixed- terminated $LaAlO_3$(001) substrate are investigated using low energy muon spin relaxation (μSR) and polarised neutron reflectivity (PNR). The behaviour of our EuO(001) film is unlike that reported in the literature for stoichiometric EuO and EuO_{1-x} films, and no increase in the T_C was detected by the μSR. Instead, a reduction of $\sim$2.6 K in the T_C is measured by the SQUID which is attributed to the lattice mismatch between the EuO(001) and the $LaAlO_3$(001) substrate. However, contradictory results were obtained by the PNR for the LaO^+-terminated sample, where a magnetic moment of 3.59 μ_B/Eu atom, which is consistent with the value reported by Barbagallo *et al.* for a 9% oxygen-deficient EuO, was detected at 20 nm from the EuO(001)/$LaAlO_3$(001) interface. Therefore, I question the accuracy of the DFT calculations.

Exchange bias and the magnetisation depth profile of the polar interface of the antiferromagnet NiO(111) with EuO are investigated using PNR, and the results are compared with those of an uncoupled EuO grown on a MgO(001) substrate. A small double shifted hysteresis loop with enhanced coercivity, which arise as a result of the competition of the random NiO(111) *S*-domains, is measured by the SQUID magnetometer for the polar interface. However, a larger spin-split in the PNR is observed for the EuO(001)/MgO(001) sample in contrast to the EuO/NiO(111). The small spin-split in the latter is attributed to the pinning of the EuO magnetisation by the randomised NiO(111) S-domains which restrict it from aligning fully with the applied field. This postulation is verified by further PNR measurements on a field-cooled EuO/NiO(111) sample, which showed equal probability for the presence of compensated and uncompensated NiO(111) spins at the interface.

A magnetic moment in graphene can be induced in the presence of a ferromagnetic layer as a result of the proximity effect. PNR measurements show that a magnetic moment of $\sim$0.57 μ_B is induced in the graphene when it is grown on Ni(111) and on Co(111) films, which is about 5$\times$ higher than that reported in the literature. The origin of the induced magnetic moment is found to be due to the opening of the graphene's Dirac cones as a result of the strong C *p*-3*d* hybridisation which is confirmed by additional measurements using a non-magnetic Ni_9Mo_1(111) substrate. The results were also validated by the Bayesian uncertainty analysis, and proved by the X-ray magnetic circular dichroism measurements.

Declaration

I hereby declare that this dissertation is the result of my own work and includes nothing which is the outcome of work done in collaboration except as declared in the Preface and specified in the text. It is not substantially the same as any that I have submitted, or, is being concurrently submitted for a degree or diploma or other qualification at the University of Cambridge or any other University or similar institution. I further state that no substantial part of my dissertation has already been submitted, or, is being concurrently submitted for any such degree, diploma or other qualification at the University of Cambridge or any other University of similar institution. This thesis contains approximately 43,000 words excluding table of contents, figure captions, list of figures, list of bibliography and acknowledgement.

Razan Omar M Aboljadayel
September 2018

Acknowledgements

First and Foremost, I praise God for his blessings and for granting me the ability and strength to work on my PhD research and to complete it successfully. Without His blessings, this achievement would not have been possible.

Life has its ups and downs, and people often say "a PhD in is an emotional rollercoaster". However, looking back at my PhD now, I can say that I have enjoyed the journey, and I was lucky to be surrounded by supportive, loving, caring and friendly people throughout this journey.

I would like to express my sincere gratitude to my supervisor, Prof. Crispin H. W. Barnes, for giving me the opportunity to join the TFM group, for his advice and encouragement, for facilitating my research needs and his continuous support.

Beside my supervisor, I wish to express my profound appreciation to Dr Adrian Ionescu, for his tremendous help and support throughout my PhD, for his generous guidance, advice and the insightful discussions. I would also like to thank former and current members of the TFM group, Hofmann group and the Cavendish Laboratory. Special thanks go to Dr Pedro Monteiro who thought me how to operate and maintain the sputtering chamber, Dr Ian Farrer for his help with the X-ray facilities, Dr Stuart Holmes for charing the Spintronics Tuesday meetings. Many thanks to Dr David Love, Dr Justin Llandro, Angadjit Singh, Jieyi Liu and all other people who have made my time at the Cavendish Laboratory enjoyable and productive.

I was lucky enough to carry out many experiments at large-scale facilities around Europe. I am very grateful for all the help and solid support I received and continue to receive from the scientists at RAL, Prof. Sean Langridge, Dr Nina-Juliane Steinke, Dr Timothy Charlton, Dr Christy Kinane and Dr Peter Baker as well as the beamline scientists at PSI Dr Carlos Vas and Dr Zaher Salman, and at ILL Dr Thomas Saerbeck.

I would also like to thank all my friends, special mention goes to Marwa, for our never-ending chat, brainstorming sessions, for your great help and understanding during my writing-up period.

Finally, but not least, I would like to thank my family, especially my loving parents for their unconditional love, prayers, support and for being in my life.

Financial support - My PhD was sponsored by the Saudi Arabia Ministry of Education through the Custodian of the Two Holy Mosques' overseas scholarship program.

Table of contents

List of figures

List of tables

List of Abbreviations

μSR	Low-energy muon spin relaxation spectroscopy
2DEG	Two-dimensional electron gas
A-N	Arrott-Noakes
AFM	Atomic force microscopy
BMP	Bound magnetic polarons
BR	Branching ratio
BS	Backscattering electrons
BZ	Brillouin zone
CB	Conduction band
CVD	Chemical vapour deposition
DR	Double-resonance
DW	Domain wall
EB	Exchange bias
FC	Field-cooling
FM	Ferromagnetic material
FOM	Figure-of-merit
FWHM	Full-wifth at half-maximum
GMR	Giant magnetoresistance

ILL	Institute Laue-Langevin
IMT	Insulator-to-metal transition
K-F	Kouvel-Fischer
LAO	$LaAlO_3$
LEED	Low-energy electron diffraction
LF	Longitudinal field
MBE	Molecular beam epitaxy
mSLD	Magnetic scattering length density
MTJ	Magnetic tunnelling junction
Mu	Muonium
NSF	Non-spin-flip
nSLD	Nuclear scattering length density
PEEM	Photo-emission electron microscopy
PNR	Polarised neutron reflectivity
PSI	Paul Scherrer Institute
RFA	Retarding-field energy analyser
RS	Raman scattering
RT	Room temperature
SA	Spin asymmetry
SE	Secondary electrons
SEM	Scanning electron microscopy
SF	Spin-flip
SLD	Scattering length density
SQUID	Superconducting quantum interference device

TF	Transverse field
TM	Transition-metal
TMR	Tunnelling magnetoresistance
TOF	Time-of-flight
u.c.	Unit cell
VB	Valence band
VdW	Van der Waals
WD	Working distance
wTF	Weak transverse field
XMCD	X-ray magnetic circular dichroism
XRD	X-ray diffraction
XRR	X-ray reflectivity
ZF	Zero-field
ZFC	Zero-field cooling

1
Introduction

Conventional electronics have been relying on the motion of charged electrons by an electric field to carry and process signals inside the materials while neglecting their degree of freedom (spin). Spintronics is the field which either adds the spin of the electrons to charge-based conventional electronics or utilises the spin of electrons alone for signal processing [1]. The effect of the addition of electron spin promises to provide devices with improved capabilities. Better functionalities such as higher processing and faster data transferring speed to increase the memory density and lower the power consumption, in comparison with the conventional semiconductor-based technology, will be possible to achieve [1]. Spin-valves and MRAM which are currently used in the hard disk read heads and other magnetic sensors are examples of spintronic devices.

Spintronics is considered as a bridging discipline connecting the field of electronics and magnetism [2]. The research in this field was started after the discovery of the magnetoresistance (GMR) effect in 1988 by the 2007 Noble prize winners Albert Fert and Peter Grünberg [3]. Although Mott was the first to suggest in 1936 that the mobility of the electrons in a ferromagnetic metal is influenced by the spin, which was proved experimentally by Tedrow and Merservey and their co-workers in the early 1970s, it was the discovery of the GMR which drove the field to its current state [4, 5].

Another breakthrough in the field of spintronics was the detection of the tunnelling magnetoresistance (TMR) and magnetic tunnelling junctions (MTJ) [2]. Therefore, ferromagnetic materials and half-metals which have a spin-splitting in their energy bands between the majority (spin-up) and minority (spin-down) spins at the Fermi energy level are potential materials for spintronics applications [1].

This field is actively expanding, and the current research focuses on the fundamental studies to understand the spin transport, spin dynamics and spin relaxation in electronic ma-

terials, and the improvement of the spin detection methods [5]. Furthermore, researches have been searching for more potential materials/systems with novel electronics properties and exploring their spin transport abilities for spintronics applications. A promising development of the field suggests the use of different systems such as single-electron and molecular spintronics. Carbon nanotubes and graphene are ones of the promising materials for spintronics applications due to their small spin-orbit couplings and their long spin diffusion lengths, where the use of such materials have been made possible owing to the advanced growth and fabrication facilities and the high sensitivity of the measuring techniques [2].

Oxide materials play a crucial role in spintronics as they can yield to one order of magnitude higher MTJ signal when they used as electrodes than that obtained with transition-metal electrodes [6]. Therefore, they have been investigated intensively with the aim of producing all-oxide-based spintronics devices [7]. Furthermore, oxide films possess additional advantages over traditional semiconductor thin films; their ions interact strongly with their surrounding ions as they are usually more polar and their crystals can be easily modified by changing their compositions [8]. However, although oxide heterostructures have been studied extensively and various changes have been reported at their interfaces such as a change in magnetism, superconductivity and electrical conductivity, understanding their interfaces is still challenging due to their complexity.

Significant interest has also been drawn to the interfaces of oxide thin film heterostructures as it was found that the abrupt offset in the band structure at the interface has a great effect on the interfacial mobile charge carriers which could act as a crucial parameter for designing spintronics devices. Therefore, in this thesis, I explore the interfaces of EuO- and graphene-based heterostructures.

Outline of the thesis

This thesis explores various effects at the interfaces of EuO(001)/$LaAlO_3$(001), EuO/NiO(111) and graphene/metal heterostructures using various structural and magnetic characterisation techniques. After the brief introduction to the field of spintronics above, the thesis outline is as follows:

Descriptions of the operating principles of the different experimental techniques used throughout the thesis are given in **Chapter 2**. The techniques are divided into growth, structural, magnetic and advanced magnetometry characterisation systems. It also explicitly explains the data analysis procedures for the advanced magnetometers: polarised neutron reflectivity (PNR), X-ray magnetic circular dichroism (XMCD) and low-energy muon spin relaxation spectroscopy (μSR).

Chapter 3 presents the experimental work carried out to study the EuO(001)/$LaAlO_3$(001) heterostructure in the attempt to investigate the formation of a spin-polarised two-dimensional electron gas (2DEG) at the interface predicted by the DFT calculations performed by Lee *et al.* and Wang *et al.* published in Ref. [9] and Ref. [10], respectively. It also summarises the properties of the EuO and $LaAlO_3$, and explains the postulated mechanisms at which a 2DEG could form at their interface. Furthermore, the sample preparation procedure which involves controlling the termination surface of the $LaAlO_3$(001) (LAO) substrate via wet etching and thermal annealing, and the growth of EuO using magnetron sputtering are also described in the chapter. Explicit discussions on the characterisation measurements that give insight into the structural and magnetic properties of the samples are presented. A conclusion summarising the findings of the study is then provided at the end of the chapter.

Chapter 4 reviews the study of the magnetisation depth profile of the EuO/NiO(111) heterostructure and the investigation of the exchange bias (EB) effect at the interface. At the beginning of the chapter, descriptions of the properties of NiO and the mechanisms which drive the EB are presented. It also discusses the results of the PNR experiments carried out to explore the effect of the random and ordered NiO(111) interfacial *S*-domains on the EB. Furthermore, it explains the sample preparation methods and the characterisation measurements carried out on the sample. A summary of the findings is then given in the conclusion, as well as an outline of the plan for the future PNR beamtime, which will be performed at the OFFSPEC instrument at ISIS, and which could provide a better insight of the in-plane distribution of the NiO(111) *S*-domains at the interface.

In **Chapter 5**, the induced magnetic moment in graphene arising from the proximity effect in the vicinity of a ferromagnetic substrate is investigated. The chapter also introduces the properties of free-standing graphene and the changes it undergoes when it is grown on a ferromagnetic transition-metal substrate such as Ni and Co. The sample preparation method which involves the deposition of the ferromagnetic substrates using magnetron sputtering and the growth of graphene by chemical vapour deposition is described along with the structural and magnetic properties of the samples. The chapter then discusses the XMCD and PNR results that are corroborated by Bayesian uncertainty analysis, which was used to validate the PNR fitting models, before a conclusion is drawn at the end of the chapter which compares the presented results with those reported by Weser *et al.* on similar structures [11].

Chapter 6 highlights the most significant outcomes of the work discussed in the thesis and proposes future experiments which could support the current results and provide better understanding of the explored interfaces.

2

Experimental Techniques

A wide range of characterisation techniques was used in this dissertation to explore the properties of the samples. The thin films were deposited using ultra-high vacuum techniques such as magnetron sputtering, molecular beam epitaxy (MBE) and chemical vapour deposition (CVD). The structural properties of the samples such as the thickness, roughness, crystallinity and the surface topographies were probed using different techniques including atomic force microscopy (AFM), scanning electron microscopy (SEM), low-energy electron diffraction (LEED), as well as Raman spectroscopy, X-ray diffraction (XRD) and X-ray reflectivity (XRR). The bulk magnetic properties of the heterostructures were studied using the superconducting quantum interference device (SQUID), whereas advanced magnetometers such as polarised neutron reflectivity (PNR), X-ray magnetic circular dichroism (XMCD) and low-energy muon spin relaxation (μSR) carried out at large-scale facilities to provide insight into the magnetic properties of the interfaces. This chapter provides a comprehensive overview of the principles of each technique, highlights the advantages of using each of them and explains the data analysis procedure of the PNR, XMCD and μSR.

2.1 Growth techniques

2.1.1 Magnetron sputtering

Magnetron sputtering is one of the most widely used growth techniques for thin films. Figure 2.1 shows the chamber used to deposit some of the films reported in this thesis which was assembled by Surrey Nanosystems LTD, whereas the software and the electrical parts were made by CEVP Gamma 1000M. As can be seen from the figure, the system consists of three interconnected chambers: magnetron sputtering, load-lock and the oxidation/milling chamber to allow the transfer of the samples using an automated mechanism without breaking the vacuum.

The sputtering chamber has six 3" targets which can all be operated using either a DC or RF current. The load-lock consists of cassettes which can hold up to four sample plates. The samples can be outgassed inside the load-lock at $T \approx 180$ °C using quartz heating lamps to clean the surface of the substrate before the growth. The sample stage inside the sputtering chamber can hold up to a 3" wafer and it can be rotated to produce a uniform growth of about 1" in diameter. The sample stage is also capable of heating the sample to a temperature up

Fig. 2.1 : The sputtering system used to grow thin films. The chamber on the left is the magnetron sputtering chamber in which the growth takes place. The chamber in the middle is the load-lock where the sample is loaded and outgassed before the growth takes place. The compartment on the right is the milling/oxidation chamber. The figure is taken from Ref. [12].

to 700 °C using a graphite heating stage, where a small magnetic field can also be applied during the growth. Each of these chambers is pumped down using individual pumps: Alcatel turbomolecular pumps for the load-lock and the oxidation chamber, and a cryopump for the growth chamber. Therefore, a base pressure of $\sim 1 \times 10^{-9}$ mTorr can be achieved inside the growth chamber and 1×10^{-7} mTorr inside the other two. Mainly, inert Ar gas is used during the growth. However, other gases such as N_2 and O_2 can also be added to grow nitride and oxide films.

During the sputtering process, when a noble gas such as argon is used, the argon atoms lose an electron to form Ar^+ ions which are then accelerated towards the target cathode by a high voltage. Upon the bombardments of the target material by the Ar^+ ions, momentum is transferred to the target, resulting in the outer layer of the target being sputtered inside the chamber which will then condense onto the surface of the substrate. At the same time, the free electrons released from the ionisation process of the argon gas are attracted to the substrate and collide with with more argon atoms. Thus, more free electrons and Ar^+ ions are generated to sustain the plasma for the growth. As the process continues, more atoms are deposited onto the substrate's surface forming a continuous film [13, 14].

In a magnetron sputtering, an additional permanent magnet is placed behind the target to confine the secondary electrons (released with the ejected target material) around the target to localise the plasma around it. This causes the free electrons to travel further distances, ionising more Ar atoms and creating a denser plasma for a higher deposition rate. Therefore, magnetron sputtering has an advantage of protecting the forming film from damage and contamination [13]. The co-deposition of Eu and Eu_2O_3 to grow EuO thin films using an Ar^+ plasma is used as an example to illustrate the principle behind the magnetron sputtering technique in Figure 2.2.

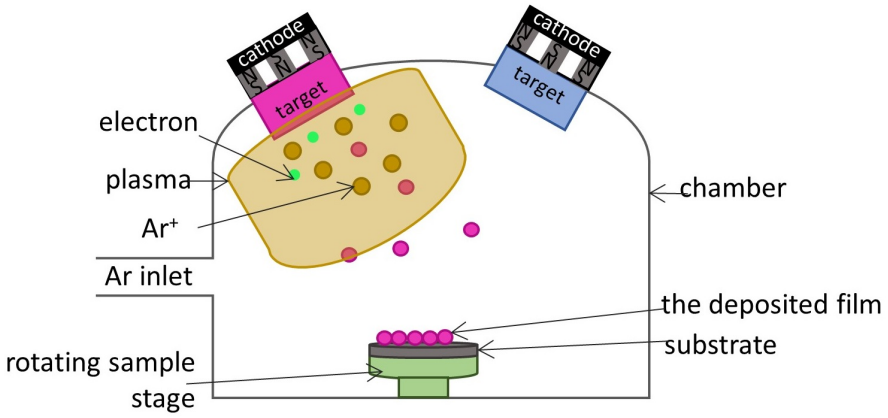

Fig. 2.2 : A schematic diagram illustrating the principle of magnetron sputtering.

2.1.2 Molecular beam epitaxy

The underlying principle of molecular-beam epitaxy (MBE) is based on heating up a solid source, until atoms evaporate, which then travel inside the chamber and land and diffuse on the surface of the substrate until a continuous film is formed. This technique provides a high precision for growing high-quality epitaxial films down to a monolayer accuracy [15].

NiO films (See Section 4) were grown using a bespoke chamber designed mainly for the growth of oxides such as NiO. The chamber has two main compartments: the growth chamber and the load-lock which are connected via a long bellows and separated by a manually operating gate-valve as shown in Figure 2.3. A base pressure of $\sim 1.5 \times 10^{-10}$ mbar can be achieved using a combination of ion, turbo and titanium sublimation pumps. The chamber has four upward facing evaporators located at the bottom of the chamber, whereas reactive gases such as O_2 can be leaked into the growth chamber via a small valve. For the growth, the sample is mounted facing downward on a manipulator while a small clamp is used to hold the sample in position. The sample is then loaded from the load-lock entry which is then pumped down to 1×10^{-6} mbar, before it is outgassed overnight at $\sim$ 180 °C. After that, the gate-valve is opened and the manipulator is lowered down manually inside the growth chamber. The sample holder can be tilted and rotated to face each crucible

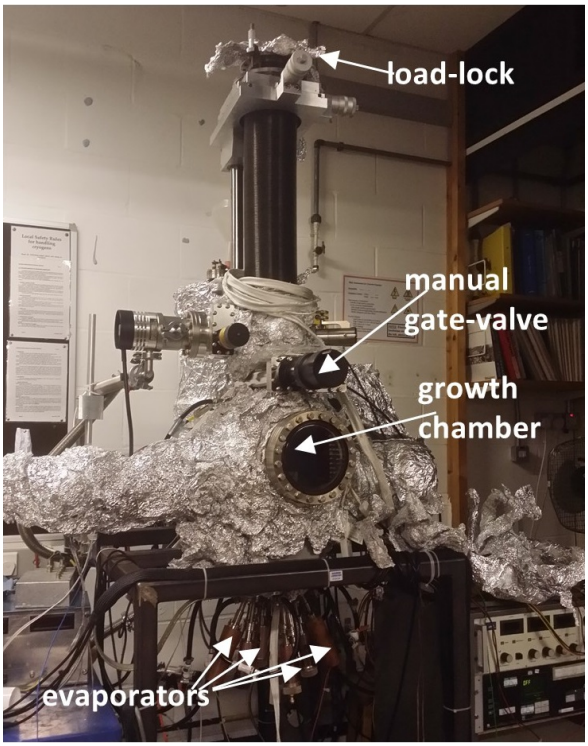

Fig. 2.3 : The bespoke MBE chamber used for the growth of NiO.

directly which makes a small angle of about 20° with the surface of the sample. The sample holder can also be heated up to 500 °C using a filament wire placed very close to the sample. The film thickness is monitored using a quartz crystal microbalance, whereas the sample temperature is measured using a thermocouple placed close to it. Therefore, the temperature reading is not very precise.

2.1.3 Chemical vapour deposition

Chemical vapour deposition (CVD) was used, by the Hofmann group at the Electrical and Electronic Engineering department at the University of Cambridge, to grow graphene as discussed in Chapter 5. During the CVD process, the substrate is placed inside the chamber and the precursor gases are then introduced to grow the film via chemical reactions occurring near the hot substrate surface. These chemical reactions can take different forms such as heat, plasma and high frequency. Therefore, there are different types of CVD including thermal, low-pressure and plasma CVD. The unreacted gases and chemical by-products are then pumped out of the chamber through an exhaust. Therefore, high-quality, pure and dense conformal thin films can be deposited using this technique [16].

2.2 Structural characterisation techniques

2.2.1 X-ray measurements

2.2.1.1 X-ray-matter interaction

X-ray measuring techniques such as X-ray reflectivity (XRR) and X-ray diffraction (XRD) are non-destructive, surface-sensitive tools which can provide insight into the crystallographic properties of the sample as the X-ray has a wavelength of about 0.01 Å and 100 Å which is comparable to the interplanar distance between the atoms in a crystal [17]. Information such as the crystallinity, lattice-strain and orientation can be obtained from these measurements [18, 19].

A description of the interaction of the X-ray with matter is presented in this section to introduce the X-ray structural characterisation techniques used in the thesis. As the theory of the X-ray scattering is covered in many textbooks, only a brief overview is presented here. I refer the interested reader to [20–22] for an extensive description of the principles of the X-ray techniques.

When X-ray interacts with a matter, it can undergo different behaviours: absorption, refraction, reflection and diffraction (i.e. scattering) as illustrated in Figure 2.4. The absorption

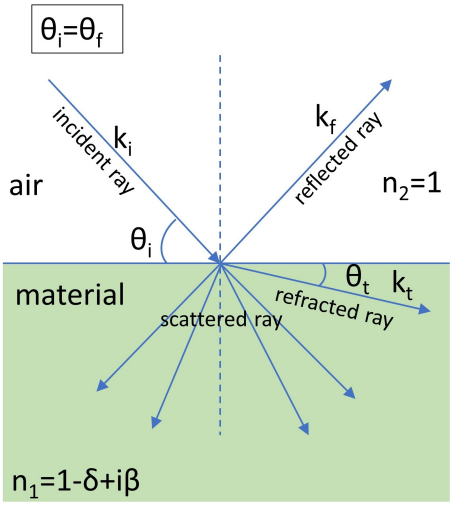

Fig. 2.4 : A schematic illustration of the refraction, reflection and the scattering of the X-ray.

of the X-ray by a material can be explained by the following equation:

$$I = I_0 \exp^{-\mu z}. \tag{2.1}$$

Where I_0 is the intensity of the incident beam, I is the reduced intensity of the beam after travelling a distance z, and μ is the linear absorption coefficient.

When the X-ray bombards a sample, it can either be reflected or refracted at the interfaces of different materials which has a different refractive index, n, which will change its direction. In general, n is defined as $n = c/v$ where c and v are the speed of light in vacuum and inside the material, respectively. For X-rays, n is a complex parameter which can be expressed as:

$$n = 1 - \delta + i\beta. \tag{2.2}$$

Here, δ and β are the dispersion and absorption coefficients, respectively. For X-rays, both coefficients are found to be positive numbers, where δ is in the order of 10^{-5} and 10^{-8} in solids and the air, respectively, and that $\beta << \delta$. Both δ and β can be expressed by the material's electron density, ρ_e, and the beam wavelength, λ, as follows:

$$\delta = \frac{\lambda^2}{2\pi} r_e \rho_e, \tag{2.3}$$

and

$$\beta = \frac{\lambda}{4\pi} \mu_x, \tag{2.4}$$

where $r_e = 2.818 \times 10^{-15}$ m is the classical electron radius, also known as the Thomson scattering length or the Lorentz length, is based on the relativistic model of the electron in which the electron is considered as a non-point particle, and μ_x is the absorption length.

The transmitted rays will refract away from the normal to the surface as they pass through two materials of a different refractive index which can be described by Snell's law:

$$n_1 \cos\theta_i = n_2 \cos\theta_t. \tag{2.5}$$

Here, n_1 and n_2 are the refractive indices for material 1 and 2, respectively. Here, θ_i and θ_t are the incident and transmitted angles, respectively.

The X-rays also experience a total internal reflection at the surface of the material if θ_i is smaller than a critical angle, θ_c. Assuming the beam is travelling from air which has $n = 1$, and by using Snell's law and substituting $\theta_1 = \theta_c$, $\theta_t = 0$ and $n_2 = 1$ (Figure 2.5), θ_c can be written in terms of δ as:

$$\theta_c = \sqrt{2(1-n)} = \sqrt{2\delta} = \frac{4\pi\rho r_e}{k}, \tag{2.6}$$

where $k = 2\pi/\lambda$ and θ_c is usually between 0.2° - 0.5°. When the incident angle increases so that $\theta_i > \theta_c$, part of the beam will be transmitted into material 1 whereas the rest will be reflected at the interface. The amplitude of transmissivity (t) and reflectivity (r) can be expressed using Fresnel's law as [21]

$$r = \frac{n_1\theta_{i,r} - n_2\theta_t}{n_1\theta_{i,r} + n_2\theta_t}, \tag{2.7}$$

and

$$t = \frac{2n_1\theta_{i,r}}{n_1\theta_{i,r} - n_2\theta_t}. \tag{2.8}$$

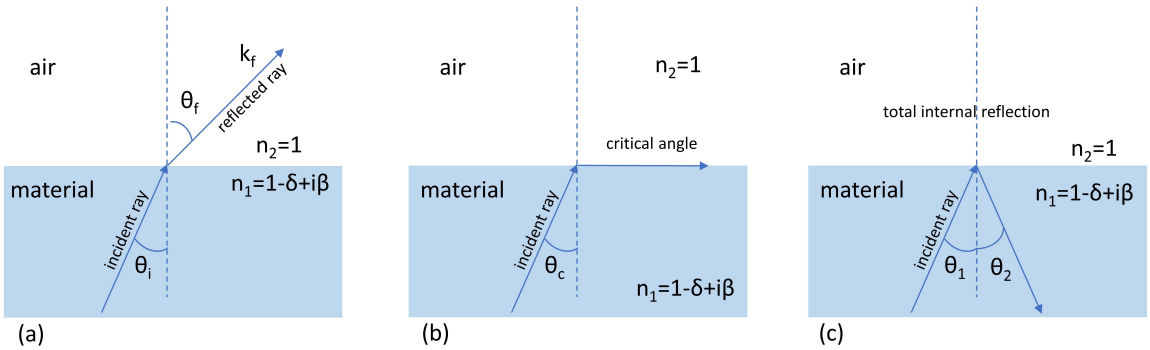

Fig. 2.5 : A schematic illustration of the total internal reflection of X-ray.

Here $\theta_{i,r}$ is the incident angle of the reflected ray, and that $r^2 + t^2 = 1$ for the conservation of energy at the interface. Therefore, as θ_i continues to increase, more of the beam will be transmitted and less will be reflected at the interface which can be detected by a drop in the reflectivity curve.

The diffraction of X-rays can be either via elastic or inelastic scattering. However, only the former will be discussed in this section. Elastic scattering takes place when the wavelengths of the incident and scattered waves are equal (i.e. no loss of energy).

The wavefunction of a travelling X-ray of a wavelength $>>$ scattering centre, and interacting with a single electron is given by:

$$\psi \propto \exp^{ik_i x}, \tag{2.9}$$

Where k_i is the wavevector of the travelling wave, and x is its travelling direction.

Upon the collision, the electromagnetic waves will set the electron to vibrate which will then radiate spherical waves, E_{rad}, which can be expressed as:

$$E_{rad}(r,t) = -\left(\frac{e^2}{mc^2}\right)\left(\frac{1}{r}\right)E_0 \exp^{[2\pi i(kr-wt)]}. \tag{2.10}$$

The first term is the classical radius of the electron, while the negative sign reflects the phase shift. The number of photons scattered as a result of the scattering of the X-ray at a solid angle, $\Delta\Omega$, collected by an area A of a detector is given as:

$$I_s = I_0 \Delta\Omega \left(\frac{d\sigma}{d\Omega}\right). \tag{2.11}$$

Here I_s and I_0 are the incident and scattered fluxes passing A per second, and $\dfrac{d\sigma}{d\Omega}$ is the differential scattering cross-section. Therefore, the efficiency of the detector can be obtained from $= I_s/I_0$.

Considering the scattering of X-rays by an atom with Z electrons, the intensity of the scattered beam by a single atom of the material can be obtained from the ratio of the amplitude of the X-ray reflected by a single electron to that scattered by a single atom, where the volume occupied by these electrons is given by:

$$Z = \int_V \rho(r) dV. \tag{2.12}$$

Here, $\rho(r)$ is the number density of the electrons and V is the volume.

The total scattering length of an atom is:

$$f = \int_V \rho(r) \exp^{2\pi Qr} dV, \tag{2.13}$$

where f is the atomic form factor and that $f = Z$ when $Q \to 0$ [21]. Therefore, the wavefunction of the scattered beam is given as [23]:

$$\psi_f \propto f(\hat{r}) \frac{\exp^{ik_f r}}{r}. \tag{2.14}$$

2.2.1.2 X-ray diffraction (XRD)

As the atoms are orderly arranged in a crystal forming a long-range order, they can be modelled by equally-spaced lattice points arranged in parallel lattice planes of an interplanar spacing d_{hkl}. These planes can be represented in terms of the normal vector to the lattice plane (g_{hkl}) of a magnitude of $1/d_{\mathrm{hkl}}$. Therefore, when a beam of a wavevector $\bar{k}_{\mathrm{i}}$ illuminates the sample's surface at a small angle θ, it scatters by the lattice points with a wave vector $\bar{k}_{\mathrm{r}}$ as illustrated in Figure 2.6. Therefore, g_{hkl} can be expressed in terms of $\bar{k}_{\mathrm{i}}$ and $\bar{k}_{\mathrm{r}}$ as follows:

$$\bar{k}_{\mathrm{r}} - \bar{k}_{\mathrm{i}} r = g_{\mathrm{hkl}}. \tag{2.15}$$

Since the distances (L) travelled by the reflected beams from adjacent planes are different, ΔL can be written as:

$$\Delta L = 2d_{\mathrm{hkl}} \sin\theta. \tag{2.16}$$

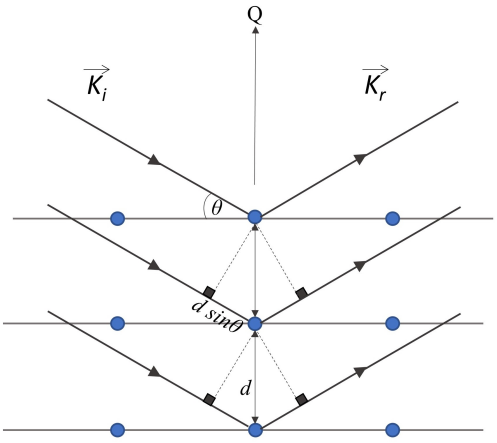

Fig. 2.6 : Bragg's law of diffraction.

To observe an XRD peak of a crystal plane, all the reflected beams from all the planes must interfere constructively, and this only happens when ΔL is of an integer number, n, of wavelengths (λ):

$$\Delta L = n\lambda. \tag{2.17}$$

Therefore, substituting Equ. (2.16) into Equ. (2.17) leads to what is known as Bragg's law of diffraction:

$$n\lambda = 2d\sin\theta. \tag{2.18}$$

A typical laboratory X-ray system consists of an X-ray source which is usually a rotating or a sealed-tube source which acts as an anode. Both sources operate in a similar fashion in which an electron beam is emitted from a hot filament that serves as a cathode is accelerated by a high voltage applied between the source and the filament. However, the only difference between the two types of sources is that the rotating anode continuously rotates to reduce the generated heat. The accelerated electrons will then collide with a metal target (usually copper). Upon collision, the target's core-shell electron will be removed from the atom creating a hole in its core-shell which will then be filled by an outer-shell electron. An X-ray photon with a wavelength equal to the difference of the two energy levels is then emitted as a result of the process, forming a continuous line spectrum. However, only one transition wavelength is used for the X-ray measurements, and that is usually the K_α line of a wavelength of $\lambda = 1.54$ Å for the Cu target. Less than 1% of the produced energy will be converted into X-rays and the rest will be lost as heat. Therefore, a water cooling system is used.

All the XRD and XRR measurements presented in the thesis were performed at room temperature using Bruker D8 Discover diffractometer unless otherwise stated. During the measurement, the sample is placed on the sample stage with five degrees of rotation and fixed in position by a vacuum line supplied to the stage. A 40 A filament current is used to generate the electron beam which is then accelerated by 40 kV towards a Cu target. Soller slits of 0.2 mm to collimate the X-ray beam, a 4-bounce Germanium-220 monochromator, a 1D detector and an absorber set to one are used to optimise the peaks intensity. Also, the incident angle, θ, the angle at which the detector is positioned with respect to the surface of the sample, 2θ, (since $\theta_\mathrm{i} = \theta_\mathrm{s}$ in a specular reflectivity) and the height of the sample, z, are refined to increase the intensity, which is displayed as a function of 2θ in the XRD scan.

2.2.1.3 X-ray reflectometry (XRR)

The XRR measurements are carried out at a grazing incident angle (between $0-10^\circ$) to a achieve total reflection of the incoming beam at the surface of the sample. A typical XRR

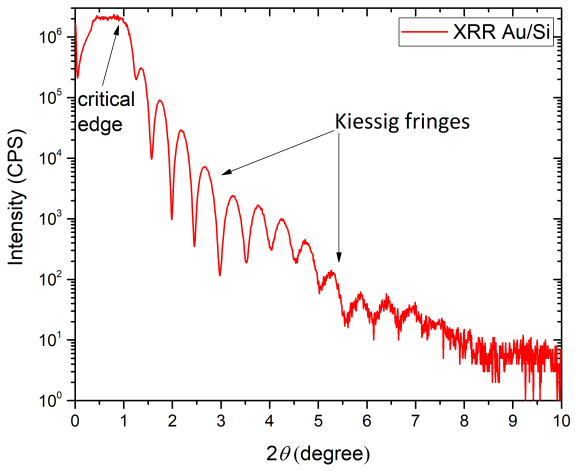

Fig. 2.7 : The XRR scan of a Au film grown on a Si substrate showing the scan's critical edge and the Kiessig fringes.

scan displays the oscillations which result from the interference of all the reflected rays from the different layers of the sample, and these oscillations are known as Kiessig fringes (Figure 2.7). Various parameters can be obtained from the XRR scan: the film thickness (z), interface roughness (σ) and the density of the material (ρ). The critical edge of the Kiessig fringes is defined by the density of the top layer, and the number of oscillations is controlled by the film thickness. The separation distance (d) between two consecutive fringes, m and $m+1$, is expressed as [24]:

$$d = \frac{\lambda}{\theta_{m+1} - \theta_m}. \tag{2.19}$$

Also, by using *Fresnel's* equation, the X-ray reflectivity, R, of a film (layer 1) deposited on an infinite substrate (layer 2) can be derived as [23]:

$$R = \left| \frac{r_1 + r_2 \exp^{-2ik_{iz}t}}{1 + r_1 r_2 \exp^{-2ik_{iz}t}} \right|^2, \tag{2.20}$$

where r_1 and r_2 are the Fresnel coefficients for the film and the substrate, respectively. Here, k_{iz} is the wavevector of the incident beam normal to the direction of the travelling wave, and t is the film thickness. Since the maximum reflectivity is achieved when the exponents of the above equation are equal to one, R can be rewritten in terms of the X-ray wavelength as:

$$2t\sqrt{\sin^2\theta_i - \sin^2\theta_c} = \lambda \Delta L, \tag{2.21}$$

where ΔL is the path difference between the reflected and transmitted waves.

For the XRR measurements, a Gobel mirror and a point detector are used instead of the Ge(220) monochromator and 1D detector as in the XRD measurements. All the scans presented in the thesis were performed using the Bruker D8 unless otherwise stated. The reflectivity curves were then fitted using LEPTOS software from Bruker to obtain the z, σ and ρ of each layer of our heterostructure samples.

2.2.2 Atomic force microscopy (AFM)

The AFM is a probing technique used for studying the surface structure of a sample by measuring the repulsive/attractive forces between the sample and the AFM tip. The probing tip in an AFM is attached to a spring cantilever as shown in Figure 2.8 (a). The tip is then scanned across the sample's surface sensing the deflection of the cantilever as a function of the lateral position, while the movement of the cantilever is usually measured by the reflection of a laser beam focused at the back of the cantilever [27]. The beam is then reflected onto a

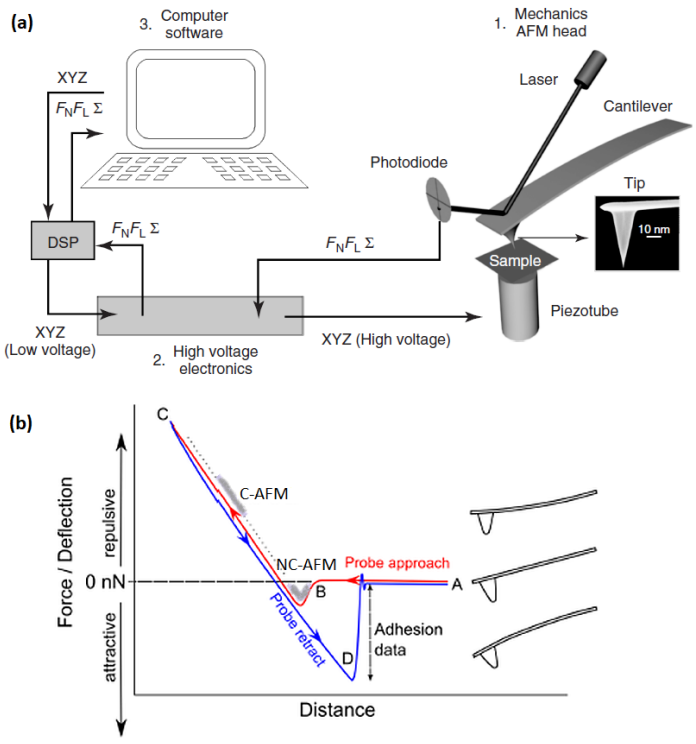

Fig. 2.8 : (a) A schematic diagram of an AFM illustrates its main components: A laser, an AFM tip, a cantilever, a photodiode, high voltage electronics and a computer display. (b) The force-distance cruve of the AFM operating regime and the behaviour of the cantilever as it approaches the sample in the C-AFM and NC-AFM modes. The images are taken from Ref. [25] and [26], respectively.

photodiode which generates a voltage based on the position of the laser. The voltage is then processed by a phase-sensitive detector (PSD) to produce a real-time image.

The AFM is classified into different operational modes. There are at least 20 modes of operation for the AFM, but the most common modes are the contact (C-AFM) and non-contact (NC-AFM) modes [26]. In the C-AFM mode, the cantilever is always in contact with the sample. As the cantilever is lowered down, it experiences an attractive force which bends it towards the sample's surface. However, as the AFM continues to push the cantilever against the sample, it reaches a point where the interaction enters a repulsive regime, and the cantilever will start to move away from the sample. As the direction of movement is reversed, the cantilever enters the attractive regime again. This keeps the probe tip constantly in contact with the sample (Figure 2.8 (a)) [26]. On the other hand, the NC-AFM mode operates in the attractive regime only. A stiff cantilever is used in this mode so it can oscillate around its resonant frequency at a constant height from the sample's surface, without entering the repulsive regime as shown in Figure 2.8 (b) [26–28].

2.2.3 Scanning electron microscopy (SEM)

This section is based on [29–38]. The SEM is a structural characterisation technique which can provide information about the sample's topography and its chemical composition. In a typical SEM, an electron beam is generated and emitted from a cathode electron gun and then accelerated by an anode. The beam follows a vertical path along the microscope through various electron lenses and apertures which are used to focus the beam on the sample. This process takes place inside a high-vacuum column to prevent the electrons from scattering by the air molecules. The SEM also has a scanning coil to scan the sample in a raster manner and a detector to process the signal into a real-time image. A schematic diagram of the SEM is shown in Figure 2.9.

The interaction of the electron beam with the sample is divided into elastic and inelastic interactions. The former scattering occurs when the beam is deflected off the sample with no loss in energy, and such electrons which scatter off at large angles $> 90^{\circ}$ are known as backscattering electrons (BS). On the other hand, inelastic scattering takes place when the incident electron beam transfers its energy to the sample and as a result of this interaction the sample's outer-shell electrons are emitted as secondary electrons (SE). Other types of emission can also take place during the process such as Auger electrons and X-rays. Therefore, different types of detectors are used depending on the generated signal. Scanning coils then scan the sample's surface in a raster manner while the signal is then processed and displayed as a real-time image. SE detection is the most common type of SEM mode used for investigating the samples topography.

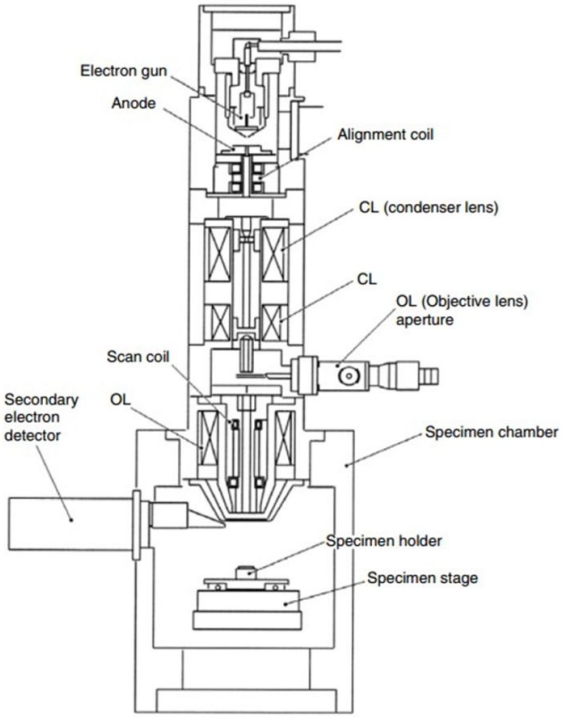

Fig. 2.9 : A schematic diagram of a typical SEM highlighting its main components. The diagram is taken from Ref. [30].

The quality of the images produced by the SEM is affected by many factors including the accelerating voltage, working distance (WD) and the beam spot size. Furthermore, the SEM magnification depends only on the excitation of the scanning coils which can be adjusted by changing the ratio of the display monitor length to the sample scanning length ($L_{\text{monitor}}/L_{\text{sample}}$). The contrast of an SEM scan is defined as $(S_2 - S_1)/S_2$ with $S_1 < S_2$, where S_1 and S_2 are the signal detected at two arbitrary locations giving minimum and maximum signal on the sample's surface.

2.2.4 Raman spectroscopy

Raman spectroscopy is a fast, versatile and non-destructive analysis technique for electronic and structural characterisations of samples [39, 40]. It is one of the main techniques used to examine the quality of graphene, as various graphene properties can be deduced from its spectrum such as the number of graphene layers, homogeneity and doping level (See Chapter 5) [39, 41].

Raman spectroscopy, which was named after its inventor C. V. Raman, probes the vibration of the sample's molecules which occurs due to their interactions with electromagnetic radiation. When a monochromatic laser irradiates a sample, it is scattered in all directions

with slightly different frequencies as a result of its interaction with the sample. Most of the incident laser power ($\sim 99.999\%$) undergoes elastic interactions with the sample, creating scattered light of an equal frequency (Rayleigh scattering). When the sample's atoms absorb the incident photons, they get excited to higher vibrational energy levels and then return to their ground states by emitting photons of the same frequency. However, a small fraction of the incident radiation ($\sim 0.001\%$) interacts with the sample via inelastic scattering creating scattered light of a different frequency (Raman scattering).

During Raman scattering, the absorbed photon excites the sample's atoms from its basic state to a higher vibrational level where some of the photon's energy is transferred to the atoms scattering light with a frequency lower than that of the incident light (Stokes frequency). However, when the photon is absorbed by an atom which is already in an excited state, it returns to its ground state releasing light with a higher frequency than that of the incident beam (anti-Stokes frequency). The shift in the Stokes lines, which are measured by the Raman spectroscopy, are usually more intense than the anti-Stokes lines and they are displayed as an intensity vs shift in the wavelength [43, 44]. Rayleigh and Raman scattering (Stokes and anti-Stokes) are illustrated in the schematic diagram shown in Figure 2.10.

A typical Raman spectroscopy is made of four main components: a laser source, a sample illumination system, a lens, a filter and a detector as shown in Figure 2.11. During the measurement, the sample is illuminated with a laser beam, and the scattered light is then collected by an optical lens and filtered by an interference filter to produce a Raman spectrum. Different types of laser beams are used in Raman spectroscopy such as Ar^+, Kr^+, He-Ne, UV and IR light. Therefore, different detectors are used depending on the type of the signal. The

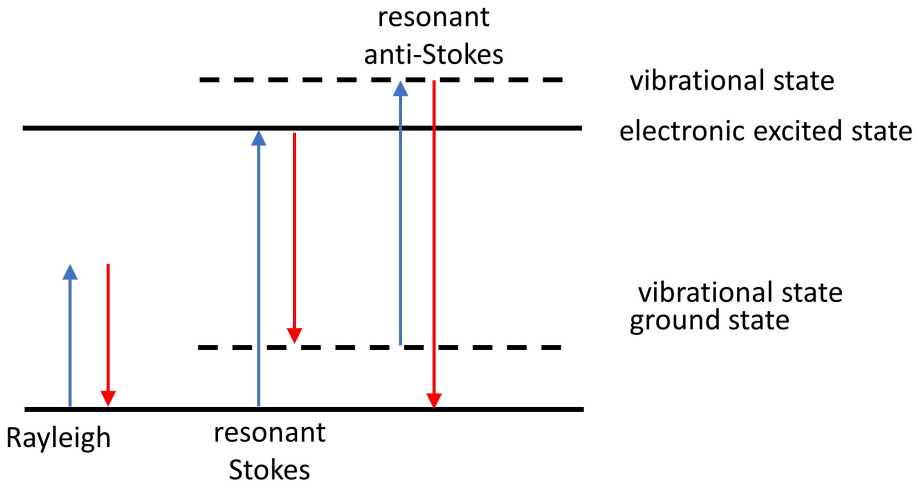

Fig. 2.10 : A schematic illustrations of the Rayleigh and Raman (Stokes and anti-Stokes) scatterings. The figure is reproduced from Ref. [42].

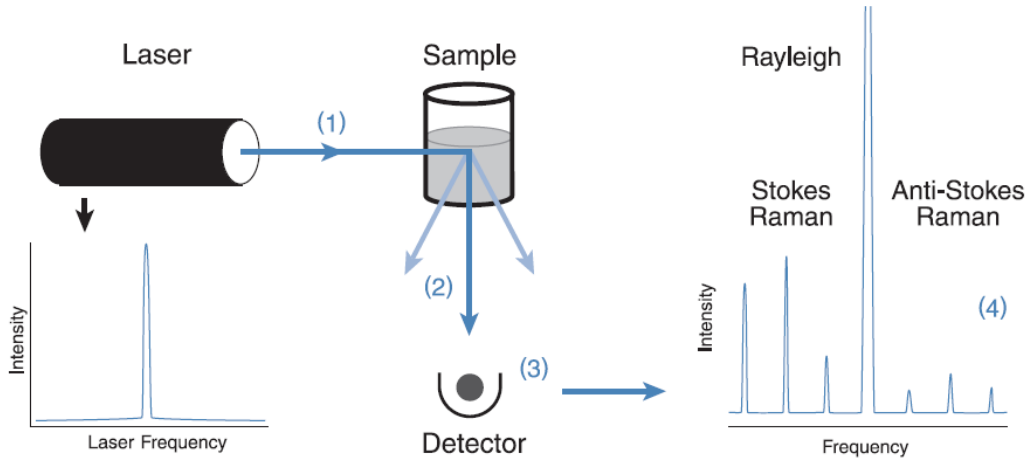

Fig. 2.11 : A schematic diagram of a typical Raman spectroscopy highlighting its main components: (1) The laser illumination of the sample. (2) The scattering of the incident light. (3) The detection of some of the scattered light (Raman Stokes lines) by the detector which produces the Raman spectrum. (4) The Raman spectrum showing the Rayleigh and the Raman Stokes and anti-Stokes lines. The Figure is taken from Ref. [45].

major disadvantage of using this technique is its low intensity due to the small fraction of the laser which scatters via Raman scattering. However, this can be overcome by increasing its sensitivity using resonance Raman spectroscopy and surface-enhanced Raman spectroscopy [43].

2.2.5 Low energy electron diffraction (LEED)

LEED is a surface-sensitive technique which is usually used to study and visualise the reciprocal-space lattice ($\mathbf{a}^*_{1,2}$) of an adsorbed layer on an epitaxial film [47, 48]. In this technique, a low-energy electron beam (10 - 500 eV) is generated by an electron gun and accelerated by a voltage potential at 90 ° along the direction of the sample's surface-normal as shown in Figure 2.12 [47]. The BS electrons created as a result of this interaction (as described in Section 2.2.3) will travel through a retarding-field energy analyser (RFA), which consists of multiple hemispherical grids, before they hit a fluorescent screen. The sample holder and Grid 1, are grounded to create a field-free region around the sample, whereas a negative potential -(V_0-ΔV) is applied to Grids 2 and 3 to eliminate all electrons that have not scattered off the sample elastically. Grid 4 is also grounded to reduce the penetration of the screen field to Grid 2 and 3. A voltage of $\sim$ 5 kV is then applied to the fluorescent screen to provide the BS electrons with sufficient energy to produce visible diffraction patterns that can be seen through a view hole placed behind the screen [46]. The real-space and reciprocal-space lattices are then constructed from these diffraction patterns.

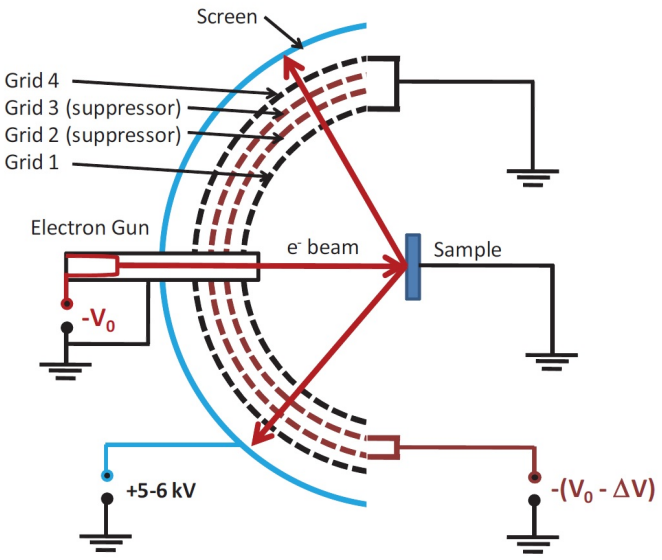

Fig. 2.12 : A schematic diagram of a standard LEED showing its main components: the electron gun, RFA and its grids, fluorescent screen and the voltages applied to each part, taken from Ref. [46].

The electron beam can be described using de Broglie's wave equation, $\lambda = h/(2meV)^{1/2}$. However, since the low-energy beam has a short penetration depth, only the sample's first few atomic layers contribute to the LEED diffraction pattern, which can then be represented as a 1D chain of a periodic atomic structure. Note that the Laue condition ($\sin\varphi$-$\sin\varphi_0 = h/d_{\mathrm{hk}}$, where $d_{\mathrm{hk}} = \mid h\mathbf{a}_1 + k\mathbf{a}_2 \mid$) must be fulfilled for the constructive interference to take place [46, 49, 50], and the patterns can be predicted using the following equation [48]:

$$\mid \mathbf{a}^*_{1,2} \mid = \frac{2\pi}{\mid \mathbf{a}_{1,2} \mid}. \tag{2.22}$$

2.3 Magnetic characterisation techniques

2.3.1 Superconducting quantum interference device (SQUID)

The superconducting quantum interference device (SQUID) is one of the most sensitive techniques to measure bulk magnetic properties. There are two kinds of SQUID: DC and RF SQUIDs. This section only discusses the DC SQUID which was the system used to measure the magnetic properties of the samples reported in this thesis. The operating principle of the DC SQUID is based on the Josephson effect and flux quantisation ($\Phi = \dfrac{nh}{2e} = n\Phi_0$). A

typical DC SQUID consists of two superconducting rings aligned parallel to each other and separated by two Josephson-junction "weak links" [51, 52]. When an external magnetic field is applied to the system, current will flow through the rings and a small fraction will tunnel through the junctions creating a voltage across the ring which is related to Φ by the following equation:

$$\Delta V = \frac{R}{L}\Delta\Phi, \tag{2.23}$$

where ΔV is the bias voltage, R is the external shunt resistor and L is the ring self-inductance. Therefore, the SQUID acts as a converter between the change in voltage and the magnetic flux to provide insight into the magnetic properties of the sample [23, 53]. I refer the interested reader to the book edited by John Clarke and Alex Braginski which covers the SQUID in great depth [54].

2.4 Advanced magnetometry techniques

2.4.1 X-ray magnetic circular dichroism (XMCD)

XMCD is a powerful magneto-optical technique for investigating the local magnetic properties of ordered materials, e.g. ferromagnets and ferrimagnets [55]. It measures the difference in the absorption cross-section of the left- (negative helicity, μ_-) and right- (positive helicity, μ_+) circularly polarised soft X-ray [56] [1], as it passes through a magnetic sample [58–60]. XMCD is an elemental-, magnetic- and chemical state-specific technique since the dichroism spectra are characteristic of the atomic core electrons' binding energies [61]. The strong resonances are observed at the element's inner shell absorption thresholds, and this is due to the electronic transitions from the core shell to unoccupied valence states. These transitions are controlled by the electric dipole selection rules ($\Delta l = \pm 1$) [61]. Therefore, the $2p \rightarrow 3d$ transitions ($L_{2,3}$-edge) are usually measured for the transition metals (TM) and $3d \rightarrow 4f$ ($M_{2,3}$-edge) for rare metals [58, 61–64].

Many structural and electronic properties can be probed by XMCD such as the sample's magnetic anisotropy, and it also used to differentiate between the material's bulk and surface properties [55, 58, 65]. However, the most significant advantage of XMCD is the ability to determine the size, direction and anisotropy of the sample's magnetic moment (to the nearest $0.01\mu_B$). Also, to distinguish between their orbital (m_o) and spin angular momentum components (m_s) using the sum rules [55, 61, 62, 66].

[1] μ_- is when the photon helicity is parallel to the sample's magnetisation, and μ_+ is when photon helicity and sample's magnetisation are aligned antiparallel to each other [57].

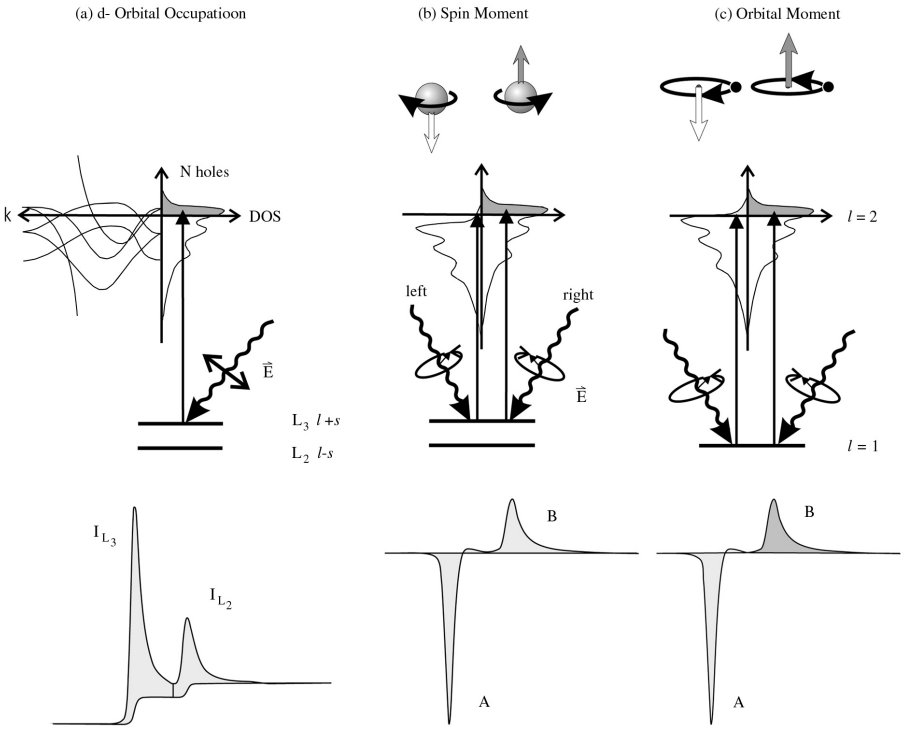

Fig. 2.13 : (a) Schematic of the electronic transitions at the *L*-edge in transition metals upon the absorption of linear x-ray, the circularly polarised light interaction with the (b) spin and (c) orbital moments in the XMCD two-step model. The corresponding XAS and XMCD signals are shown in the third row. The image is taken from Ref. [67].

The fundamental principle of XMCD can be described by a two-step model, proposed by Stohr and Wu [68], as illustrated in Figure 2.13. In this model, the m_s of the d states of TMs arise from the spin imbalance of the spin-up and spin-down electrons [61]. The first step takes place when core electrons of the $2p_{1/2}$ and $2p_{3/2}$ levels absorb polarised photons, forming spin-up and spin-down photoelectrons [56]. If these photoelectrons are formed at spin-split states, such as $p_{3/2}$, the photons' angular momentum can be partially transferred to the spin via spin-orbit coupling ($j = l \pm s$) [61]. Therefore, left circularly polarised light (+$\hbar$) excites mainly spin-up photoelectrons, whereas right polarised light (-$\hbar$) creates spin-down photoelectrons, due to their opposite momentum [61]. However, a reverse effect occurs at the $2p_{1/2}$ due to the opposing spin-orbit coupling [56, 61]. The $3d$ valence bands act as a spin detector for these photoelectrons in the second step, and thus the absorption cross section differs between the two helicities at the $3d$ bands [56]. Therefore, owing to the spin conservation rule, +$\hbar$ (-$\hbar$) photons excites an excess of spin-up (spin-down) photoelectrons from $2p_{3,2} \rightarrow d$ bands [56]. Since the transition intensity is proportional to the number of unoccupied d states, for a given spin [61], a higher signal is detected at the L_3 edge than at

the L_2 edge [56]. Thus the XMCD signal reflects the difference in spin polarisation at the final ($3d$) states [69]. The timescale for the excitation of photoelectrons and the formation of core hole (τ_0) is found to be 10^{-20} s, whereas the rearrangement of the electrons in the valence band (τ_1) to be in the range $10^{-16} - 10^{-15}$ s [56].

The bottom panel of Figure 2.13 (a) shows the absorption spectroscopy (μ_{XAS}) which represents the absorption coefficient of unpolarised radiation [69, 70]. Therefore, μ_{XAS} can provide information on the sample's electronic properties and its local structure [55]. On the other hand, the spectra which are shown in Figure 2.13 (b) and (c) are the μ_{XMCD} spectra arising from the spin and orbital angular momentum. Both μ_{XAS} and μ_{XMCD} can be calculated from the μ_+ and μ_- spectra using the following formulae:

$$\mu_{XAS} = \frac{1}{2}(\mu_+ + \mu_-) \tag{2.24}$$

$$\mu_{XMCD} = \mu_+ - \mu_-. \tag{2.25}$$

μ_+ and μ_- are the absorption coefficients parallel and antiparallel to the light propagation vector, respectively, normalised to a common value [66, 71].

The main components of a typical XMCD system consist of circularly polarised X-rays, a monochromator, X-ray optics, a magnet and a detector [62, 72]. The XMCD standard modes of detection are fluorescence, transmission and electron yield [72], where the latter is classified into a total and partial electron yield, TEY and PEY, respectively [59]. Additional retarding voltage is required in the PEY mode, to filter out the low-energy photoelectrons, which makes it more surface sensitive compared to TEY. However, it has a poor signal-to-noise signal [59]. During the experiment, the sample under investigation is placed in an ultra-high vacuum environment, and a magnetic field is applied to magnetise it [62], whereas the left- and right- polarised X-rays can be obtained by selecting radiations above or below the field's orbit plane, respectively [61].

2.4.1.1 SIM beamline

The XMCD data presented in Chapter 5 was collected at the SIM endstation, located at the Paul Scherrer Institute (PSI) in Switzerland, and a schematic of the beamline outline is shown in Figure 2.14. This end-station uses a high flux (1x10^{15} photons/s) of soft X-rays. It also has two independent permanent magnet helical undulators to generate variable polarisation with a spot size of 30 µm x 100 µm. The samples can be measured in this beamline in a temperature range of 20 K to 600 K, and with an applied magnetic field of up to $\pm$ 130 mT. This beamline is designed to be operated for XMCD and Photo-Emission Electron Microscopy (PEEM), and further details of its specifications can be found in Ref. [73].

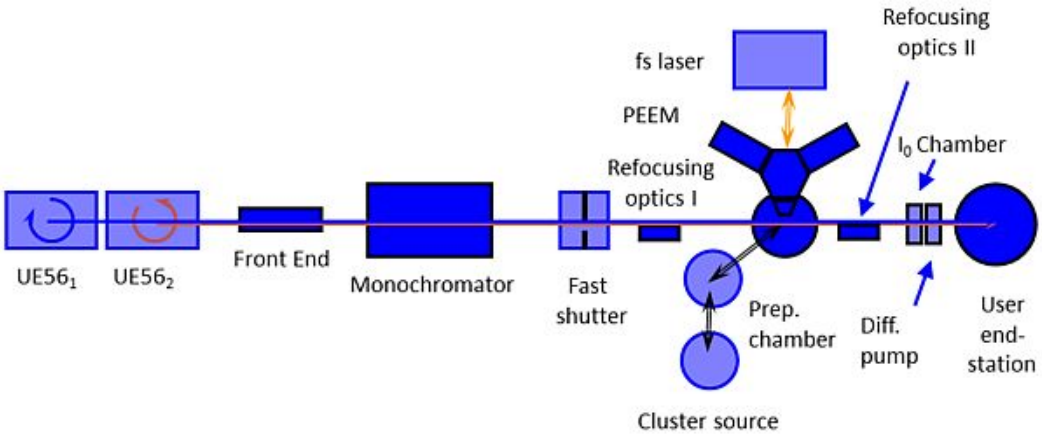

Fig. 2.14 : An outline of the SIM beamline showing its main parts including the undulators ($UE56_1$ and $UE56_2$), a monochromator, a shutter, optics and PEEM. The diagram is taken from Ref. [73].

2.4.1.2 Sum rules

The sum rules were derived by Thole and Carra, and other co-workers between 1992 and 1993 [56]. They were derived within the framework of a single ion in a crystal field with a partially filled valence band [56]. The first sum (magnetic) rule states that the integral of the XMCD signal is proportional to the ground-level orbital angular momentum expectation value, $<L_z>$, acting on the final state shell [74]. The second sum (spin) rule relates the XMCD signal to the spin-split edge of the core-shell and the average of the spin angular momentum expectation value, $<S_z>$, and the magnetic dipole operator, $<T_z>$, of the final-state that receives the excited photoelectron [68, 74]. Therefore, m_o and m_s can be written in terms of $<L_z>$, $<S_z>$ and $<T_z>$ [64], which can be obtained from the μ_{XAS} and μ_{XMCD} spectra using the following formulae [75]:

$$m_o = -\frac{4}{3}\frac{\int_{L_{2,3}}(\mu_+ - \mu_-)dE}{\int_{L_{2,3}}(\mu_+ + \mu_-)dE}(n_h), \tag{2.26}$$

$$m_s = -\frac{6\int_{L_3}(\mu_+ - \mu_-)dE - 4\int_{L_3+L_2}(\mu_+ - \mu_-)dE}{\int_{L_3+L_2}(\mu_+ + \mu_-)dE}(n_h)\left(1 + \frac{7 < T_z >}{2 < S_z >}\right). \tag{2.27}$$

$n_h = (10 - n_d)$ is the number of holes in the $3d$ states, whereas n_d is the electron occupation number of the $3d$ states. $L_{2,3}$ represent the integration range over the L_2 and L_3 edges, and $<T_z>$ is measured to be very small in transition metals, and hence can be ignored [63].

μ_{XMCD} must be corrected for the light degree of polarisation, P_{ol}, and the light's incident angle, θ. Therefore, it is multiplied by a factor $\frac{1}{P_{ol}\cos\theta}$ [71], where θ is measured with

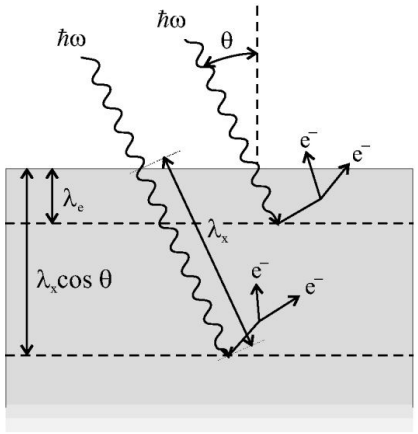

Fig. 2.15 : Illustrations of the saturation effect in the XMCD electron-yield mode. λ_e is the average depth from where the spin-up and spin-down originate, λ_x is the X-ray penetration length and θ is the incident angle. The image is adapted from Ref. [76].

respect to the sample's surface, but μ_{XAS} remains unchanged [59]. TEY and fluorescence detection modes of ultrathin films must also be corrected for the saturation (self-absorption) effect [62, 76, 77]. This effect takes place when the sampling depth of the electron yield (escape depth), λ_e, is larger or equivalent to the X-ray penetration depth [76], where λ_e is defined as the average depth from where the spin-up and spin-down electrons originate [76]. The sample's thickness, t, also has a significant effect on the XMCD measurement [58], and this is because it is unlikely for primary and secondary Auger electrons to escape from a thick sample as shown in Figure 2.15. λ_x measures the X-ray penetration length, and it is equal to the inverse of μ, where μ is the decay constant. Therefore, $\lambda_x \cos\theta$ is the X-ray penetration depth, and that the correction factor for the saturation effect, f_s, is given by the following equation [76]:

$$f_s = C\frac{1}{1+\left(\frac{\lambda_e}{\lambda_x\cos\theta}\right)}\left\{1-e^{-t\left(\frac{1}{\lambda_e}+\frac{1}{\lambda_x\cos\theta}\right)}\right\}\mu \tag{2.28}$$

By correcting μ_{XMCD} for P_{ol}, θ and f_s, and substituting Equ. (2.25), (2.24) and (2.28) into Equ. (2.26) and (2.27), letting $(\Delta A_3 + \Delta A_2)$ be $\int_{L_3+L_2}\mu_{XMCD}$, with ΔA_3 and ΔA_2 to be $\int_{L_3}\mu_{XMCD}$ and $\int_{L_2}\mu_{XMCD}$, respectively, and $A_3 + A_2 = \int_{L_3+L_2}\mu_{XAS}$, m_o and m_s can be

re-written as:

$$m_o = -\frac{2}{3P_{ol}\cos\theta}\frac{\Delta A_3 + \Delta A_2}{A_3 + A_2}\frac{n_h}{1+\left(\frac{\lambda_e}{\lambda_x\cos\theta}\right)} \tag{2.29}$$

and

$$m_s = -\frac{1}{P_{ol}\cos\theta}\frac{\Delta A_3 - 2\Delta A_2}{A_3 + A_2}\frac{n_h}{1+\left(\frac{\lambda_e}{\lambda_x\cos\theta}\right)}. \tag{2.30}$$

Although the sum rules have been known for a while, their validity is still under debate as their reported accuracy varies widely, between 50% and 95% [56, 77]. However, their applicability for late 3*d* TMs has already been proved in many cases [56]. This is because the calculations of the sum rules are restricted only to the dipole-allowed transitions. Therefore, the core-level exchange splitting, as well as the *s* to *p* transitions, and the difference between the $d_{3/2}$ and $d_{5/2}$, are ignored [69]. Other assumptions were also made which are found to yield to higher uncertainties in the m_o and m_s calculations. For example, the term $< T_m >$ was found to be non-negligible in many cases in addition to the large variations in the reported n_h values. It was also realised that these rules cannot be applied for *d* metals that experience a substantial overlap in their L_3 and L_2 states, such as V, as there must be enough separation between the excitation edges for the sum rules to be valid [78].

Since the XMCD at the *K*-edge measures the transitions from a non-spin-split *s* orbital to *p* orbital, m_s becomes zero, and m_o is calculated as:

$$m_o = \frac{n_h}{P_{ol}\cos\theta}\frac{\Delta A}{A} \tag{2.31}$$

ΔA is the $\int \mu_{\mathrm{XMCD}}$ and A is $\int \mu_{\mathrm{XAS}}$ across the entire *K*-edge. For the *K*-edge, n_h becomes equal to $6 - n_p$, where n_p is the electron occupation number in the $2p$ bands [75].

2.4.1.3 Data analysis

The raw data must be processed first to obtain μ_{XAS}, μ_{XMCD}, before the application of the sum rules. This section explains explicitly how the *L*- and *K*-edges data were handled. First of all, the c- and c+ raw absorption spectra were normalised to the incident high flux measured at the gold mesh placed before the sample. The pre- and post-edge linear background of the chosen pair was then subtracted to eliminate the non-resonance contribution [66]. The c- and c+ spectra are found to have a different number of data points. Therefore, their intensities were interpolated to a common number, between 6700 and 6800. The energy range was also

linearly interpolated, to be used for both spectra using the equation below:

$$E(\mathrm{eV}) = (i-1) \times \frac{E_\mathrm{f} - E_\mathrm{i}}{n-1} + E_\mathrm{i}, \tag{2.32}$$

with i= $1,2,3,.....,n$, where n is the number of the interpolated data points for both spectra, whereas E_f and E_i are the electron initial and final energy values.

The spectra were then corrected for energy shifts to match the values reported in the database [79]. This was done because even a minimal change, as small as 50 meV, has been reported to yield a significant error in the sum rules [80]. The spectra were then normalised by setting the pre-edge value to zero and the post-edge to one, to obtain the magnetic moment per atom [81]. However, since the sum rules take into account only the $2p \rightarrow 3d$ transitions, μ_step must be removed before applying the sum rule because μ_step is a result of the electronic excitations $2p \rightarrow s$ and to the continuum [60], even if they contribute to only about $\approx 2\%$ in the case for $3d$ TMs [81]. μ_step is approximated by an arctangent function positioned at the L_3 and L_2 peaks using the following equation:

$$\mu_\mathrm{Step} = R_{L_3} \arctan((E - L_3) \times W) + R_{L_2} \arctan((E - L_2) \times W). \tag{2.33}$$

R_{L_3} and R_{L_2} are the relative step heights (branching ratio, BR) of L_3:L_2 which measures the ratio of the absorption coefficient jumps at the two peaks [82]. The L-edge BR is expected to be close to 2 : 1 as it reflects the number of $3p_{3/2}$ and $3p_{1/2}$ sublevels [66, 69, 83]. However, the ratio can be slightly modified to place the steps at the foot of the L_3 and L_2 post-edges. E_{L_3} and E_{L_2} are the L_3 and L_2 peak positions, and W is the step width. The W value can be adjusted so that μ_step matches the pre-edge and thus yield to a zero intensity after the subtraction of μ_step from the white line.

Similar procedure was followed to process the carbon K-edge raw data. However, the data shows a non-linear pre-edge background after they were normalised to the gold mesh, as shown in Figure 2.16. This apparent drop in the intensity is due to a negative voltage offset contributing to the TEY signal, which appears as a consequence of a significant reduction in the incoming intensity at this particular energy value due to the C contamination of the X-ray optical elements. We corrected for this background using the following equation:

$$\frac{\mu_{+\mathrm{or}-} - CF}{\mu_\mathrm{gold}}, \tag{2.34}$$

where μ_gold is the absorption spectrum of the gold mesh. CF is the correcting factor applied for both μ_+ and μ_- and it was between 0.005 - 0.008. The linear background generated from the above formula was corrected as for the L-edge. The other difference was in the μ_step

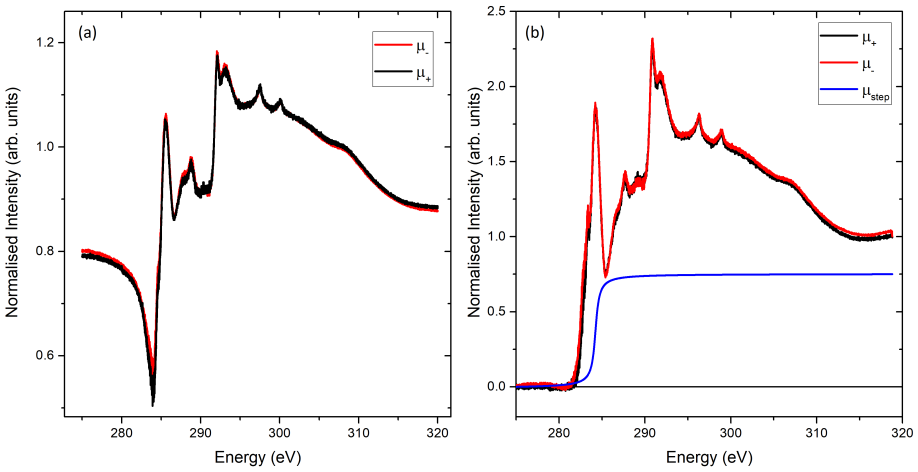

Fig. 2.16 : (a) C K-edge absorption spectra normalised to the gold mesh showing the non-linear background at the pre-edge. (b) C K-edge spectra after they have been corrected and the post-edges are normalised to unity, and μ_{step}.

formula; since there is only one step, Equ. (2.33) was reduced to Equ. (2.35) where K is the peak position for the C π orbital (284.2 eV) [79]:

$$\mu_{Step} = \arctan((E-K)\times W). \tag{2.35}$$

There were a few challenges in processing the C K-edge data which are discussed in more details in Chapter 5.

2.4.2 Neutron measurements

A brief introduction to the neutron measuring techniques and their principle of operation presented here. For a more comprehensive description, the reader is referred to [84, 85].

Neutron techniques are non-destructive surface-sensitive probing tools. The advantage of these techniques is that neutrons are neutral particles which can penetrate deeply into the sample ($\sim$ 3000 Å) which makes probing interfacial structures and studying buried layers possible [86]. The neutron wavelength is comparable to the atomic interplanar spacing between the atoms. Therefore, insight into the structure of the samples down to atomic resolution can be obtained. Furthermore, neutrons interact with the nuclei of the atoms and with their surrounding unpaired electron, yielding information about the structural and magnetic properties of the probed sample.

2.4.2.1 Production of neutrons

Neutrons are produced either by nuclear fission or by the spallation process. During nuclear fission, neutrons are generated from the nuclei of certain elements, such as U and Pu, which naturally undergo fission reactions. On the other hand, in the spallation process, clusters of protons are accelerated by ~ 1 GeV towards a heavy metal target such as W, U or Ta. Sub-atomic particles such as neutrons, pions and protons are produced as a result of these collisions. These emitted particles have sufficient energy to collide again with the target, and then leave the nucleus in an excited state. Approximately 25 high-energy neutrons (~ 25 meV) with a wavelength ~ 1 Å are produced with every collision, and they will then travel through a hydrogenous moderator to slow them down via successive inelastic scatterings with other light-weight particles inside a moderator, and then guided through various neutrons optics towards beamline instruments.

Table 2.1 lists some of the fundamental properties of neutrons. Neutrons are neutral particles as they consist of one up and two down quarks where their wavelength, λ_{n}, is described using de Broglie equation as:

$$\lambda_{\mathrm{n}} = \frac{h}{m_{\mathrm{n}} v_{\mathrm{n}}}, \tag{2.36}$$

where h is the Planck constant, m_{n} is the mass of the neutron and v_{n} is the velocity. Therefore, the neutron kinetic energy is expressed as:

$$E = \frac{1}{2} m_{\mathrm{n}} v_{\mathrm{n}}^2, \tag{2.37}$$

which can also be rewritten as follows:

$$E = \frac{\hbar^2 k^2}{2 m_{\mathrm{n}}}. \tag{2.38}$$

Quantity	Value
Mass	$m_{\mathrm{n}} = 1.674928 \times 10^{-27}$ kg
Charge	0
Spin	$1/2$
Magnetic Moment	$-9.6491783 \times 10^{-27} \mu_{\mathrm{n}}$
Lifetime	$\tau_{\mathrm{n}}(\mathrm{avg}) = 885.9 \pm 0.9$ s
Nuclear Magneton (μ_{n})	5.051×10^{-27} J/T

Table 2.1: The fundamental properties of neutrons [87].

The principle of scattering of neutrons is similar to that of X-rays. However, the mechanism is more complicated for neutrons as two main interactions take place; the interactions of neutrons with the nuclei of the atoms and their magnetic interactions with the magnetic moments (i.e. unpaired electrons).

2.4.2.2 Polarised neutron reflectivity (PNR)

Polarised neutron reflectivity (PNR) can take place in two forms; specular and off-specular. However, the latter is beyond the scope of the thesis. Therefore, the discussion will be limited to the specular reflectivity (i.e. $\theta_i = \theta_f$, where θ_i is the incident angle, and θ_f is the reflected angle).

During the PNR experiment, the neutron beam strikes the surface of the sample at small θ_i, where $0 < \theta_\mathrm{i} < 2^\circ$. The neutrons then interact with the sample and get reflected at an angle θ_f. The scattering vector Q_z can be expressed as:

$$|Q_\mathrm{z}| = \left|\overrightarrow{k_\mathrm{f}} - \overrightarrow{k_\mathrm{f}}\right| = \frac{4\pi}{\lambda}\sin\theta_\mathrm{i}. \tag{2.39}$$

Here, Q_z is known as the normal momentum transfer, $\overrightarrow{k_\mathrm{i}}$ and $\overrightarrow{k_\mathrm{f}}$ are the incident and reflected beam wavevectors, respectively, and λ is the neutron beam wavelength [88].

The PNR curve measures the reflected beam as a function of Q_z. By fitting the reflectivity curves one can determine the film thickness, interface roughness, the density and a magnetisation depth-profile of the layers. Also, the nuclear and magnetic density profiles normal to the surface are extracted.

The principle of specular PNR can be explained in terms of the refractive index, n, which is found to be $n = 1 - \delta$ for the neutrons. Furthermore, n is related to the quantum-mechanical potential, U, experienced by the neutron as it strikes the sample surface with kinetic energy E, by the following equation:

$$n = \left(1 - \frac{U}{E}\right)^{1/2}. \tag{2.40}$$

The neutron's nuclear potential, U_n, can be written in terms of the number density, N, and the coherent scattering length, b, as:

$$U_n = Nb. \tag{2.41}$$

Therefore, the nuclear density profile of the measured sample can be extracted from U_n [89].

By treating the neutron-matter interaction as a 1D problem, the resultant effective step potential, V, of the layer is the sum of the nuclear and magnetic contributions of the sample.

Therefore, V can be written as:

$$V^{-} = \frac{2\pi\hbar^2}{m} N b^{\text{nuc}} \pm \vec{\mu} \cdot \vec{B} = \frac{2\pi\hbar^2}{m} N[b(r) \pm p(r)], \tag{2.42}$$

where $\hbar$ is the reduced Planck constant, N is the atomic density, b^{nuc} is the coherent scattering length, $\vec{B}$ is the sample's magnetic induction, m is the neutron mass, $\vec{\mu}$ is the neutron magnetic moment, $p(r)$ is the magnetic moment per scattering event where the $+$ve and $-$ve signs correspond to the spin-up and spin-down neutrons, respectively. The first term of the equation reflects the nucleus-neutron interaction. Therefore, Nb^{nuc} is known as the nuclear scattering-length density (nSLD). The second term of the equation arises from the magnetic interaction, and it is sensitive to the direction of the magnetic induction with respect to the neutrons' magnetic moments.

Furthermore, $\vec{\mu} \cdot \vec{B}$ can also be written in terms of the magnetic scattering-length density (mSLD) as Nb^{mag}. Since the magnetic part of the voltage is sensitive to the direction of the magnetic induction inside the sample, mSLD is different for the spin-up and spin-down neutrons [88]. Thus, the mSLD can be expressed as:

$$V^{\pm} = \frac{2\pi\hbar^2}{m} (N b^{\text{nuc}} \pm N b^{\text{mag}}). \tag{2.43}$$

A sketch of the neutron SLD showing the contribution of the mSLD and nSLD is shown in Figure 2.17. Also, the critical edge (q_c), at which total reflection occurs, is different for the spin-up and spin-down neutrons as it is related to the mSLD by:

$$q_c^{\pm} = \sqrt{16\pi N(b^{\text{nuc}} \pm b^{\text{mag}})}. \tag{2.44}$$

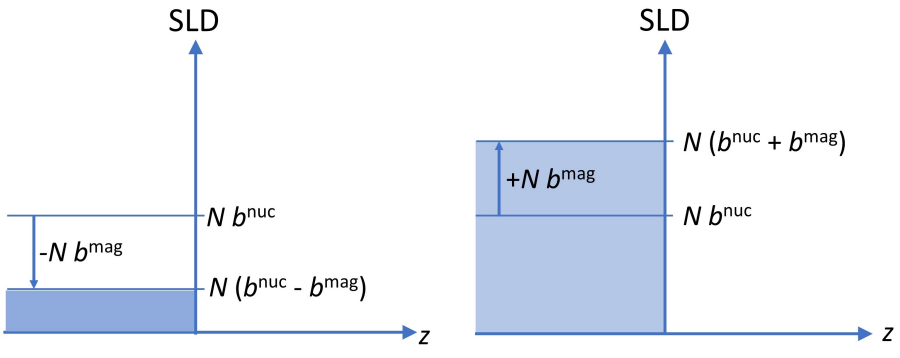

Fig. 2.17 : The SLD profile for the (a) spin-up and (b) spin-down neutrons showing the nSLD (Nb^{nuc}) and mSLD (Nb^{mag}) components. The figure is reconstructed from Ref. [88].

Neutron reflectometers can be operated in two modes; time-of-flight (TOF) and monochromatic. In the TOF, a rotating chopper is used to generate a pulsed neutron beam of a fixed θ and various wavelength. Therefore, λ can be determined from the time of flight of the neutrons from the chopper to the detector. On the other hand, in the monochromatic mode, the reflectivity is measured using a beam of a constant wavelength over a range of θ [86]. The advantage of TOF over the monochromatic mode is that a wide Q range is covered by collecting the data at a few incident angles. However, the acquisition times for both modes are similar [90].

The neutron beam is transmitted into the probed sample as long as $\theta_i \leqq \theta_c$, where θ_c is the critical angle. However, as θ exceeds θ_c, the neutron beam will experience total external reflection.

The POLREF instrument at ISIS

TOF POLREF reflectometer is located at target station 2 at the ISIS neutron pulsed source in the UK. Neutrons at ISIS are generated via the spallation method in which protons are accelerated towards a Cs target [91]. The neutrons are then slowed down by a coupled groove cold H_2/CH_4 moderator resulting in a neutron beam width of 0.6 cm x 0.3 cm, with a flight path of 23 mm that covers a wavelength range of 1-15 Å [92]. A 0.5 T magnet is inserted in the sample position during the PNR experiments, and a continuous-flow cryostat was used for the low-temperature measurements.

The D17 instrument at Institute Laue-Langevin (ILL)

The neutron beam at the ILL is generated via the fission reaction of a highly-enriched ^{235}U nuclear reactor, where D_2O water is used as a reactor coolant and moderator to slow down the neutrons [93]. The D17 end-station can be operated in four modes: a polarised and a non-polarised TOF, a polarised and a non-polarised monochromatic modes with a full polarisation analysis [94]. For the reported experiments in the thesis carried out at the D17, only a polarised monochromatic beam of a wavelength of $\sim$ 5.5 Å, generated by a multilayer Fe/Si monochromator was used (see Sections 3.4 and 4.2.2) [95]. The monochromatic beam is allowed through the D17 by stopping the choppers and rotating the collimator by 4°, whereas the contamination by long-wavelength neutrons is removed by the monochromator.

2.4.2.3 Data reduction and data analysis

The reduction process of the PNR data converts the large volume of produced data into datasets with physical units [96]. Different software/programs were used to reduce the

data obtained during our experiments. For instance, the data collected from the D17 was visualised and treated using the Large Array Manipulation Program (LAMP). LAMP was initially designed specifically for processing neutron-scattering data collected at ILL before becoming a general piece of software to analyse data in the IDL language[2] [97, 98].

LAMP allows the user to define the background region to be subtracted from the data based on the direct beam. It also offers three choices for rebinning the data: the default 'smpl' method, 'tth' and 'q'. The default mode keeps the data in a (x-pixel, scan) space which is ideal for visualising the data for samples with defined and narrow specular reflectivity, and a minimum off-specular contribution. The second mode, 'tth', presents the data in a (2θ, scan) space which is a useful presentation mode for bent or faceted samples as it calculates Q_z based on the assumption that $\theta_{\text{incident}} = 2\theta/2$. Furthermore, the third mode,'q', converts the data into a (p_i-p_f,p_i+p_f) scan which is suitable for analysing the data of a rough multilayered sample which has a significant off-specular contribution as it interpolates the data onto a central pixel and then subtracts the background to the same Q_z value [97]. The former and the latter modes were used to process the data for the NiO(111)/EuO and the $LaAlO_3$/EuO(001) heterostructures, respectively.

Full polarisation analyses were carried out during the experiments, and the data were then corrected for the polarisation inefficiencies. Footprint corrections were also implemented, and a careful selection of a scaling factor was chosen to stitch the data for the low and high q.

On the other hand, POLREF data were reduced using the Manipulation and Analysis Toolkit for Instrument Data (Mantid) [96, 99]. Mantid runs in the *C++* language and python bindings while ParaView was used as the visualisation tool. A good choice of the stitching factor is also required to stitch the low, mid- and high q angles as in LAMP. After that, the data processed with LAMP and Mantid were exported and both were fitted using the GenX software [100]. GenX utilises a differential evolution algorithm, a genetic algorithm to fit the X-ray and neutron reflectivity data[3]. This algorithm is ideal for fitting reflectivity data as it prevents the fitted parameter to be trapped in the local minima [100]. The quality of the fits is then assessed based on the figure-of-merit (FOM) function. During the fitting run, the data and the simulation curves are continuously evaluated against an algorithmic scale, and a small FOM value is obtained when a good agreement between the raw data and the simulation is achieved. The optimisation of the fits was judged by the least-squares technique of the χ^2 value. This method asses sees the quality of reproduction of a given parameter, a,

[2]IDL: Interactive Data Language

[3]The genetic algorithm is an optimisation technique used to solve constrained and unconstrained optimisation or search problems. This method alters the population of individual solutions repeatedly, and randomly chooses individuals from a current parent and uses them as parents to generate new solutions until an optimal solution is reached over successive iteration runs [101].

and it is given by:

$$\chi^2 = \sum_{j=1}^{N_j} w_j \sum_i, l^{N_i} (O_j^{\exp}(i) - O_j^{\mathrm{mod}}(i,a))(M^{-1})_{il}(O_j^{\exp}(l) - O_j^{\mathrm{mod}}(l,a)), \tag{2.45}$$

where $O_i^{\exp}$ and $O_j^{\mathrm{mod}}(i,a)$ are the experimental and model values obtained for the observable jth in the i argument. Furthermore, M is the experimental covariance from which the uncertainty of the experiment can be obtained, and it is expressed as:

$$M_{il} = < \Delta r(Q_i) \Delta r(Q_l) > . \tag{2.46}$$

Here, $\Delta r(Q_i)$ and $\Delta r(Q_i)$ are the total error [86].

GenX allows the user to create a fitting model using the sample structure, define the fitted parameters and set the fitting range by adjusting the minimum and maximum values for each parameter. Constructing a proper model is a crucial step to achieve a good fit with GenX. PNR data contains many fitted parameters such as the sample's thickness (z), roughness (σ), density (ρ), coherent scattering length (b), number density (N) and magnetic moment (μ_B). Therefore, z and σ (obtained from the XRR measurements), b (found in the tables in Ref. [87, 102]) and N (calculated using the bulk density of the material) were fixed for all the layers at the start of the fitting procedure. More or different parameters were then allowed to vary at each iteration to optimise the fit. For example, only the layer thicknesses and roughnesses were allowed to change, and then the magnetic moment, etc. However, b was always kept constant while fitting ρ. Different models were tested and many attempts were carried out to ensure that the fit is fully converged into meaningful physical results, even when all the parameters were free to vary. More on the fitting procedures is discussed in Chapter 3, Chapter 4 and Chapter 5.

2.4.2.4 Bayesian uncertainty analysis for PNR measurements

A brief introduction to basic concepts of the Bayesian analysis, without the use of mathematical equations (which are beyond the scope of the thesis), is presented here. I refer the interested reader to [103] for a comprehensive understanding.

Bayesian uncertainty is a statistical method based on Baye's theorem which computes the probability distributions of unknown parameters in a specific model based on background knowledge [104]. In contrast, classical statistics calculates the probability of an event in the long run of experiment and counts its frequency of occurrence, and it is known as frequentist statistics [105]. Furthermore, the main difference between the two methods is that the

parameter of interest is presumed to be unknown of a fixed value (i.e. to have one true value) in frequentism, whereas the Bayesian statistics describes all unknown parameters by probability distributions [104].

Bayesian statistics is based on three components; the background knowledge (posterior inference) which is represented by a normal distribution. The second component, the information obtained from the collected data themselves (likelihood function). The third component is the posterior inference which is the combination of the posterior inference and the likelihood function. In this method, the distribution width (variance) reflects the level of uncertainty of the population value of a particular parameter, and the height difference indicates the difference in the likelihood of different values [106]. Therefore, the smaller the variance, the higher the precision.

The correlations between two parameters of the same model can be obtained from what is known as joint posterior distributions (Figure 2.18 (a)). Also, the marginal posterior distribution of each parameter can be extracted from the joint posterior distribution by changing the view angle of the latter. For instance, the marginal posterior distribution of parameter 2 (Figure 2.18 (b)) of a two-parameter model can be obtained by looking at the model's joint posterior distribution (Figure 2.18 (a)) from the y-axis and ignoring the x-axis. Furthermore, the marginal distribution of parameter 1 (Figure 2.18 (c)) is extracted by looking at the joint posterior distribution curve from the x-axis and ignoring the y-axis, whereas the dashed lines represent the prior distribution of the parameter [107].

Bayesian uncertainty analysis was used in this thesis to assess the accuracy of the estimated PNR fitted parameters. For this purpose, the prior knowledge about the sample such as the thickness and roughness of the layers, the coherent scattering length of the material and the density profile is needed to construct the model. Note that the Bayesian statistics

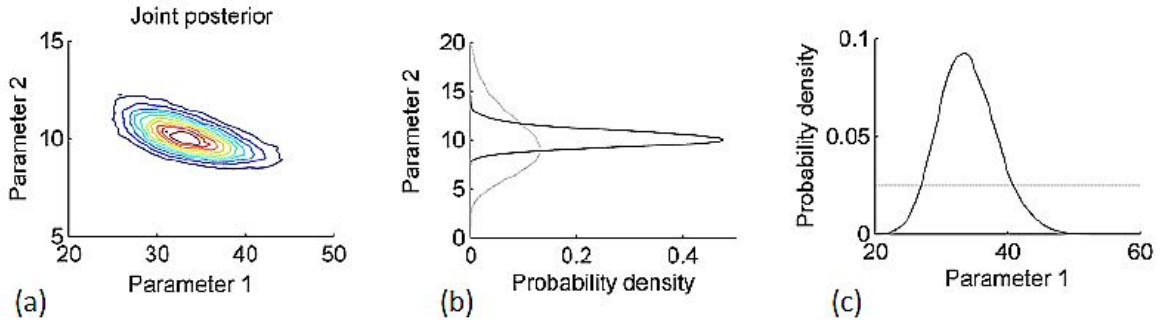

Fig. 2.18 : (a) A joint posterior distribution of a two-parameter model. (b)-(c) The obtained marginal distributions of parameters 2 and 1, respectively, (solid lines); the dashed lines represent the prior distributions of the parameters. The figure is taken from Ref. [107].

presented in this thesis was carried out by Dr Timothy Charlton using the Refl1D program which produces probability distribution histograms and parameter-parameter correlation simulations (See Section 5.3) [108].

2.4.3 Low-energy muon spin relaxation

Muon spin relaxation (μSR) is a technique used to probe the structural and magnetic dynamics of materials down to a microscopic level. This is done by implanting polarised muons in the sample of interest and detecting the effect of the sample's local field on the spin of the muons [109–112], where the μ acronym stands for the spin rotation, relaxation, or the resonance of the muons [111, 113].

The principle of the μSR experimental setup can be divided into several stages:

Muon generation: Muons are produced naturally as a result of the interaction of high-energy particles with atomic nuclei of the gases in the atmosphere [114]. However, for μSR experiments, muons are generated from pions, $\pi^{\pm}$, which are produced when a high-energy beam of protons ($\sim$4 MeV) hits a light-element target, usually graphite. The bombardment of the target's protons (p) and neutrons (n) with the incoming protons results in the creation of $\pi^{\pm}$ [112, 114]:

$$p + p \rightarrow p + n + \pi^{+} \qquad p + n \rightarrow p + p + \pi^{-}. \tag{2.47}$$

π^{+} has a lifetime $\tau_{\pi^{+}}$=26 ns before it decays by a weak interaction of a two-body decay process into a muon (μ) and a muon neutrino (ν_{μ}) [112, 114]. For the conservation of momentum, when the decaying π^{+} is at rest, μ and ν_{μ} are emitted in opposite directions. Also, since $\pi^{\pm}$ is a zero-spin particle, and the neutrino's spin is opposite to its momentum, a 100% polarised muon beam is produced along the direction of emission [109, 115].

$$\pi^{+} \rightarrow \mu^{+} + \nu_{\mu} \qquad \pi^{-} \rightarrow \mu^{-} + \bar{\nu_{\mu}} \tag{2.48}$$

Property	value
mass (m)	105.7 MeV/c^2
charge (q)	+1.602$\times 10^{-19}$ C
Spin (S)	½
magnetic moment (μ_{μ^+})	0.000488 μ_B
gyromagnetic ratio (γ)	136 kHz/mT
lifetime (t_{μ^+})	2.197 μs

Table 2.2: Properties of the muon, where m_e is the mass of the electron

Equ. (2.48) describes the processes that produce positive and negative muons ($\mu^{\pm}$) from the corresponding pions. μ^{+} is usually used in the investigation of condensed matter [110, 111], while μ^{-} is captured by the sample's atomic nuclei [115–117]. Therefore, only μ^{+} is considered in this thesis, and it will be referred to it simply as the muon (μ). A summary of the muon's properties is given in Table 2.2.

Interaction of muons with the sample: Once inside the sample, muons evolve and precess in response to the internal field at the local muon sites [110]. However, due to inelastic scattering, such as Coulomb interactions, muons lose their momentum [111, 115], but since only electrostatic interactions take place, they preserve their spins [119]. Muons can also relax and lose a little of their spin polarisation in the presence of static or dynamic local field [116], and this process is known as thermalisation.

On the other hand, inside insulating and semiconducting materials, low energy muons will repeatedly pair up with and release an electron forming a diamagnetic state known as

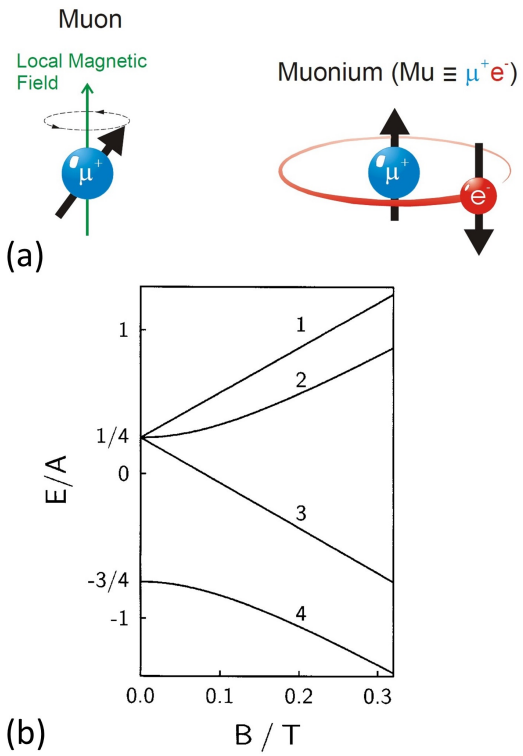

Fig. 2.19 (a) The creation of a muonium state via the coupling of muon with an electron, the image is taken from Ref. [118]. (b) Breit-Rabi diagram of a muonium in vacuum with a hyperfine constant of 4463 MHz which shows the splitting of the energy level into a triplet and singlet states, graph is taken from Ref. [109].

muonium, Mu [111, 112, 114, 120]. At this state, μ^+ and e are coupled by the hyperfine interaction which will split the energy level into higher and lower energy levels, triplet and singlet states, respectively, as shown in Figure 2.19, in which the former level will further split in the presence of a magnetic field [109]. Mu has not been reported in good metals [121], and this is because the free conduction electrons form clouds surrounding μ^+. Therefore, thermalisation in metals takes place in the form of free paramagnetic muons [120]. As a result, muons lose their energy at a high rate and slow down until they eventually come to rest [112, 114].

Muon decay: Muons are unstable, and it decays by a three-body process into a positron (e^+) and two neutrinos (ν_e and $\bar{\nu}_\mu$) [111]:

$$\mu^+ \rightarrow e^+ + \nu_e + \bar{\nu}_\mu \tag{2.49}$$

Detection: e^+ is then emitted from the sample, preferentially in the direction of the muon spin prior to the decay. Thus, providing details on the muon spin interaction within the measured sample by reconstructing the change in muon spin direction as a function of time [111, 114]. Details on how the detectors at LEM work can be found in Ref. [122].

μSR Experimental setup

A typical μSR setup is shown in Figure 2.20. Since muons decay in an asymmetric fashion, at least two detectors, backwards (B) and forwards (F), relative to the initial path of muons, are needed to count the number of emitted e^+ and their direction. The muon's polarisation as a function of time can also be obtained by measuring their decay asymmetry which is defined as [119]:

$$A(t) = \frac{N_F - \alpha N_B}{N_F + \alpha N_B}. \tag{2.50}$$

In an ideal situation, $A(t)$ at $t = 0$ is expected to be 33.3 %. However, due to many factors, such as the efficiency of the detectors and the stopping of some muons in the beamline apparatus, this value is reduced to $\sim$ 25 % and this is considered as the typical $A(t = 0)$ value [121]. N_F and N_B are the number of detected e^+ by the F and B detectors, and α is the detector efficiency which is defined by many factors such as the position of the sample and the detector geometries [115].

μSR can be operated in three different modes: longitudinal field (LF), transverse field (TF) and Zero-field (ZF). In LF and TF configurations, an external magnetic field is applied parallel and perpendicular to the direction of the initial muon polarisation, respectively, whereas muons are implanted into a sample with zero applied field in the ZF mode. The

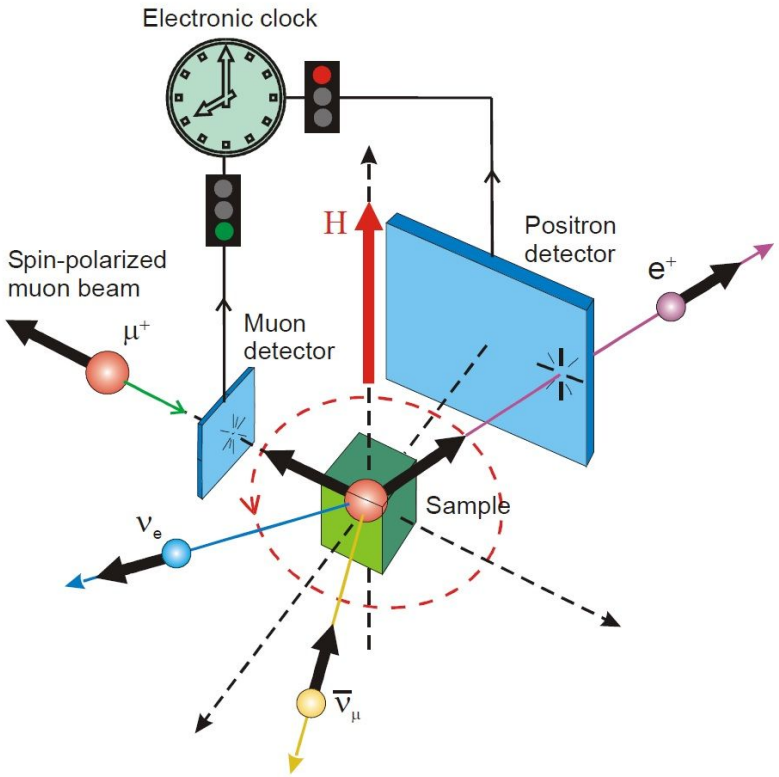

Fig. 2.20 A schematic diagram of a typical μSR setup in a TF mode. The image is taken from Ref. [118].

latter is performed to investigate the depolarisation (i.e. relaxation) of the implanted muons which may arise from irreversible processes such the flipping of muon spin as a result of the hyperfine interactions between muons, electrons and the atomic nuclei [115]. Dephasing of the muon spin may also occur due to the static distribution or the fluctuating of the internal field [121]. It is also suitable for detecting very weak magnetism [118]. Therefore, ZF is an ideal configuration for studying short and long-range magnetic ordering as well as magnetic phase separation [23]. In short, the principle of the μSR technique is to investigate the change in muon polarisation as a function of time [111].

The advantages of this technique are: its high sensitivity to the internal magnetism of the samples [113]. It can detect very small magnetic fields due to their large magnetic moment and γ_μ value [111, 117]. As a fully polarised muon beam is used, ZF measurements can be carried out to study the microscopic magnetic properties of the samples [117]. On the other hand, the drawback of this technique is the short experimental time frame due to the short t_μ, and the difficulties of specifying the exact stopping sites [115].

High-energy muons have a penetration depth of a few mm. Therefore, low-energy muons were created to study thin films, in which muons are stopped by a moderator before it goes through successive re-acceleration phases with an applied electric field [114]. Therefore low-energy μSR in ZF and TF modes were used to study the interface of $EuO/LaAlO_3$ presented in Chapter 3.

LEM

μSR can be operated using a pulsed or continuous beam. The μSR results presented in Chapter 3 were collected using the latter approach at the LEM beamline at PSI. In this mode, only a single muon is implanted into the sample at a time [114]. The arrival of muons into the sample is determined using a start detector placed just upstream of the sample, and their decay is recorded by the positron detectors [111]. Therefore, measurements can be done with higher timing resolution using a continuous beamline in comparison with a pulsed source [119].

At LEM, muons with an energy of ∼4 MeV, pass through a moderator made of a silver substrate with a thin film of deposited nitrogen, cooled down by a He cryostat to ∼ 10 K.

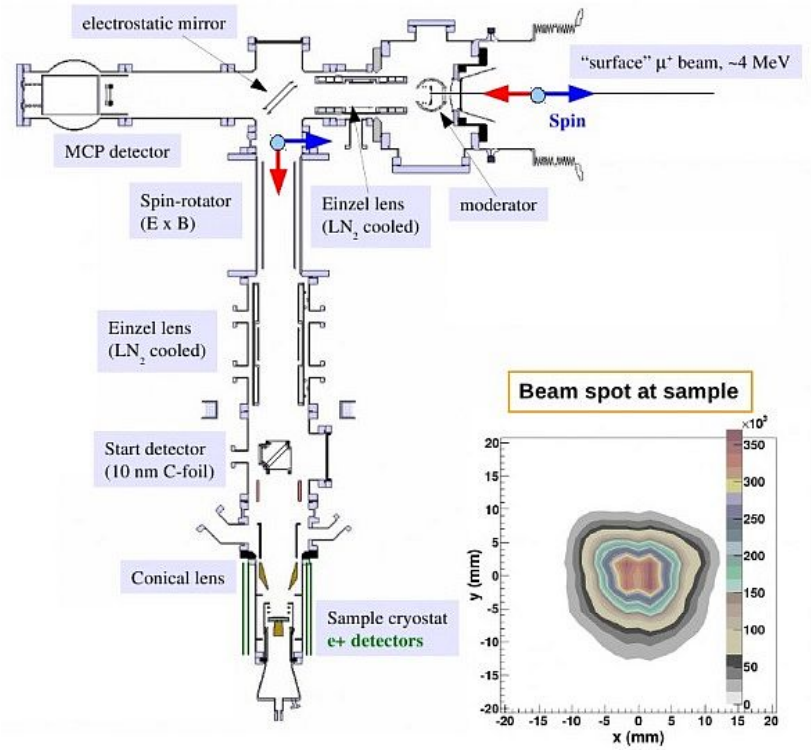

Fig. 2.21 A schematic diagram of the LEM beamline at PSI, Switzerland, showing the main components of the setup. Figure is taken from Ref. [123].

Slow muons can then be accelerated up to 20 keV and separated from the main beam by a special electromagnetic system as shown in Figure 2.21. Measurements at LEM can be carried out between 2.5 and 570 K, with an applied field of up to 0.34 T [123]. The energy range of the generated slow muons leads to a penetration depth of subnanometre to hundreds of nanometres which makes it an ideal setup to study the interfaces of thin films. At this beamline, samples can be investigated in ZF-, TF- and LF- modes. Further details of LEM can be found in Ref. [123].

2.4.3.1 Data analysis

μSR data were fitted using the Windows Muons Data Analysis (WiMDA) analysis package which allows for online and off-line data analysis [124]. A detailed description of the fitting procedure for the μSR data is discussed in Chapter 3.

3

EuO-$LaAlO_3$ Interface

Oxides play a critical role in modern electronic applications as they exhibit excellent physical, magnetic and conductivity properties, particularly when they are grown in heterostructures. Recently, new functional features were found at the interfaces of oxide heterostructures while leaving their bulk properties unchanged. For example, a two-dimensional electron gas (2DEG) is formed when the carriers of a particular system are confined in a potential well and their motion is restricted in a quantised 2D K-momentum plane normal to the confining potential [125]. For instance, these conducting carriers were found to be localised a few nanometres away from the interface of polar/non-polar heterostructures, and superconductivity was even reported at the $LaAlO_3$/STO interface [126]. The formation of 2DEGs in oxide heterostructures has attracted great attention as high electron densities have been detected in such structures, almost two orders of magnitude higher than those measured in semiconductor heterostructures [127]. Therefore, they are expected to have a wide range of technological applications such as in oxide-field-effect devices, transparent transistors and high-frequency filters [127].

This chapter reviews the experimental work carried out to investigate the non-polar/polar EuO(001)/$LaAlO_3$(001) interface. Europium monoxide (EuO) is a ferromagnetic semicon-

ductor that drew attention for its ability to manipulate a spin-polarised electric current and for its high magnetic moment (7 μ_B per Eu atom) besides other excellent properties as described in this chapter [128, 129]. Section 3.1 discusses the properties of EuO and $LaAlO_3$ and explains the theory which predicts the formation of a 2DEG at their interface. Sample fabrication and their structural and magnetic properties are presented in Section 3.2. Section 3.3 and 3.4 discuss extensively the μSR and PNR experiments carried out to investigate the interface of EuO/LAO, and conclusions provided in Section 3.5 summarise the results and highlight the future work suggested for this project.

3.1 Introduction

3.1.1 Properties of EuO

EuO crystallises into an *fcc* rocksalt structure, space group $Fm\bar{3}m$ with a lattice parameter $a = 5.144$ Å as shown in Figure 3.1 [130, 131]. EuO is a paramagnetic semiconductor with a large band gap of 1.1 eV at RT between the half-filled $4f$ states and the $5d$ conduction band (CB) [130, 132]. The CB of a stoichiometric EuO comprises the unoccupied Eu $5d$ and $6s$ states that lie at lower and higher energy levels, respectively, where the O $2p$ states are the highest occupied valence band (VB) and are positioned well below the Fermi energy (E_f) [133, 134]. The bulk EuO becomes a ferromagnet below the Curie temperature (T_C) of 69 K, and the Zeeman field created by the $7e^-$ occupying the $4f$ orbital spin-splits the CB by a large exchange splitting of $0.54 - 0.6$ eV into lower (spin-up) and higher (spin-down) states below its T_C. Therefore, EuO can produce a nearly 100% spin-polarised current (i.e. EuO is considered as a half-metal) and thus can be used as a spin filter in tunnel

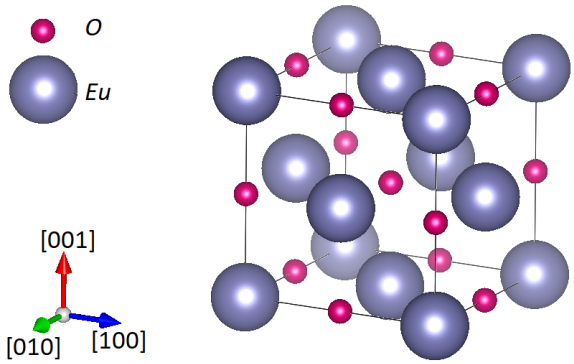

Fig. 3.1 : The *fcc* rocksalt crystallographic structure of pristine EuO in which the small magenta and large blue spheres represent the O and Eu atoms, respectively.

junctions [132, 135]. The easy and hard magnetic axes of pristine EuO are oriented along the [111] and [100] directions, respectively, with a small magnetocrystalline anisotropy constant ($K_1 = -4.36 \times 10^5$ erg/cm^3) at 2 K [130].

The high magnetic moment of EuO (7 μ_B/Eu atom) arises from the localisation of the Eu^{2+} $4f^7$ between the VB and CB, well below the Fermi level (E_f). The effect of the crystal field is negligible due to this localisation. Therefore, Hund's rules apply to the 7 e^- of the $4f$ orbital. Thus, they align parallel to each other and yield $S = 7/2$ at the Eu^2+ ions [23, 134, 136].

EuO is considered as an ideal Heisenberg ferromagnet [130, 132], where the Heisenberg Hamiltonian ($\hat{H}$) is given by:

$$\hat{H} = -\sum_{i \neq j} J_{ij} \hat{S}_i \cdot \hat{S}_j, \tag{3.1}$$

J_{ij} indicates the interaction strength between adjacent spins $\hat{S}_i$ and $\hat{S}_j$ where i and j are two different sites in the lattice [23]. As a result of the localisation of the $4f$ state, the exchange coupling between the Eu^{2+} ions will take place via indirect (J_1) and superexchange (J_2) mechanisms rather than the direct overlap of the $4f$ state [137]. J_{ij} can be either a positive or negative value depending on the spin interaction of the neighbouring Eu atoms. For instance, a positive J_{ij} indicates a ferromagnetic alignment of the spins of adjacent Eu atoms, while a negative value is for the antiferromagnetic interaction. For EuO, these parameters were measured by neutron scattering to be $J_1/k_B = (0.606 \pm 0.008)$ K and $J_2/k_B = (0.119 \pm 0.015)$ K [137].

J_1 is known as an indirect exchange or Ruderman-Kittel-Kasuya-Yosida (RKKY) interaction in which a $4f$ electron of one Eu atom is transferred into an unoccupied $5d$ CB and couples ferromagnetically to the $4f$ spin of the nearest neighbouring Eu atom via d - f exchange interaction, before it returns to its initial state. This is because the wave functions of the $5d$ can extend more than those of the $4f$ to overlap and create an unoccupied CB [136, 137].

On the other hand, J_2 is a form of a superexchange interaction which occurs between one Eu atom and its next-nearest neighbouring (NNN) Eu atom through the $2p$ state of a non-magnetic anionic site (O) which can take place via different mechanisms: i) Kramers-Anderson, ii) d-f exchange interaction or iii) crossed term between the Kramers-Anderson and d-f interactions [23, 136]. The **Kramers-Anderson** interactions occur as a result of the transfer of a $4f$ electron of one Eu atom to its NNN Eu atom $4f$ orbital via the O $2p$ state. Although the EuO CB is empty, there is still a ferromagnetic interaction between the $4f$ and the CB. However, in the ***d-f* superexchange interactions**, the O $2p$ electron is transferred to the Eu $5d$ CB which will then experience a d - f interaction. A much weaker interaction,

s-f, can also occur but it has a negligible contribution to J_2 [136]. Finally, the **crossed term** occurs when an interchange between the two mechanisms takes place.

The drawback of using EuO in spintronic applications, normally its low T_C of 69 K, has been overcome by electronic doping such as introducing oxygen-vacancies, doping EuO with another element such as Gd or La, or changing the lattice parameter by applying strain to the EuO crystal [130, 138]. The enhancement of the T_C is always identified by a characteristic double-dome feature in the *M(T)* curve and its deviation from the Brillouin function. An increase in the T_C up to 140 K has been reported using the former method [139]. Also, the electrical resistivity of doped EuO drops significantly (by 12 orders of magnitude) below T_C, experiencing an insulator-to-metal transition (IMT) [140]. Furthermore, an increase above 200 K was measured when a hydrostatic pressure ($0-23$ GPa) was applied to the EuO [141].

The origin of the increase of the ordering temperature is still ambiguous [130]. Two scenarios have been suggested: bound magnetic polarons (BMP) and indirect exchange by a RKKY-type interaction [130, 142]. The former theory was postulated by Torrance *et al.* to explain the IMT behaviour that is observed in EuO_{1-x} below T_C. At $T < T_C$ heavy carriers are formed as a result of the exchange interaction between the localised Eu $4f$ which are then bound to the deep local donor states of oxygen vacancies and polarise their surrounding $4f$ electrons. However, at $T > T_C$, these magnetic polaron states are released to the CB forming new states between the ferromagnetic and paramagnetic levels which leads to a phase separation, i.e. ferromagnetic and paramagnetic phases coexist [133, 140]. When EuO is doped with rare earth metals such as La and Gd, the dopant element creates free electrons by replacing the Eu^{2+} with a trivalent ion such as Gd^{3+}[133], increasing the number of conduction electrons which are involved in a RKKY-type interaction and thus increasing the magnetic moment to 7.13 μ_B [139]. Therefore, T_C was found to increase with increasing the doping concentration. However, each missing O anion in EuO_{1-x} should produce two electrons to take part in the exchange interaction but only one is considered, as the second is still described as a localised e^- [134]. Doped EuO is, however, beyond the scope of this thesis, so it will not be discussed any further.

A significant challenge lies in growing pristine, defect-free EuO thin films as EuO is a metastable phase of europium oxide which readily oxidises further to form the more stable, non-magnetic oxide phase, Eu_2O_3. Therefore, a precise growth protocol must be followed (see Section 3.2.2).

3.1.2 Properties of $LaAlO_3$

The single crystal perovskite oxide, lanthanum aluminate, $LaAlO_3$ (LAO), is used as one of the most common substrates due to its excellent physical, chemical and electronic properties

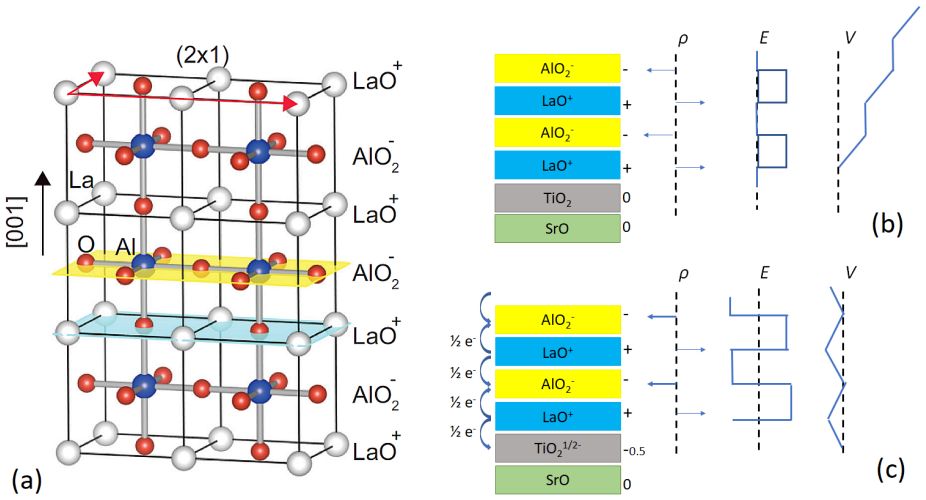

Fig. 3.2 : (a) Cubic crystal structure of the perovskite $LaAlO_3$ showing the alternating LaO^+ and AlO_2^- planes (The figure is taking from Ref. [152]). The variation of the electric potential (V), net charge (ρ) and electric field (E) across the LAO planes due to the polar catastrophe (b) and (c) the transfer of half an electron per unit cell from the LaO^+ layers to the adjacent layers which leads to the formation of the 2DEG in a TiO_2-terminated $SrTiO_3$(001) substrate.

[143]. It has a high melting point of 2180 °C [144], a dielectric constant of 25-30 [145], and a large band gap of 5.6 eV [146]. However, the disadvantage of using LAO substrates is the twinning effect of the crystal at low temperatures ($T < 820$ K) which is caused by the formation of domain structures with the cations shifted from their equilibrium positions [147].

LAO crystallises into a bulk rhombohedral crystal (space group $R\bar{3}c$) at room temperature with a pseudocubic lattice constant of 3.79 Å [147, 148], but it experiences a phase transition into a simple cubic structure at ~820 K with a minimal geometry distortion [143, 149]. A unit cell of LAO consists of two cations (La^{3+} and Al^{3+}) and three anions (O^{2-}) [150]. The latter bind with La^+ and Al^+ forming oxygen octahedra which define the crystal structure of the perovskite unit cell [150]. Therefore, LAO(001) is usually presented by alternating polar planes LaO^+ and AlO_2^- whereas the bulk LAO remains neutral as shown in Figure 3.2 (a). Hence, LAO(001) creates a robust polar surface.

In a simple ionic picture in the bulk LAO structure, LaO^+ planes can be imagined to donate half an electron per unit cell (u.c.) to the adjacent AlO_2^- planes as shown in Figure 3.2 (b) and (c). However, due to the breaking of symmetry at the surface along the [001] direction, excess or deficient 0.5 e^- per u.c. will form (depending on the surface termination of the LAO), due to the missing AlO_2^- or LaO^+ plane [151].

3.1.3 2DEGs at the interface of oxide heterostructures

2DEGs have been reported to occur at different oxide heterostructures, especially between polar/non-polar perovskite insulators such as at the interface of $LaAlO_3/SrTiO_3$ (LAO/STO) [153–156]. However, the origin of this effect is still under debate and different mechanisms have been suggested such as the polar catastrophe and the creation of oxygen vacancies [9, 127, 156–158]. A polar catastrophe, in which a polarity discontinuity occurs at the interface of the oxide layers, and as a result, a new electronic reconstruction occurs at the interface to compensate for this polarity discontinuity, is the widely accepted model to drive the formation of the 2DEG in oxide heterostructures [126]. This is because the electrostatic potential difference across the LAO which arises from the alternating planes leads to intrinsic ionic reconstruction at the interface. This involves a transfer of electrons from the LAO layer into the conduction band (CB) of the adjacent layer, thus forming a conductive interface [126, 154]. Figure 3.2 (b) shows the divergence of the electrostatic potential with increasing LAO thickness as a result of the polar discontinuity. Half of an electron per u.c. is then transferred from the LAO to the non-polar layer to avoid the divergence in the electrostatic potential (Figure 3.2 (c)), neutralising the overall structure and forming a 2DEG at the interface [10, 127]. This model predicts precisely the critical thickness, t_c, of the LAO film required for observing the 2DEG [154]. It was also found to provide a physical explanation for most of the 2DEG features detected in oxide heterostructures, although some discrepancy between the measured carrier density and that predicted by this model has been recorded [126].

The creation of oxygen vacancies during the sample preparation was proposed, as it is considered as one of the most common structural defects in oxides, and thus they can be produced in high concentrations [159]. In this scenario, oxygen vacancies are proposed to act as electron donors by creating a shallow donor state just below the STO CB [147]. 2DEG was observed in STO/LAO when oxygen vacancies were introduced to the system by growing the samples in a certain oxygen partial pressure and/or post-annealing them in oxygen as reported in Ref. [160, 161].

A 2DEG was also suggested to form at the interface of a polar oxide and a ferromagnetic insulator such as LAO(001)/EuO(001) [10, 9]. Lee *et al.* investigated the interface of pristine EuO and a LaO^+-terminated stoichiometric LAO layer to allow for a finite electric field in the LAO film along the EuO(001)/LAO(001) direction. By using DFT calculations, they found that the electrostatic doping introduces 0.025 e^-/Eu atom into the EuO layer as shown in the schematic diagram of the energy bands of EuO and LAO at the interface illustrated in Figure 3.3. The study also estimated that t_c must be at least 15.3 Å for the LAO thickness to build-up an efficient electrostatic potential to overcome the energy difference of 3.3 eV

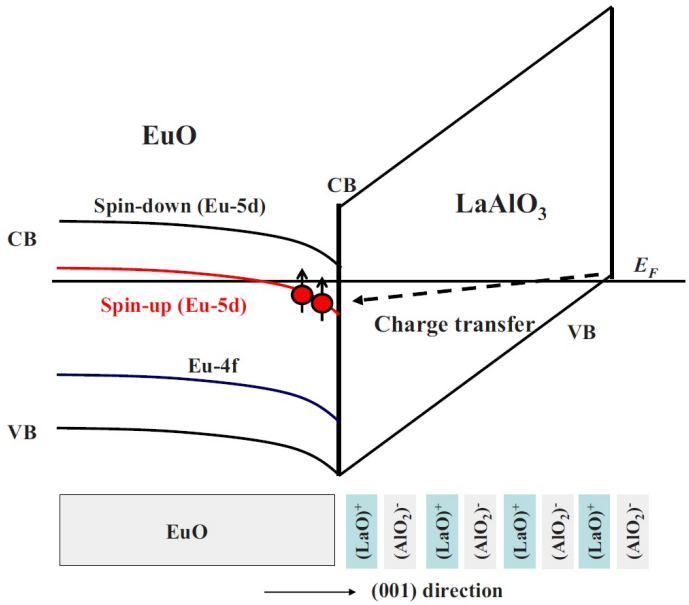

Fig. 3.3 : A schematic diagram illustrating the proposed transfer of electrons from LAO into EuO layer during the electrostatic doping process. Figure is adopted from Ref. [9].

between the Eu 5*d* spin-up and the O 2*p* orbital. Thus, only above this thickness it transfer carriers into the EuO surface. They also estimated a charge density of $\sim 4.0 \times 10^{13}$ cm^{-2} to be transferred into the EuO edge, forming a 100% spin-polarised 2DEG within the first 10 Å of the EuO film from the interface and increasing the T_C of spin-polarised EuO by 35 K. The localisation of the charge carriers in the EuO side of the interface was attributed to the bending of the electrostatic bands at the interface.

Furthermore, Wang *et al.* investigated the interface of EuO(001) with a non-stoichiometric LAO layer (terminated with LAO$^-$ on both sides). They suggested that an "extra" electron will be transferred from the non-stoichiometric LAO to the CB of the EuO, and since the EuO CB is spin-split due to the exchange splitting of the 5*d* states, a polarised 2DEG is formed below the T_C of EuO. Although their first-principles calculations showed that at the interface the O$^-$ were displaced from their original position with respect to the positive cations (i.e. Eu$^+$, La$^+$ and Al$^+$), thereby distorting the interface polarity, the atoms far away from the interface reverted to their original positions of their bulk structures. The density of states revealed that the VBs of the first monolayers (away from the interface) of the EuO and the LaO$^+$-terminated LAO are occupied below the Fermi energy (E_f) with a large mismatch between the majority and minority spins. The authors have taken this as indicative of the formation of a spin-polarised *n*-type 2DEG. They also attributed the spin-splitting observed in the LAO layer to be the result of the exchange interactions of the La 5*d* with the Eu 4*f*

states across the interface. However, due to the large difference between the CB and VB of the LAO in comparison to that in the EuO, and since the EuO CB lies below that of the LAO, the 2DEG was found to accumulate mainly in the EuO interface layer.

3.2 Sample preparation

For our measurements, the EuO film was grown on an LAO(001) substrate using magnetron sputtering. The film was subsequently capped with Au to prevent the oxidation of the EuO to the most stable oxide phase (Eu_2O_3). A 1 mm thick substrate was used to avoid sample bending which would affect the PNR measurements and to ensure that the t_c is surpassed.

As discussed in the previous section, the realisation of the 2DEG requires a single LaO^+-terminated LAO film as the AlO_2^--termination is an insulating layer [126]. Therefore, preparing the LAO surface was the initial step for fabricating the samples before growing the EuO layer.

3.2.1 Preparation of $LaAlO_3$ substrate

Wet etching, followed by heat treatment in oxygen flow has been reported to produce a single-terminated LaO^+ surface. The chemical reactivity and the solubility of La and Al were taken into account while choosing the appropriate chemical etchant. This is because the wet etching for ABO_3 perovskites was proposed to take place in two steps to create and dissolve the hydroxide as follow [162]:

$$AO_{(s)} \rightarrow A(OH)^n_{(s)} \rightarrow A(OH)^n_{(aq)} \tag{3.2}$$

and

$$BO_{2(s)} \rightarrow B(OH)^m_{(s)} \rightarrow B(OH)^m_{(aq)}, \tag{3.3}$$

Where n and m vary depending on the valence of the cations, whereas (s) and (aq) stands for the solid and aqueous states, respectively.

Since LaO reacts only with acid, whereas Al reacts with both strong bases and acids, a strong base (NaOH) and a strong acid (HCl) were used to etch the AlO_2^- and LaO^+ layers, respectively [163]. The chemically-treated samples were then annealed at 1000 °C in oxygen flow. This is because thermal treatment induces surface reconstruction to obtain regular terraces and atomically flat surfaces [163, 164].

Wet etching

LaO^+-terminated LAO: To obtain the LaO^+-termination, a chemical etching process similar to that reported by Wan was adopted as it was confirmed to produce a single LaO^+-terminated LAO [163]. The substrate was immersed in 12 M NaOH solution for 45 minutes and then transferred into an ultrasonic bath for 15 minutes. The LAO was then placed in a less concentrated NaOH solution of 4 M and etched for an additional 15 minutes before it was ultrasonicated for 10 minutes. The substrate was then rinsed with DI water and followed by cleaning in Isopropanol (IPA). This step is crucial because AlO^{2-} will form insoluble Al(OH) in response to a sudden substantial change in the pH value between the 4 M NaOH (pH=14) and that of DI (pH=7), which will then crystallise into Al_2O_3 particles during the annealing process [163].
AlO_2-terminated LAO: The substrate was soaked in 27-34% concentrated HCl for 5 minutes before it was rinsed with DI water and then with IPA. This method was reported in Ref. [164–166] to produce a single AlO_2^--terminated LAO by selectively etching the LaO^+.

Heat treatment

The samples were then transferred into a one-zone furnace where they were heated at 1000 °C in oxygen flow. The setup was custom-made where the furnace chamber is connected via a gas line to a transparent cylinder containing thick oil-like liquid, and the oxygen flow rate was monitored by counting the number of bubbles/second forming at the surface of the liquid. AFM surface micrographs of the etched and annealed samples are presented in Figure 3.4 and 3.5. The heat treatment and the AFM scans were performed with the help of Dr Angelo Di Bernardo from the Department of Materials Science and Metallurgy at the University of Cambridge.

There has been a disagreement on whether thermal annealing by itself can promote a single-terminated LAO surface [165, 167]. Therefore, a test was also carried out on an as-received substrate. Figure 3.4 shows 2D micrographs of the as-received, HCl-etched and NaOH-etched LAO substrates after they have been heat-treated for 2.5 hours, 4 hours and 6 hours in oxygen. Small particles were formed on the surface of the as-received LAO substrate after 2.5 hours of annealing (Figure 3.4 (a)). However, irregular or incomplete terraces started to form after the 4-hour annealing (Figure 3.4 (d)). Figure 3.4 (b) shows underdeveloped terraces on the surface of the HCl-etched substrate after 2.5 hours of heat treatment. They started then to develop further after an extended (4-hour) annealing (Figure 3.4 (e)). On the other hand, NaOH-etched LAO shows irregular terraces after 2.5 hours of thermal annealing (Figure 3.4 (c)) which became more defined and regular after 4 hours of heating (Figure 3.4

(f)). However, annealing the sample for 6 hours induced surface defects as seen in Figure 3.4 (g). The absence of the small particles on the surface of the NaOH-etched LAO substrate indicates that the particulates, observed in Figure 3.4 (a) and (e), are not debris but rather an intermediate by-product of the annealing of AlO_2^-.

The attempt to produce LaO^+-terminated LAO was repeated on a NaOH-etched LAO for a higher oxygen flow rate of 6 bubbles/sec as compared to 4 bubbles/sec for the first test while fixing the annealing time to 4 hours. This resulted in clear and regular terraces with an average step height of ~ 4 Å which is equivalent to the LAO pseudocubic lattice parameter as shown in Figure 3.5 (b) [168]. On the other hand, the annealing time for the HCl-etched sample was increased to 6 hours (Figure 3.5 (a)). However, the AFM micrograph and the surface profile suggested mixed-terminated LAO as incomplete terraces with a variable step

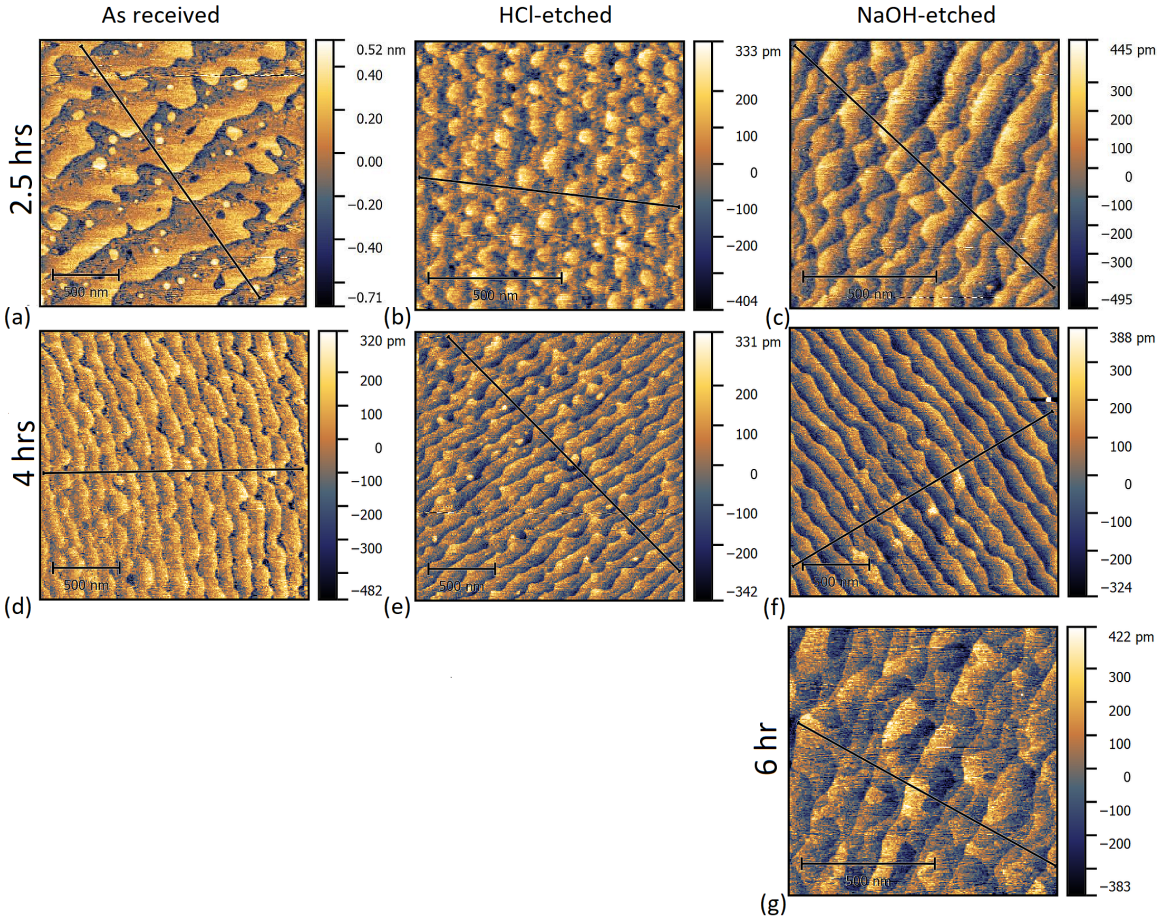

Fig. 3.4 : 2D AFM micrograph scans showing the effect of the annealing time on the uniformity of the terraces formed on the surface of as-received (a,d), HCl-etched (b,e), and NaOH-etched (c,f,g) LAO substrates after 2.5-, 4- and 6-hours of annealing at 1000 °C in oxygen.

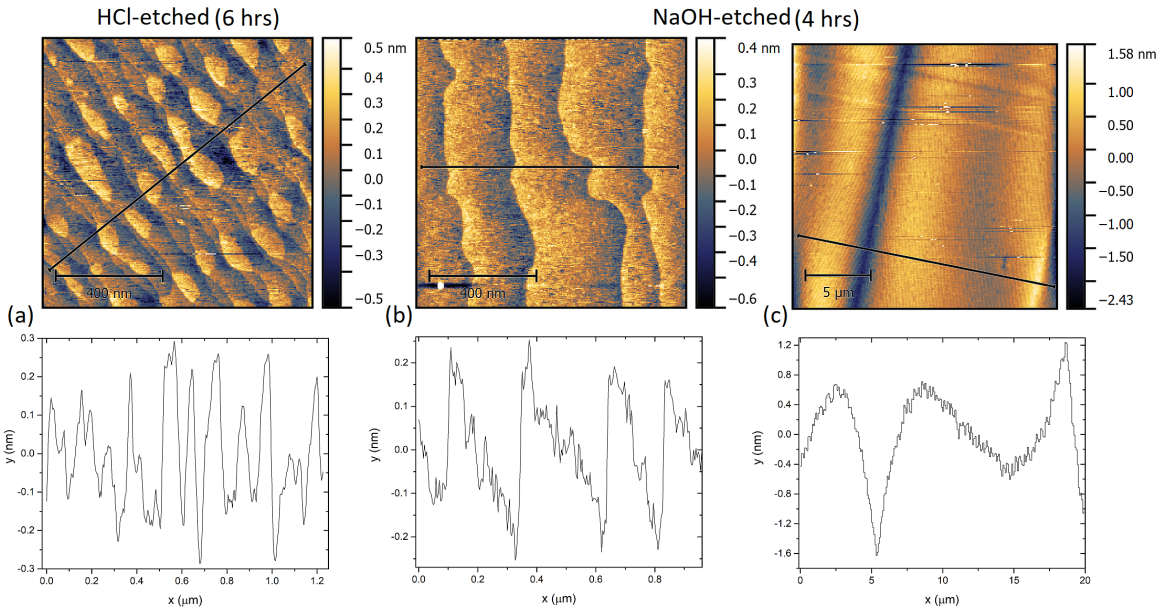

Fig. 3.5 : 2D AFM micrographs and surface profile of the terraces which form on the (a) mixed- and (b) single LaO^{+}-terminated LAO substrates after 6- and 4-hour oxygen heat treatment at 1000 °C, respectively. The twinning boundry of the LaO^{+}-single terminated LAO is shown in (c).

height and width across the surface are formed, and they are similar to those reported in Ref. [165] for a mixed-terminated LAO. The difference in the annealing time required for the single LaO^{+}- and AlO_2^{-}- LAO termination can be attributed to the large size of the La atoms in comparison to the Al atoms. Figure 3.5 (c) shows the twinning boundary of ∼15 µm of the single LaO^{+}-terminated sample. Due to time constraints, the development of a single AlO_2^{-}-terminated LAO was not carried further and the decision for studying the effect of the LaO^{+}- and mixed-terminated LAO on the creation of a 2DEG at the interface of EuO(001)/LAO(001) was made.

3.2.2 Growth of EuO

LAO substrates were ultrasonicated in acetone, followed by a rinse in IPA for 5 minutes each and then drying with a dry N_2 gas gun. The substrates were then transferred into the load-lock chamber were they were outgassed in ($\sim 1 \times 10^{-6}$ mTorr) vacuum at $\sim$ 180 °C three times for 5 minutes each to avoid overheating the samples. Then they were left for 1 hour to cool down. After that, the samples were transferred into the magnetron sputtering growth chamber of a base pressure of 1.4×10^{-8} Torr without breaking the vacuum. The EuO film was grown at RT by co-sputtering a 99.99 % pure Eu and a 99.99% Eu_2O_3 targets

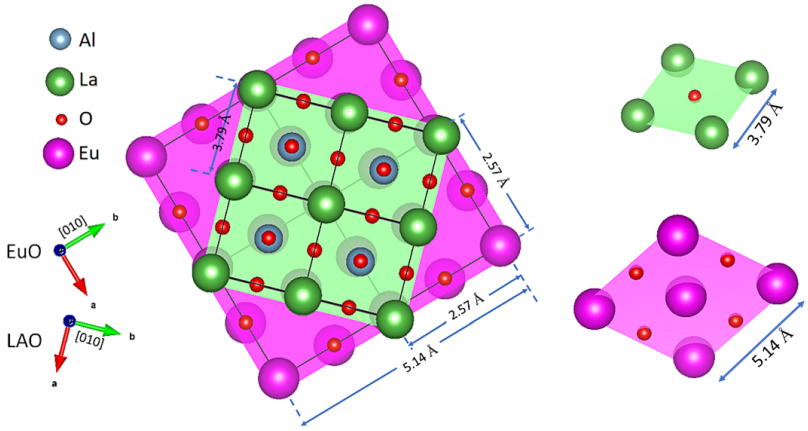

Fig. 3.6 : Bottom-view of the growth of a (2x2x1) slab EuO(001) on an LAO(001) substrate (2x2x2). EuO is rotated by 45 ° to minimise the lattice mismatch to $\sim 4.1\%$. The axes show the orientation of the two (001) planes with respect to each other, whereas the shaded planes are the (001) for LAO (green) and EuO (magenta).

in Ar^+ plasma. The growth conditions were kept constants throughout the process; an Ar^+ flow rate of 14 sccm [1], the RF and DC currents for the Eu_2O_3 and Eu targets at 80 W and 0.65 A, respectively, and at a pressure of 2 mTorr. These conditions produced a 50 nm thick stoichiometric EuO film at a deposition rate of 0.042 nm/s. 15 nm of Au capping layer was grown subsequently, at a rate of 0.072 nm/s, to prevent the oxidation of the EuO layer. Therefore, as-received, mixed- and a LaO^+-terminated LAO(001)/EuO (50 nm)/Au (15 nm) samples were grown at the same time.

A bottom view of the orientation of a (2x2x1) EuO(001) slab grown on an LAO(001) substrate (2x2x2) is illustrated in Figure 3.6. EuO(001) is expected to rotate by 45° in the (001) plane to reduce the lattice mismatch with the substrate. This will lead to a compressive strain of $\sim 4.1\%$ experienced by the first few EuO monolayers at the interface. However, the rest of the film will then relax to the crystal lattice of a stoichiometric EuO [9]. Therefore, EuO will undergo a tetragonal distortion $c/a = 0.95$ which has a minor effect on its electronic structure [10].

Structural characterisation

Stoichiometric EuO is a metastable material. Therefore, establishing a growth recipe for a pristine EuO requires precise control of the Eu:O flux to avoid the formation of the most stable oxide phase Eu_2O_3, or even EuO_{1-x} or $Eu_{1-x}O$. Therefore, post-growth structural and magnetic characterisation measurements were carried out to investigate the properties

[1] sccm is Standard Cubic Centimetres per Minute (cm^3/min) at a standard pressure and temperature.

of the grown film. Figure 3.7 shows the XRD and XRR measurements performed on the samples. The XRD spectrum shown in Figure 3.7 (a) is for the LaO^{+}-terminated sample where the peaks are labelled with their equivalent layer(plane). The scan shows a highly oriented EuO(001) film grown on the LAO(001) substrate with no sign of any impurities or other phases of Eu-oxides, such as Eu_2O_3. The peaks positioned at 2θ=34.59° and 72.89° correspond to the EuO(002) and (004) plane, respectively, whereas the small shift in the peak positions is due to the strain induced by the LAO mismatch. Furthermore, the XRR scans and their corresponding fits of the simultaneously grown samples, EuO film grown on an

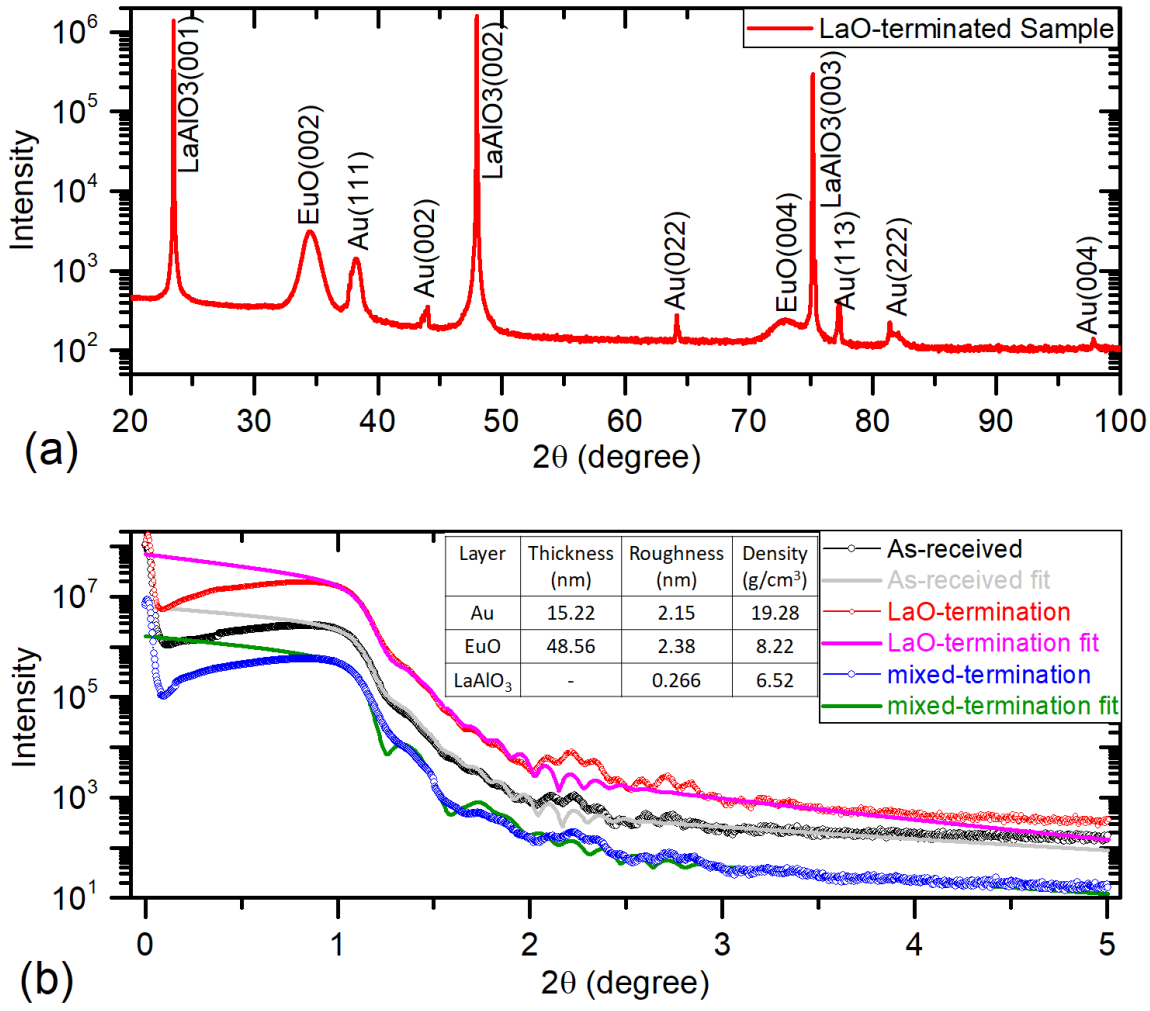

Fig. 3.7 : X-ray measurements carried out for the LAO/EuO/Au sample. (a) Diffraction scan performed using a monochromator from 20°-100° showing a highly oriented EuO(001) film grown on an LAO(001) substrate, (b) 0°-5° XRR scans of the as-received- (black), mixed- (blue) and LaO^{+}- (magenta) terminated samples and their corresponding fits. The values of the deduced parameters are listed in the inset.

as-received, LaO^+- and AlO_2^--terminated LAO substrate, are shown in Figure 3.7 (b). The reflectivity curves show that the sharpest interfaces between the layers (LAO/EuO/Au) is obtained in the LaO^+-terminated sample as clearer fringes are observed in its XRR curve compared to those of the as-received and AlO_2^--terminated samples. However, obtaining good fits for all the samples was quite challenging due to the low intensity at 2θ of $\sim$1.75°-5° which can be attributed to the surface terraces and the twinning of the LAO substrates. Therefore, the averages of the fitted parameters of the three samples were considered and listed in the inset. The value of the density obtained from the XRR fits and the position of the EuO(001) diffraction peaks observed in the XRD spectrum provide strong evidence that a high-quality crystalline stoichiometric EuO is grown on the LAO substrate.

The possibility of growing epitaxial EuO(001) on an LAO(001) substrate was suggested in Ref. [169]. Therefore, X-ray ϕ (0°-360°) scans were carried out for the substrate and EuO(001) film for the LaO^+-terminated sample. The scans on the EuO(113) and LAO(2111) planes are shown in Figure 3.8 (a). The twinned planes of the LAO substrate which are rotated by 36.8° with respect to each other can be seen in the ϕ spectrum. The repetition of the twinned planes every 90° confirms the cubic crystal structure of the LAO substrate. On the other hand, the epitaxy of EuO(001) can also be inferred from the alignment of the EuO peaks on top of those of the LAO twinned planes. However, the broadening of the full-width at half-maximum (FWHM) of the peaks of the red spectrum in comparison to the black spectrum confirms that the former belongs to the EuO film and the latter is from the LAO substrate.

Figure 3.8 (b) shows a bottom view of a (4x4x1) EuO(001) plane grown on a (2x2x1) LAO(001) by rotating its crystal by 45° as mentioned earlier. The [10] and [01] directions are shown for both layers with the LAO(211) and EuO(113) parallel to each other. Therefore, for an epitaxial EuO(001)/LAO(001) the ϕ spectrum for the EuO(113) plane is expected to lay on top of that of the LAO(211) plane. Thus, the phi scan confirms the epitaxial growth of the EuO(001) on top of the LAO(001) substrate.

Magnetic characterisation

Investigating the magnetic characteristics of the grown EuO(001) film is crucial to confirm the growth of pristine EuO(001) as many properties can be detected, such as measuring the T_C of the samples. The hysteresis loops at 5 K have small coercivities of 32 Oe and 49 Oe for the single- and mixed-terminated sample, respectively. Figure 3.9 shows some of the loops taken on the LaO^+- and mixed-terminated samples. Although the higher T measurements (the insets of Figure 3.9) show hysteresis loops with finite coercivities, the noise level in the

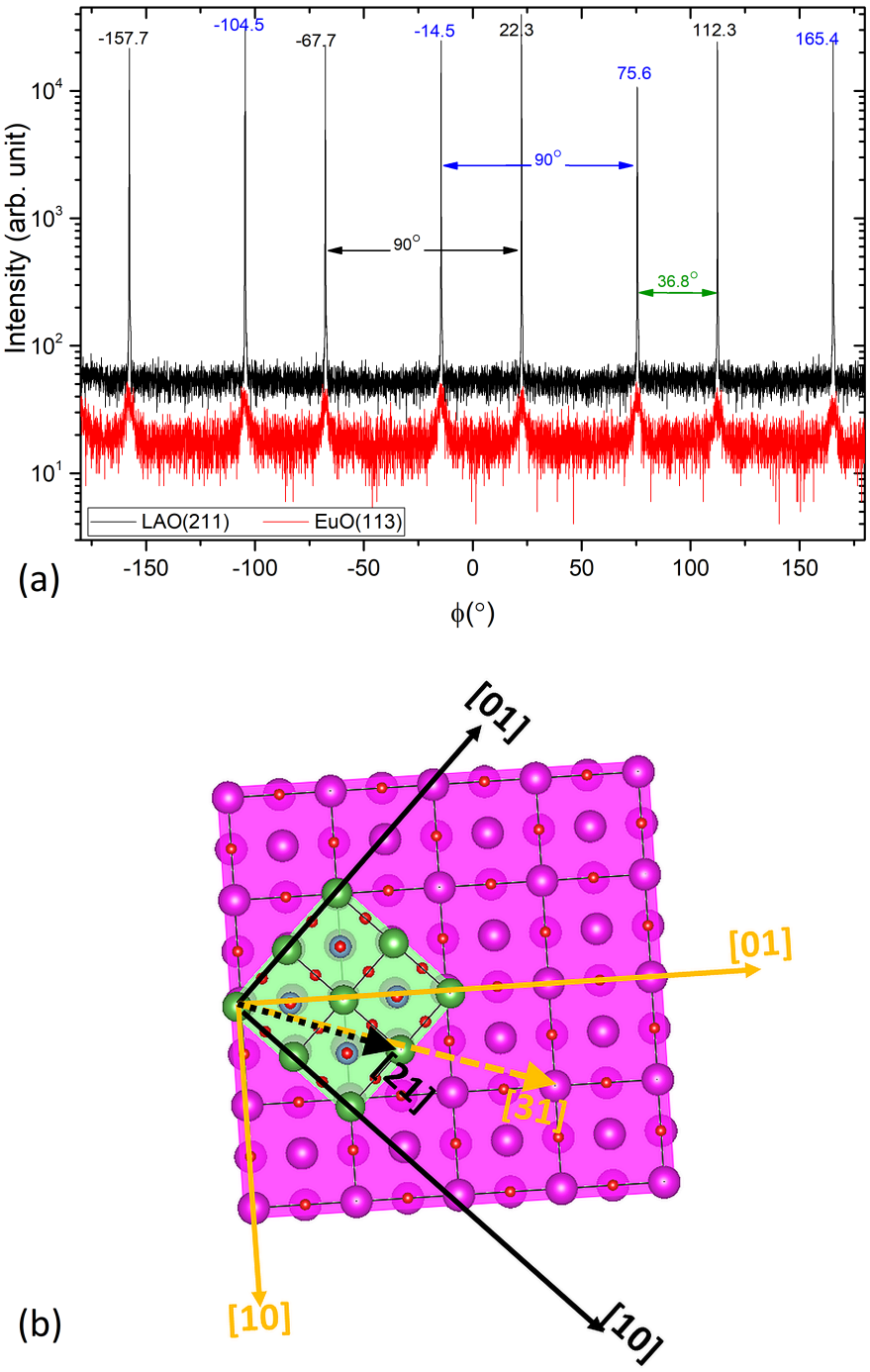

Fig. 3.8 : (a) 360° ϕ-scan of the LAO(211) (black) and EuO(113) (red) planes of the LaO^{+}-terminated sample showing the twinned LAO planes aligned at 36.8° to each other and the 90° cubic rotation. (b) Bottom-view of the grown EuO(001) on an LAO(001) substrate highlighting the adaptation of the EuO(001) to the LAO(001) lattice parameter.

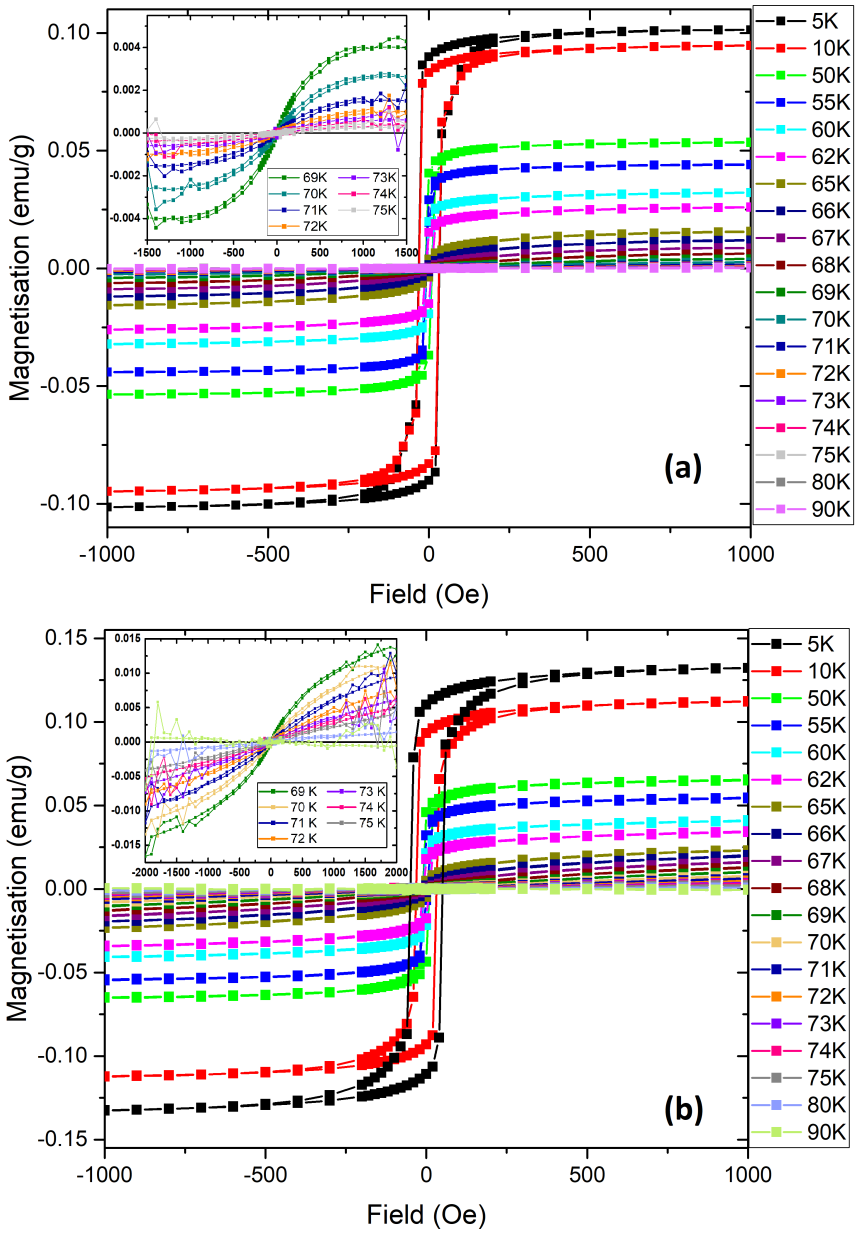

Fig. 3.9 : Volume magnetisation as a function of the magnetic field applied in-plane measured at different temperatures for the LaO^{+}- (a) and mixed-terminated (b) samples. The inset shows a zoomed-in view of the hysteresis loops measured at higher temperatures (69 K to 75 K).

measurements is comparable with the coercive field. Therefore, the detected coercivities can be attributed to artefacts in the SQUID measurements.

Figure 3.10 shows the temperature (T) dependence magnetisation measured by the SQUID at remanence for both samples. The samples were first field-cooled (FC) with the

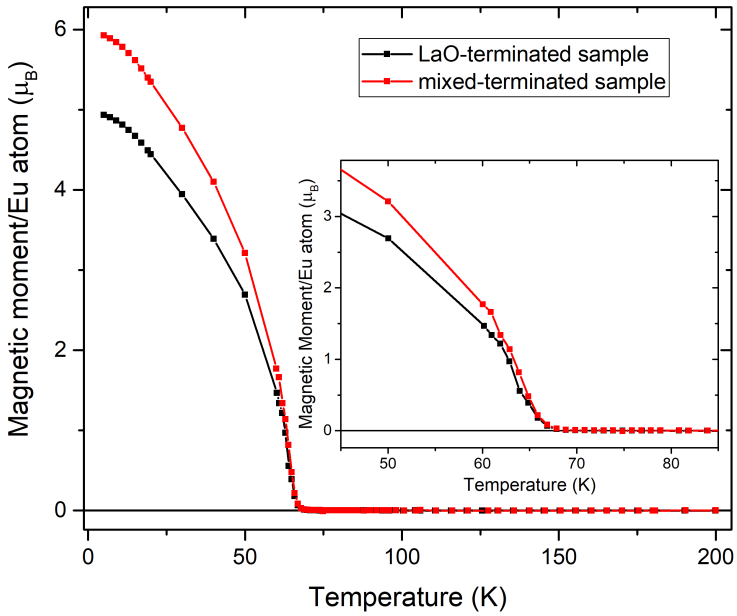

Fig. 3.10 : The temperature dependence of the magnetisation measured at remanence for the mixed- and LaO^+-terminated samples. The inset show tails observed at around T_C which leads to inaccurate estimation of the T_C

magnetic field (H) applied parallel to the film plane to saturate the magnetisation (M) in the direction of the applied field. The field was then switched off prior to taking the M vs T measurements. The samples show a reduction in the magnetic moment which could be due to the uncertainty in measuring the sample size, a slight oxidation in the EuO film, or the misalignment of the sample with respect to the direction of the applied field during the field cooling process as a remanence of $\sim 89\%$ and $\sim 83\%$ is detected for the LaO^+- and AlO_2^--terminated samples, respectively. Furthermore, the graphs follow a Brillouin function at low T with no indication of non-reacted Eu, nor O, in the samples as no paramagnetic nor diamagnetic shoulders are observed, which is an indication of the growth of stoichiometric EuO films.

The M vs T measurement is one of the standard methods to obtain the T_C of a ferromagnetic material. However, a small tail is often observed at around the T_C (as shown in the inset of Figure 3.10) which leads to an inaccurate estimation of the T_C. This behaviour is usually attributed either to an inhomogeneity in the film or that a residual external field is still persisting in the SQUID [170]. Therefore, a more precise, M vs H, approach needs to be implemented to determine the T_C of the samples.

Arrott plots, which are based on the mean-field theory, are another well-known method to estimate the T_C of a ferromagnet. In this approach, as $M^{1/\beta}$ vs $(H/M)^{1/\gamma}$ plot is fitted

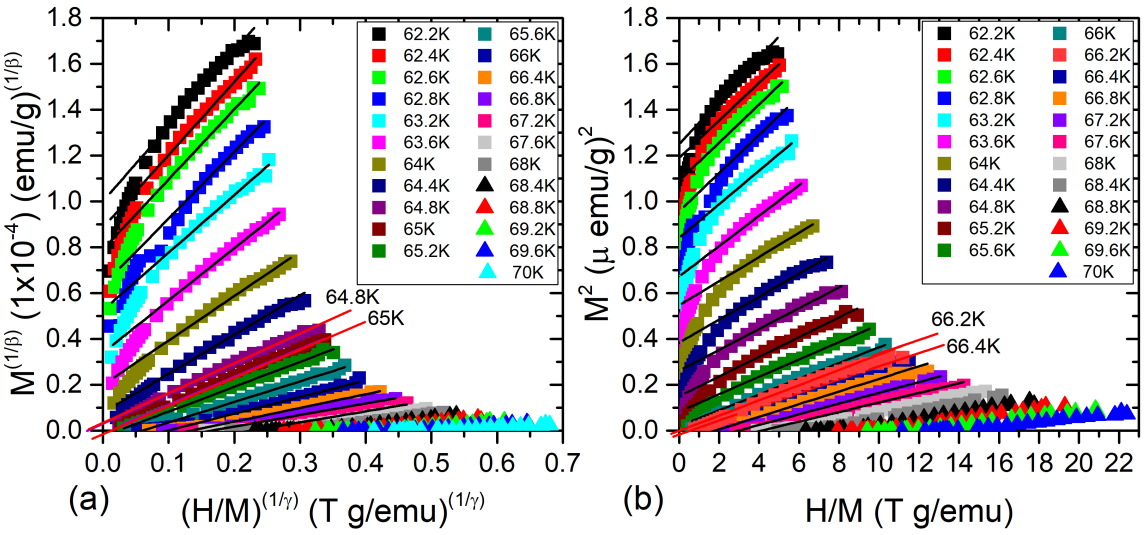

Fig. 3.11 : The Arrott plots of the LaO$^+$-terminated sample at temperatures between 62.2 K-70 K using the critical exponent values of: (a) 3D Heisenberg and (b) mean field model.

with a straight line in the high-field regime and the curve in which the fitted line passes through the origin indicates the T_C of the material. Here, β and γ are the critical exponents where $\beta = 0.5$ and $\gamma = 1$ for the mean-field theory. The Arrott relation was the found to accept other β and γ values based on the universality class of the ferromagnet, and it is now known as the modified Arrott plots or the Arrott-Noakes (A-N) plots [171]. For example, $\beta = 0.369$ and $\gamma = 1.396$ for the 3D Heisenberg class ferromagnet. Therefore, M vs H measurements were taken at different temperatures to obtain the Arrott plots. Since EuO is considered an ideal 3D Heisenberg ferromagnet, its T_C is expected to be accurately estimated by using the critical exponents of the 3D Heisenberg model. However, the fitted lines for the LaO$^+$-terminated sample are not parallel below T_C in the high field regime when using the 3D Heisenberg Arrott plot as can be seen in Figure 3.11 (a). Surprisingly, slightly better results are obtained by using the mean field critical exponents (Figure 3.11 (b)). Nonetheless, fitting straight lines passing all the data points for both models are not possible as the graphs are non-linear in the low $(H/M)^{(1/\gamma)}$ range. The gradients vary significantly below the T_C in the 3D Heisenberg Arrott plot in comparison to that of the mean field. Therefore, the Kouvel-Fischer (K-F) method was then implemented to calculate the values of the critical exponents more accurately.

K-F defines the magnetisation (M) and susceptibility (χ) in terms of γ, β and T_C as [172]:

$$\left(\frac{\mathrm{d}\ln M}{\mathrm{d}T}\right)^{-1} = -\frac{1}{\beta}(T_C - T) \tag{3.4}$$

and

$$\left(\frac{\mathrm{dln}\chi}{\mathrm{d}T}\right)^{-1} = -\frac{1}{\gamma}(T - T_C). \tag{3.5}$$

Therefore, γ and β can be obtained from the gradients of $(\mathrm{dln}M/\mathrm{d}T)^{-1}$ and $(\mathrm{dln}\chi/\mathrm{d}T)^{-1}$ vs T plots, while the T_C is the intercept on the T axis.

Obtaining the critical exponent β

According to Equ. (3.4), β can be obtained from the gradient of the linear part of $(\mathrm{dln}M/\mathrm{d}T)^{-1}$ vs T at $T < T_C$ as shown in Figure 3.12 for the single- and mixed-terminated samples. The fitted line in $(\mathrm{dln}M/\mathrm{d}T)^{-1}$ vs T intercepts the x-axis at $T = (63.4 \pm 0.68)$ K with $\beta = (0.47 \pm 0.09)$ for the LaO^+-terminated sample and at $T = (64.4 \pm 0.34)$ K and $\beta = (0.46 \pm 0.04)$ for the mixed-terminated sample. The range considered for fitting the data (yellow area in the figure) for both samples is different due to the scattered data points in the LaO^+-terminated sample below 45 K. However, it was found that using the same range as for the mixed-terminated sample (i.e. from ~25 K to ~65 K) while eliminating the highlighted data-points at $T = 36$ K and 44 K increased β to (0.493 ± 0.03), i.e. closer to the value of the mean field model, and the T_C to (63.6 ± 0.23) K.

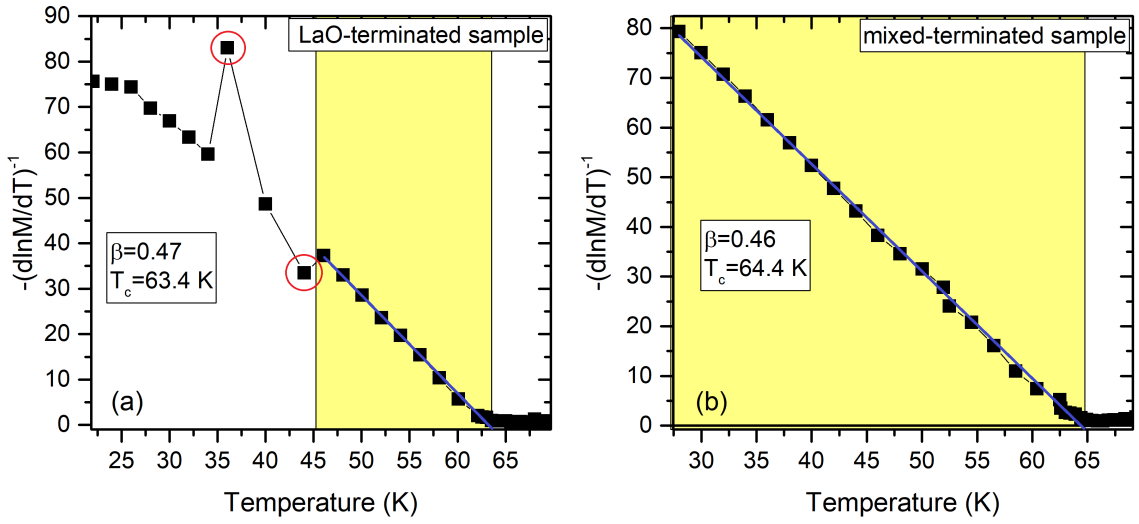

Fig. 3.12 : The K-F plot of $(\mathrm{dln}M/\mathrm{d}T)^{-1}$ vs T for: (a) the LaO^+-terminated and (b) mixed-terminated samples. The yellow regions present the area included to produce the linear fit (blue line) for $T < T_C$.

Determining the critical exponent γ

Isotherms from 62 K to 75 K in steps of 0.2 T were collected for both samples to obtain γ. Since $\chi = M/H$, the isotherms were first corrected so that $M(H=0) = 0$ emu/g before calculating the gradient of the initial part $M(H=0) \rightarrow M(H=100)$ to obtain χ. Figure 3.13 shows $-(\mathrm{d}\ln\chi/\mathrm{d}T)^{-1}$ vs T for the single and double-terminated samples. γ and T_C were then estimated for the samples by fitting a linear line for $T > T_C$. γ [T_C] was found to be (0.96 ± 0.29) [(67.5 ± 1.0) K] and (0.95 ± 0.57) [(67.3 ± 2.0) K] for the LaO^+- and mixed-terminated sample, respectively. The scattered data points at $T > T_C$ lead to a large error in the predicted T_C which is due to the poor signal-to-noise ratio of our SQUID system. Therefore, the T_C values obtained from estimating β are believed to be more accurate. An A-N plot was then used as a sanity check for the accuracy of the predicted values.

For A-N plots, $M^{(1/\beta)}$ vs $(H/M)^{(1/\gamma)}$ were plotted using the values of the critical exponents obtained from the K-F method. The results for both samples are shown in Figure 3.14, where the insets show the curve at the T_C= 66.4 K for both samples, which is similar to the value deduced from plotting the Arrott plots using the mean field critical exponents (Figure 3.11).

The SQUID measurements carried out on the grown EuO(001)/LAO(001) films show that there is a reduction by 2.6 K in the T_C of our films and that this result is consistent with that reported by Caspers of a similar heterostructure with a thickness of 30 nm [169]. However, the hysteresis loops of our samples are magnetically easier, i.e. more of a rectangular shape.

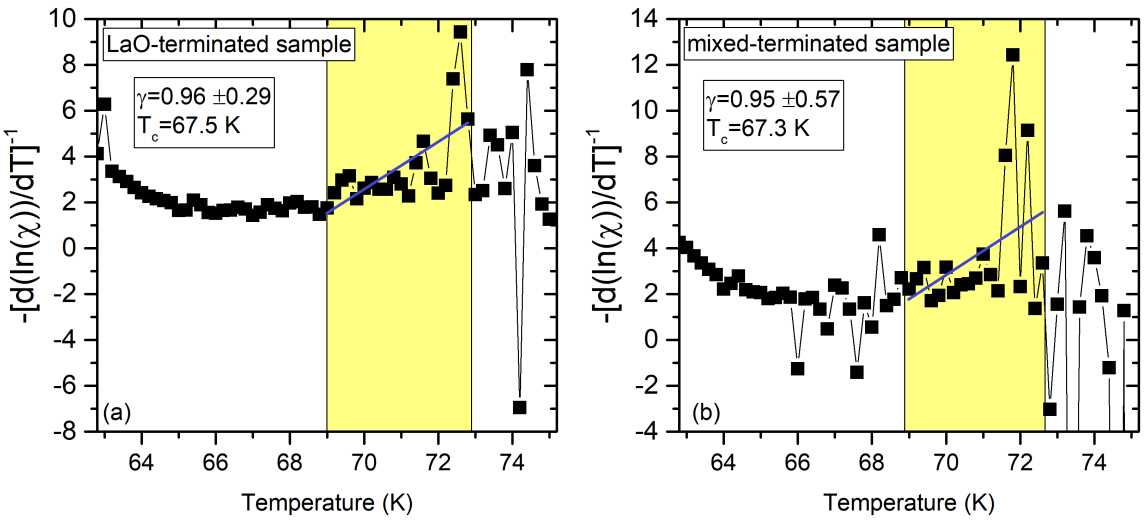

Fig. 3.13 : The K-F plot of $-(\mathrm{d}\ln\chi/\mathrm{d}T)^{-1}$ vs T for: (a) the LaO-terminated and (b) mixed-terminated samples. The yellow regions present the area considered to produce the linear fit (blue line) for $T > T_C$.

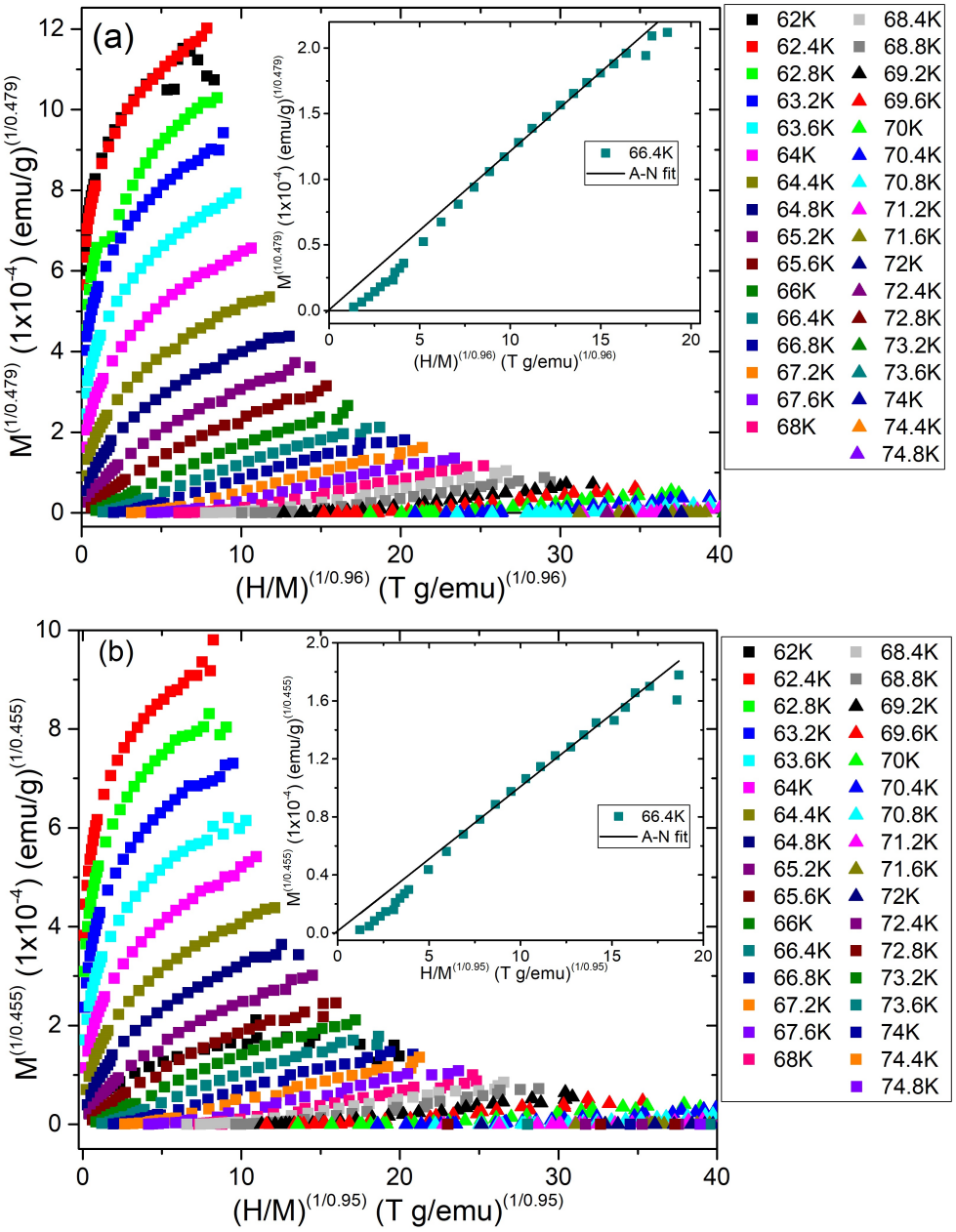

Fig. 3.14 : The A-N plots from 62 K to 74.8 K using the values of the critical exponents obtained from K-F method for: (a) LaO^{+}-terminated sample and (b) mixed-terminated sample. The insets show the A-N plot and the linear fit at the T_C.

Caspers attributed his rounded-shape hysteresis loop to a mosaic-like structure detected by a reciprocal-space mapping measurement [169]. While the reduction in the T_C to be solely due to the lateral strain induced by the lattice mismatch between the film and the substrate rather than the small thickness of the EuO film, which should also be the case for our samples as

50 nm thick EuO films are expected to exhibit the bulk-like behaviour of EuO [169]. Also reported studies on the thickness dependence of the magnetic properties of polycrystalline stoichiometric EuO and $EuO_{0.96}$ films showed that only the films with thicknesses less than 10 nm exhibited a decrease in their T_C which was attributed to the reduction of the number of nearest neighbouring atoms leading to band bending as a result of the surface electronic doping which partially depletes the $4f$ states of Eu [132, 139, 173]. Since band bending is expected to occur as a result of the electron transfer of 0.5 e^- from the LaO^+ to EuO, we speculate that this can affect greatly the EuO/LAO interface and thus the T_C. However, further research is required to confirm this assumption.

3.3 μSR measurements

In order to ascertain the internal magnetic fields in our samples, to study local inhomogeneities in the EuO films and to look for a spin-polarised 2DEG at the EuO(001)/LAO(001) interface we have employed μSR measurements. First, Monte Carlo simulations using the TRIM:SP package [120, 174] were carried out by Dr Peter Baker to determine the probability of the muon stopping inside the samples for different implantation energies. The calculations presented in Figure 3.15 show that 6 keV muons will not reach the LAO substrate and ∼79% of the muons will be stopped inside the EuO film and ∼ 21% at the Au capping layer. Therefore, 6 keV was used as the shallow energy to investigate the properties of "bulk" EuO. On the other hand, to study the properties of the EuO film at the interface with the LAO

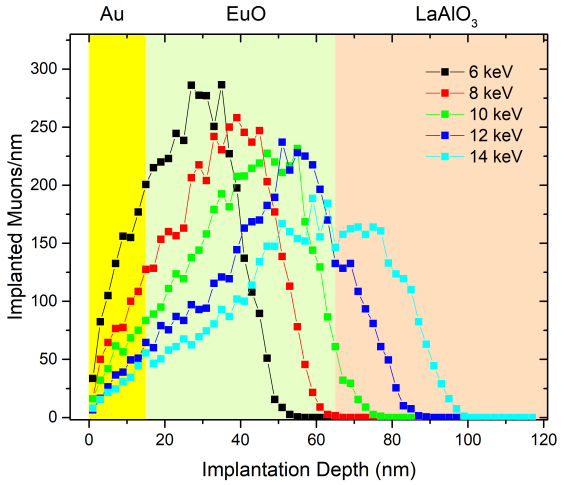

Implantation Energy (keV)	Percentage of stopped muon (%)		
	Au	EuO	LAO
6	21.1	78.9	0.0
8	12.2	87.8	0.02
10	8.39	89.0	2.6
12	5.5	78.1	16.5
14	4.3	58.3	37.4

Fig. 3.15 : Monte Carlo simulations of different penetration energies 6 keV, 8 keV, 10 keV, 12 keV and 14 keV for a LAO/EuO (50nm)/Au(15nm) sample. Calculations were performed by Dr. Peter Baker using the TRIM:SP program [120, 174].

substrate, muons with higher energies were considered (i.e. 10 keV, 12 keV and 14 keV). The latter was then excluded as $\sim 37\%$ of the muons will penetrate into the substrate. Muons with 10 keV and 12 keV will travel 10 nm and 20 nm deep inside the substrate, respectively, while a small number of muons will be stopped at the capping layer ($\sim 8\%$ with 10 keV and $\sim 5\%$ with 12 keV). However, a significant number of muons are implanted into the bulk EuO at 10 keV. Therefore, 11 keV is expected to allow the muons to penetrate deeper into the EuO film, close to the interface with the LAO substrate.

As mentioned in Section 2.4.3, the μSR experiment was carried out using low-energy muons at the LEM beamline at PSI. The samples were mounted on a Ni sample holder and fixed with silver paint. Ni was used as a back plating as it has a low energy-independent relaxation rate [(0.01 - 0.02) μ s^{-1}] [175]. The simulations were then tested by performing depth-dependent scans at 10 K and 298 K, with different penetration energies (6 keV, 8 keV, 10 keV, 11 keV, 14 keV and 18 keV) while applying a weak transverse field (wTF) of 30 G. Before carrying out the measurements, the sample space was pumped down to $\sim 3\times10^{-9}$ mbar and then it was left for 20 minutes for the temperature to stabilise. The results are shown in Figure 3.16. At $T = 298$ K, the measurements show precession signals with high, almost undamped, amplitudes. On the other hand, the $T = 10$ K measurements show higher damping rates and that most of the asymmetry is decaying at $t < 1$ μs, as expected. This is because in a wTF measurement, when the applied field, B_0, is much larger than the sample's internal field B_i experienced by the muons, the muons will precess with the Larmor frequency,

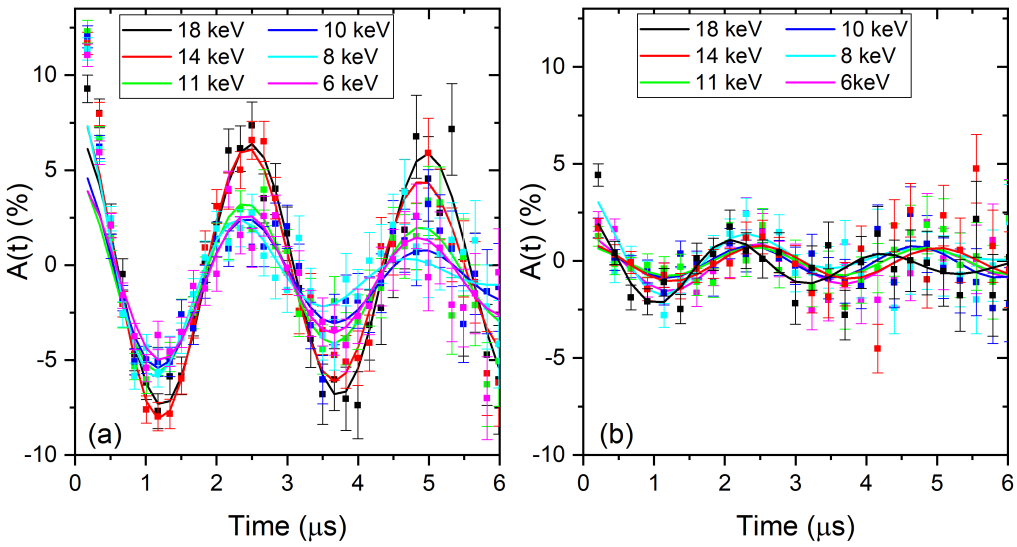

Fig. 3.16 : Raw data and the corresponding fits of the energy dependent wTF measurements using 6 keV, 8 keV, 10 keV, 11 keV, 14 keV and 18 keV taken on the LaO^{+}-terminated sample at 298 K (a) and 10 K (b).

$\omega_L = \gamma_\mu B_0$. However, below the T_C of EuO, here at $T = 10$ K, when the internal field $B_i >> B_0$, muons implanted in the magnetic layer of the sample will experience a strong static magnetic field, and due to the limited resolution of the μSR, $A(t = 0)$ appears as a damped signal [176]. A weak transverse field (wTF) of 30 G was chosen to replicate the experimental conditions used for previous μSR experiments carried out on EuO [130, 177] and as a higher field was found to smear out the transition.

Based on the results presented in Figure 3.15 and 3.16, the ZF and 30 G wTF measurements were both performed on the samples with shallow (6 keV) and deep (11 keV) penetration energies. The former was carried out to study the changes in the static and dynamic spontaneous magnetic fields at the muon sites. The latter was used to obtain details about the temperature dependence of the samples' static magnetic volume fraction and whether or not EuO possesses a magnetic phase separation [23]. The shallow ZF raw data collected at different temperatures and their corresponding fits of the LaO^+-terminated sample are shown in Figure 3.17, although the data were fitted for $t = 0 - 11.20$ μs, only $t = 0 - 6$ μs are presented here.

The ZF data are best expressed by the sum of the fast and slow relaxation exponential terms and the background signal of the measurements as follows:

$$A(t) = A_1 e^{-\lambda t} + A_2 e^{-\Lambda t} + A_{BG}, \tag{3.6}$$

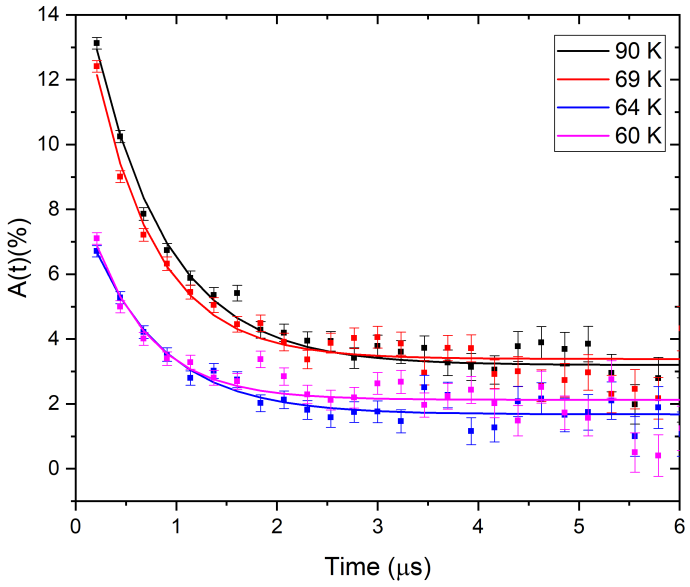

Fig. 3.17 : Raw data of the ZF measurements taken at different temperatures (60 K, 64 K, 69 K and 90 K) and their corresponding fits for the LaO^+-terminated sample at 6 keV.

where $A(t)$ is the muon decay symmetry. The first term ($A_1 e^{-\lambda t}$) defines the slow muon relaxation rate. This term measures the fluctuations of the paramagnetic medium at $T > T_C$ and the local magnetic sites parallel to the muon spin at $T < T_C$. This is because at $T > T_C$, the magnetic moments of the ferromagnet are randomly oriented with no preferred direction. However, as T is decreased, the atoms lose their thermal energy and the magnetic moments align in the same direction within their magnetic domains, breaking the rotational symmetry of the ferromagnet. Therefore, $A_1 e^{-\lambda t}$ will reflect the interaction of the muons with the aligned magnetic moments at $T < T_C$. The second term ($A_2 e^{-\Lambda t}$) describes the fast relaxation rate of the muons, and expresses their incoherent precession about the field pointing at 90° to their spin polarisation [23]. Therefore, Λ reflects the changes in the magnetic ordering at the muon stopping site inside the material as a function of temperature and it is expected to match the bulk magnetic properties of the film. It was also found to be zero at $T > T_C$. A_1 and A_2 are the parallel and perpendicular oscillating amplitudes of the corresponding exponential terms, respectively. Therefore, at $T > T_C$, A_2 tends to zero and the signal is described by a single exponential term ($A_1 e^{-\lambda t}$) only. A_{BG} is the background signal and it was fixed to zero while fitting the data as the signals were initially corrected for the background effect. Thus, it is not expected to vary with T. On the other hand, for $T < T_C$, data were fitted with the two exponential terms. The slow and fast relaxation parameters were set as $\lambda < \Lambda$. Both samples show lower $A(t)$ at 11 keV in contrast to the shallow measurements as more muons being stopped in the magnetic volume of the sample, i.e. EuO layer. Although an initial drop in the muon decay asymmetry is observed in the ZF data at $T < T_C$, our data is unlike that of the polycrystalline EuO reported by Blundell *et al.*, where consistent oscillations were observed at $T < T_C$ [131]. Although we measured an epitaxial EuO film, the twinning of the LAO substrate is believed to induce defects throughout the EuO film such as facets and grain boundary-like behaviour which leads to a small variation of the internal field experienced by the muons, which is similar to that observed in polycrystalline EuO_{1-x} [130].

Details on the magnetically ordered volume fraction of the sample at a specific temperature, P_{mag}, can also be obtained from the ZF measurements using the following equation:

$$P_{mag} = 1.5 \times \frac{A_2}{A_1 + A_2}. \tag{3.7}$$

The above equation presumes that the measured sample is a polycrystalline material and that A_2:$A_1 \sim 2$. This is because in a polycrystalline sample the field directions are random compared to the muon spin direction. Therefore, if one assumes that at $t = 0$ all muons are polarised along the x-direction, on average 1/3 of the muons will experience a net field projected along the x-, y- and the z-axes. Thus, one in three muons will have a field directed

along the x-axis and will not precess and two in three muons will have a field projected perpendicular to their initial spin direction. Therefore, 1/3 of the muons will be depolarised by spin flips only and 2/3 will be depolarised by oscillations, which can be expressed by the Kubo-Toyabe relaxation function:

$$P_z(t) = \frac{1}{3} + \frac{2}{3}(1 - \gamma_\mu^2 \Delta^2 t^2) exp(-\frac{1}{2}\gamma_\mu^2 \Delta_\mu^2 t^2], \tag{3.8}$$

where $P_z(t)$ is the muon spin precession, γ_μ is the muon gyromagnetic ratio, Δ is the distribution width, which can be expressed in terms of the depolarisation field (H) at the muon stopping site as $\Delta^2 = \frac{1}{3} < H^2 >$, and t is the relaxation time [178–181].

Muons' fast and slow relaxations can also be observed in the wTF measurements, where they reflect the internal field of the sample and the wTF applied during the experiment experienced by the muons, respectively [130]. Thus, providing a more accurate estimation of the magnetically ordered volume of the sample.

The slow muon relaxation is expressed by the following function:

$$A(t) = A_r e^{(-\eta t)} cos(\gamma_\mu B + \phi), \tag{3.9}$$

where η is the relaxation rate which measures the depolarisation rate of the muon precession in the presence of the wTF, B is the applied magnetic field experienced by the muons and ϕ is the phase offset of the implanted muons spin rotation with respect to the detectors [130]. Here, γ_μ is the gyromagnetic ratio of the muon and $\gamma_{text\mu}/2\pi = 135.5$ MHz/T. Including the initial fast relaxation ($t = 0 - 0.5$ µs) while fitting the data led to a poorer fit quality. This is because excluding the first 0.5 µs works as a band-pass filter such that the fit describes the non-magnetic portion of the sample only. Thus, the first 0.5 µs was eliminated. Figure 3.18 shows the effect of including the contribution of the fast relaxation on the quality of the wTF fits by comparing the $t = 0 - 8$ µs and $t = 0.5 - 8$ µs fits for the LaO^+-terminated sample with a 6 keV implantation energy, at 10 K and 90 K. The graphs show that excluding the $t < 0.5$ µs region leads to a better fit of the muons' slow relaxation rate, which is more pronounced in the 90 K fit in comparison to the 10 K fit of the magnetisation due to the damping impact in the latter. It is worth noting that varying the initial time frame for fast relaxation within a certain narrow range, e.g. $0.25 < t < 0.5$ µs, considered for fitting the wTF signal was reported to have a negligible effect on the fitted parameters of equ. (3.9) [23].

Furthermore, muonium states (Mu) are known to form additional oscillations in the wTF data, and this is because the spin polarisation of the µ and Mu would decay at different rates

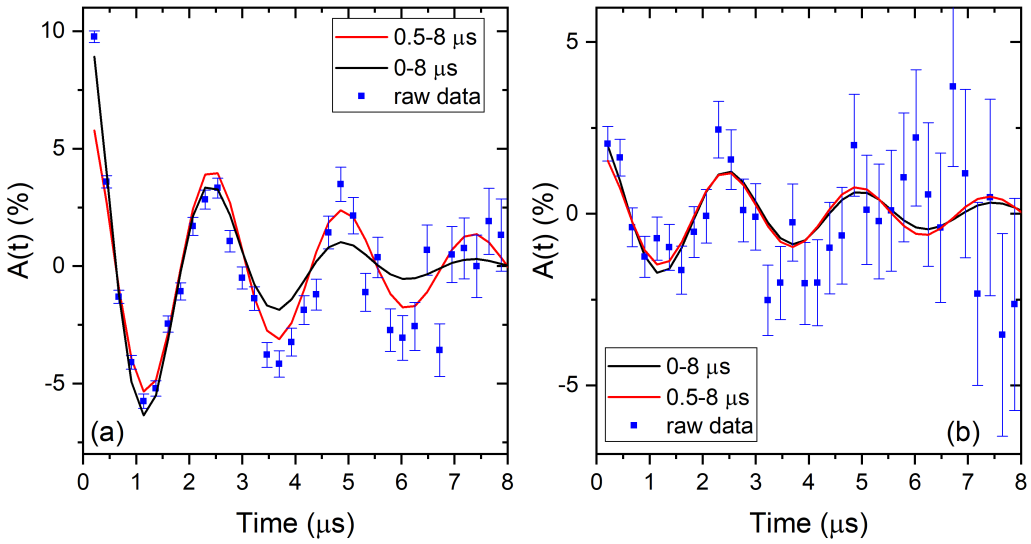

Fig. 3.18 : The fitting results of the wTF signal of the LaO^{+}-terminated sample measured at (a) 90 K and (b) 10 K with 6 keV showing the effect of including and excluding the contribution from the muon fast relaxation.

due to their different hyperfine couplings [182]. Therefore, the missing additional beatings in our wTF data indicate that no Mu is formed in our samples.

The temperature dependence of the fitting parameters were obtained from equ. (3.6), (3.7) and (3.9) for the LaO^{+}- and mixed-terminated samples, measured with 6 keV and 11 keV, and are presented in Figure 3.19. In Figure 3.19 (a) the muon slow relaxation rate, λ, increases as the sample is cooled down from 90 K, until it reaches a maximum value at $\sim T_C$. A sharp drop is then observed before it continued to increase again between $T = 60 - 64$ K. The changes in Λ as a function of T appear to be similar to the bulk magnetisation of the samples measured by the SQUID (Figure 3.10). The Λ value of the deep LaO^{+}-terminated sample at $T = 60$ K is close to the beamline resolution limit. Therefore, a considerably large error bar on that data point is seen. Nonetheless, both SQUID and μSR show consistent results. Figure 3.19 (c) depicts the variation of P_{mag} as a function of temperature and shows that the total volume of both samples developed quasistatic magnetic fields at around $T = 69$ K. The high P_{mag} percentage $>100\%$ can be attributed to the degree of epitaxial behaviour exhibited by the twinned EuO film as the formula assumes a polycrystalline sample. Also, the average A_2:A_1 ratios were calculated to be 2.1 and 3.7 for the single- and mixed-terminated samples, respectively. Therefore, the P_{mag} vs T plot is in agreement with the X-ray ϕ-scan shown in Figure 3.8 which indicates epitaxial growth.

The fitted parameters of the wTF measurements are presented in Figure 3.19 (d)-(f). Figure 3.19 (d) shows the variation of A_r as a function of T. Both measurements possess

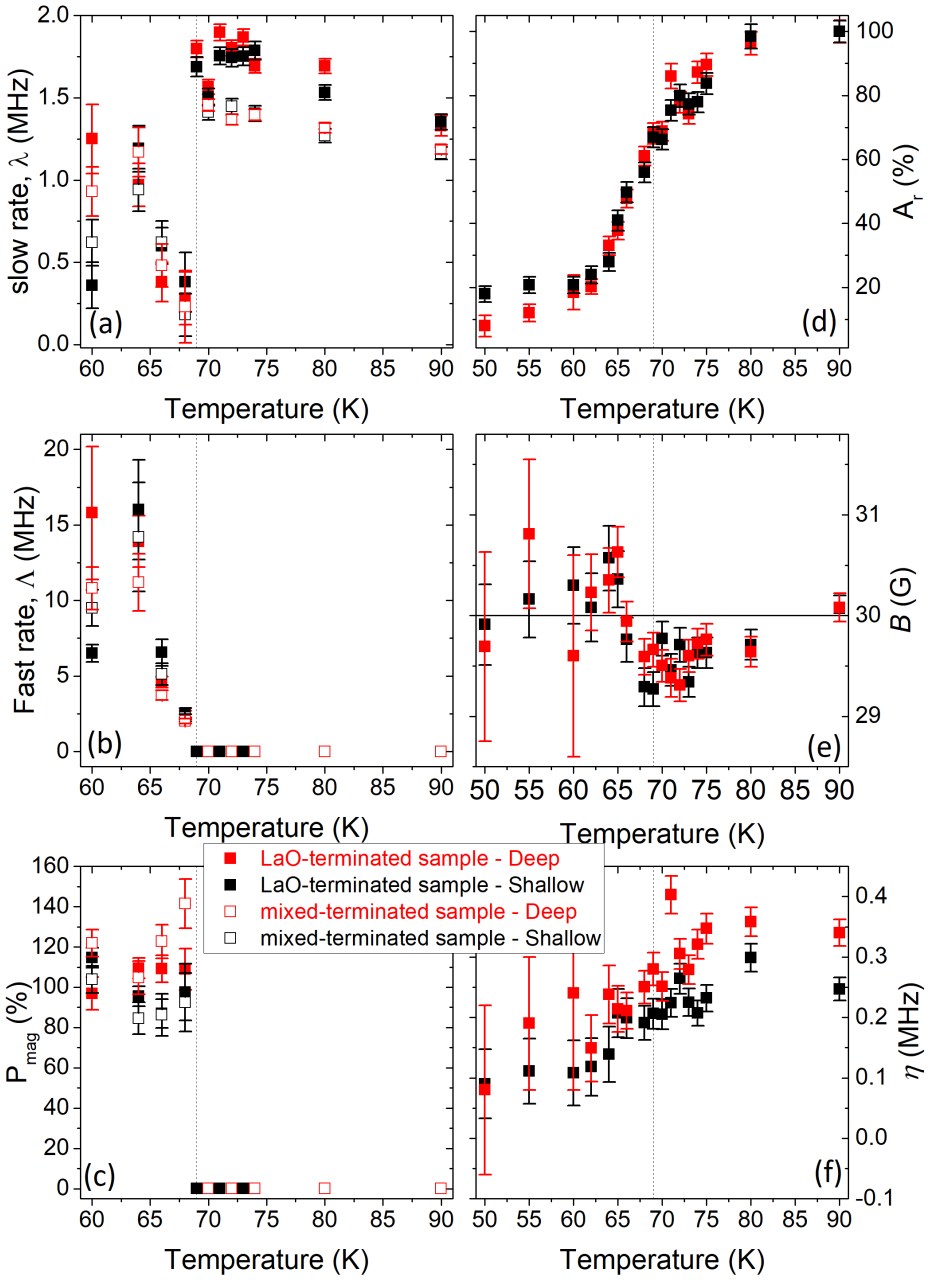

Fig. 3.19 : The results of the μSR fitting for LaO^+-terminated and mixed-terminated LAO/EuO/Au samples measured with shallow (6 keV) and deep (11 keV) penetration energies. ZF results are presented in (a-c) and wTF results are shown in (d-f) as a function of temperature. The vertical dashed lines denote the position of the stoichiometric EuO T_C value. (a) The slow muon relaxation rate, λ. (b) The fast relaxation, Λ. (c) The static magnetic volume of the sample, P_{mag}. (d) The wTF relaxing asymmetry, A_r. (e) The magnetic field, B, experienced by the muons, and (f) The wTF relaxation rate, η.

similar behaviour while the deep measurement has a lower initial asymmetry in comparison to the shallow one. This is perhaps due to more muons being implanted inside the LAO substrate during the run in contrast with the 6 keV measurements. Also, the value of $A_r(t)$ is found to agree with that shown in Figure 3.17. A sharp drop in the amplitude of the $A_r(t)$ is always observed at low T when Mu states are formed inside the sample as their spin polarisation cannot be resolved due to their quick decaying rate which result in a decrease in the $A_r(t)$ signal. Therefore, the absence of this drop in our $A_r(t)$ confirms the statement made from the wTF fits that no Mu states are present in the samples. The temperature dependences of the other fitted parameters obtained from the wTF, B and η are presented in Figure 3.19 (e) and (f), respectively. The solid horizontal line in Figure 3.19 (e) indicates the position of the 30 G applied during the measurements. The graph also shows the variation of the actual B experienced by the muons. The fluctuation of B around 30 G could be due to the twinning of the LAO which produces a faceted EuO film with grains oriented in different directions. The same reasoning can also be applied to explain the behaviour of η as presented in Figure 3.19 (f).

As seen from the results of the ZF and wTF measurements presented in Figure 3.19, both samples possess similar behaviour and there is no evidence of the increase of T_C as predicted by Lee *et al.* and Wang *et al.* as discussed in Section 3.1.3. At the same time, our EuO films are unlike the polycrystalline pristine EuO, or EuO_{1-x} measured by Monteiro *et al.* reported in Ref. [130]. For convenience, their results are represented in Figure 3.20. Although Λ in our samples and theirs exhibit similar changes as in the M vs T SQUID measurements, the pristine EuO in Figure 3.20 shows a sharp transition at $T = T_C = 68$ K, whereas $EuO_{0.91}$ and $EuO_{0.975}$ reveal a "double-dome" which is a feature widely observed in $EuO_{1\text{-}x}$ [130]. However, the Λ of our samples gradually increase as T decreases revealing a T_C of ~ 69 K (Figure 3.19 (b)). On the other hand, λ reported by Monteiro *et al.* shows a sharp peak at T_C in pristine EuO and a less pronounced ones in $EuO_{0.91}$ and $EuO_{0.975}$. However, the λ of our samples exhibit a drop around $T = 69$ K, but more data points between $64 - 70$ K would be needed to make a conclusive statement about the shape of our λ vs T graph and whether the dip shown in Figure 3.19 (a) is real or just a random scatter. Also, our samples develop an abrupt change in P_{mag} as T approaches 69 K, and this indicates that the entire sample volume enters the magnetic order phase below $T = 69$ K. A similar behaviour is also observed in the $EuO_{0.91}$ sample whereas a broader transition is reported in stoichiometric EuO in Figure 3.20. Nonetheless, our P_{mag} results show no sign of phase separation in our EuO film, but suggest a relatively high degree of epitaxy as mentioned before.

From the wTF measurements $A_r(t)$, B and η can be obtained as illustrated in Equ. (3.9) and the results are plotted and presented in Figure 3.19 while Monteiro *et al.* results are shown

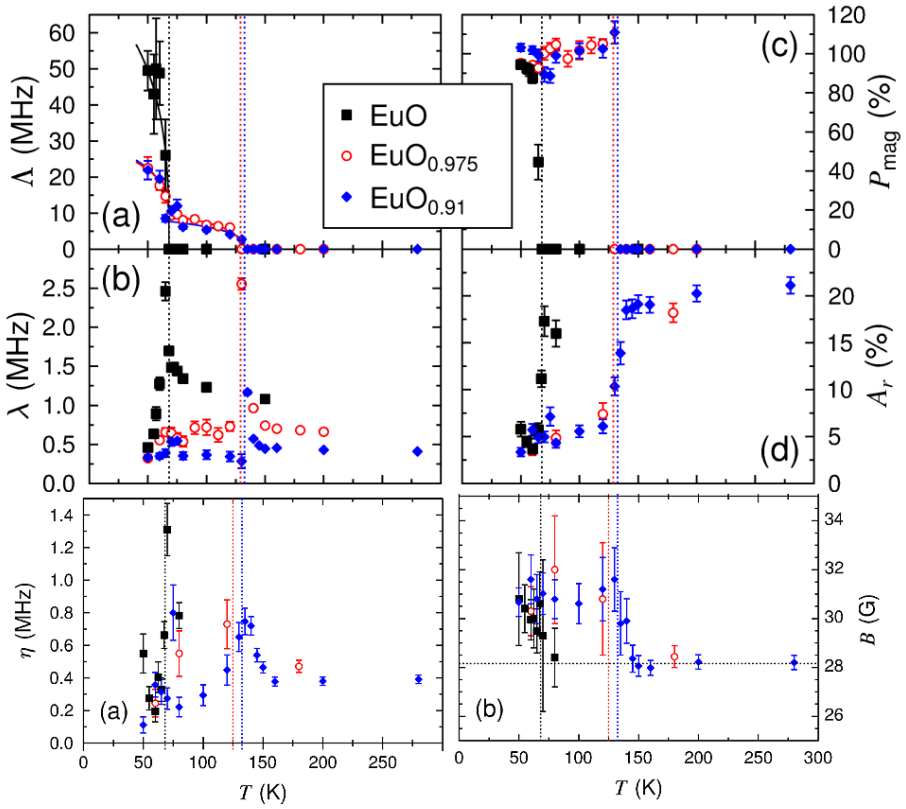

Fig. 3.20 : The results of the μSR experiments carried out by Monteiro *et al.* on pristine EuO, $EuO_{0.975}$ and $EuO_{0.91}$ samples measured at LEM beamline at PSI. The figure is taken from Ref. [130].

in Figure 3.20. Although only a few data points were collected to plot the $A_r(t)$ temperature dependence for the stoichiometric EuO shown in Figure 3.20, the sample exhibits a sharper transition at the T_C in comparison with the $EuO_{0.91}$, $EuO_{0.975}$ and our films. We also noticed that the B experienced by the muons implanted in our samples slightly decreases as T drops from 90 K to ∼68 K before it started to increase as T decreases further, below T_C. Although the sign of this change is different from those measured by Monteiro *et al.*, but since all of our measurements show a similar trend, we can conclude that the magnetic ordering in all of our measured samples is the same. Unexpectedly, η of our samples shows no peaks at the T_C as those reported by Monteiro *et al*. It rather seems to increase with the temperature until it plateaus at high $T > 75$ K.

No remark on the presence of the Mu state was made by Monteiro *et al*. However, signs of the presence of Mu is seen in their fitted plots for the stoichiometric EuO. For instance, η is expected to show a high increase in signal in the presence of Mu and a drop in the $A_r(t)$ vs

T plot which is the case for their pristine EuO. However, more analysis is needed to prove this assumption.

Clearly, the results of the μSR measurements show that our EuO films are not behaving as pristine or oxygen-deficient EuO. Therefore, it is certainly different from them and the change cannot readily be explained by oxygen vacancies occurring during the growth. Even though our measurements show no evidence of the increase of T_C, a conclusion that there is no spin-polarised 2DEG formed at the interface of the EuO(001)/LAO(001) cannot be drawn. A recent paper by Salman *et al.* reported the observation of a shallow Mu state in $SrTiO_3$, which acts as a shallow donor by occupying an interstitial site at the oxygen octahedron in STO and alters the optical and electronic properties of interfaces of STO-based heterostructures [182]. Since Mu behaves as a H atom, they proposed that H doping could provide a possible justification for the formation of a 2DEG at the interface of a STO/LAO heterostructure. Therefore, other possible interpretations can be made about our results which need further investigation such as: i) a 2DEG exists in our systems but it has no effect on the T_C of EuO, ii) a Mu is present but it is not clearly evident, iii) the 2DEG exists but it is so thin (< 2 nm) that the μSR experiment does not probe the effect, iv) the 2DEG exists but the effect is not as theoretically predicted, v) the 2DEG does not exist whether or not there is any Mu or H-doping.

In the attempt to clarify the third hypothesis, PNR measurements were carried out, as the technique has the advantage of measuring the magnetic properties of each layer of the heterostructure system. The PNR experiments and their outcomes are discussed in the following section.

3.4 PNR measurements

The PNR measurements were carried out at the D17 beamline at ILL. Since a large proportion ($\sim 47.86\%$) of naturally occurring Eu contains the isotope ^{151}Eu, which has an energy-dependent coherent scattering length [183], a monochromatic polarised beam of neutrons was used to determine the magnetic moments of the EuO layer and the interface accurately.

At the beamline, the LaO^+-terminated sample was loaded and the sample space was then pumped down to high vacuum before a field of 1 T was applied to the sample. A 195 K measurement was taken first before cooling down the sample to 5 K with an applied field of 0.1 T. The field cooling (FC) was carried out to ensure that the EuO film is saturated in the direction of the applied field. The field and temperature were left to stabilise before taking the 5 K measurement. After that the field was reduced to 350 Oe to collect the data at 64 K, 69 K, 72K and 80 K to avoid smearing out the paramagnetic to ferromagnetic transition. All

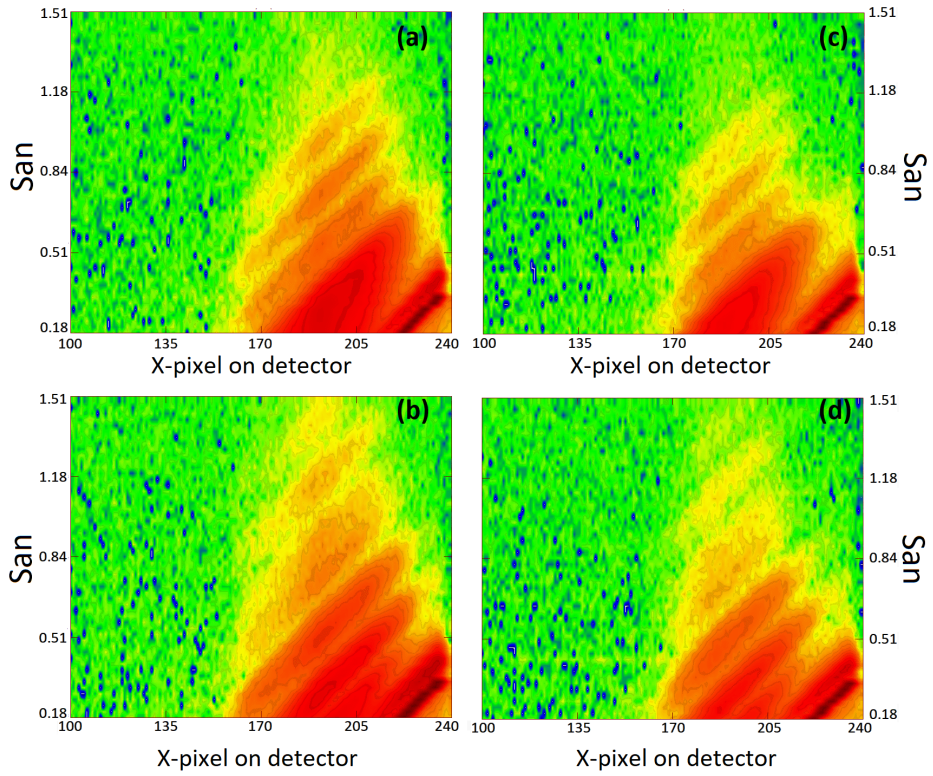

Fig. 3.21 : The low q 2D plots of the reflected neutron beam off the LaO-terminated sample (a) spin-up and (b) spin-down, and off the mixed-terminated sample (c) spin-up and (d) spin-down.

the measurements were taken at two different angles (low and high q): q from 0.005 $Å^{-1}$ to 0.06 $Å^{-1}$ and q from 0.04 $Å^{-1}$ to 0.11 $Å^{-1}$, respectively. However, due to time constraints,

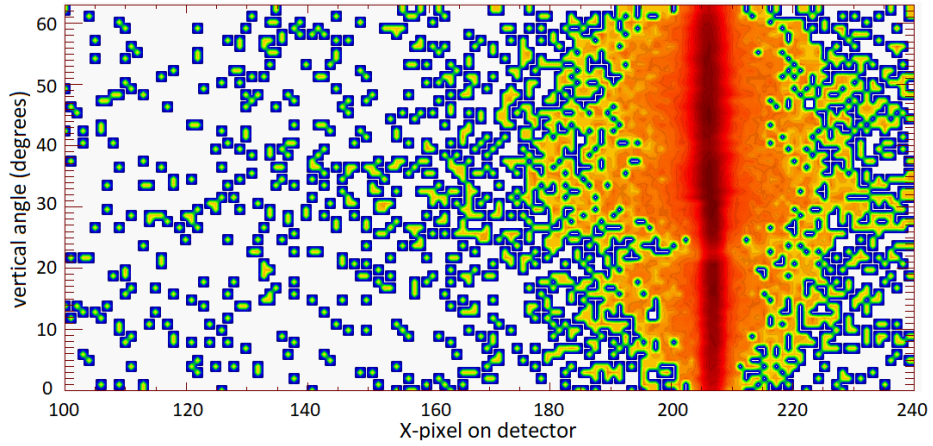

Fig. 3.22 : A 2D plot of the straight through beam showing the spread of the beam in the detector space.

the 80 K of the LaO^{+}-terminated sample was measured in the low q range only. After that, the sample was warmed up and replaced with the mixed-terminated one. Again, due to the

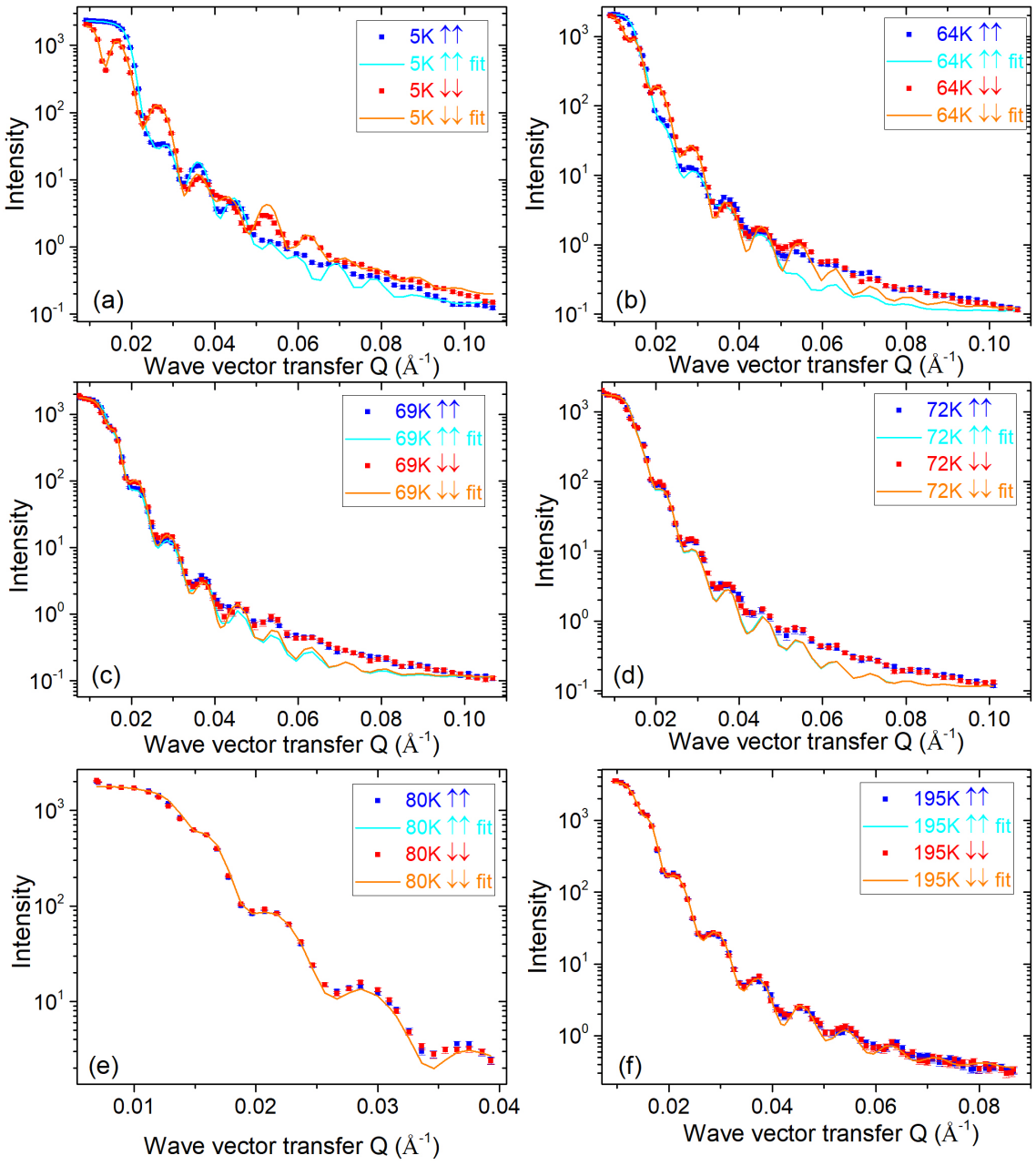

Fig. 3.23 : The PNR results of the LaO^{+}-terminated sample measured at different temperatures: (a) 5 K, (b) 64 K, (c) 69 K, (d) 72 K, (e) 80 K and (f) 195 K and their corresponding fits.

limited time which remained for the second sample, it was measured only at 5 K, 64 K, 69 K and 72 K.

The faceted surfaces of the samples caused by the twinning of the LAO, as well as the chemical etching, produced broader reflected beams. Figure 3.21 and Figure 3.22 show the 2D detector space plots of the beam reflected off the samples in the low q range and the straight-through beam, respectively. The number of x-pixels indicates the spreading of the beams, and thus the reflected beam is $\sim 1.6\times$ broader than the straight-through beam. Therefore, fitting the PNR data for the samples was expected to be a very challenging task.

The results of the PNR fits, for the data collected at different temperatures for the single and double terminated samples (after stitching the low and high q measurements and removing the overlapped data points) are presented in Figure 3.23 and Figure 3.26, respectively. Note that the data were scaled up or down for easier comparability. A model consisting of multi-layers of EuO was used to fit the data of both samples.

An initial attempt to fit the data was performed by using a model consisting of a single layer of EuO. However, to obtain good fits with such a model was not possible. Therefore, more layers of EuO were added until low χ^2 values were achieved with a model with five layers. Furthermore, considering each run individually led to a significant unrealistic discrepancy in the structural properties of the samples at different temperatures. For instance, the EuO and Au thicknesses in the fits varied by more than 20 nm from one measurement to another for the same sample. Therefore, the data of the low (5 K) and high (195 K) temperatures were fitted together to lock the structural properties of the sample, while

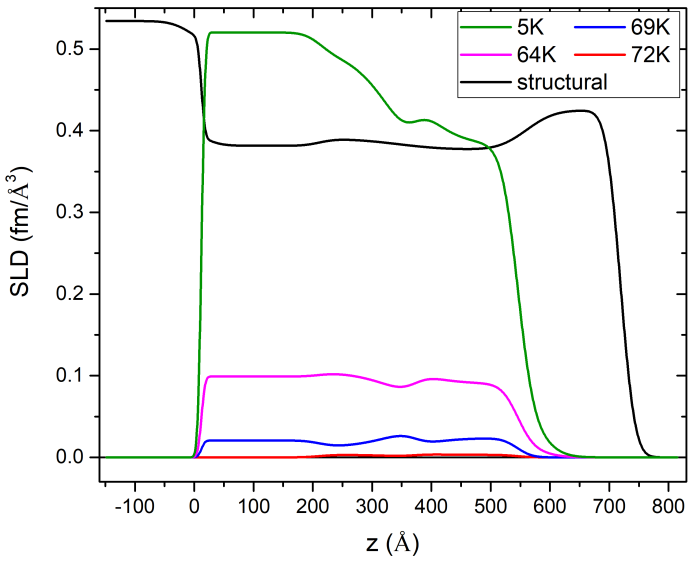

Fig. 3.24 : The SLD profiles of the LaO-terminated sample fitted for different temperatures.

obtaining the magnetic characterisation at 5 K as that of the 195 K was fixed to zero. After that, the intermediate temperature measurements (64 K, 69 K, 72 K and 80 K) were added one at a time while leaving the thickness, roughness and density of the layers obtained from fitting the 5 K and 195 K constant. The SLD profile of the single terminated sample at different temperatures showing the inhomogeneity of the EuO film is presented in Figure 3.24.

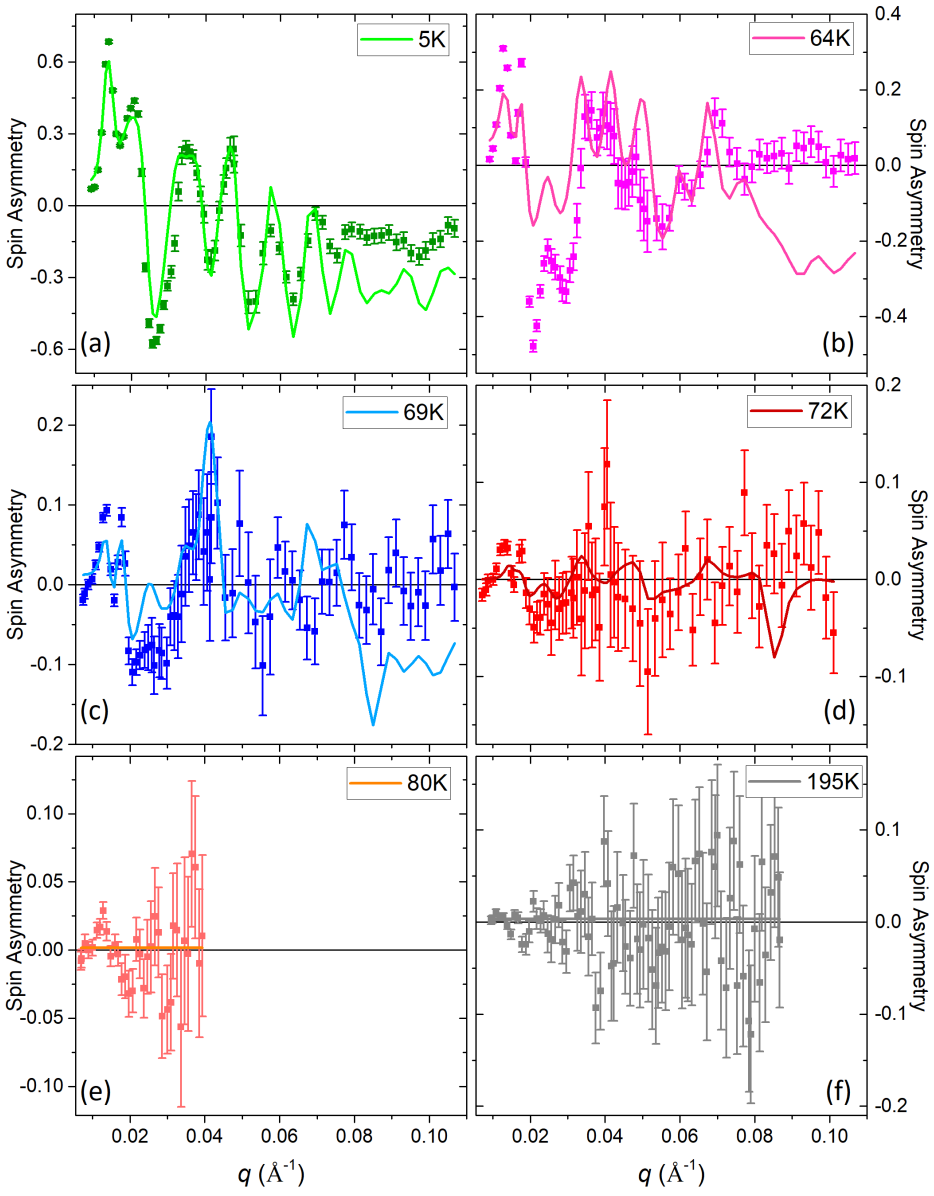

Fig. 3.25 : The spin asymmetry of the fitted results from the LaO^{+}-terminated sample for the (a) 5 K, (b) 64 K, (c) 69 K, (d) 72 K, (e) 80 K and (f) 195 K measurements.

GenX tended to overestimate the maximum intensity (I_0) and the background of the intermediate temperatures. Therefore, they were assessed manually and then kept fixed. The fits presented in Figure 3.23 show that the implemented approach for fitting the data led to poorer fits between $q \sim 0.04 - 0.06$ Å, especially for the 64 K, 69 K and 72 K data. For these fits, the program tended to overestimate the magnetic moment of the EuO layers to compensate for the drop of the fitted lines below the actual data. Therefore, a closer look was then taken at these measurements individually to determine the magnetic moment more

Thickness [Å]	
Layer	Value
Au	158.1
EuO_5	16.3
EuO_4	172.8
EuO_3	27.4
EuO_2	132.5
EuO_1	199.9
LAO	-
Roughness [Å]	
Layer	Value
Au	132.6
EuO_5	19.2
EuO_4	37.2
EuO_3	20.1
EuO_2	61.4
EuO_1	21.7
LAO	29.7
Atomic Number Density N [10^{28} mm^{-3}]	
Layer	Value
Au	0.0561
EuO_5	0.0471
EuO_4	0.0534
EuO_3	0.0501
EuO_2	0.0536
EuO_1	0.0549
LAO	0.0918

Table 3.1: The fitted parameters of the best PNR fit (thickness, roughness, atomic number density (N)) for the LaO^+-terminated sample obtained from fitting the 5 K and 195 K data together, where the count for the EuO layers 1 to 5 starts from the interface with the LAO substrate.

	Magnetic Moment [μ_B/atom]			
Layer	5 K	64 K	69 K	72 K
EuO_5	0.95±0.26	0.25±0.16	0.0±0.26	0.0±0.05
EuO_4	2.73±0.09	0.64±0.072	0.19±0.26	0.018±0.018
EuO_3	2.44±0.73	0.48±0.30	0.17±0.26	0.02±0.033
EuO_2	3.50±0.26	0.73±0.26	0.16±0.26	0.02±0.97
EuO_1	3.59±0.26	0.68±0.26	0.11±0.26	0.00±0.97

Table 3.2: The magnetic moments of the LaO^+-terminated sample deduced from the PNR fits of the 5 K, 64 K , 69 K and 72 K measurements.

accurately. For example, by examining the 72 K data, an infinitesimal spin splitting was observed around $q = 0.03$ Å^{-1}. However, the value of the magnetic moment is within the instrument resolution limit. Hence, it is very difficult to conclude that a small magnetic moment persisted in the EuO film up to 72 K. Therefore, the spin asymmetry (SA) of each run was plotted to determine how close we have predicted the magnetic moments of the EuO layers correctly. The SA plots of all the different measurements taken on the LaO^+-terminated sample are presented in Figure 3.25. The SA lines were produced from fitting the spin-up and spin-down data only. The plots show that our fits match the SA raw data up to $q = 0.08$ Å^{-1} for all the temperatures, except for the 64 K where the fit seems to underestimate the SA at about $q = 0.03$ Å^{-1}. This anomaly is also observed in the PNR fit which caused the spin-up line to drop below the raw data (Figure 3.23 (b)). However, since the significant spin splitting of the PNR, especially for the higher temperatures, occurs in the low q range, we believe that our model and the approach we used to fit the data offer the best estimation of the EuO magnetic moment. Table 3.1 summarise the fitted parameters; thickness, roughness and the atomic number density (N) of each layer of our model, whereas the EuO magnetic moment deduced from fitting the 5 K, 64 K, 69 K and 72 K measurements is listed in Table 3.2.

The data for the mixed-terminated sample was treated similarly. However, since the highest temperature measured for this sample is 72 K, we relied mainly on the 5 K data to lock the sample's structural and the magnetic properties. Therefore, fitting the data for this sample was even more challenging and the results are shown in Figure 3.26. They are not as good as those for the LaO^+-terminated sample. As seen in the figure, the fits yield larger fringes than the actual data at $q \sim 0.04$ Å^{-1}, which becomes more pronounced as T increase above 5 K. The SLD profile of the sample is presented in Figure 3.27. This SLD is different from that of the LaO^+-terminated sample. For instance, the hump in the structural SLD at $Z \sim 300$ Å is more prominent. Although only the 5 K measurements of both samples show

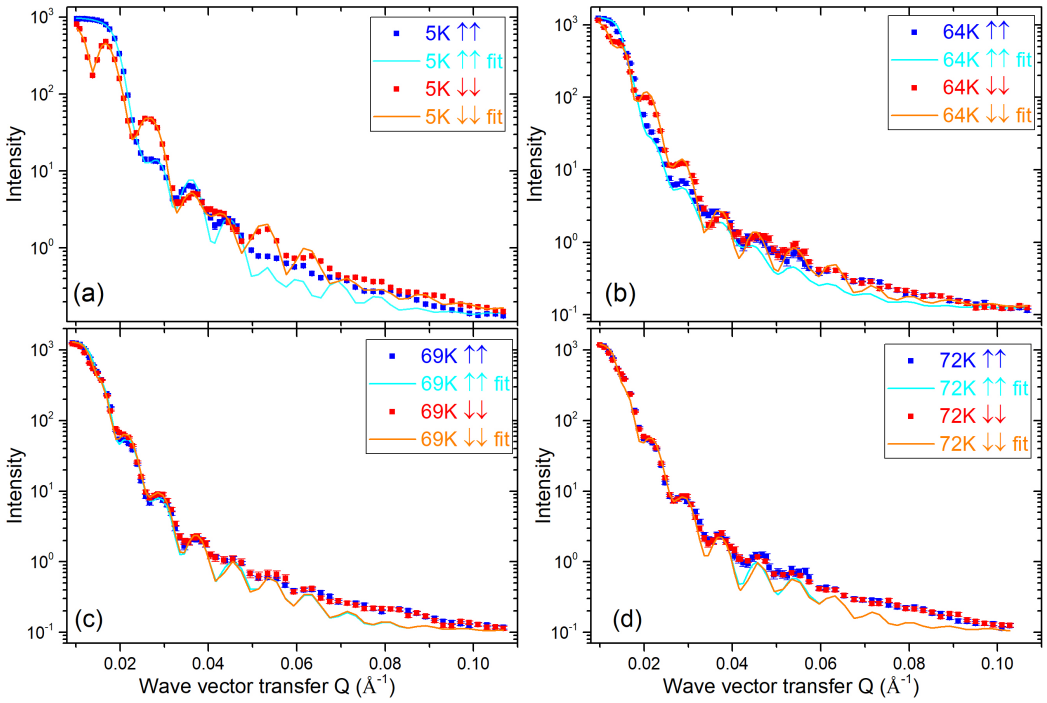

Fig. 3.26 : The PNR data fits of the mixed-terminated sample measured at (a) 5 K, (b) 64 K, (c) 69 K and (d) 72 K.

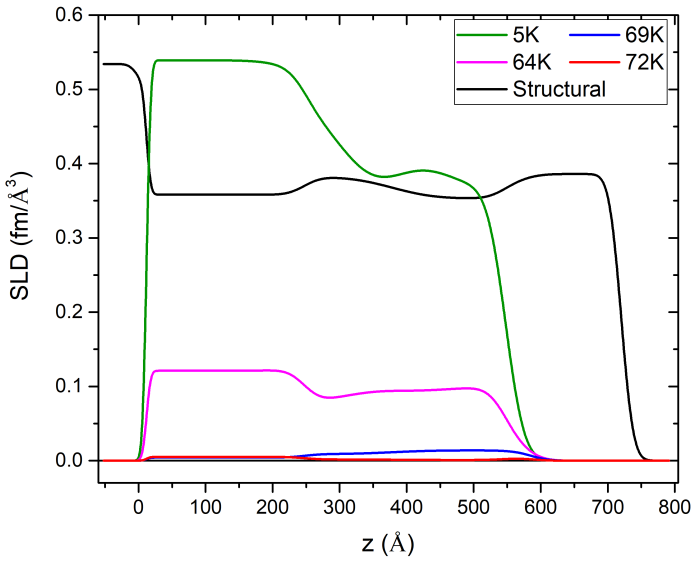

Fig. 3.27 : The SLD profile of the mixed-terminated sample showing the structural and magnetic contributions deduced from the PNR measurements taken at 5 K, 64 K, 69 K and 72 K.

large variations in the magnetic SLD profile, this is an indication of possibility inhomogeneity in the samples. The agreement of the fits with the raw data was also tested by plotting the SA

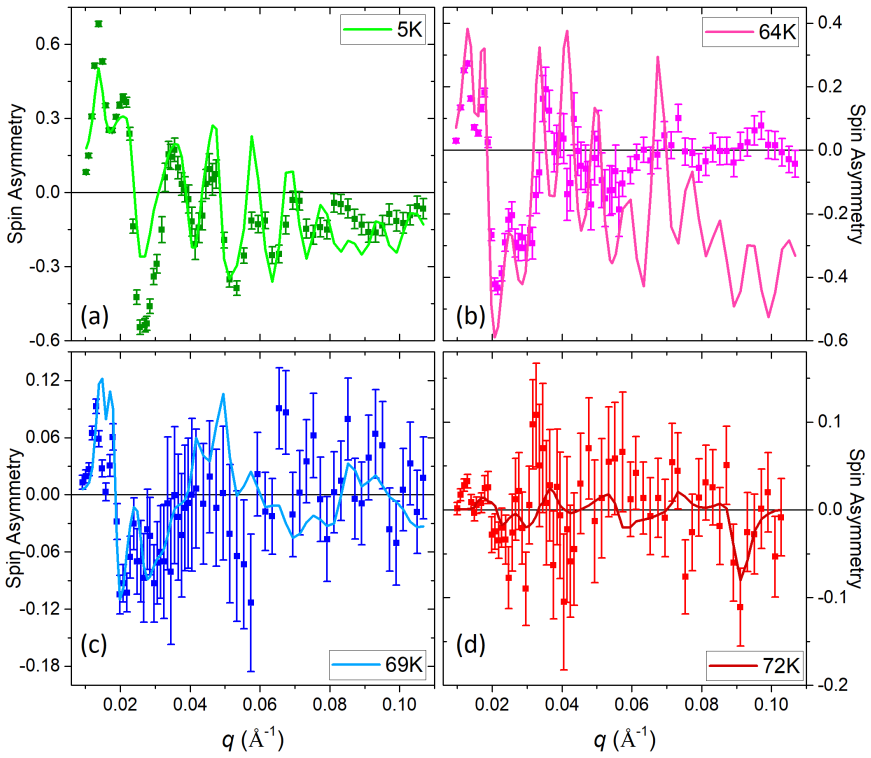

Fig. 3.28 : The SA and the corresponding fit lines of the PNR results of the mixed-terminated sample for the (a) 5 K, (b) 64 K, (c) 69 K and (d) 72 K measurements.

as shown in Figure 3.28. The graphs show that the fits match the SA data to a large extent although they underestimate the SA at $q \sim 0.03$ Å^{-1} for the 5 K data and completely misses the SA at $q > 0.06$ Å^{-1} for the 64 K. Table 3.3 and Table 3.4 lists the fitted parameters and the deduced EuO magnetic moments from the PNR measurements, respectively.

The magnetic moments of the EuO layers in each sample are summarised in the graph shown in Figure 3.29. The thicknesses of the Au and EuO layers in both samples are consistent, they differ by only 1.24 nm and 0.93 nm, respectively. The use of multi-layers of EuO, which reflects the inhomogeneity in the EuO film, may raise the question as whether that number of layers was really needed to model the PNR data especially as this inhomogeneity was not detected by the μSR measurement. However, having multiple layers distinct in PNR does not necessarily mean they should be detected by μSR as they may be within a single distribution of the μSR measurement, especially as these are facetted samples as well as epitaxial where the lattice relaxes with the thickness.

The PNR fits of the 5 K measurement of the single-terminated sample deduce an enhanced magnetic moment of 3.59 μ_B/Eu atom in the EuO film ~ 20 nm away from the EuO(001)/LAO(001) interface, whereas no increase of the EuO magnetic moment is de-

Thickness [Å]	
Layer	Value
Au	145.7
EuO_5	37.9
EuO_4	85.5
EuO_3	191.4
EuO_2	200.6
EuO_1	42.8
LAO	-
Roughness [Å]	
Layer	Value
Au	132.6
EuO_5	2.00
EuO_4	27.2
EuO_3	16.7
EuO_2	74.7
EuO_1	45.4
LAO	5.6
Atomic Number Density N [10^{28} mm^{-3}]	
Layer	Value
Au	0.0535
EuO_5	0.0583
EuO_4	0.0585
EuO_3	0.0494
EuO_2	0.0496
EuO_1	0.0584
LAO	0.0918

Table 3.3: The fitted parameters of the best PNR fit of the mixed-terminated sample: thickness, roughness, atomic number density (N) obtained from fitting the 5 K and 72 K data together.

tected for the mixed-terminated sample. The value of the enhanced magnetic moment in the LaO^+-terminated sample is consistent with that reported by Barbagallo *et al.* for a 9% oxygen-deficient EuO [184]. However, it is much thicker than the value predicted by the DFT calculations. Therefore, further investigations are needed, such as transport measurements, to infer the presence of a spin-polarised 2DEG at the EuO(001)/LAO(001) interface.

	Magnetic Moment [μ_B/atom]			
Layer	5 K	64 K	69 K	72 K
EuO_5	0.35±0.001	0.30±0.001	0.03±0.061	0.001±0.0005
EuO_4	2.71±0.015	0.56±0.002	0.07±0.012	0.004±0.0008
EuO_3	2.55±0.018	0.67±0.005	0.21±0.026	0.08±0.03
EuO_2	3.04±0.002	0.78±0.007	0.16±0.003	0.03±0.007
EuO_1	3.50±0.016	0.57±0.005	0.19±0.001	0.03±0.001

Table 3.4: The magnetic moments of the mixed-terminated sample deduced from fitting the PNR data for the 5 K, 64 K, 69 K and 72 K measurements.

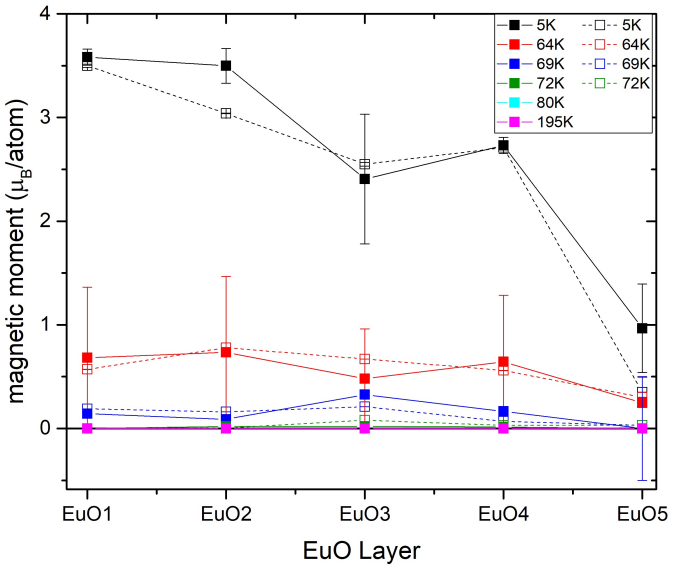

Fig. 3.29 : The magnetic moments of the EuO layers 1 →5 (the count starting from the interface with the LAO substrate) deduced from the the PNR fits of the single- and double-terminated samples presented by the solid and dashed lines, respectively.

3.5 Conclusion

This chapter reviewed the experimental work carried out to investigate the EuO(001)/LAO(001) interface. The AFM topographies confirm the successful production of a LaO^+-terminated LAO substrate via chemical and thermal treatments performed on the LAO. The structural and magnetic characterisation measurements have proved that high quality epitaxial EuO films were grown by magnetron sputtering on the treated LAO substrates. The lateral strain on the grown EuO films reduced their T_C by ∼2.6 K, which is found to be consistent with that reported by Caspers on a similar, but slightly thinner, heterostructure [169]. However, further investigations are required to study the effect of the EuO thickness on the T_C of strained EuO

films, which can be done by growing EuO films of various thicknesses on a LaO^+-terminated substrate. Furthermore, the A-N plots of our samples determined the critical exponents, β and γ to be (0.0493 ± 0.09) and (0.96 ± 0.29), respectively, for the LaO^+-terminated sample and (0.455 ± 0.04) and (0.95 ± 0.57), respectively, for the mixed-terminated sample which showed that our grown EuO films follows the mean field theory rather than the 3D Heisenberg model.

μSR measurements were then carried out on the EuO/LAO samples of LaO- and mixed-terminated substrates which showed that no magnetic phase separation is found in our epitaxial EuO films, but that they do not behave as a polycrystalline EuO or EuO_{1-x} as reported by Monteiro *et al.* [23, 130, 177]. It is believed that the LAO substrate indeed modified the magnetic behaviour of the EuO. However, it was not readily possible to explain it from the μSR experiment.

This chapter also discussed the results of the PNR measurements carried out on the LaO^+- and mixed-terminated samples. Models with multiple layers of EuO films were used to fit the data and a small magnetic moment was detected at 72 K. However, they are within the resolution limit of the PNR instrument (D17). Therefore, it is difficult to make a conclusion whether or not these magnetic moments are real and hint towards an increase in T_C. Furthermore, the PNR 5 K measurement on the LaO^+-terminated sample showed an enhanced magnetic moment in the EuO film at ~ 20 nm away from the interface, which is consistent with the value reported by Barbagallo *et al.* for a 9% oxygen-deficient EuO. However, more investigation is needed to verify this increase of the magnetic moment, especially given that it was not detected by the μSR technique. Therefore, transport measurements supported with DFT calculation may provide a better understanding of our experimental results.

4

EuO-NiO Interface

As mentioned in Chapter 3, new properties were measured at the interface of heterostructures while leaving the bulk properties of the films unchanged. Therefore, modern applications of magnetic thin-film heterostructures require precise control of their interface and magnetic properties. For example, ferromagnet/antiferromagnet interfaces are one of those well-studied heterostructures with technological spintronics applications such as in spin valves and magnetic read heads [185]. In such systems, the interactions between FM and AFM layers were found to strive to dominate the magnetic ordering at the interface. For example, FM order in thin films is usually stable at high temperatures with unstable orientation due to their small anisotropy and large exchange parameter, whereas AFM materials exhibit a large anisotropy and a small exchange parameter which lead to unstable AFM order at high temperature, but a stable orientation. Therefore, the interactions between the FM and AFM layers in such heterostructures can produce a very stable magnetic ordering with strong anisotropy at the interface [186]. A unique phenomenon known as exchange bias (EB) was reported to occur at the interface of such heterostructures.

This chapter gives an overview of the work carried out to explore the EB at the interface of EuO/NiO(111) heterostructure. Since a detailed description of the properties of EuO was

given in Section 3.1.1, a literature review of only the NiO structural, magnetic and electronic properties is provided in Section 4.1.1. The EB phenomena and the postulated mechanisms which derive the effect, with a particular emphasis on FM/AFM thin films, are described in Section 4.1.2. Section 4.2 discusses the experiments carried out to investigate the EB at the interface of NiO(111)/EuO and provides a detailed descriptions of the samples preparation procedures, structural and magnetic properties of the samples characterised by XRR, XRD, SQUID and PNR. A conclusion summarising the outcome of these experiments along with suggested measurements is given in Section 4.3.

4.1 Introduction

4.1.1 Properties of NiO

NiO is an antiferromagnet at room temperature (RT) and a paramagnet above its Néel temperature (T_N= 523 K) [188, 189]. It crystallises into an *fcc* crystal structure, $Fm\bar{3}m$ space group, as NaCl and EuO (with $a = 4.1758$ Å at RT) [190]. At $T < T_N$, the spins of the Ni^{2+} ions are aligned ferromagnetically along the <11$\bar{2}$> axes in the {111} planes as a result of the superexchange interactions between the Ni-O-Ni bonds in the [100] direction, and antiferromagnetically to the adjacent planes as shown in Figure 4.1 [191]. Therefore, NiO possesses trigonal magnetic anisotropy [192, 193]. It also experiences a contraction along the four <111> cubic directions causing a small, but temperature sensitive, rhombohedral distortion to its cubic lattice below T_N as a result of the magnetostriction [191]. Four

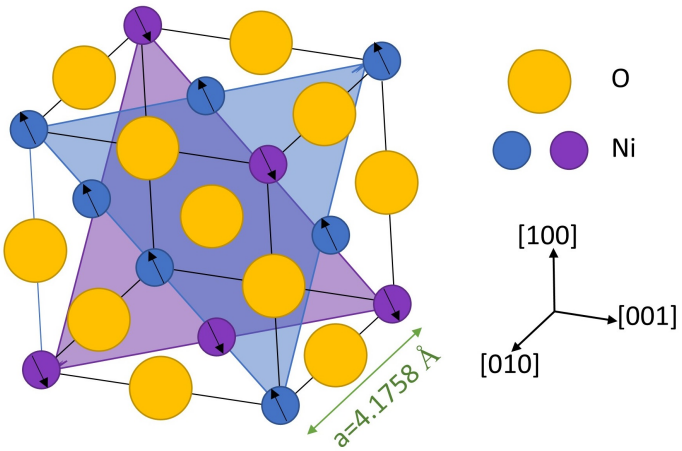

Fig. 4.1 : A schematic diagram of the NiO *fcc* crystal structure showing the ferromagnetic arrangement parallel to the (111) plane and the antiferromagnetic relation in the alternating planes where the spin direction is pointing in the <$\bar{2}$11> directions.

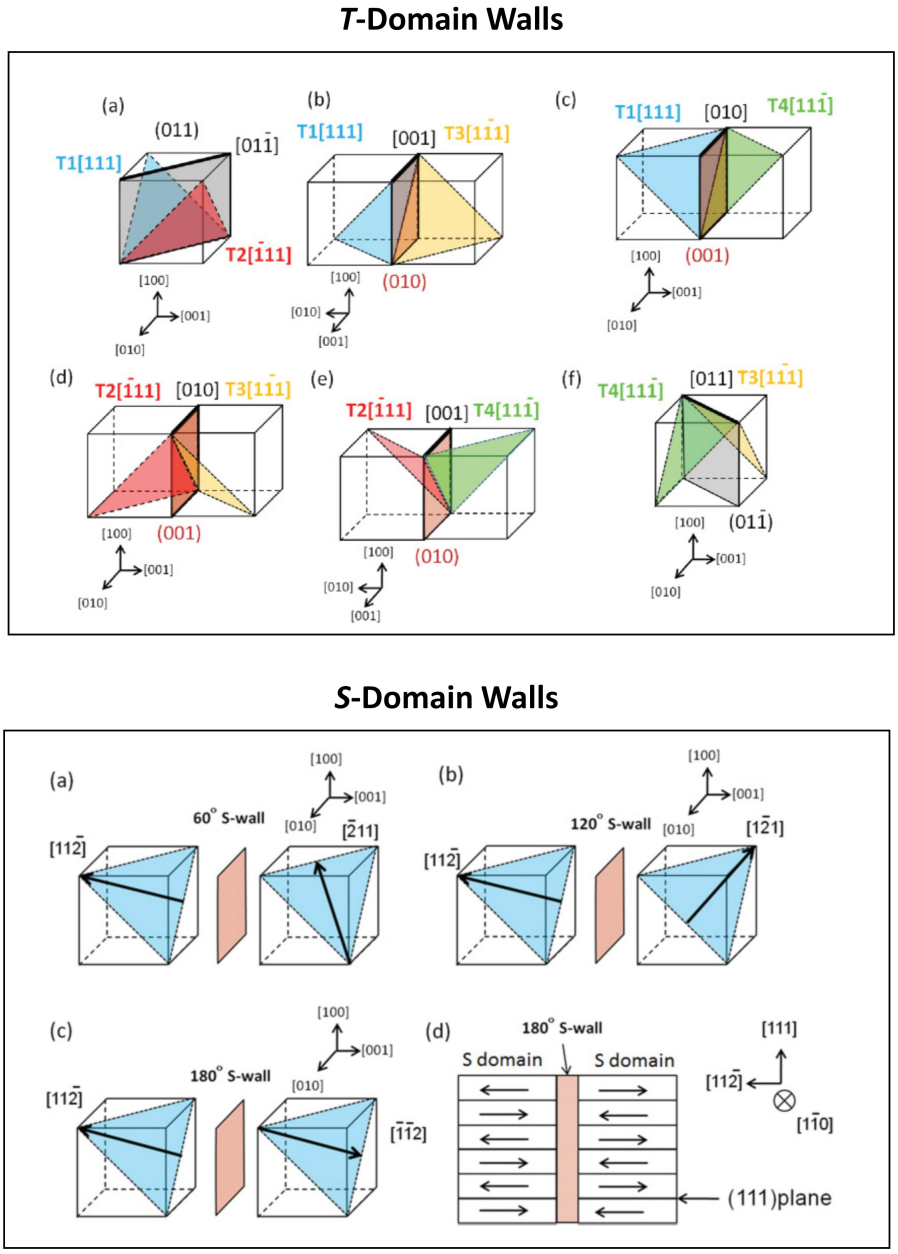

Fig. 4.2 : Illustrations of the two types of domains (*T*- and *S*- domains) formed in the NiO crystal and their corresponding domain walls (DWs) (*T*- and *S*- DWs). The top panel shows all the possible orientations of the *T*- DWs. (a) and (f) being the *T*-walls along the (110) planes separating the T1-T2 and T3-T4 domains. (b)-(e) are the (100) *T* DWs formed between the T1-T3, T1-T4, T2-T3 and T2-T4. The bottom panel presents the possible orientations of the *S* DWs formed at 60° (a), 120° (b) and (c-d) 180° between the *S*- domains. The Figure is taken from Ref. [187].

twinning domains (T-domains) are formed as a result of this deformation where each of these T-domains has three equivalent easy spin axes along the <11$\bar{2}$> directions creating a total of 12 magnetic spin domains (S-domains) [187–189, 192]. Domain walls (DWs), similar to those in a FM, were observed between these domains leading to two different types of DWs: T- and S- walls [187, 191]. The former DWs are formed along the {001} and {011} planes as a result of a crystallographic rotation of the AFM arrangement along the easy axes (i.e. (111) planes). The latter are created from the rotation of the direction of the magnetic moments within a single T-domain and that they make either 60° or 120° with their next S-domains of the same spin direction. Therefore, T and S DWs separate domains of different contraction axes and those with no contraction axes within the FM sheet, respectively, as shown in Figure 4.2 [187, 191, 193, 194].

NiO is considered as a p-type semiconductor with an optical band gap ranging from 3.6 eV - 4 eV and it is transparent for visible, infrared and UV radiations. Therefore, it is a potential material for many applications such as for photovoltaic and metal-oxide-semiconductor devices [196, 197]. NiO usually has an extra oxygen atom which cannot be inserted into its structure creating Ni^{2+} vacancies leading to its p-type semiconductor behaviour (i.e. it is not a fully ionic compound). Therefore, it is difficult to obtain a stoichiometric NiO film [198]. Furthermore, covalent bonding, to some extent, exists in the NiO crystal and calculations showed that occupancies of $3d^{8.22}$ and $3d^{8.76}$ occur in the Ni. However, since the overlap of

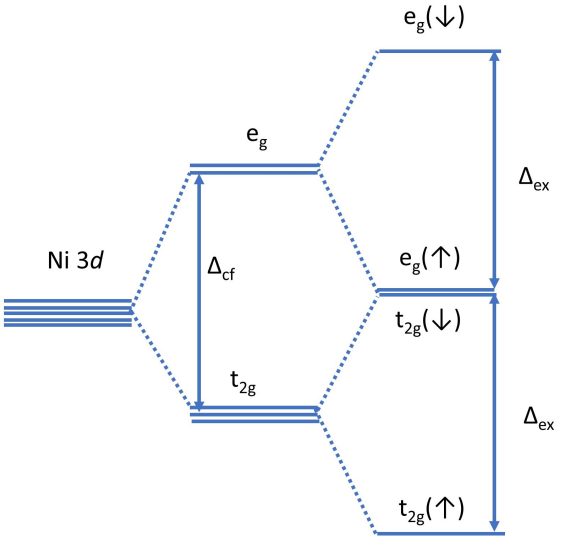

Fig. 4.3 : A schematic diagram of the NiO band structure highlighting the split of the Ni 3d orbital into two e_g and three t_{2g} degenerate levels as a result of the electron exchange (Δ_{ex}) and the crystal field effect (Δ_{cf}). The figure is constructed from Ref. [195].

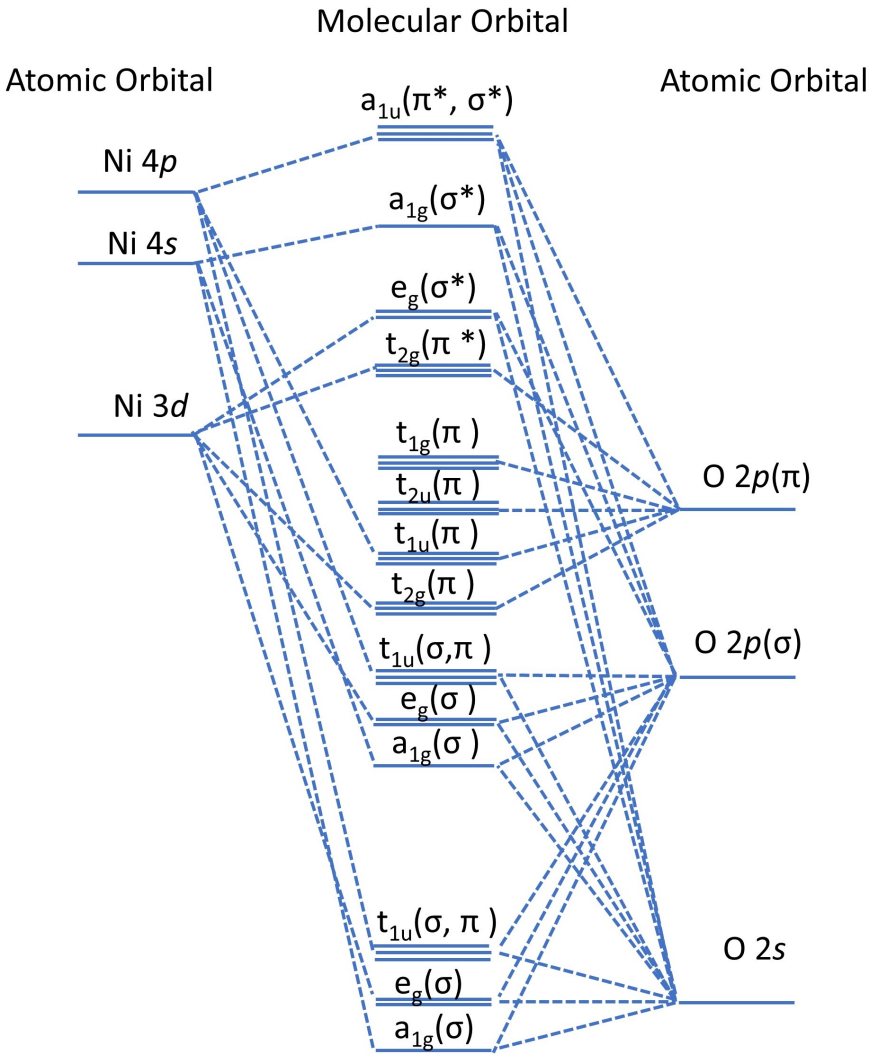

Fig. 4.4 : The molecular orbital diagram of the NiO showing the new stated created as a result of the Ni t_{2g} and e_g interactions with the O $2p$ orbitals and the exchange splitting. The figure is reconstructed from Ref. [195].

orbitals are small, the description of the NiO electronic structure is usually given in terms of the major constituent of the orbital. The conduction band (CB) of the NiO is made of the unfilled Ni $3d$, $4s$ and $4p$ orbitals, whereas the valence band (VB) consists of the O $2p$ and the filled Ni $3d$ orbitals, with a band gap of ~ 3.8 eV separating the CB and VB. The Ni $3d$ orbitals are then split, by the effect of the crystal field, into a three t_{2g} ($3d_{xz}$, $3d_{yz}$ and $3d_{xy}$) and two e_g ($3d_{x^2-y^2}$ and $3d_{z^2}$) degenerate levels, with the e_g orbitals being higher than those t_{2g} as shown in Figure 4.3. These levels will then interact differently with the O $2p$ orbital separating it into $2p_\sigma$ and $2p_\pi$. As a result of this exchange splitting, the Ni $3d_{eg}$ and

$3d_{t2g}$ are then split into majority ($\uparrow$) and minority ($\downarrow$) electrons. In a fully ionic NiO with a $3d^3$ occupancy, all the $3d$ orbitals are occupied except for the $e_g(\downarrow)$ state forming degenerate $e_g(\uparrow)$ and $t_{2g}(\downarrow)$ levels as shown in Figure 4.4 [195].

4.1.2 Exchange bias

The EB effect occurs at the interface of FM/AFM heterostructures in which the T_C of the FM$>>T_N$ of the AFM when they are field-cooled (FC) from above the T_N due to the exchange interactions between the FM and AFM across the interface [185]. This effect is observed mainly as a shift of the magnetic hysteresis loop with respect to the origin (i.e. $H = 0$) to $H_E \neq 0$, where H_E is the exchange bias field [199]. This phenomenon was discovered in 1956 by Meiklejohn and Bean in nanoparticles made out of a FM Co core coated with an AFM CoO shell [185]. It was then reported in different systems such as in single crystals, thin films and inhomogeneous materials [185]. However, this chapter focuses only on EB at the interfaces of FM/AFM insulator thin films.

When an external static magnetic field is applied to an FM/AFM structure, with $T_C>>T_N$, from above T_N (i.e. $T_N< T <T_C$) the hysteresis loop is usually shifted in a direction opposite to that of the applied field. An enhancement of the magnetic coercivity is another feature associated with the EB effect. An intuitive phenomenological model is usually used to explain the EB effect. This macroscopic picture presumes that the FM and AFM spins are parallel to the interface during the FC process as shown in Figure 4.5 [199]. When a FM/AFM heterostructure, with the AFM material of high magnetic anisotropy (K_{AFM}), is field-cooled (FC) with a high magnetic field from above T_N, the FM spins saturate in the direction of the field while the AFM spins remain random. However, due to the external interactions between the FM and AFM layers across the interface, the interfacial AFM spins will align in the direction of the FM spins as a result of the ferromagnetic interaction, while the bulk of the AFM retains the AFM arrangements. Thus, the bulk AFM will have a zero net magnetisation (Figure 4.5 (a)). After that, the FM spins rotate when the field is reversed to align with it. However, since the AFM exhibits a high K_{AFM}, its spins remain unchanged. Thus, the AFM spins at the interface will exert a microscopic torque on the FM spin to keep them in their original direction and retain the ferromagnetic alignment (Figure 4.5 (b)). Therefore, a higher field is required to overcome the AFM torque to rotate the FM spins (Figure 4.5 (c)). However, when the applied field is returned back to its initial direction, the AFM spins assist the rotation by applying a torque on the FM spin in the field direction. Therefore, the FM spins will start to turn in the direction of the field even in a small applied field (Figure 4.5 (d)). As a result, the magnetic hysteresis loop is shifted by H_E from $H = 0$ in a direction opposite to the initial direction of the external field [185, 200].

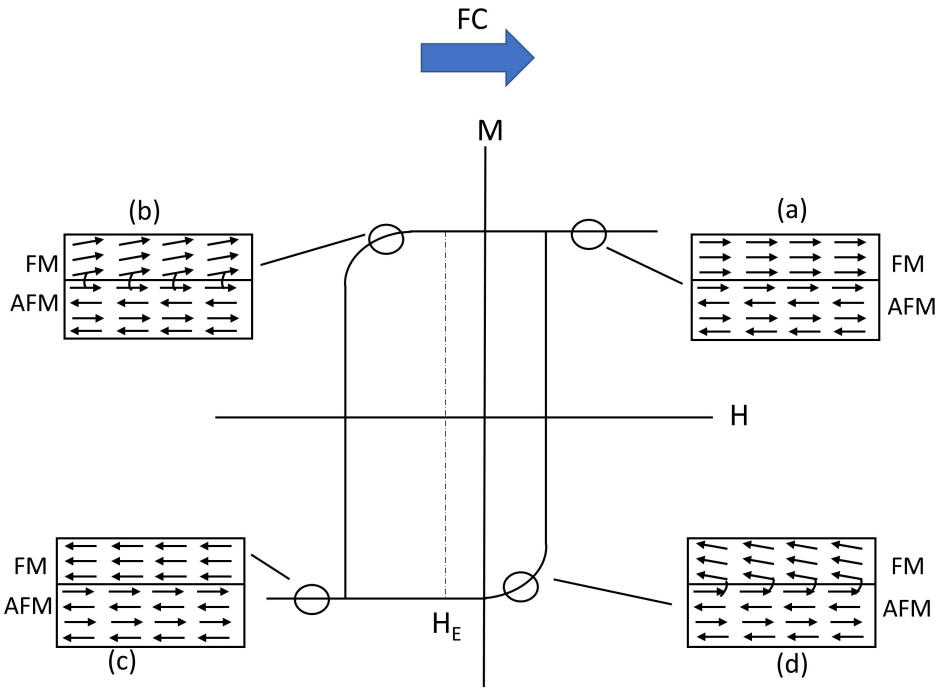

Fig. 4.5 : A schematic diagram illustrating the spin configurations of a FM layer and a strong anisotropy AFM film coupled together at different stages of a M vs H measurement with the shifted magnetic hysteresis loop due to the exchange bias field (H_{E}). The blue arrow indicates the field cooling direction.

On the other hand, the spins will behave differently when a strong external magnetic field is applied to a FM layer grown on the top of an AFM film with low K_{AFM} (Figure 4.6). In this case, the spins in both layers align with the applied field as shown in Figure 4.6 (a). When the field is reversed, the FM spins rotate with the field and turn the AFM interface spins with them due to the small K_{AFM} of the AFM film (Figure 4.6 (b)). Therefore, the additional energy generated from rotating the AFM spins is observed as an enhancement in the magnetic coercivity with no shift in the hysteresis loop. This is because a higher field will be required to completely reverse both the FM and AFM interfacial spins to saturate the spins in both directions (Figure 4.6 (c) and (d)) [200].

As can be deduced from this intuitive model, the FM spins have only one stable configuration (i.e. when they are aligned ferromagnetically with the AFM interface spins). Therefore, the induced unidirectional anisotropy (K_{ud}) is also considered as another feature associated with the EB. It was found that the angular magnetic torque (Γ) has a $K_{\mathrm{ud}}\cos\theta$ dependence in EB systems rather than a $K_{\mathrm{ua}}\sin\theta$ dependence as illustrated in Figure 4.7, where K_{ua} is the FM cubic magneto-crystalline anisotropy. Here, θ is the angle between the field-cooling direction and the applied field [185, 200]. Also, the EB effect was found to diminish as T

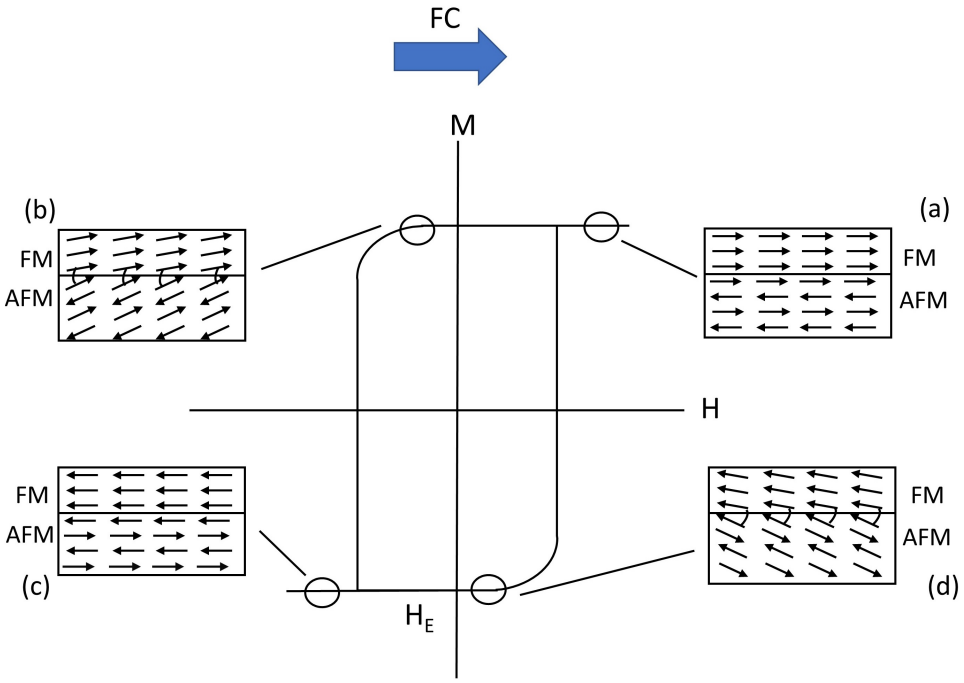

Fig. 4.6 : A schematic diagram illustrating the spin configurations of a FM layer and an AFM film with small K_{AFM} coupled together at different stages of the magnetic hysteresis loop during the FC process below T_{N}, which results in an enhancement of the magnetic coercivity.

increases towards the T_{N} of the AFM, until it disappears at a certain temperature known as the blocking temperature (T_{B}). Although T_{B} is usually $\approx T_{\mathrm{N}}$ in high-quality films, it can be much lower in nanoparticles, ultra-thin or polycrystalline samples. Besides these features, a "training effect" in which the H_{E} reduces with successive magnetic hysteresis

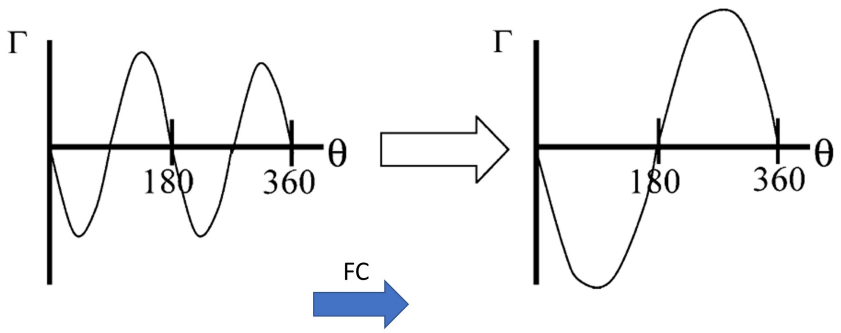

Fig. 4.7 : A sketch of the changes in the angular dependence of the magnetic anisotropy during the FC process from a ($K_{\mathrm{ua}}\sin\theta$) to a ($K_{\mathrm{ud}}\cos\theta$) relation in the presence of EB. The Figure is taken from Ref. [200].

loop measurements taken at a constant temperature was also reported in some EB system [201].

Although this macroscopic picture gives a general understanding of the EB a concise theory on the mechanism which derives the EB is still missing. Therefore, different theoretical models have been proposed in the attempt to provide a better understanding of this phenomenon [199]. Some of the postulated models managed to estimate reasonable H_E values, but compared to those measured experimentally they are still debatable. The reader is referred to some review papers where these models are discussed explicitly such as in Ref. [185, 186, 199, 200, 202–204].

4.2 Exchange bias experiments

Conventional EB systems require T_N to be lower than the T_C of the FM. However, the effect was also observed at interfaces where $T_N \geq T_C$ such as in Gd/Cr (293.2 K/308 K) and $Ni_{0.75}Cu_{0.25}$/NiO [205, 206]. In systems where $T_N \leq T_C$, EB can be established via various methods such as applying a sufficient magnetic field during the sample growth or during the post-annealing process to a temperature higher than the T_N of the AFM but lower than T_C. However, these approaches are inefficient to create EB in systems where $T_C \leq T_N$ as the AFM order can only be reached when the FM is in its paramagnetic state [206].

This section discusses the investigation of the magnetisation depth profile of the polar interface of NiO(111)/EuO and the possibility of the formation of the EB effect. For this purpose, two experiments were carried out on this heterostructure: zero-field cooling (ZFC) and field-cooling (FC) experiments to study the effect of the randomised and ordered AFM domains on the magnetisation of the EuO at the interface.

For the experiments, a MgO(111) substrates was used due to its thermal stability due to its high melting point, $T_{melting} = 3050$ K, and because NiO is known to grow epitaxially on top of it due to the small lattice mismatch of 0.9% (MgO lattice parameter, $a = 4.216$ Å). However, as the EuO film is produced from the co-sputtering of Eu and Eu_2O_3 as mentioned in Chapter 3.2.2 and since Eu is readily oxidised in the presence of O_2, the NiO(111) and EuO were grown in different chambers as discussed below.

4.2.1 Zero-field cooling (ZFC) experiment

4.2.1.1 Sample preparation

A 10 nm NiO(111) film was deposited on a ~ 0.5 cm $\times$ 1 cm MgO(111) substrate by Gleb Cheglakov (a member of the TFM group at the Cavendish Laboratory) using a bespoke MBE

machine designed mainly for the growth of oxides (see Section 2.1.2). The MgO(111) was ultrasonicated in acetone and then in IPA for 10 minutes each before it was loaded into the sample space load-lock which was then pumped down to 1×10^{-9} mbar. After that, the substrate was annealed at 300 °C for 12 hours to remove adsorbed contaminations. It was then lowered into the growth chamber with a pressure of 3×10^{-9} mbar and heated again to 300 °C for the growth of NiO. An evaporation rate of 0.23 nm/min was established for the Ni evaporator and O_2 gas was leaked into the growth chamber with a partial pressure of 1×10^{-7} mbar. The shutter was then opened to start the growth of the NiO film where the growth conditions were maintained throughout the process to obtain a homogeneous NiO film. After that, the sample along with a cleaned MgO(001) substrate, was transferred into the magnetron sputtering chamber for the growth of a 20 nm thick EuO film which was deposited, in a similar approach to that mentioned in Chapter 3.2.2, at a rate of 0.042 nm/sec, and capped with 15 nm of Au.

4.2.1.2 Structural characterisation

Figure 4.8 shows the XRD of the polar and non-polar samples, MgO(111)/NiO(111)/EuO/Au and MgO(001)/EuO/Au, respectively, from 20°- 100°. The missing EuO and Au peaks in the NiO(111)/EuO sample is an indication that amorphous EuO and Au layers were grown on the MgO(111)/NiO(111) sample which could be attributed to the large lattice mismatch between the EuO and the NiO crystals. Although the NiO(111) peaks is also missing, NiO(111) was grown with the same procedure in the past produced epitaxial NiO(111) on a MgO(111) substrate. Therefore, high-resolution XRD is needed to see the NiO(1111) and NiO(222) peaks. Considering all the possible crystal configurations in which the EuO might grow on a NiO(111) plane; EuO(111)/NiO(111) and EuO(001)/NiO(111) would result in lattice mismatches of $\sim$28.9% and $\sim$12.9%, respectively, as illustrated in Figure 4.9. In addition, the latter triggers also the difficulty of growing a cubic structure (EuO) on a hexagonal structure (NiO(111)).

On the other hand, despite the large mismatch between the EuO and MgO crystal of about 22%, EuO(001) has been reported to grow epitaxially on a MgO(001) substrate [169]. It was suggested that EuO and MgO would take a special structural arrangement to reduce the strain caused by the lattice mismatch such as 1:1, 4:5 and rotational stacking and that electrostatic interactions must be taken into account to understand the most favourable configuration [169, 207]. For instance, in a cube-on-cube of a 1:1 configuration, the growth of an atomically flat EuO on a MgO substrate is equivalent to substituting a Mg^{2+} ion at the surface with a bigger Eu^{2+} ion. Thus, increasing the O-O bond length from 0.298 nm to 0.363 nm. Therefore, the Eu and O atoms of the EuO film will find an equilibrium positions

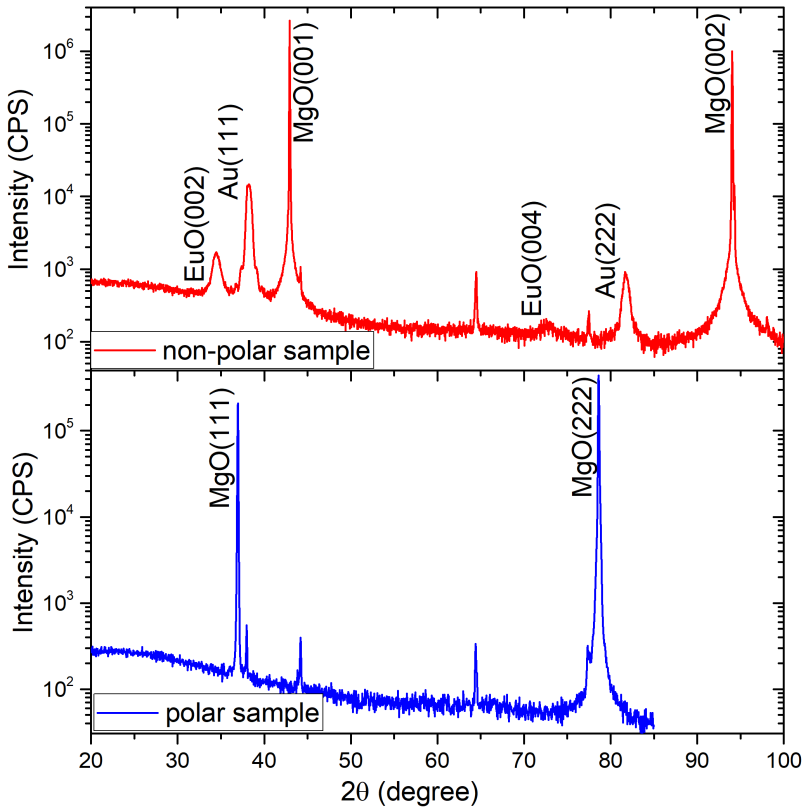

Fig. 4.8 : XRD scan of the MgO(001)/EuO/Au and MgO(111)/NiO(111)/EuO/Au samples carried out using a monochromator with a 1D detector from 20°-100°.

by roughening the surface (Figure 4.10 (a)). Alternatively, in the 4:5 arrangement (Figure 4.10 (b)), 4 unit cells (u.c.) of EuO are grown on 5 u.c. of MgO, where the first and the centre Eu^{2+} ions will position themselves on the top of an O^{2-} ion and a Mg^{2+} ion, respectively. The first O^{2-} ion of the EuO layer will be above an O^{2-} ion of the MgO(001) substrate.

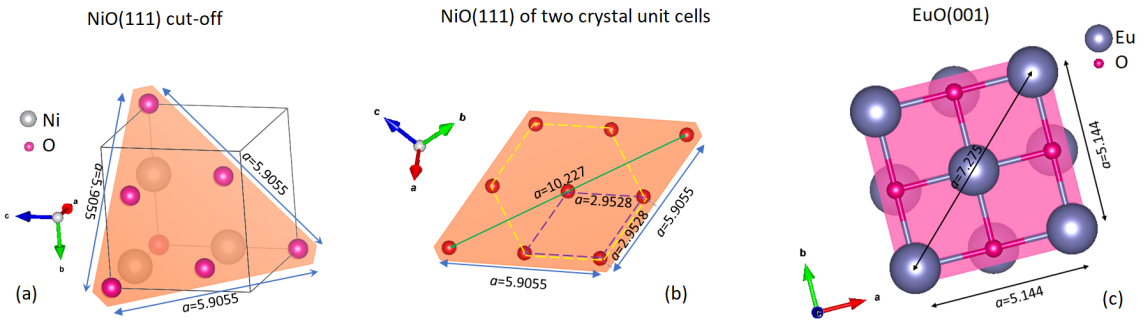

Fig. 4.9 : Schematic illustrations of the NiO(111) cut-off (a), NiO(111) plane in two cubic crystal unit cells (b) and EuO(001) plane (c).

This stacking will create strong Coulomb repulsive forces between the cations and anions which makes it unstable. Thus, a rough EuO will be deposited on the MgO substrate. A 45° in-plane rotation of the EuO layer relative to the MgO substrate was also considered as it removes the effect of the ion-size. However, it is still energetically unfavourable due to the Coulomb repulsions between the O^{2-} ions since they lay on top of each other. A

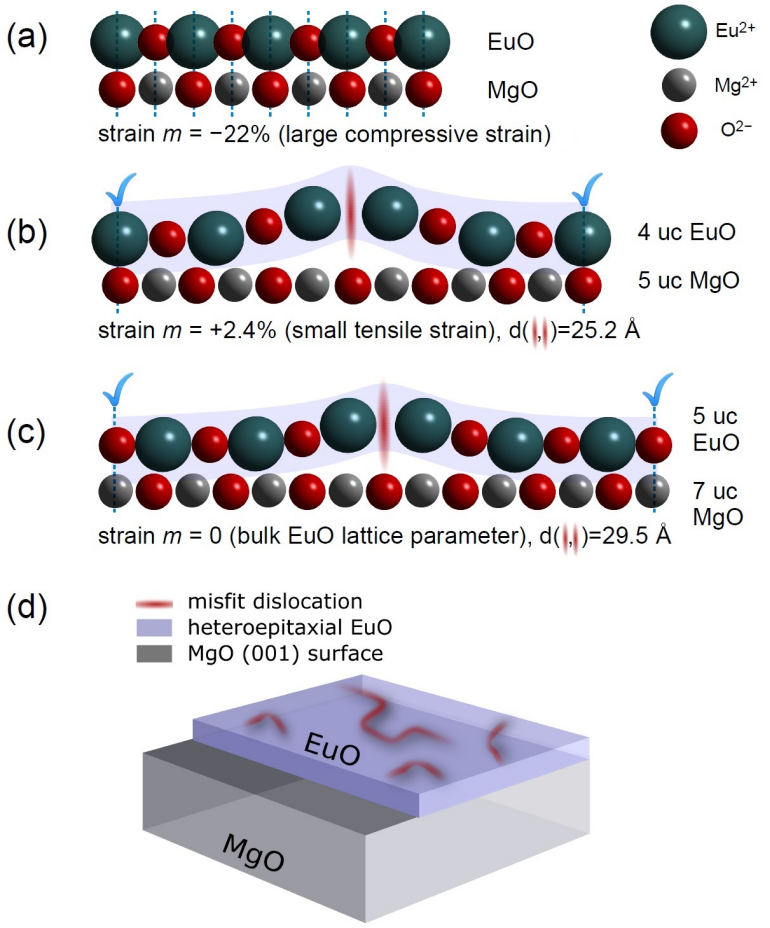

Fig. 4.10 : Schematic illustrations of the atomic arrangements of the EuO and MgO layers to produce heteroepitaxial EuO(001)/MgO(001) structure. (a) A cube-on-cube (1:1) stacking in which the effect of ion-size makes it an unfavourable arrangement and produces a 22% compressive strain on the EuO interface layer. (b) The 5:4 arrangement which causes a 2.4% lateral strain on the EuO interfacial layer as a result of the Coulomb repulsion between the ions. (c) and (d) the growth of relaxed EuO on a MgO substrate with no cube-on-cube relation, where a crystal dislocation is formed in the first EuO monolayer to restore a matched EuO(001)/MgO(001) staking which will then develop into a high-quality epitaxial EuO film with no lateral strain. The figure is taken from Ref. [169].

fourth configuration was proposed by Caspers based on the observation of an *in-situ* RHEED measurement collected during the growth of epitaxial EuO on a MgO(001) substrate [169]. It was suggested that after the growth of several relaxed EuO u.c. on a MgO wafer, a structural distortion takes place in the first monolayers of EuO to establish a new arrangement to maintain the matched EuO/MgO stacking and the in-plane heteroepitaxy as illustrated in Figure 4.10 (c) - (d). Thus, no strain is induced in the EuO film. These dislocations will only exist in the first monolayer of the EuO which will then develop into a single-crystalline EuO film as the thickness increases to more than 2 nm [169]. Although there is no presence of Eu or Eu-oxides peaks observed in the XRD of the non-polar sample, except for the highly oriented EuO(002) and EuO(004) peaks, X-ray ϕ-scan is needed to clarify whether an epitaxial or a textured EuO is grown on the MgO(001) substrate.

Figure 4.11 shows the fitted XRR measurements which confirm the presence of NiO, EuO and Au films on the MgO(111) substrate as it was impossible to fit the data without those layers. Also, the densities of the NiO, EuO and Au are consistent with the theoretical values. However, the fit of the polar sample overestimates the density of the NiO layer which can be seen from the estimated value in the inset of Figure 4.11 (b) and from the fit line at $2\theta \approx 1.3°$ and $2\theta \approx 1.7°$.

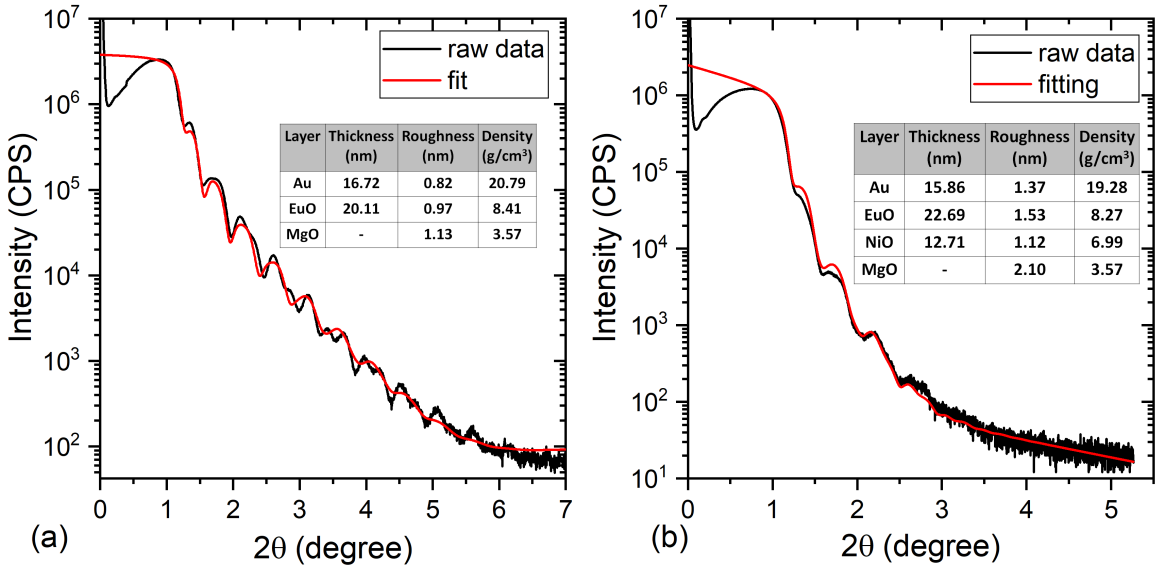

Fig. 4.11 : XRR measurements of (a) the MgO(001)/EuO/Au and (b) MgO(111)/NiO(111)/EuO(001)/Au samples (black lines) and the corresponding fits (red lines). The insets show the values of the thickness, roughness and density as deduced from the fits.

4.2.1.3 Magnetic characterisation

Since the shift of the hysteresis loop is the characteristic feature of the EB, the M vs H measurements of the samples were carried out at 5 K using a SQUID magnetometer and the results are presented in Figure 4.12. The hysteresis of the non-polar sample exhibits an almost square-shaped loop with a coercive field (H_c) of 61 Oe, which is lower than that reported in Ref. [208] for a similar heteroepitaxy of a comparable thickness. A remanence of $\sim 83\%$ of the saturated magnetisation indicates that the applied field was not aligned along the EuO easy axis (i.e. [111]) during the measurement.

On the other hand, a small double-shifted hysteresis loop with an increased $H_c \sim 85$ Oe is observed in the M vs H of the polar sample. The enhancement of H_c is expected due to the small K_{AFM} of NiO in which the interfacial spins can be easily tilted in the direction of the applied field due to its ferromagnetic coupling with the EuO magnetic domains as discussed in Section 4.1.2. However, the double-shifted behaviour of the hysteresis loop is due to the competition of two NiO S-domains pointing in different directions as presented in the schematic diagram in Figure 4.14. The arrows illustrate the direction of the spins in a particular S-domain within the NiO(111) plane. Since the NiO S-domains are randomised

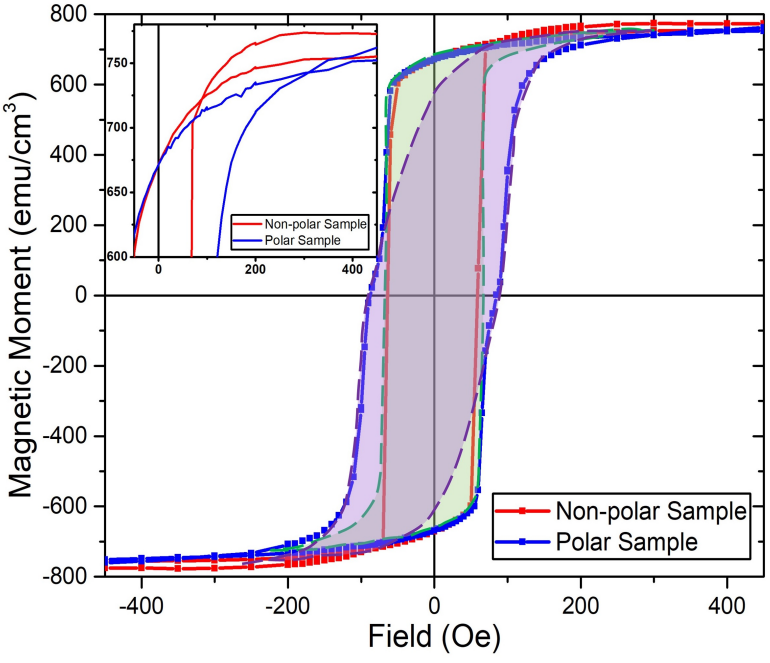

Fig. 4.12 : M vs H measurements of the polar and non-polar samples showing a small double-shifted hysteresis loop with an enhanced coercivity of 23 Oe in the former. The shaded areas represents the hystereses arising from the different NiO S-domains. The inset highlights the crossover of the ascending branch of the loop.

initially due to the ZFC, the ratio of the three directions of the *S*-domains are assumed to be 1:1:1. Therefore, when the field is swept in-plane, in the direction indicated by the double-ended black arrow in the figure, the spins will rotate in-plane to align with it. However, it will be easier to align the spins of those domains that make a smaller angle with the field than those with large angles. By referring to Figure 4.14, it will be easier to turn the green and then the yellow domains. Hence, the hysteresis loop arising from the green *S*-domains will have a small H_c and would saturate at a smaller field than those of the yellow *S*-domains. Although the hysteresis loop of the sample is expected to be the sum of all the *S*-domains, in fact, the contributions of only two types of *S*-domains are observed (highlighted with dashed lines) in the field-dependent magnetisation curve shown in Figure 4.12. The third *S*-domain is possibly pinned by a *T*-domain and therefore does not turn with the applied field and is not shown in Figure 4.14.

A crossover between the ascending and descending branches of the loops are observed in both samples at about $\pm$320 Oe and $\pm$87 Oe for the polar and non-polar samples, respectively, which could be attributed to measurement artefacts (inset of Figure 4.12). However, further investigations are needed to understand the origin of this behaviour.

The *M* vs *T* measurements collected for both samples with an external field of 100 Oe are presented in Figure 4.13. Although the non-polar sample does not seem to be saturated with 100 Oe applied field, Brillouin-shaped curves with no paramagnetic contributions indicating

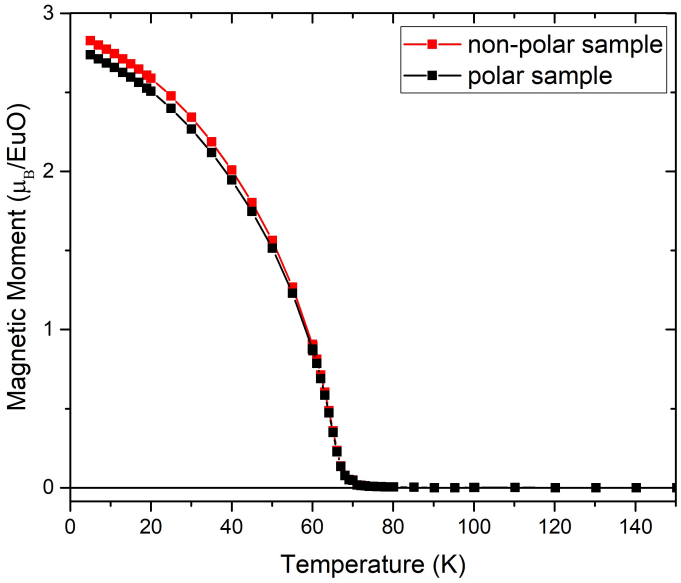

Fig. 4.13 : The *M* vs *T* measurements collected with an applied field of 100 Oe on the MgO(001)/EuO (red) and MgO(111)/NiO(111)/EuO (black) samples after the subtraction of the contributions of the substrates where the EuO of both samples possess a T_C of 69 K.

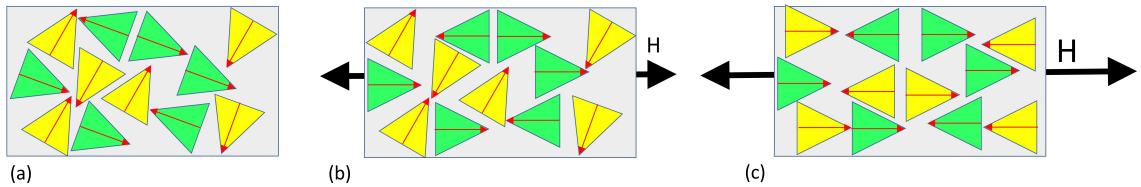

Fig. 4.14 : A schematic diagram illustrating the arrangement of the NiO(111) *S*-domains which respond to the applied field (H) during the SQUID measurement, when (a) $H = 0$ Oe, (b) when $H > 0$ Oe and (c) when $H >> 0$ Oe, where the black arrows indicate the direction of the applied field during the sweep and the size of the arrows reflects the H strength.

a T_C of 69 K of the EuO film in both samples are observed. However, the reduced magnetic moment can be attributed to a large error arising from measuring the dimensions of the samples, the misalignment of the samples along the easy axes during the measurements as discussed above or the slight oxidation of the EuO film.

4.2.1.4 PNR measurements

Although the characteristic feature of the EB (i.e. the horizontal shift of the hysteresis loop) was investigated using the SQUID magnetometer as discussed in the previous section, PNR measurements were carried out to confirm the spin arrangements suggested above, and to obtain a better understanding of the structural and magnetic depth profile of the samples.

The PNR experiments were collected at the POLREF beamline at ISIS spallation source using the TOF mode. At the station, the polar sample was loaded first and pumped down to ultra-high vacuum. It was then field-cooled to 5 K with an applied in-plane magnetic field of 700 Oe to ensure the saturation of the EuO film. After completing the 5 K measurement, the sample was warmed up to 67 K where data was collected in the same field. The polar sample was then removed and the MgO(001)/EuO(001)/Au was loaded and measured at 67 K only, due to time constraints, in an equivalent in-plane magnetic field of 700 Oe. The results of the PNR measurements of both samples are shown in Figure 4.15.

The non-polar sample was fitted first as it is more straightforward compared with those of the polar sample. Initially, a model consisting of a single layer of EuO was used. However, it was difficult to fit the features at 0.029 Å$^{-1} < q < 0.035$ Å^{-1}. Therefore, the number of the EuO layers was increased to three layers until a good fit with $\bar{\chi}^2 = 1.63$ was obtained for the fit shown in Figure 4.15 (a). The values of the fitted parameters obtained from this fit were used to fit the SA data (Figure 4.15 (c)) and to plot the resultant structural, real and imaginary magnetic SLD which signifies the neutron scattering and the neutron absorption by the nucleus, respectively (Figure 4.15 (b)) [85].

Since the NiO(111) *S*-domains are randomised and as three layers of EuO (EuO_{top}, EuO_{mid} and EuO_{bottom}) were used to fit the non-polar sample, the same number of layers was

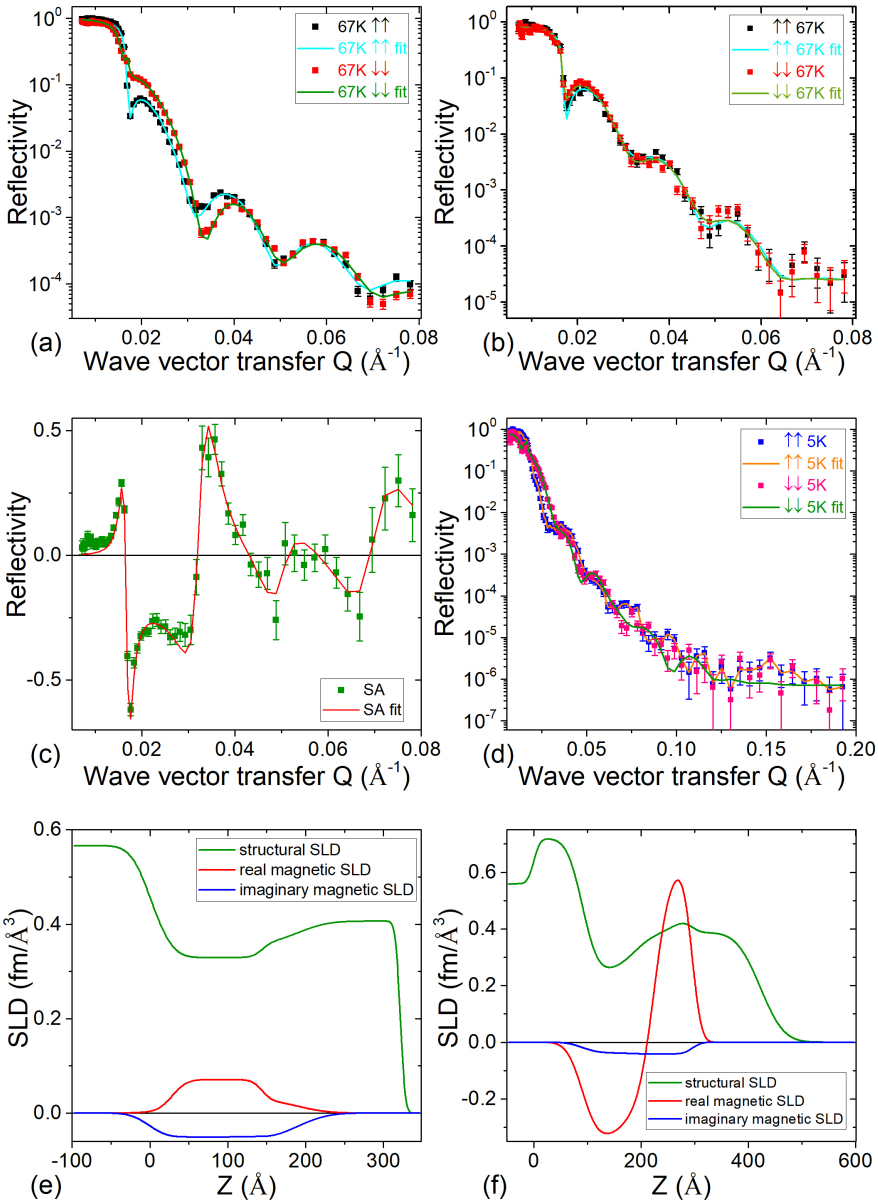

Fig. 4.15 : The results of the PNR experiments carried out on the non-polar (MgO(001)/EuO) and polar (NiO(111)/EuO) samples with an applied field of 700 Oe. (a) The 67 K PNR data and the corresponding fits for the MgO(001)/EuO/Au sample. (b) The 67 K PNR data and the corresponding fits for the ZFC NiO(111)/EuO sample. (c) The SA for the 67 K data for the non-polar sample. (d) The 5 K PNR data and the corresponding fits for the polar sample. (e) The SA of 67 K PNR data for the non-polar sample. (f) The SA of the 5 K PNR data for the polar sample.

used to construct a more complex model to fit the 5 K PNR data of the ZFC polar sample. In this model, the sample is then divided into three segments where each one has a different spin arrangement as illustrated in Figure 4.16 (a). In Section 1, the EuO_{bottom} and NiO interfacial spins align fully along the direction of the applied field, in the opposite direction to the field in Section 2 and perpendicular to the applied field in Section 3. However, different scenarios are expected to occur in the EuO_{mid} and EuO_{top} layers. The pinning effect of the NiO(111) interfacial spins becomes weaker by increasing the distance between the EuO layer and the EuO/NiO(111) interface until it disappears closer to the EuO/Au interface, where the EuO spins will be influenced only by the applied field. Therefore, in Section 2, the spins will start to turn in the direction of the applied field, until they point perpendicularly to the external field in the EuO_{mid} layer before they align fully with it in the EuO_{top} layer. The spins of the EuO of Section 3 will also start to rotate with the field in EuO_{mid} until they point parallel to the field in EuO_{top}.

Figure 4.16 (b) presents the model used to fit the 67 K data. At 67 K, the magnetism in the EuO is very weak since it is close to the T_C and the majority of the spins will have sufficient thermal energy to break away from their ferromagnetic coupling. Therefore, they will easily turn in the direction of the field even when a small field is applied. Since short-range exchange interactions between the NiO and EuO are formed across the interface, the NiO will only ferromagnetically couple the EuO interfacial spins, whereas the rest of the EuO layer will be aligned with the field.

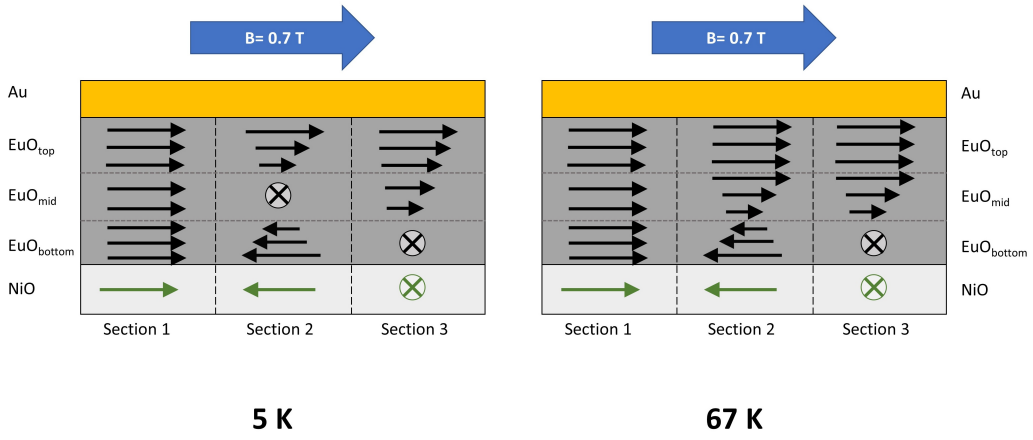

Fig. 4.16 : Illustration of the 5 K and 67 K PNR fitting models for the ZFC polar sample consisting of three EuO layers (top, middle and bottom) a layer of NiO and Au. Each of the NiO and EuO layers is divided into three sections with different spin arrangements: the NiO interface spins are projected to be aligned in the direction of the applied field (Section 1), antiparallel to the field (Section 2) and perpendicular to the applied field (Section 3). The blue arrow represents the direction of the applied field of 0.7 T.

Thickness [Å]		
Layer	MgO(001)/EuO	NiO(111)/EuO
Au	132.6	127.25
EuO_{top}	44.80	70.31
EuO_{mid}	114.8	14.66
EuO_{bottom}	30.2	119.35
NiO		90.82
Roughness [Å]		
Layer	MgO(001)/EuO	NiO(111)/EuO
Au	5.00	34.78
EuO_{top}	30.00	13.73
EuO_{mid}	5.00	21.33
EuO_{bottom}	14.00	45.0
NiO		22.88
MgO	18.57	9.49
Atomic Number Density N [10^{28} mm^{-3}]		
Layer	MgO(001)/EuO	NiO(111)/EuO
Au	0.053	0.056
EuO_{top}	0.055	0.051
EuO_{mid}	0.050	0.068
EuO_{bottom}	0.055	0.077
NiO		0.037
MgO	0.054	0.045
Magnetic Moment [μ_B/atom]		
Layer	MgO(001)/EuO [67 K]	NiO(111)/EuO [5 K]
EuO_{top}	0.20 $\pm$0.1	0.71$\pm$0.07
EuO_{mid}	0.53$\pm$0.05	3.50$\pm$0.42
EuO_{bottom}	0.38$\pm$0.07	3.54$\pm$0.31

Table 4.1: The fitted parameters of the best PNR fit of the uncoupled (MgO(001)/EuO) and coupled (NiO(111)/EuO) samples: thickness, roughness, atomic number density (N) and the magnetic moment of the 67 K and 5 K measurements.

The 5 K and 67 K data were fitted together using the models discussed above to lock the structure and magnetic properties of the polar sample, and the results are shown in Figure 4.15 (b) and (d). The same two models with different numbers of EuO and NiO layers such as 3 EuO + 2 NiO layers and 4 EuO +1 NiO layers were tested. However, the fitting software (GenX) tends to minimise the thicknesses of the 4th EuO and 2nd NiO layers to zero and

indicates that no magnetism is induced in the NiO layers. Therefore, the model with 3 EuO, 1 NiO and 1 Au layers was considered the best.

By comparing the PNR fits at 67 K of the polar and non-polar samples, an unexpected larger spin-splitting is observed in the latter than in the former. This may be due to the presence of the randomised NiO *S*-domains at the interface which prevent the EuO interfacial spins aligning fully with the applied field. However, further understanding of the spin distribution at the interface between the NiO and EuO films is needed to obtain a better insight into the role of the NiO(111) *S*-domains. Therefore, additional PNR measurements were performed which will be discussed in the next section.

The best PNR fit of the polar sample shows that the magnetic moment of the EuO layer at 67 K is (0.13 ± 0.04) μ_B/EuO which is much lower than that for EuO(001)/MgO(001), measured at the same temperature, which supports the assumption of the NiO(111) pinning effect. The results also show that $(58.7 \pm 0.6)\%$ of the EuO adapts the scenario of Section 1, $(11.3 \pm 0.2)\%$ that of Section 2 and $(30.1 \pm 0.4)\%$ the Section 3 scenario. The values of all the fitted parameters of the best PNR fits of the polar and non-polar samples are listed in Table 4.1.

4.2.2 Field-cooling (FC) experiment

A field-cooled NiO layer for a NiO(111)/EuO sample was prepared and measured to verify the assumption made in the previous section with regards to the pinning of the EuO spins by the randomised NiO *S*-domains. During the PNR measurements, the field was applied in the original FC direction of the NiO, and then the sample was rotated 90° in-plane to measure the pinned and unpinned spins of the NiO *S*-domains separately. Also, all the four channels of the PNR: R^{++}, R^{--}, R^{+-} and R^{-+} were measured during the experiments, as discussed in more details in Section 4.2.2.4.

4.2.2.1 Sample preparation

A 20 nm thick NiO(111) film was grown on a MgO(111) substrate similarly to that for the ZFC experiment (Section 4.2.1) with the help of Dr Adrian Ionescu from the TFM group at the University of Cambridge. The MgO(111) substrate was ultrasonicated in Semico-Clean for 15 minutes and then transferred into DI water for 30 minutes, before it was dried with a N_2 gun. The substrate was then loaded into the load-lock of the MBE chamber and pumped down to 1×10^{-6} mbar and then degassed at 300°C for 12 hours. After that, it was lowered down into the growth chamber at the base pressure of 3.7×10^{-11} mbar and annealed again at $\sim$300 °C for the growth of NiO. An evaporation rate of 0.069 nm/min was used for the Ni rod.

O_2 was introduced into the growth chamber at a partial pressure of 8.1×10^{-6} mbar while keeping the temperature at $\sim$ 306 °C. The shutter was then opened to start the deposition of the NiO film with an average rate of ∼4.2 Hz/min which was achieved by maintaining a constant Ni flux. When a 20 nm of the NiO(111) film was grown, the shutter was closed, O_2 flow was stopped and the sample was cooled down in vacuum to RT. After that, it was annealed again to 300 °C (above T_N) and placed between the poles of a magnet and an in-plane field of 362.5 Oe ± 2.5 Oe applied and the sample was then FC to RT.

The FC NiO(111)/MgO(111) sample was then transferred into the magnetron sputtering chamber with a base pressure of 2×10^{-8} Torr. A 20 nm thick EuO(001) film was then deposited at a rate of 0.033 nm/sec and capped with 12 nm of Ta.

4.2.2.2 Structural characterisation

The structural characterisation of the sample was carried out before and after the FC process and the growth of the EuO by using XRR and XRD and the results are shown in Figure 4.17 and Figure 4.18, respectively. The XRR scan performed after the FC and EuO growth shows an increase in the roughness of the sample which made it difficult to obtain a good XRR fit. Although the fit obtained after the FC process is not as good as that for the as-deposited MgO(111)/NiO(111), the decrease in the NiO density may be an indication that oxygen reduction occurred during the FC treatment, especially as the thickness is consistent before and after the FC process. The values of all the fitted parameters, thickness, roughness and density of the sample before and after the FC treatment, are listed in the table in Figure 4.17.

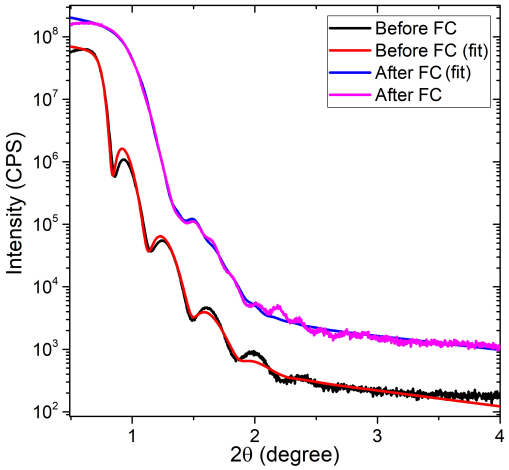

As-deposited MgO(111)/NiO(111)

Layer	Thickness (nm)	Roughness (nm)	Density (g/cm^3)
NiO	20.34	2.16	6.88
MgO	-	2.21	3.57

After FC + the growth of EuO and Ta

Layer	Thickness (nm)	Roughness (nm)	Density (g/cm^3)
Ta	9.47	2.10	15.11
EuO	22.10	2.31	8.21
NiO	18.32	2.22	5.89
MgO	-	2.08	3.57

Fig. 4.17 : XRR scans of the samples before (black) and after the FC process and the growth of the EuO and Ta layers (blue) and their corresponding fits. The table lists the deduced values of the layers' thickness, roughness and density of the sample before and after the growth of EuO and Ta.

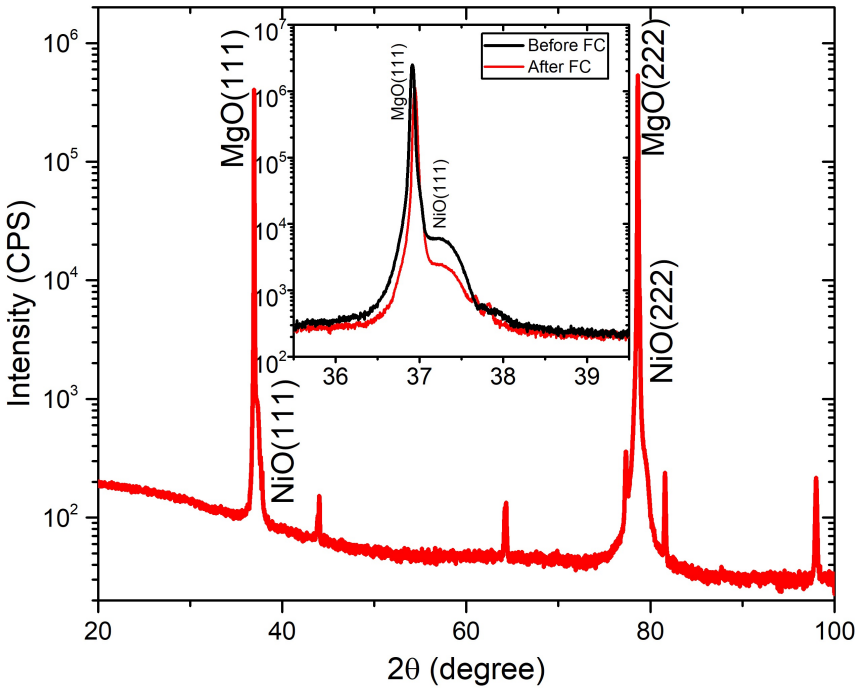

Fig. 4.18 : XRD scan of the MgO(111)/NiO(111)/EuO/Ta sample carried out after the FC treatment and the growth of the EuO and Ta layers using a monochromator with a 1D detector from 20°-100°. The high background at $2\theta > 40°$ is a sign of the amorphous nature of the grown EuO film. The inset is a zoomed view of the MgO(111) and NiO(111) peaks before and after the FC process.

Figure 4.18 shows the XRD scans of the sample before and after the FC and the growth of EuO process. Again, no presence of the EuO nor the Ta peaks is observed. Hence, the EuO film grown on the FC NiO(111) is amorphous as in the case of the ZFC sample. The inset is a high-resolution XRD view of the MgO(111) and NiO(111) peaks, which highlights the highly-textured NiO(111) grown on the MgO(111) substrate and changes it experienced as a result of the FC treatment and the EuO/Ta growth. The reduction in the intensity of the NiO peak observed in the XRD scan after normalising the two spectra at the MgO(111) peak confirms the XRR results and the assumption that an oxygen reduction reaction has taken place during the post-annealing process which could have been avoided if the post-annealing treatment was completed in an oxygen partial pressure.

4.2.2.3 Magnetic characterisation

The volume magnetisation field-dependence of the FC sample measured at 5 K with the field applied parallel to the original FC direction is shown in Figure 4.19. There is neither

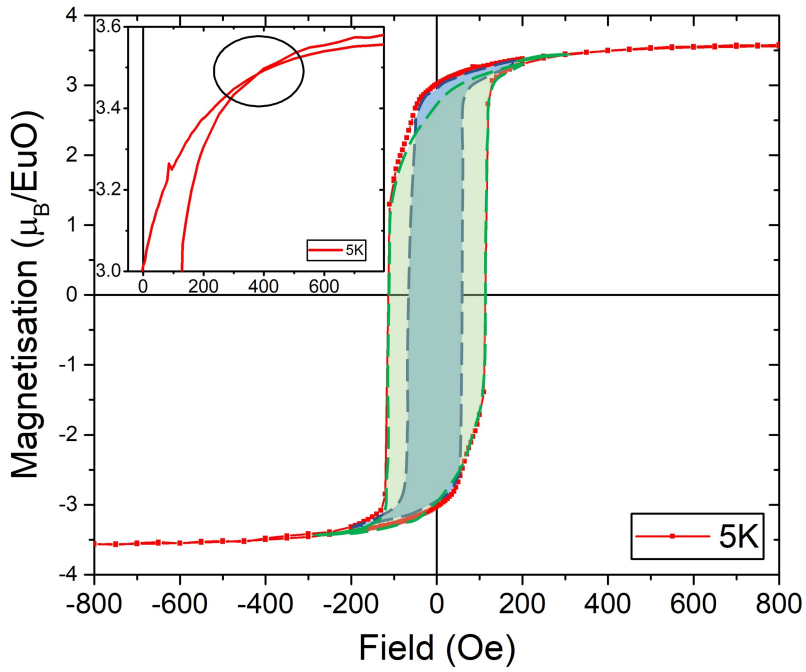

Fig. 4.19 : The 5 K M vs H measurement of the FC NiO(111)/EuO sample with an enhanced $H_c = \pm 113.6$ Oe. The blue and green dashed-line loops arise from the pinned and rotating unpinned NiO(111) *S*-domains at the interface of the NiO(111)/EuO. The shaded regions shows the contributions of different NiO(111) *S*-domains. The inset highlights the crossover of the ascending branch of the hysteresis loop.

a shift nor a double shift observed in the hysteresis. However, a deformed loop with a higher enhancement in its coercivity of a $H_c = \pm 113.6$ Oe, a remanence of about 84% of the saturated magnetisation and a crossover of its ascending and descending branches at ± 400 Oe is found.

When the NiO(111) film is FC, a large number of its *S*-domains are expected to turn in the field direction while a few pinned ones remain in their initial positions. However, the majority of the unpinned domains rotate back along the easy axis, when the field is removed. Therefore, if the sample was FC along its easy axis, most of the rotated domains will remain pointing in the FC direction. However, if the sample was FC parallel to a hard axis, most of the unpinned *S*-domains will relax along the easy axis. When the field is removed while only a few unpinned ones may remain pointing in the FC direction, assuming that the pinning effect of the surface defects is negligible. In both cases, the EuO interfacial spins will rotate with the NiO interface *S*-domains via the ferromagnetic coupling at the interface. Therefore, it will be easier to saturate some NiO *S*- domains. Thus, two hystereses arise from easy and hard to rotate spins (marked by the dashed lines in Figure 4.19).

4.2.2.4 PNR measurements

The FC MgO(111)/NiO(111)/EuO/Ta sample was measured at the D17 beamline at ILL using a monochromatic beam as in the case of the LAO/EuO experiments discussed in Section 3.

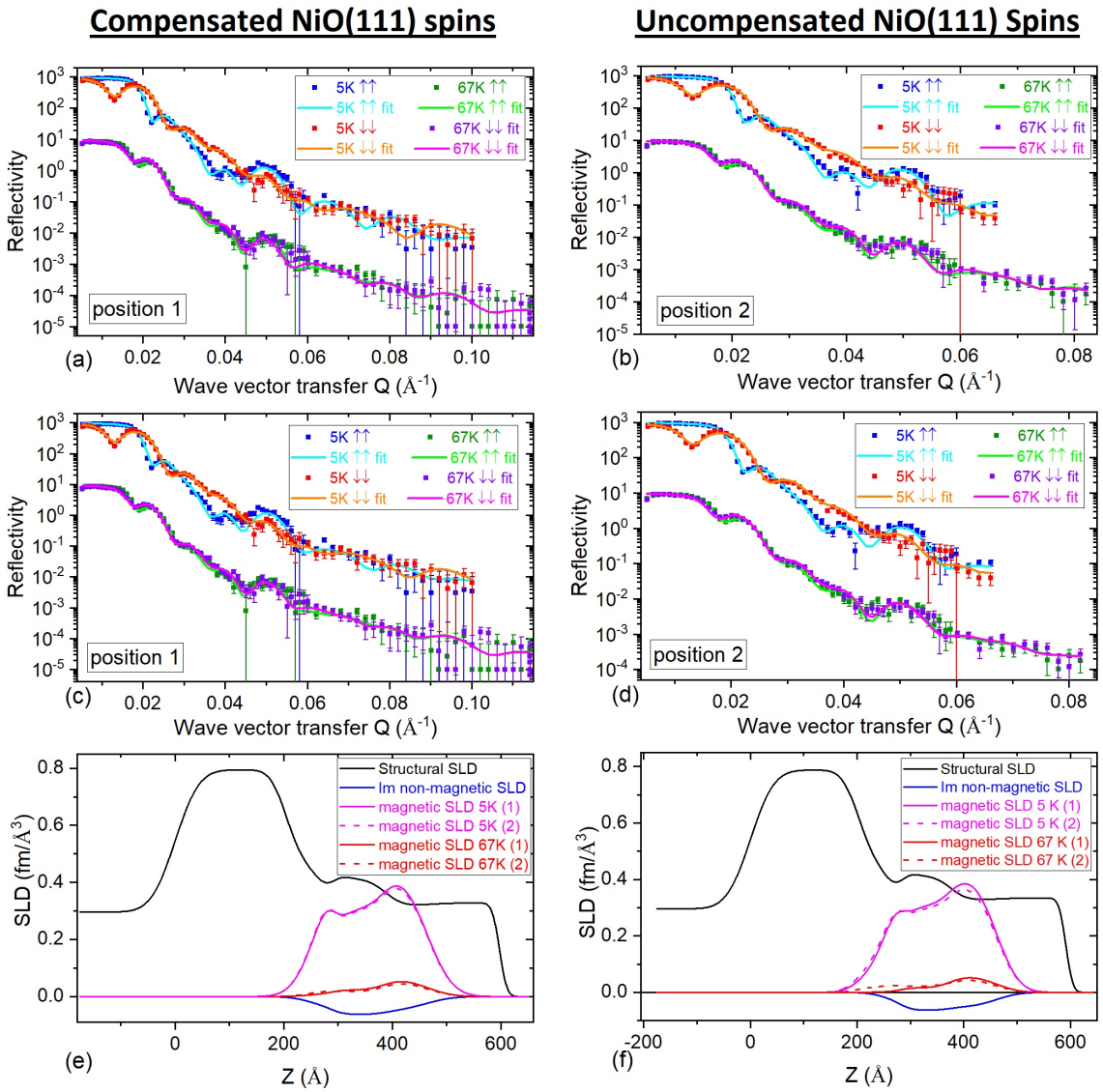

Fig. 4.20 : The PNR results of the 5 K and 67 K measurements and their corresponding fits using the compensated and uncompensate NiO(111) spins scenarios (a) The Compensated NiO(111) spins of position 1, where the field is applied in the original FC direction and (b) The uncompensated NiO(111) spins of position 1, where the field is applied parallel to the FC direction. (c) The compensated NiO(111) spins of position 2, where the field if applied perpendicular to the original FC direction. (d) The uncompensated NiO(111) spins of position 2, where the field is applied perpendicular to the direction of the initial FC. (e) The resultant SLD of position 1 and 2 using the compensated NiO(111) spin scenario. (f) The resultant SLD plot of position 1 and 2 using the uncompensated NiO(111) spin scenario.

The sample was FC to 67 K with a magnetic field of 600 Oe applied in the same direction as the original FC (position 1). The sample was measured at low and high angles, q ranging from 0.005 $Å^{-1}$- 0.06 $Å^{-1}$ and 0.04 $Å^{-1}$- 0.11 $Å^{-1}$, respectively. After that, the sample was rotated 90° in-plane (position 2) and measured in 600 Oe. The sample was then turned back to position 1 and FC to 5 K by maintaining a constant field of 600 Oe for the second 5 K measurement before it was rotated again to position 2. The PNR results and the SLD of the 5 K and 67 K data with the sample positioned along and perpendicular to the original FC direction are all shown in Figure 4.20.

The PNR spin-flip (SF) channels were not fitted due to their poor statistics and low intensities which make it very challenging to obtain reasonable results as shown in Figure 4.21. On the other hand, the non-spin flip (NSF) channels measured at 5 K and 67 K with the sample aligned along and perpendicular to the initial FC direction were fitted together to lock the structural parameters of the sample. Since the crystallographic orientation of the applied field during the FC process is unknown, two models presuming compensated and uncompensated spins in the NiO interface layers were tested, both consisting of a double

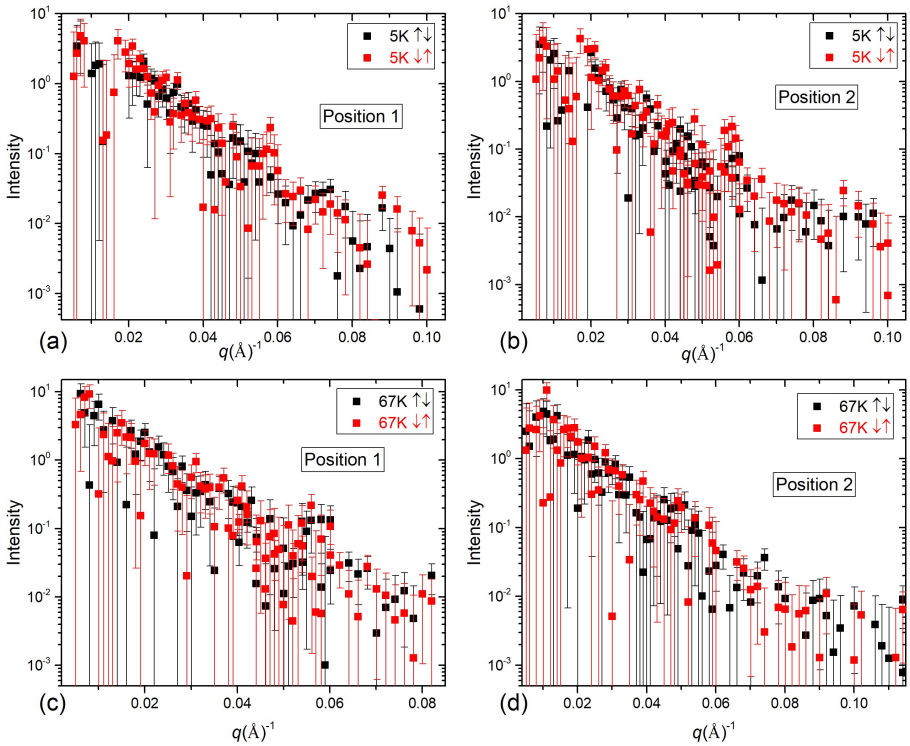

Fig. 4.21 : The raw data of spin-flip PNR measurements of the spin-flip channels with a 700 Oe field applied (a) in the direction of the initial FC at 5K, (b) perpendicular to the direction of the initial FC at 5 K, (c) in the direction of the initial FC at 67 K, and (d) perpendicular to the direction of the initial FC at 67 K.

Thickness [Å]		
Layer	Compensated spins	Uncompensated spins
Ta	134.82	129.59
EuO_{top}	74.73	86.08
EuO_{mid}	96.97	92.43
EuO_{bottom}	30.78	21.63
$NiO_{interface}$	57.96	60.93
NiO	202.20	200.74
Roughness [Å]		
Layer	Compensated spins	Uncompensated spins
Ta	10.77	10.42
EuO_{top}	38.00	33.14
EuO_{mid}	25.36	23.73
EuO_{bottom}	14.39	15.09
$NiO_{interface}$	34.99	29.76
NiO	22.45	23.95
MgO	35.00	35.00
Atomic Number Density N [10^{28} mm^{-3}]		
Layer	Compensated spins	Uncompensated spins
Ta	0.0475	0.0484
EuO_{top}	0.0488	0.0504
EuO_{mid}	0.0632	0.0633
EuO_{bottom}	0.0501	0.0455
$NiO_{interface}$	0.0320	0.0300
NiO	0.0494	0.0489
MgO	0.053	0.053

Table 4.2: The fitted parameters of the best PNR fit of the FC NiO(111)/EuO sample: thickness, roughness, atomic number density (N) obtained from fitting the PNR curves using the compensated and uncompensated fitting models.

layer of NiO, three layers of EuO and single MgO and Ta layers. For the compensated-spin scenario, the magnetic moment of the $NiO_{interface}$ layer was fixed to zero while it was allowed to vary for the uncompensated case. The models yielded a fit quality of $\bar{\chi}^2 = 7.8$ and $\bar{\chi}^2 = 7.5$ for the compensated and uncompensated pictures, respectively. The fitted PNR curves and the resultant SLD obtained from both models are presented in Figure 4.20, while the values of the fitting parameters are listed in Table 4.2 and Table 4.3. Other models made up of a single NiO layer were also tested, but they were not considered as they produced poor fits.

Magnetic Moment (5 K) [μ_B/atom]				
Layer	Compensated spins		Uncompensated spins	
	Position 1	Position 2	Position 1	Position 2
EuO_{top}	3.50 ±0.26	3.42±0.26	3.10±0.16	2.91±0.16
EuO_{mid}	1.85±0.10	1.82±0.16	1.84±0.0076	1.78±0.032
EuO_{bottom}	3.51±0.35	3.60±0.51	3.6±0.92	3.56±1.11
$NiO_{interface}$	-	-	0.80±0.032	1.07 ±0.092
Magnetic Moment (67 K) [μ_B/atom]				
Layer	Compensated spins		Uncompensated spins	
	Position 1	Position 2	Position 1	Position 2
EuO_{top}	0.50±0.26	0.43±0.16	0.44±0.05	0.35±0.040
EuO_{mid}	0.14±0.09	0.11±0.072	0.10±0.018	0.14±0.014
EuO_{bottom}	0.11±0.73	0.21±0.30	0.052±0.033	0.24±0.17
$NiO_{interface}$	-	-	0±0.97	0.24±0.036

Table 4.3: The magnetic moments of the FC NiO(111)/EuO sample deduced from fitting the 5 K and 67 K PNR data with the field applied parallel (position 1) and perpendicular (position 2) to the initial FC direction using the compensated and uncompensated fitting models.

Since the crystallographic direction of the applied (FC) field was unknown and as questionable results are obtained from the two uncompensated and compensated models, a new model similar to that used for the ZFC sample is proposed.

The proposed model consists of 3 layers of EuO with a single layer of NiO, MgO and Ta, where the NiO and the EuO layers are divided into two sections as shown in Figure 4.22. Section 1 and Section 2 represent the influence of the unpinned and pinned NiO *S*-domains, respectively. Assuming the samples FC along the easy axis, the majority of the NiO *S*-domains and EuO spins are expected to align in the direction of the field and will be detected by the NSF channels. Therefore, Section 1 is denoted by a larger area than Section 2. Since only in-plane spins can be measured by PNR, the magnetic moments of Section 2 which are detected by the SF channels will be set to zero. However, when the sample is rotated in-plane by 90°, the areas which are measured by the SF and NSF channels will switch. As only a few pinned NiO *S*-domains are expected to be present in the sample, the magnetic moments measured by the NSF channels with the sample measured in position 1 is supposed to be higher than those detected from position 2. Therefore, to implement this model all the four measurements of the four channels (i.e. 16 runs) must be fitted together to lock the structural and magnetic properties of the sample. Also, determining the crystallographic direction of the FC will be required to obtain a quantitative understanding of the magnetic

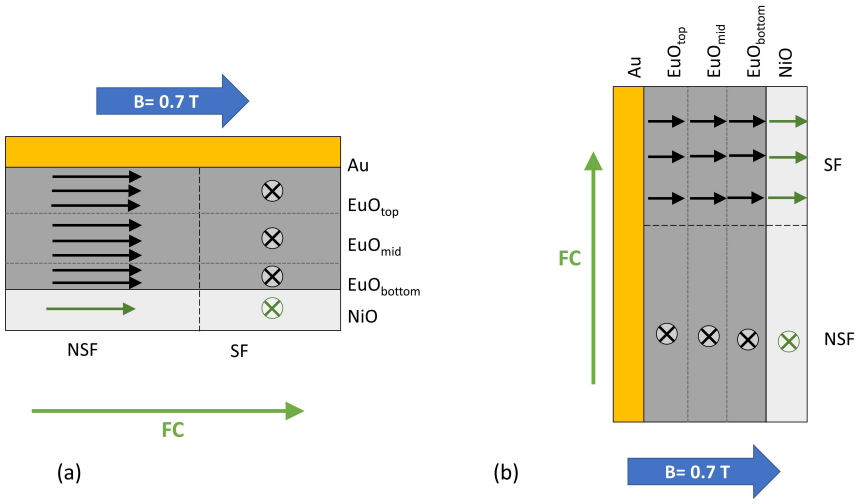

Fig. 4.22 : The proposed model to fit the PNR data of the FC NiO(111)/EuO sample measured at 5 K and 67 K with (a) the field applied along and (b) perpendicular to the original FC direction. The two sections of the NiO and EuO layers indicate portions of the sample being measured by the SF and NSF channels in each measurement.

depth profile of the sample. This can be achieved by observing the NiO *S*-domains optically using a microscope made up of on non-magnetic materials with linearly polarised light and placed between the poles of a magnet or by neutron diffraction [191, 193].

4.3 Conclusion

This chapter discussed the experimental work carried out to investigate the magnetic depth profile and the effect of pinned and unpinned NiO(111) *S*-domains at the interface of NiO(111)-EuO. The randomised AFM spins were found to pin the EuO spins at the interface which resulted in a smaller spin splitting in the PNR curves as compared with those of uncoupled EuO(001) grown on a MgO(001) substrate. Furthermore, a small double-shifted hysteresis with enhanced coercivity was detected by the SQUID magnetometry. A larger H_c was then found in the FC sample. The preliminary PNR fits of NSF channels of the FC sample show that the two scenarios of compensated and uncompensated NiO(111) *S*-domains can occur at the interface. Therefore, a new model was proposed to take into account the presence of pinned and unpinned AFM domains simultaneously.

4.4 Outlook

As a result of the discussed PNR experiments, a beamtime proposal at OFFSPEC end-station at ISIS has been awarded. Two samples are proposed for the beamtime, where polar and non-polar FC NiO/EuO heterostructures will be measured and where the measurements aim to understand the in-plane distributions of the NiO *S*-domains at the interface to characterise the EB of this system fully. Also, the PNR fits of the FC sample presented in this chapter will be refined further using the proposed model and an optical system will be set up to observe the NiO *S*-domains.

5

Graphene-Metal Interface

Graphene is unique material, with exceptional mechanical, optical and transport properties. It is a hard material with a Young's modulus of 1 TPa and intrinsic strength of 130 GPa [209], and it is expected to remain stable at a high temperature up to 3000 °C [210]. It is impermeable to standard gases including helium [211] and a single layer of graphene can be visualised using optical microscopy which makes it a suitable candidate for photonics and optoelectronics applications [212, 213]. Graphene is a perfect material for many technological and future spintronic device applications such as spin-filters [214, 215], spin-valves and spin field-effect transistors [210, 216] due to its excellent transport properties. It has a higher intrinsic charge carrier mobility than any other material of 120,000 cm^2/Vs at 240 K [217] and large spin relaxation times as a result of its long electron mean free path and its negligible spin-orbit and hyperfine couplings [215, 218].

The realisation of these graphene-based spintronic devices is held back due to two major challenges: the low efficiency of spin injection into a monolayer of graphene [215] and the difficulty of manipulating spins directly in its layer due to its negligible spin-orbit coupling [218]. Many studies show that the latter can be addressed by various approaches such as the

proximity-induced effect [11, 219–221], chemical doping of the graphene's surface [218] or through a chemically-induced sublattice [222]. The first method, which implies utilising the exchange coupling of local moments between graphene and a ferromagnetic material, is the approach adopted in our study.

Section 5.1 gives a brief introduction to carbon allotropes, the crystallographic and electronic structures of free-standing graphene and explicitly explains the changes it undergoes in the presence of a metallic substrate. The sample fabrication processes and their characteristic properties are highlighted in Section 5.2. Section 5.3 discusses the results of the PNR measurements that were performed to measure the induced magnetic moment in graphene. In addition to the PNR results, Bayesian uncertainty analysis, performed by Dr Timothy Charlton, is presented to confirm the robustness of the PNR fits. Section 5.4 elaborates on the complementary XMCD measurements that were carried out to investigate further the magnetic interaction between the graphene and the underlying substrate and to locate the additional magnetic moment measured by PNR. The XMCD results are then compared with the those previously reported by Weser *et al.* [11, 215].

5.1 Introduction

5.1.1 Carbon allotropes

Carbon (C) is one of the most abundant and vital elements on Earth due to its crucial role in organic chemistry as it creates a large number of substances [223–225]. However, only eight materials are known so far to be made of pure carbon. These are called carbon allotropes, and they include: diamond (3D), graphite (3D), graphene (2D), carbon nanotubes (1D) and buckyballs/fullerene (0D) as shown in Figure 5.1.

Carbon is a stable, but short-lived material in nature and its allotropes are formed as a result of the different types of hybridisation of C atoms, which leads to different structural geometries. For example, diamond is made of sp^3 hybridised C atoms, and graphite consists of sp^2 hybridised C atoms forming hexagonal layers bonded loosely with neighbouring sheets via weak van-der-Waals forces. In addition, a mixture of sp^3 and sp^2 hybridisation forms fullerene and carbon nanotubes [215, 225]. Graphene, the topic of this chapter, is discussed in more details in the following sections.

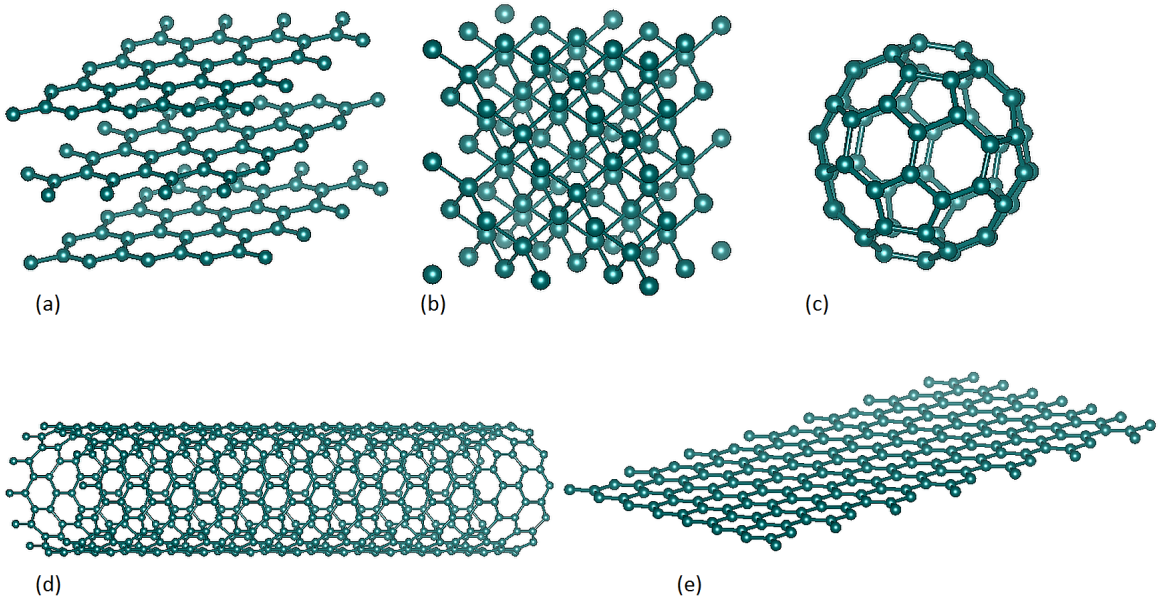

Fig. 5.1 : Natural occurring carbon allotropes of different crystallographic structures as a result of different forms of hybridisation of C atoms. (a) 3D graphite, (b) 3D diamond, (c) 0D fullerene, (d) 1D carbon nanotube and (e) 2D graphene. (These models were constructed using VESTA^{TM} software).

5.1.2 Free-standing graphene

Graphene has a 2D structure identical to a single layer of graphite and is considered as the building block of the carbon allotropes with sp^2 hybridised C atoms [217]. The atoms are arranged in a hexagonal honeycomb-like lattice, with a triangular Bravais lattice consisting of two carbon atoms per unit cell, and a lattice constant of $a = 2.46$ Å as shown in Figure 5.2 (a) [226, 227]. The real-space lattice vectors labelled as $\vec{a}$ and $\vec{b}$ are given by [228]:

$$\vec{a} = \frac{a}{2}(3, \sqrt{3}), \tag{5.1}$$

$$\vec{b} = \frac{a}{2}(3, -\sqrt{3}). \tag{5.2}$$

The sp^2 hybridisation of neighbouring C atoms results in strong in-plane σ bonding with bond lengths of $\sigma = \lambda = 1.42$ Å, which is the average of single (C-C) and double (C=C) σ bonds [229, 230]. These completely filled bands create deep valence bands for a layer of graphene. On the other hand, the unaffected half-filled $2p_z$ orbitals, which define the unique electronic properties of graphene, create the out-of-plane bonding (π) and antibonding (π^*) bands, valence and conduction bands, respectively (Figure 5.2 (b)) [217, 226, 229, 231].

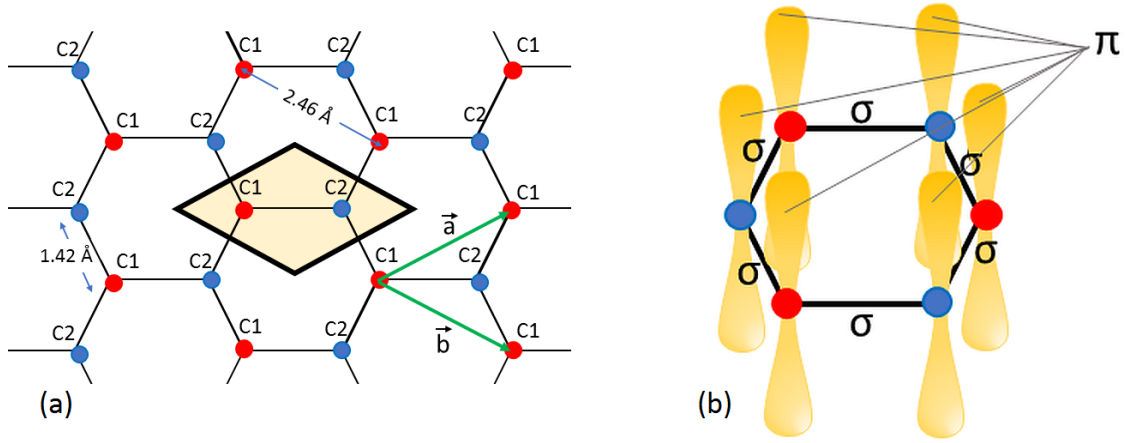

Fig. 5.2 : The crystallographic and orbital structures of graphene. (a) The honeycomb lattice of graphene consists of two sublattices labelled C1 (red) and C2 (blue), with a lattice constant of 2.46 Å and a sigma bonding distance of 1.42 Å. The black parallelogram shows the unit cell. (b) The in-plane σ and out-of-plane π bonds in a hexagonal graphene lattice.

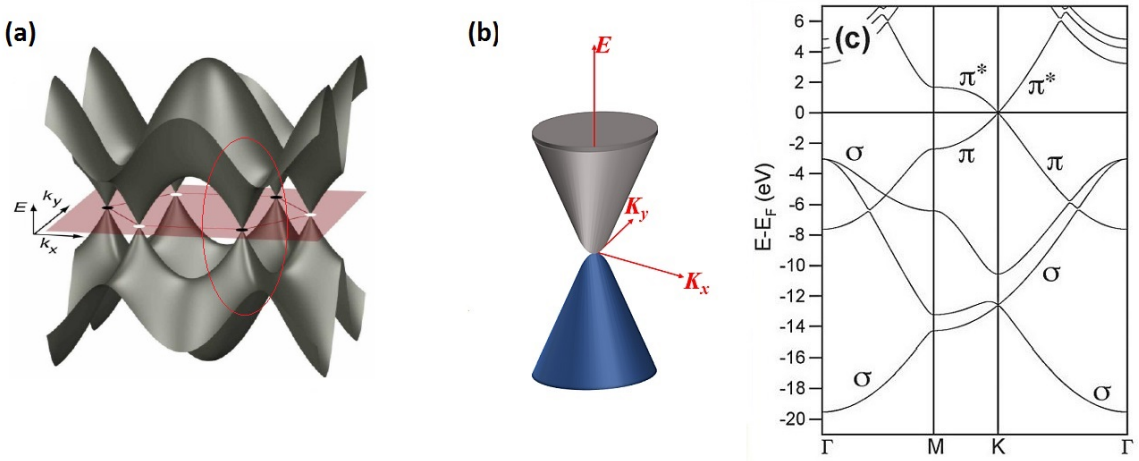

Fig. 5.3 : (a) A 3D representation of the tight-binding approximation of the graphene electronic structure. Figure is taken from Ref. [235]. (b) The Dirac cone around one of the K points showing the linear energy dispersion with the electron-hole symmetry, Figure is taken from Ref. [228]. (c) The DFT calculation of the graphene's band structure showing the zero-gap behaviour around the K point. The figure is adapted from Ref. [236].

Graphene is classified as a zero-gap semiconductor (i.e. semimetal) [229, 232]; this is because π and π^* bands meet at the Fermi energy level (E_F), at the corner of the graphene's Brillouin zone (K points), at degenerate points known as Dirac points (E_D) as shown in Figure 5.3 [233], where the electronic structure of these bands can be described using the tight-binding model [226, 234].

5.1.3 Graphene on a metallic substrate

Structure

Graphene has been successfully grown by chemical vapour deposition (CVD) directly on top of many transition-metal (TM) substrates including Ni, Co, Cu, Ir, Au and Ru [41]. The graphene-metal interface state results from the strong hybridisation between the 3*d*-valence band of the TM and the graphene's π orbital which leads to a partial transfer of the spin-polarised electrons to the graphene's unoccupied π^* states in the case of Ni and Co [229]. The graphene structure grown on such metals is strongly influenced by the crystal-lattice mismatch between the graphene and the metal, and the graphene-ferromagnet interaction strength which can be measured by their bond lengths [41]. For example, we look at a lattice-matched material, such as Ni(111) (-1.2%) and a lattice-mismatched material, such as Ru(0001) (8.8%) [237, 238]. Although their bond lengths with graphene are relatively close, 2.07 Å and 2.2-2.3 Å, respectively, graphene forms two different structures on those metals. It creates a (1x1) structure on top of Ni(111) and a weak Moiré-like superstructure on Ru(0001). Therefore, to induce a significant magnetic moment in graphene, a high quality, close-packed, lattice-matched substrate, with a small interface separation to graphene, is needed to form a strong exchange interaction [53].

DFT calculations show that there are four high-symmetry, low-energy adsorption configurations for which graphene's carbon atoms are arranged on a highly-packed (111) surface of a strongly interacting and lattice-matched metal. These configurations are illustrated in Figure 5.4 and classified as: **Hollow-'*fcc-hcp*'** site, where the C atoms are located on top of the atoms in the second and third layers of the TM substrate. **Top-'*fcc*'** site, where the C atoms are placed on top of the atoms in the first and third layers of the TM substrate. **Top-'*hcp*'** site, at which the C atoms are positioned on the top of the atoms in the first and second layers of the TM substrate. **Bridge** site at which the C atoms are bridged by the TM surface atoms [41, 229]. However, it is widely accepted that graphene's C atoms are assembled in the top-'*fcc*' configuration on top of *fcc* Ni(111) and Co(111) films. DFT calculations have also shown that the top-'*fcc*' is the most stable arrangement with the lowest energy among the other suggested configurations [229, 239, 240].

Electronic structure

The adsorption of graphene on a strongly interacting metal distorts the graphene's intrinsic band structure around the Dirac point, E_{D}, as a result of the *n* or *p* doping and/or the overlap of the graphene's valence band with that of the metal substrate [226]. Voloshina and Dedkov proposed a *universal* model which describes this graphene-metal interactions quantitatively

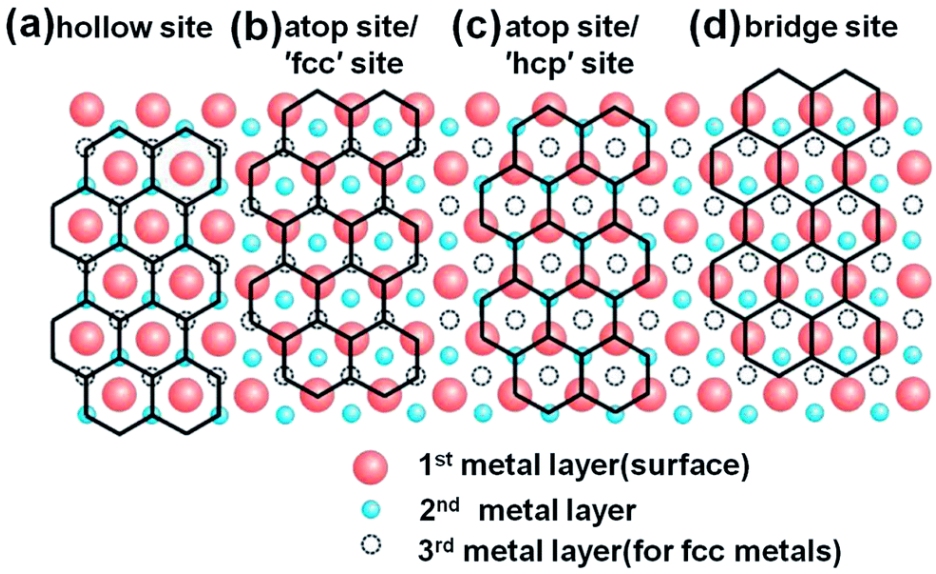

Fig. 5.4 : The top-view of the four possible low-energy arrangements of the graphene on top of a metallic substrate: (a) Hollow or a *fcc-hcp* site: the C atoms are aligned with the metallic atoms on the second and third layer of the substrate. (b) Top-*fcc* site: the C atoms are placed on the top of the atoms of the metallic substrate in the first and third metallic layer. (c) Top-*hcp* site: the C atoms are positioned on the top of the atoms of the metal substrate in the first and second layer. (d) Bridge site is where the C atoms are linked together by the surface atoms of the metallic substrate. The figure is taken from Ref. [41].

and they validated their model by several DFT calculations [241]. This model considers three scenarios for graphene grown on a close-packed lattice-matched metallic substrate: *sp*-, open *d*- and closed *d*-metals. In the case of the *sp*-metal, the graphene is *n*-doped by the mobile *sp*-electrons which fill the graphene's unoccupied π^* bands and shift its E_{D} below the E_{F}. The localisation of the electrons in the π orbital increases the Van der Waals (VdW) interaction at the graphene-metal interface without destroying the Dirac cone as shown in Figure 5.5 (a). However, for *p*-doped graphene, where the electrons transfer from graphene to the metal, the E_{D} is shifted upwards, and the interface VdW interactions are weakened.

In an open *d*-metal system, the doping of graphene is also governed by the mobile *sp*-electrons, but the interactions at the interface are more complicated. In such a system, the E_{D} of graphene is shifted within the metal *d*-band, forming several hybrid π-*d* states around the *K* points (Figure 5.5 (b)). The arrangement of the graphene's C_{top} and C_{fcc} atoms and the metal's surface atoms (M_s) leading to the formation of these states, in a close-packed (111) system is shown in Figure 5.5 (d). The p_z orbital of the C_{top} atom is aligned directly on top of $\mathrm{M_s}$ d_{z^2} orbital creating the $P_z{}^{C_{\mathrm{top}}}$-d_{z^2} hybrid state, whereas the p_z orbital of the C_{fcc} forms the $P_z{}^{C_{fcc}}$-$d_{xz,yz}$ hybrid with the $\mathrm{M_s}$ $d_{xz,yz}$ orbital. As these hybrid states are of different

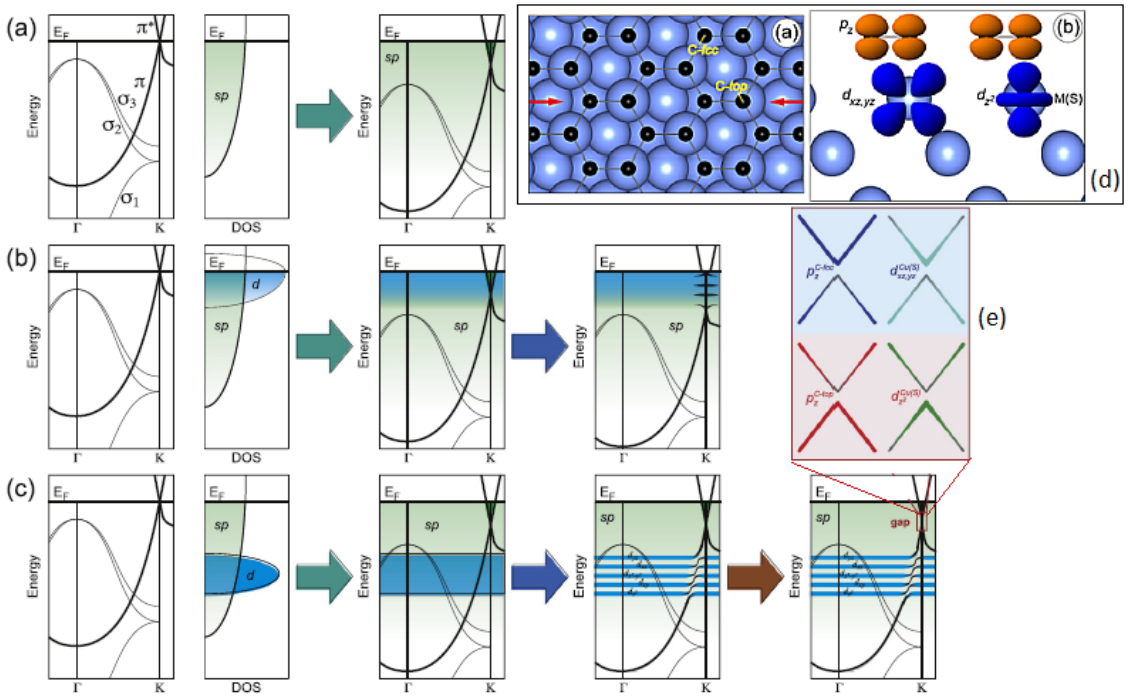

Fig. 5.5 : The electronic energy band structure of the *universal* model proposed by Voloshina and Dedkov. (a) Graphene-*sp* metal interaction: *n*-doping of graphene by mobile *sp* electrons and the preservation of E_{D} at the *K* point. (b) Graphene-open *d*-metal system: the initial doping of graphene, formation of the hybrid states with the opening of the E_{D} at the *K* point. (c) Graphene-closed *d* metal: the position of the filled *d* orbital far below E_{D}, the initial doping of graphene, the formation of the $P_z{}^{C_{\mathrm{top}}}$-d_{z^2} and $P_z{}^{C_{fcc}}$-$d_{xz,yz}$ and the gap opening at E_{D}. (d) The top and side-views of the graphene and the surface layer of the metallic substrate M_{S}: the out-of-plane *d* orbitals (d_{xz}, d_{yz} and d_{z^2}) and the graphene's C_{P_z} orbital. (e) The zoom-in view of the avoided crossing at the *K* point. Figure adapted from Ref. [241].

orbital symmetry, the degeneracy breaks destroying the Dirac cone entirely and opening up a gap at the *K* point as demonstrated in Figure 5.5 (b). The same principle is applied when graphene is grown on top of a metallic film with filled *d* orbital (i.e. closed *d*-metal). However, the filled *d* band of $\mathrm{M_s}$ is positioned deep into the valence band and thus forms hybrid π-*d* states far below the E_{D} as shown in Figure 5.5 (c). Therefore, it can be concluded that the two factors required to open up the graphene's Dirac cones are the breaking of the graphene's sublattice symmetry and strong π-*d* hybridisation [236]. I refer the interested reader to the original publication [241] for an extensive view of the model and the supported DFT calculations. On the other hand, weakly interacting metal does not affect the graphene's electronic structure because only weak VdW forces are formed at the interface with bond lengths of $\sim$0.21 nm, which is close to the VdW forces between the graphite sheets (0.33 nm) [41].

Phonon dispersion

Graphene has six phonon dispersion branches; three optic (O) and three acoustic (A) phonon bands. Each of these branches is further divided into in-plane longitudinal (L), in-plane transverse (T) and out-of-plane transverse (Z) modes [243, 244], where the term "plane" refers to the graphene's plane. The phonon dispersion of free-standing graphene, around the high-symmetry line Γ-K-M-Γ, obtained using density-functional perturbation theory is shown with black lines in Figure 5.6 (a). The most prominent features of these curves are the positive gradient in the LO curve and the kink in the TO curve at Γ and K lines, respectively [244]. The latter is known as Kohn anomaly, which results from the strong electron-phonon coupling, whereas their gradients measure the electron-phonon coupling with the graphene's π bonding [41, 244]. The red dotted lines in Figure 5.6 (a) illustrate the effect on its phonon dispersion by stretching the lattice constant of a free-standing graphene by $\sim$1.5 %. TO and LO branches are greatly downshifted by $\sim$ 100 cm^{-1}, while the ZO branch remains almost at the same frequency at Γ line. However, when graphene forms strong bonds with a lattice-matched substrate, such as Ni(111), additional changes in the phonon dispersion are observed as a result of the graphene adsorption into the substrate as shown in Figure 5.6 (b). The ZO branch is now significantly softened by 160 cm^{-1} due to the strong graphene-substrate interaction [242]. The degeneracy of ZA and ZO is also lifted and a gap of $\sim$155 cm^{-1} opens at the K line due to the broken of symmetry of the adsorbed graphene as a consequence of the alternating adsorption site, discussed earlier [41]. However, the third, and the most pronounced, change is the disappearance of the Kohn anomalies at the optical

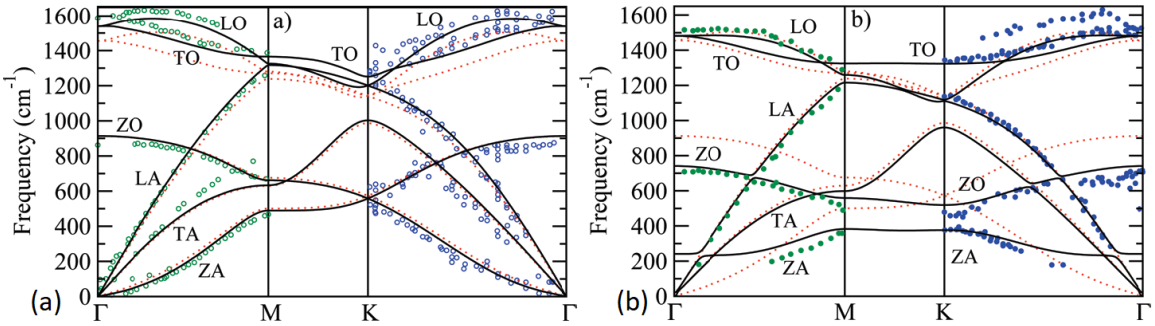

Fig. 5.6 : Density-functional perturbation theory calculation for the graphene's phonon dispersion around the high symmetry line Γ-K-M-Γ, highlighting the changes which occur in the six branches; LO, TO, ZO, LA, TA and ZA when graphene is grown on Ni(111). The black solid lines represent the the calculation carried out for unstretched graphene, the red lines are for 1.5% stretched graphene to match the lattice constant of Ni(111), the green and blue circles are the experimental restuls for: (a) free-standing graphene and (b) graphene on Ni(111). The image is taken from Ref. [242].

branches at the Γ and *K* lines. This is because the opening of the graphene's electronic band gap, as a result of the π-*d* hybridisation, destroys the electron-phonon coupling completely, and thus flattens the *LO* and *TO* bands at Γ and *K* lines, respectively [41, 242]. On the other hand, when graphene is grown on a weakly-bonded metallic substrate, its Kohn anomalies are slightly perturbed, while maintaining its phonon dispersion [242].

5.2 Sample preparation and characterisation

As discussed in the previous section, strong electronic coupling between the graphene and the ferromagnet is needed to induce a magnetic moment in graphene. Therefore graphene layers on Ni(111) and Co(111) substrates were the primary focus of our study. Graphene layers on Cu(001) and Ni_9Mo_1(111) substrates were used for further investigations on the effect of a non-magnetic substrate on the graphene's π and σ orbitals. The main properties of the graphene-transition metal (TM) interactions of these systems are listed in Table 5.1.

The purpose for using Ni_9Mo_1(111) is to provide a substrate with a similar crystallographic structure to that of Ni(111), but with a diminished magnetic moment. There is no theoretical study reported so far on graphene/Ni_9Mo_1(111). Therefore, the properties of such a system are missing from Table 5.1. However, since the Ni is doped by 10% only, the lattice mismatch and bond length are expected to be closer to that of Ni(111), but the *d*-orbital position considerably downshifted with respect to E_F. The sample preparation for the intended study involved two steps: the growth of the TM films on sapphire substrates using magnetron sputtering and the graphene growth by CVD directly on these films.

5.2.1 Growth of the transition-metal films

1 mm thick Al_2O_3(0001) substrates were cleaned in an ultrasonic bath with isopropanol and then with acetone, for three minutes each. The substrates were then dried with a dry N_2 gun before they were outgassed at about 180 °C in vacuum for five minutes in three cycles. The substrates were left to cool down to room temperature before they were transferred *in situ* to

TM substrate	Lattice mismatch (%)	Graphene-TM bond length (Å)	*d* orbital position relative to E_F
Ni(111)	-1.2	2.03-2.1	-1.29
Co(111)	-1.6	2.04-2.2	-1.17
Cu(001)	-31	3.4	-2.67

Table 5.1: Properties of the TM substrates used in the study. The values are taken from Ref. [41, 214, 237, 239, 245, 246].

the magnetron sputtering chamber with a base pressure of (1.2-2)x10^{-8} Torr. Then 99.99% pure Ni, Co and Ni_9Mo_1 targets were used to DC sputter 80 nm thick Ni(111), Co(111) and Ni_9Mo_1(111) films, respectively. A constant DC current of 0.1 A was used to grow the films with a rate of 0.02 nm/s. A constant flow (14 sccm) of pure argon gas was maintained throughout the growth to create a plasma pressure of 2 mTorr (3 mTorr for Ni_9Mo_1). Thick substrates were used to reduce the possibility of producing bendy samples which could affect the PNR and XRR measurements. The Cu(001) film was deposited on a clean 0.5 mm thick Al_2O_3(0001) substrate using a thermal evaporator with a base pressure of 3.75x10^{-7} mbar. The growth parameters were tuned to evaporate a 950 nm thick film with an evaporation rate of 0.2 nm/s. Figure 5.7 shows the XRD measurements of the deposited films acquired with Bruker D8 Discover HRXRD with a Cu Kα monochromatic beam (40 kV, 40 mA) and a scanning range of 40° - 48°. The scans show highly textured pure films oriented in the (111) direction for Ni, Co and Ni_9Mo_1 (Figure 5.7 (a) - (c)) and in the (001) orientation for the Cu film (Figure 5.7 (d)).

5.2.2 Growth of graphene by CVD

The CVD growth of graphene directly on Ni(111), Co(111), Ni_9Mo_1(111) and Cu(0001) films was carried out by Dr Robert Weatherup, Dr Marie-Blandine Martin and Dr Philipp Braeuninger, respectively, from the Hofmann Group at the Electrical and Electronic En-

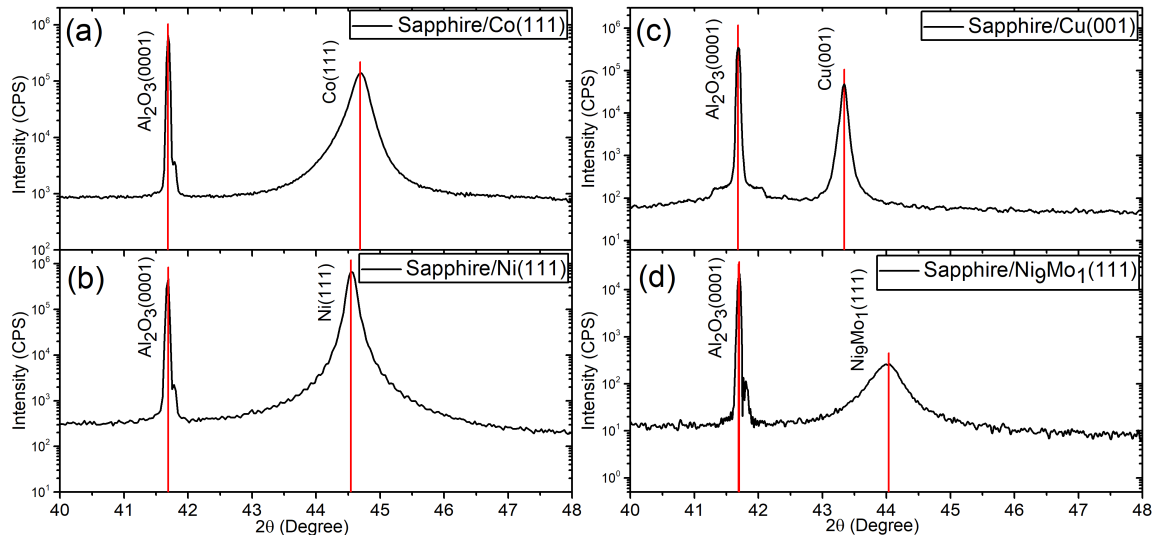

Fig. 5.7 : X-ray diffraction measurements of highly textured films: (a) Al_2O_3(0001)/Co(111). (b) Al_2O_3(0001)/Ni(111). (c) Al_2O_3(0001)/Cu(001) and (d) Al_2O_3(0001)/Ni_9Mo_1(111). The vertical red lines are the theoretical peak positions. The Al_2O_3(0001)/Cu(001) sample was measured by Dr Christy Kinane at ISIS.

gineering Department, University of Cambridge. The growth parameters were tuned to obtain almost full coverage, on $\sim$ 2 cm x 2 cm samples of epitaxial and rotated-domain graphene on the sputtered films. On Ni(111), the former graphene structure is produced at a low temperature (below 500 °C) as a result of the conversion mechanism of the surface carbide. The latter is grown at a higher temperature (above 500 °C) via the replacement mechanism of the surface ferromagnetic layer. A schematic diagram of both mechanisms on a graphene/Ni(111) sample is illustrated in Figure 5.8. Rotated-domain graphene was grown on Co(111) by first introducing H_2 gas at a rate of 180 sccm to the CVD chamber of a base pressure of 2.7 x 10 $^{-6}$ mbar. After that, the growth chamber was heated to 627 °C for 12 minutes. The sample was then exposed to C_2H_4 (0.63 sccm) for 60 minutes, before it was cooled down to RT in vacuum. The growth conditions were tuned to also grow rotated-domain graphene on a $Ni_9Mo_1(111)$ substrate. For this film, H_2 gas was introduced to the CVD at a flow rate of 200 sccm and the samples were then heated to 650 °C, again for 12 minutes before introducing C_2H_4 at a rate of 0.24 sccm for 40 minutes and then cooled down to RT. The deposition recipes for graphene on Ni(111) and Cu(001) are explained explicitly in Ref. [247] and Ref. [248], respectively.

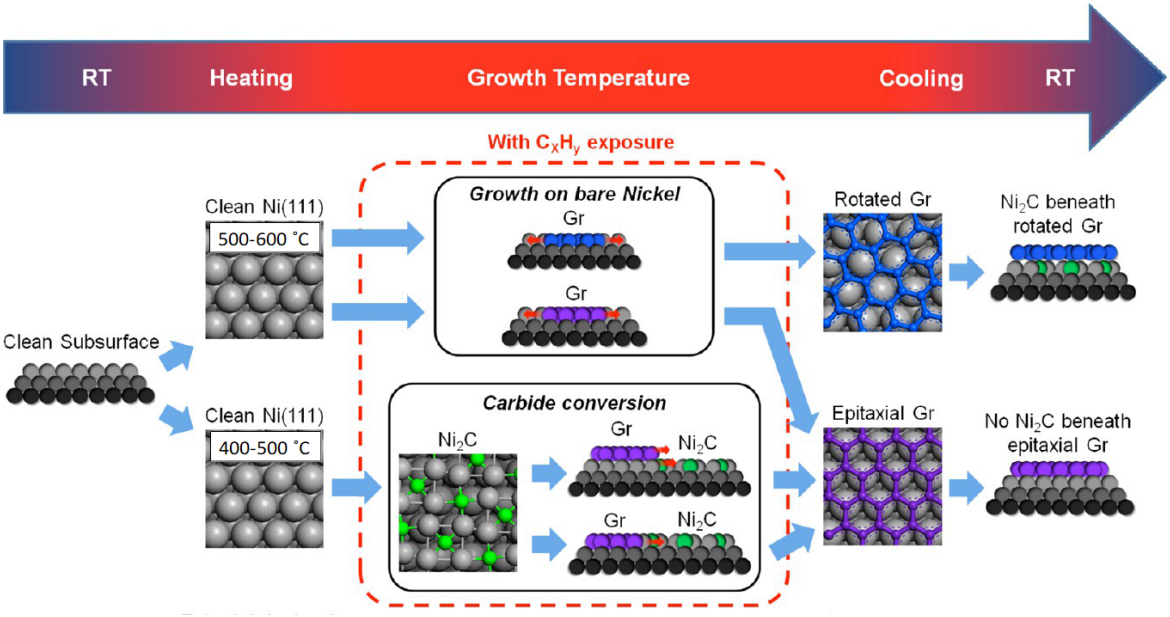

Fig. 5.8 : A schematic diagram summarising the graphene growth mechanisms on a clean Ni(111) film. Above 500 °C: graphene is formed directly on Ni(111) via the replacement mechanism which yields either epitaxial and/or rotated-domain graphene. Below 500 °C: an intermediate Ni_2C layer is formed before it converts into an epitaxial graphene by the conversion mechanism. The figure is reproduced from Ref. [247].

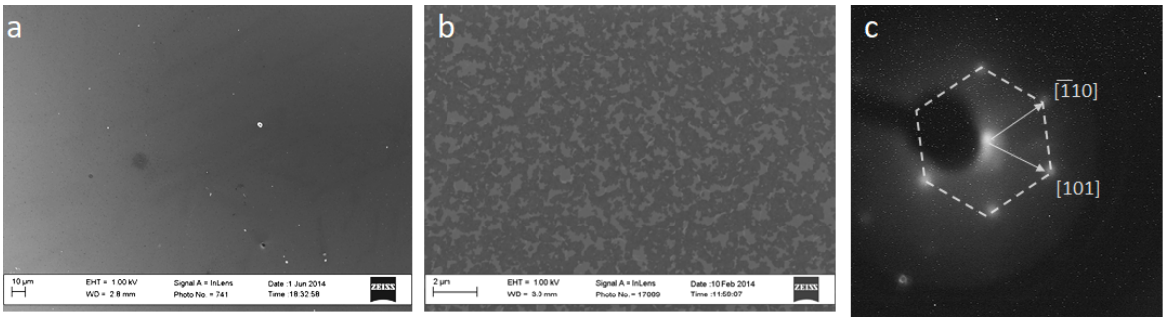

Fig. 5.9 : SEM scans showing the graphene domains using a Zeiss SEM at 1 KV for (a) epitaxial graphene/Ni(111) and (b) rotated graphene/Ni(111). (c) LEED diffraction pattern of epitaxial graphene on a Ni(111) substrate at 300 eV taking by Dr. Adrian Ionescu.

The grown graphene was investigated using a SEM. The images shown in Figure 5.9 (a) and (b), taken by Dr Weathrup, illustrate the structure of epitaxial and rotated graphene on Ni(111) with a surface coverage of $\sim 90\%$. Figure 5.9 (a) shows a homogeneous monolayer of graphene, whereas the dark grey areas in Figure 5.9 (b) are the bilayer or different oriented graphene domains. Figure 5.9 (c) shows the LEED diffraction of epitaxial graphene on Ni(111) obtained with an applied field of 300 eV (the measurement was taken by Dr Adrian Ionescu from the Thin Film Magnetism group at the Cavendish Laboratory). The sample was first annealed to 180 °C in vacuum to clean the surface of the sample without forming Ni_2C at the interface. The LEED diffraction shows only the graphene's hexagonal pattern with no contribution from the Ni(111) substrate due to the small lattice mismatch between graphene and Ni(111), as discussed earlier. Also, since no additional diffraction spots are observed, the LEED pattern confirms the high quality of the (1x1) graphene structure.

Raman measurements

Room-temperature Raman spectra of the grown graphene samples are shown in Figure 5.11. These measurements were acquired by Dr Philipp Braeuninger using an excitation laser of 532 nm, a low excitation power to avoid heating up the samples, with a 50X objective lens and accumulation time of 10 seconds. However, before taking these measurements, the graphene was transferred by a chemical etching process from the metallic films onto a Si substrate with a 300 nm thermally annealed SiO_2 layer by Dr Robert Weathrup, similar to the method reported in Ref. [249]. This was done because the adsorption of graphene onto a closely lattice-matched TM film causes a loss in the resonance conditions for observing Raman spectra as a result of the strong chemical interaction between the graphene π orbitals and the *d*-states of Co and Ni, which also alters the graphene's P_z orbitals. Furthermore, the increase in the C-C bond length to match the lattice of these ferromagnets leads to significant changes

in the graphene's phonon spectrum, as described earlier in Section 5.1.3. A Si/SiO_2(300 nm) substrate was used as it has a broad and weak Raman signal between 900 - 1000 cm^{-1} and because it was found that the graphene's weak first order Raman peak is greatly enhanced when it is transferred onto such a Si substrate with an appropriate SiO_2 thickness [39].

For the transfer process, the samples were cleaved into ∼5 mm x 5 mm squares and then covered with a homogeneous layer of 950K molecular weight PMMA, while paying particular attention to the samples' edges. 68% nitric acid was used as the chemical reagent and it was further diluted to 5% (for Ni_9Mo_1), 10% (for Ni) and 20% (for Co) to slowly etch the metallic films, while preserving the graphene layer. The samples were left to dry and then placed into the diluted nitric acid of the right concentration to remove any metal residuals. After the initial PMMA/graphene peeling started, the samples were placed inside RT DI water to assist the peeling of the samples' edges manually. They were then placed back in the diluted nitric acid to detach the PMMA/graphene completely. The suspended PMMA/graphene was then fished-out using the Si/SiO_2 substrate. After that, the samples were baked at 80 °C for 3 minutes to remove excess water, then dipped in acetone to remove the PMMA, rinsed in IPA and ethanol, and then dried with dry N_2 gas.

Graphene has two characteristic peaks in the Raman spectra, the G at ∼1582 cm^{-1} and $2D$ at ∼2700 cm^{-1}, with a laser of 532 nm. The former is a first-order Raman scattering (RS) peak, which corresponds to the excitation of a single phonon in the first Brillouin zone (BZ), and is located at the frequency of the LO and TO branches at the Γ line [242, 243]. On the other hand, the $2D$ peak is a second order (double-resonance, DR) RS peak in which two phonons are excited in the scattering process. The RS for the $2D$ line is known as an intervalley process and it is usually used as an indication of a perfect crystalline honeycomb-like structure [243, 250], whereas G is a graphite-like line that can be observed in different carbon-based materials [250]. Graphene also possesses other second-order RS peaks such as D+D'' located at ∼2450 cm^{-1} and $2D'$ at ∼3200 cm^{-1} and disorder-induced peaks such as D at ∼1350 cm^{-1} and D' at ∼1600 cm^{-1} [243]. The RS processes in graphene are shown in Figure 5.10.

This subsection discusses how the Raman spectra can be used to obtain various details on the graphene samples such as the quality and the number of graphene layers, the doping and defect (stress and strain) level [243, 250]. Raman measurements were taken at different spots on the transferred graphene from Co(111), No(111) and Ni_9Mo_1(111), as well as non-transferred graphene on the Cu(001) sample. Their averages are shown in Figure 5.11. It was reported that the $2D$ peak of a single layer of graphene should be fitted with a single Lorentzian with a full-width at half-maximum (FWHM) of less than 40 cm^{-1} and a I_{2D}/I_G greater than 2 [252]. Therefore, our measurements are compared against these values. The

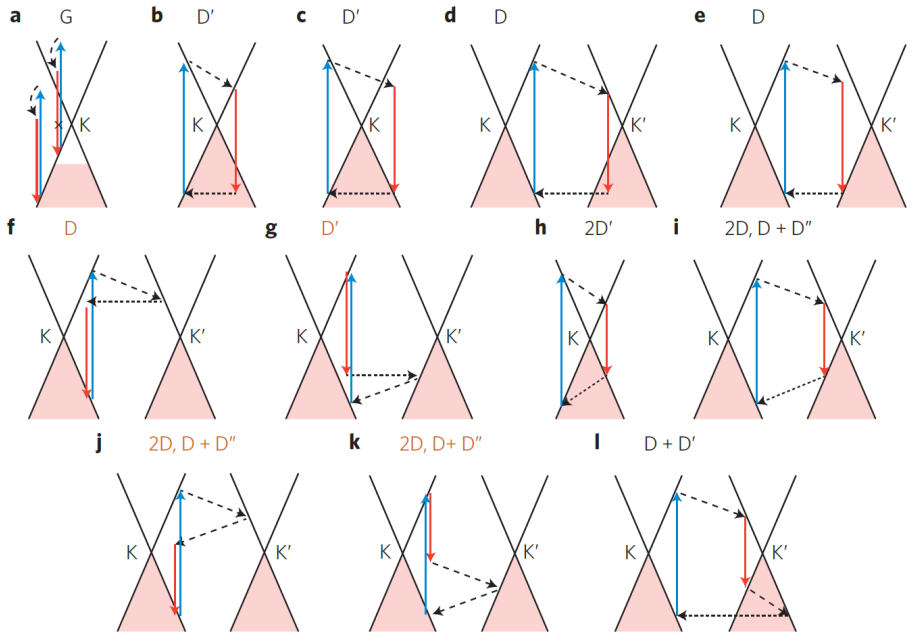

Fig. 5.10 : Raman scattering processes in graphene showing the electron dispersion (solid black line), the occupied states (shaded areas), photon absorption and emission (blue and red arrows), intra-band phonon transitions (dashed arrows) and electron scattering by defects (dotted arrows) around the *K* point. (a) The *G* line produced via the first order RS. (b)-(g) The cancel out processes by defects in which the *D'* line is produced via the intravalley scattering in (b) and (c), and the *D* line in (d) and (e) via the electron-hole or hole-electron participation. (f) The *D* line produced via the electron-electron participation. (g) The *D'* line formed by the hole-hole participation in the intravalley scattering. (h)-(k) The two-phonon intravalley scattering processes in which the 2*D'* line (h) and the 2*D'* and *D* + *D″* lines (i)-(k) are produced by the emission of two photons for the conservation of momentum. (l) The electron-electron and hole-hole intravalley scattering in which the *D* + *D'* lines are produced by the emission of a single photon. (i)-(k). The image is adapted from Ref. [251].

peaks are identified in the spectra as shown in Figure 5.11, whereas Table 5.2 summarises the peak positions, 2*D* FWHM, I_{2D}/I_G and the I_D/I_G. As can be seen from the spectra, all the samples possess the *D*, *G*, *D'*, *D*+*D″* and 2*D* peaks, except for the graphene/Cu(001) sample which shows only the graphene's characteristic Raman peaks. The 2*D* peaks of all the samples were fitted with a single Lorentzian, the FWHM ranging from 39.6-47.7 cm^{-1} as listed in the table.

The *D* peak was reported to change in shape, position and width by increasing the number of graphene layers. On the other hand, the *G* peak is known to downshift with increasing number of graphene layers, but upshift by increasing the number of doping level [243]. I_D/I_G is usually used as an indicator of defects present in the graphene and it grows with increasing disorder-induced in the graphene structure [250]. It is also known that the width

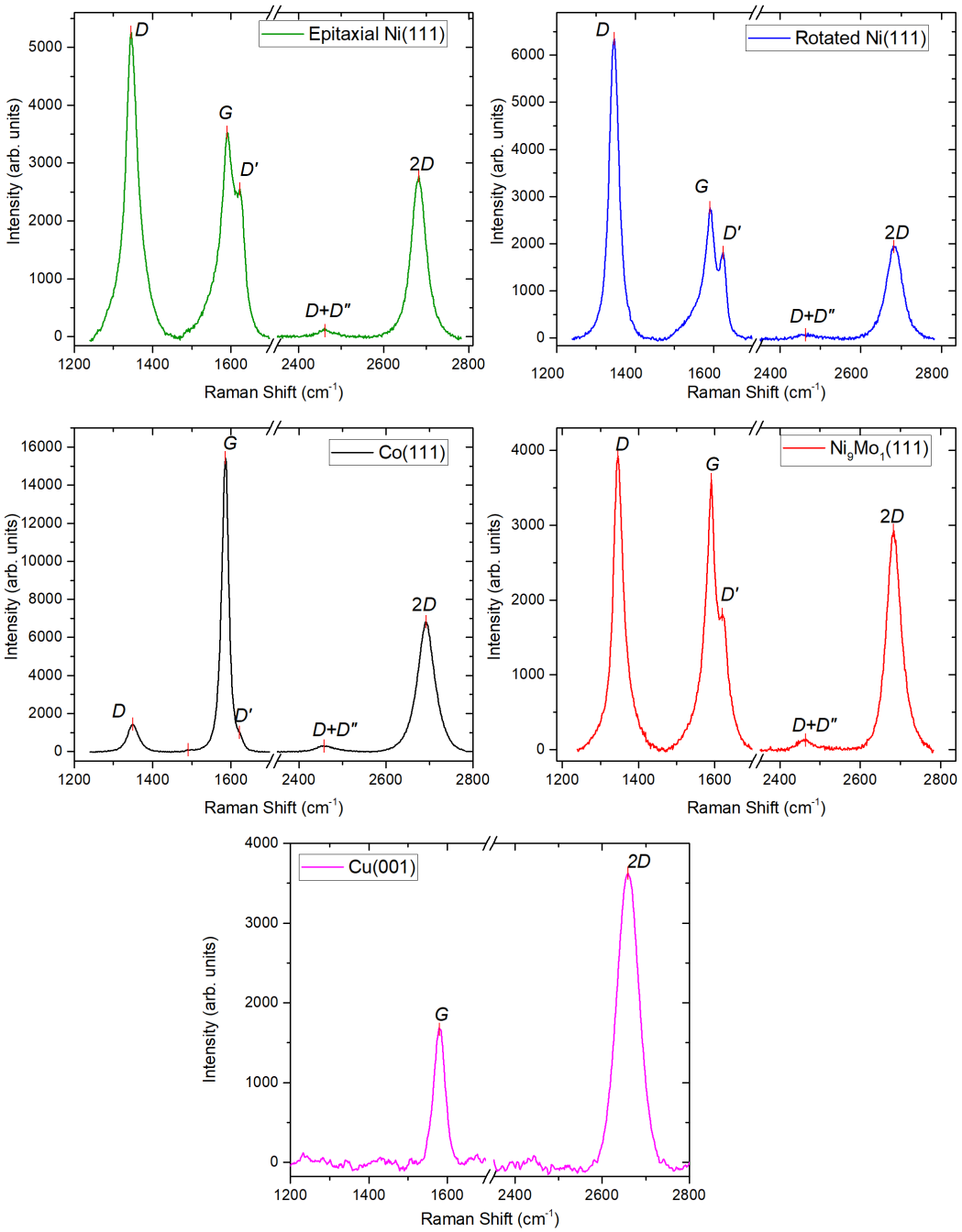

Fig. 5.11 : Room-temperature Raman spectroscopy measurements showing the graphene's characteristic peaks of the transferred graphene from (a) rotated Co(111), (b) epitaxial Ni(111), (c) rotated Ni_9Mo_1(111), (d) rotated Ni(111) and (e) graphene/Cu(0001) samples.

of the *D'* peak increases with increasing the number of defects, while the intensities of the *D* peak remains unchanged. The upshift of the *G* peak and the broadness of the *D'* peak in the Raman spectrum of the transferred graphene from the Co(111) suggest that it

is a multilayer graphene. However, the very low I_D/I_G ratio is an indication that it is a good-quality graphene. Therefore, we conclude that a multilayer, with relatively low defect density graphene was grown on the Co(111) film. On the another hand, the mixed features observed in the other samples' spectra make it difficult to reach a conclusion about the overall quality of the graphene. For instance, $I_{D'}$ is very high in the transferred graphene from $Ni_9Mo_1(111)$ and Ni(111) substrates in comparison with that transferred from the Co(111) film. This means that these samples show a higher disorder level. However, the FWHM of the rotated Ni_9Mo_1 structure is smaller than that in the latter. These results are in agreement with those reported by Patera et *al*. where many defects associated with Ni were found trapped in the graphene lattice [247]. The defect induced-peaks are missing entirely from the graphene/Cu(001) sample, and the I_{2D}/I_G of about 2 reveals that a defect-free monolayer of graphene was grown on the Cu(001) film. The 2*D* is known to broaden by increasing the number of graphene layer due to the splitting of phonon bands [243]. However, the broad 2*D* peak of the graphene/Cu(001) sample may either be due to the coupled Cu(001) substrate or due to the presence of defects in the graphene lattice, which is also proved by the upshift of the 2*D* peak.

Although a full judgment on the quality and quantity of the grown graphene layers from the Raman measurements cannot be derived, the spectra nonetheless confirm that the top layers grown by CVD are indeed graphene, not graphite or any form of carbides or other carbon allotropes. For example, the presence of the *G* and 2*D*, the position of all the peaks, as well as the fitting of the 2*D* peak using a single Lorentzian which is considered as an important Raman spectroscopy feature of a single layer of graphene as it is not affected by the defect density as the other features. This is because the 2*D* peak is fitted with four peaks (D_1, D_2, D_3, D_4) in graphite as reported in Ref. [253]. Also, we can also infer that even if

Sample	*D* (cm^{-1})	*G* (cm^{-1})	*D'* (cm^{-1})	*D*+*D''* (cm^{-1})	2*D* (cm^{-1})	2*D* FWHM (cm^{-1})	I_D/I_G	I_{2D}/I_G
Co(111)	1349.6	1586.9	1621.7	2457.8	2692.3	42.4	0.09	0.44
$Ni_9Mo_1(111)$	1346.3	1590.7	1619.9	2464.0	2682.6	39.6	1.23	0.95
Epitaxial Ni(111)	1344.6	1590.7	1623.1	2462.6	2682.6	39.9	1.49	0.79
Rotated Ni(111)	1346.3	1590.7	1624.8	2464.2	2681.9	46.5	2.27	0.70
Cu(001)	-	1580.3	-	-	2658.9	47.7	-	2.18
Free-standing Gr	1350.0	1582.0	1600.0	2450.0	2700.0	40.0		2.00

Table 5.2: Graphene Raman measurement results on transferred graphene from Co(111), $Ni_9Mo_1(111)$, rotated Ni(111), epitaxial Ni(111) and Gr/Cu(001) compared with the theoretical values of a free-standing graphene.

some of the samples consist of a few layers of graphene, these layers are less than 5 in total as it was reported that only the Raman spectrum of graphene with up to 5 layers could be distinguished from that of graphite [253].

XRR

Figure 5.12 shows the RT high angle XRR measurements, taken by Dr Christy Kinane at ISIS, and their corresponding fits, their scattering length density (SLD) profiles (insets). The fitting parameters (thickness (z), roughness (σ) and density (ρ)) of each layer of all the samples are summarised in Table 5.3. Fitting a monolayer of graphene is very challenging as the graphene's thickness is at the limit of the measuring capability in reflectivity. Therefore, the parameters were allowed to vary within small ranges, but large enough to obtain good fits with the most realistic values and smooth SLD profile transitions as shown in Figure 5.12. A simple model of substrate/TM/graphene was used to fit all the samples, except for the sapphire/Cu(001)/graphene. No fringes are observed in the XRR scan of the latter due to the extreme thickness of the Cu film, which adds to the difficulty of fitting the data. Also, the high growth rate of the thermal evaporator as compared to magnetron sputtering and the high growth temperature used during the growth of the graphene (close to the melting point of Cu) may have created inhomogeneity in the Cu film. Therefore the model consists of two Cu films of different densities which were used to fit the data shown in Figure 5.12 (d). The fact

Sample	Layer	z (nm)	σ (nm)	ρ (atoms/Å^3)
Al_2O_3/Ni/Gr (rotated)	Gr	0.97	0.58	0.12
	Ni	80.0	1.89	0.08
	Al_2O_3	1000	0.15	0.030
Al_2O_3/Co/Gr	Gr	0.98	0.24	0.11
	Co	80.33	1.12	0.091
	Al_2O_3	1000	0.57	0.024
Al_2O_3/Ni_9Mo_1/Gr	Gr	0.15	0.13	0.079
	Ni_9Mo_1	75.02	1.49	0.085
	Al_2O_3	1000	1.07	0.0235
Al_2O_3/Cu/Gr	Gr	0.2	0.52	0.025
	Cu	965.2	2.62	0.041
	Cu	631.3	16.0	0.215
	Al_2O_3	500	950	0.024

Table 5.3: Summary of the XRR fit parameters for the samples: rotated Al_2O_3/Ni/Gr, Al_2O_3/Co/Gr, Al_2O_3/Ni_9Mo_1/Gr and Al_2O_3/Cu/Gr.

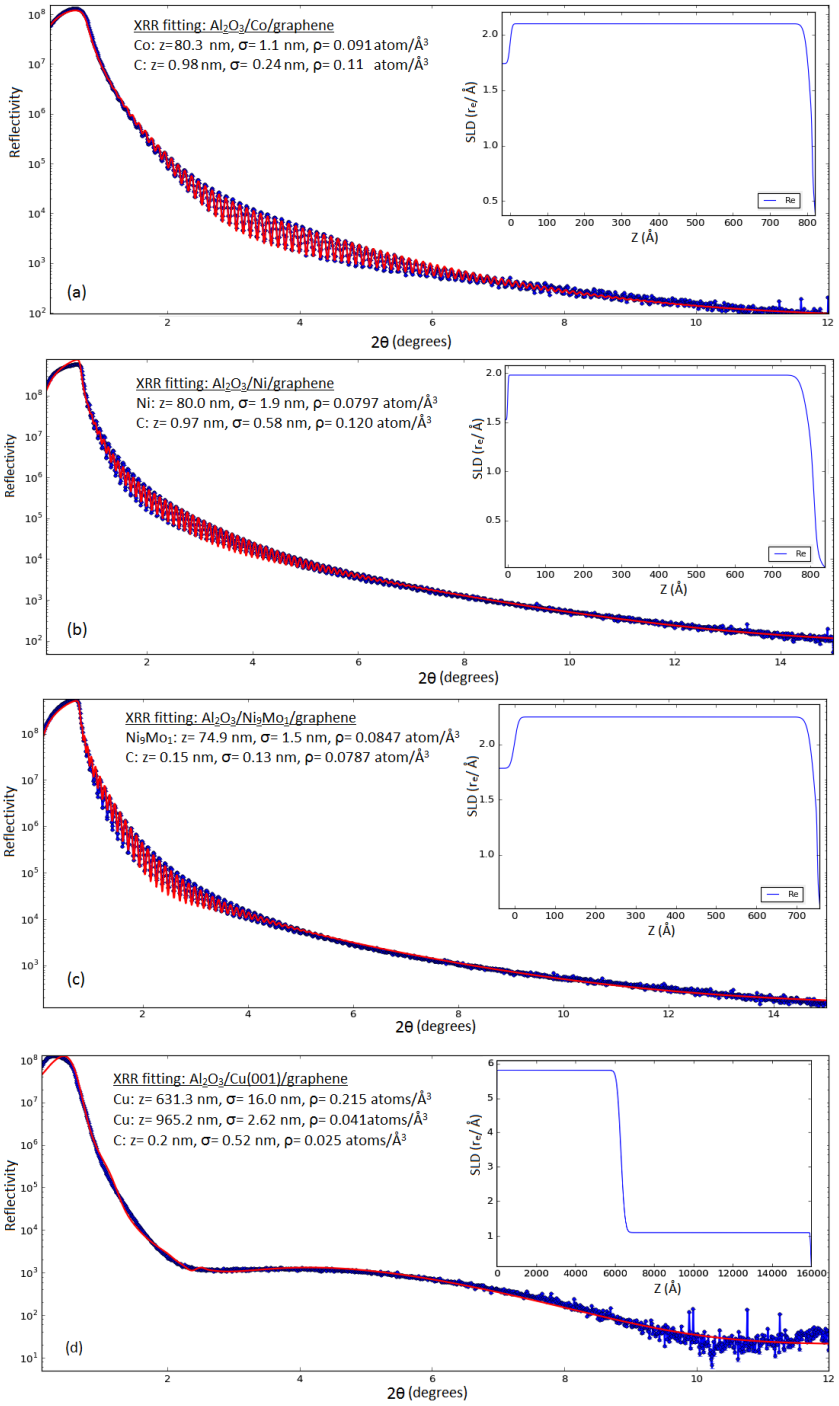

Fig. 5.12 : RT high-angle XRR measurements of (a) Al_2O_3/Co/graphene, (b) rotated Al_2O_3/Ni/graphene, (c) Al_2O_3/Ni_9Mo_1/graphene and (d) Al_2O_3/Cu/graphene. The insets show the samples' SLD profiles. Measurements taken by Dr. Christy Kinane at ISIS, using Rigaku Smartlab.

that the XRR measures thicker graphene layers than those reported in the literature could be due to the occasional multi-layer of graphene as indicated by the results of the SEM images and Raman spectra.

5.3 PNR measurements

The samples were measured with PNR at 300 K and 10 K and in an applied field of 0.5 T, using the Polref instrument at ISIS. The PNR reflectivity, spin asymmetry and their corresponding fits, with the SLD profiles and the FOM scans of the graphene's magnetic moment are shown in Figure 5.13 to Figure 5.17. The fitting procedure was started by pinning z, σ and ρ to the values obtained from the XRR measurements while fitting all other parameters: magnetic moment, instrument resolution, background and the maximum intensity (I_0). The XRR fitting parameters were then allowed to vary again within restricted limits as they tend to drift to unrealistic values if no boundaries are set. All the variables were regularly reset to ensure that the fitting routine converges to the same results. Furthermore, different scenarios were tested. For example, the oxidation of the TM layer and the formation of TM-carbide were examined by embedding an intermediate TM-oxide and TM-carbide layer at the interface between the TM and graphene, but the program rejected the existence of such layers which was also confirmed by the Raman measurements (see Section 5.2.2). Other models, such as the presence of an interdiffusion layers were also assessed, but they lead to poorer fits and the best results were achieved using a simple model: Sapphire/a single layer of TM layer/graphene, except for the Al_2O_3/Cu(001)/Gr sample where a model of two Cu layers was used as for the XRR fitting.

Figure 5.13 and Figure 5.14 show the results obtained for epitaxial and rotated-domain graphene grown on a Ni(111) film, respectively. The fits indicate a thicker epitaxial graphene than the rotated-domain graphene, which reflects the low accuracy of the graphene's thickness and roughness estimation expected from a reflectivity technique. However, these values are consistent in the 10 K and 300 K data. Since Ni and Co are both ferromagnetic (FM) at RT, the 10 K and 300 K are expected to measure consistent values of their magnetic moments, with small discrepancies due to measurement artefacts and the low sensitivity of the PNR to the thickness and roughness of the layers. However, despite the fact that both measurements (10 K and 300 K) measure the same thickness (z), roughness (σ) and density (ρ), a larger moment is measured in the epitaxial graphene on Ni(111) at 10 K, and this is due to the lower thermal excitations of the electron spin. Therefore, the 10 K measurements are expected to provide a better estimation of the induced magnetic moments. Also, the results show that the structure of the graphene has a subtle, if any, influence on the amount of the induced

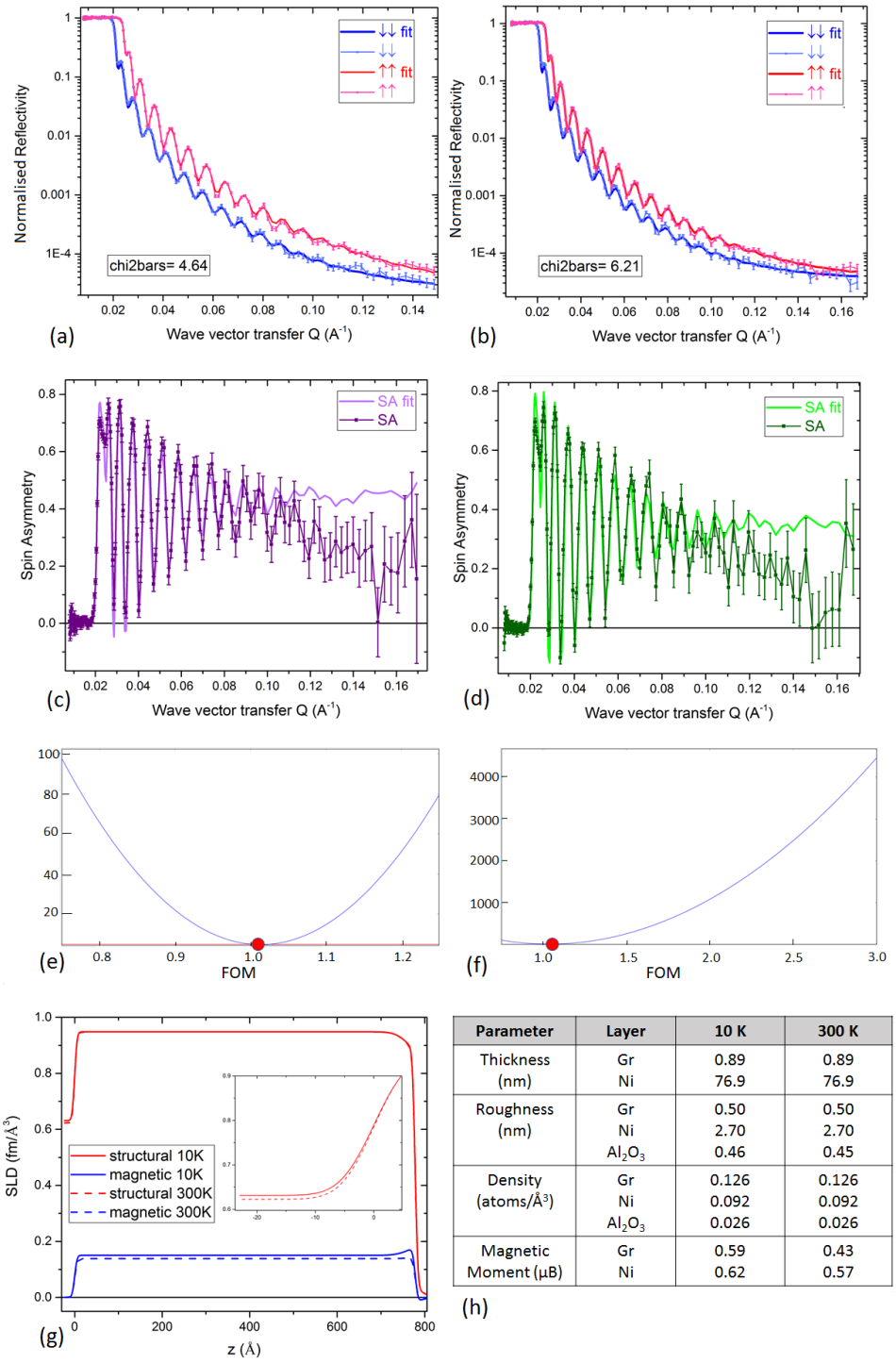

Parameter	Layer	10 K	300 K
Thickness (nm)	Gr Ni	0.89 76.9	0.89 76.9
Roughness (nm)	Gr Ni Al_2O_3	0.50 2.70 0.46	0.50 2.70 0.45
Density (atoms/Å^3)	Gr Ni Al_2O_3	0.126 0.092 0.026	0.126 0.092 0.026
Magnetic Moment (μB)	Gr Ni	0.59 0.62	0.43 0.57

(h)

Fig. 5.13 : PNR results of epitaxial graphene grown on a Ni(111) film measured at 10 K and 300 K. (a) PNR 10 K, (b) PNR 300 K, (c) spin asymmetry 10 K, (d) spin asymmetry 300 K, (e) FOM 10 K, (f) FOM 300 K, (g) SLD 10 K and 300 K and (h) the results summary and comparison between the 10 K and 300 K measurements.

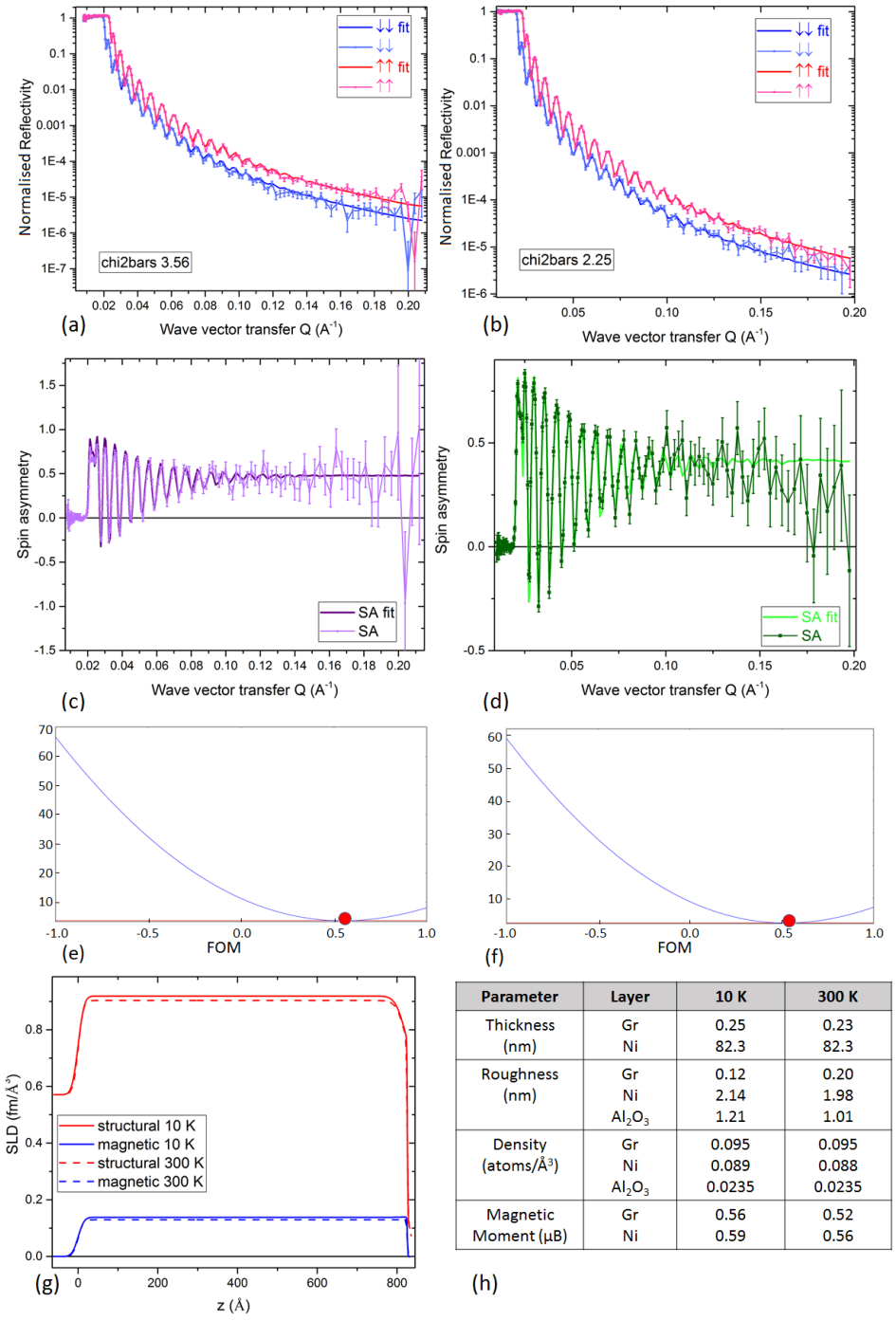

Parameter	Layer	10 K	300 K
Thickness (nm)	Gr Ni	0.25 82.3	0.23 82.3
Roughness (nm)	Gr Ni Al_2O_3	0.12 2.14 1.21	0.20 1.98 1.01
Density (atoms/Å^3)	Gr Ni Al_2O_3	0.095 0.089 0.0235	0.095 0.088 0.0235
Magnetic Moment (μB)	Gr Ni	0.56 0.59	0.52 0.56

Fig. 5.14 : PNR results of rotated domains graphene grown on a Ni(111) film measured at 10 K and 300 K. (a) PNR 10 K, (b) PNR 300 K, (c) spin asymmetry 10 K, (d) spin asymmetry 300 K, (e) FOM 10 K, (f) FOM 300 K, (g) SLD 10 K and 300 K and (h) results summary and comparison between the 10 K and 300 K measurements.

magnetisation. The figure of merit (FOM) scans of the graphene's induced moments in both samples are presented in Figure 5.13 (e) and Figure 5.14 (e), where the red dot represents the deduced value which should be at the minimum of the FOM scan to resemble a good fit. The quality of the fit can also be evaluated from the FOM factor and the SLD profile and is therefore shown for all the measured samples.

The best fits of the PNR measurements on the rotated domain graphene on the Co(111) film are illustrated in Figure 5.15. Fitting the data for this sample is harder than the Ni(111)/graphene samples due to the small fringe oscillations in the spin-up data and the significant differences in the graphene's magnetic moment ($0.58\mu_B$) in comparison with that of the Co(111) ($1.64\mu_B$) layer. The suppression of the spin-up oscillations compared to that of the spin down is due to the weak contrast in the Co spin-up SLD. The SLD contrast for the spin-up ($\rho_{\uparrow\uparrow}$) and spin-down ($\rho_{\downarrow\downarrow}$) neutrons is different. Here, $\rho_{\uparrow\uparrow} = \rho_m + \rho_s$ whereas $\rho_{\downarrow\downarrow} = \rho_s - \rho_m$ and ρ_s and ρ_m are the structural and magnetic contributions to the SLD, respectively (see Section 2.4.2). By looking at the 10 K SLD profile for the Co(111)/graphene sample, $\rho_{\uparrow\uparrow}$(Gr)$\sim$ 0.5, $\rho_{\uparrow\uparrow}$(Co)$\sim$ 0.6 and $\rho_{\uparrow\uparrow}$(sapphire)$\sim$ 0.6. Therefore, a poor contrast is seen by the spin-up neutrons. On the other hand, the $\rho_{\downarrow\downarrow}(Gr)\sim$ 0.3, $\rho_{\downarrow\downarrow}(Co)\sim$ 0.2 and $\rho_{\downarrow\downarrow}$(sapphire)$\sim$ 0.6. Thus, a good contrast is experienced by the spin-down neutrons. The fitting routine regularly gave a greater roughness in the graphene layer than its thickness which led to the dip in the SLD structural contribution as shown in the inset of Figure 5.15 (g) and significant differences in the estimation of z and σ. The PNR fits of this sample indicate that a similar magnetic moment is induced in the graphene as that in Ni(111)/graphene and this can be attributed to the compensation of the larger magnetic moment in Co by the relatively large lattice mismatch between Gr and Co(111) and the relative position of the d-orbital to E_F.

Further PNR experiments were carried out to clarify whether the results are merely due to the $3d$-p_z hybridisation as postulated in Ref. [11, 246] or because of the chemical bonds between the C and TM atoms, as for fullerene/non-magnetic TM as proposed in Ref. [254]. For this purpose, a Ni_9Mo_1(111) film was used with the aim of preserving the *fcc* crystal structure of Ni(111) while suppressing its magnetisation, as suggested in Ref. [255]. The results for the 10 K and 300 K PNR measurements of the Ni_9Mo_1/graphene sample are illustrated in Figure 5.16. A small, but yet detectable spin splitting and a minute variation in the spin asymmetry are observed in the 10 K measurement. The fits for the 10 K and 300 K data lead to similar values for the structural parameters, but the graphene's density tends to mimic that of the Ni_9Mo_1(111) film. Surprisingly, at 10 K a higher magnetisation is detected in graphene (0.15 μ_B) than that of the Ni_9Mo_1 film (0.08 μ_B), which can be attributed to the small residual moment of the Ni_9Mo_1. Since a little magnetism persisted in Ni_9Mo_1(111)

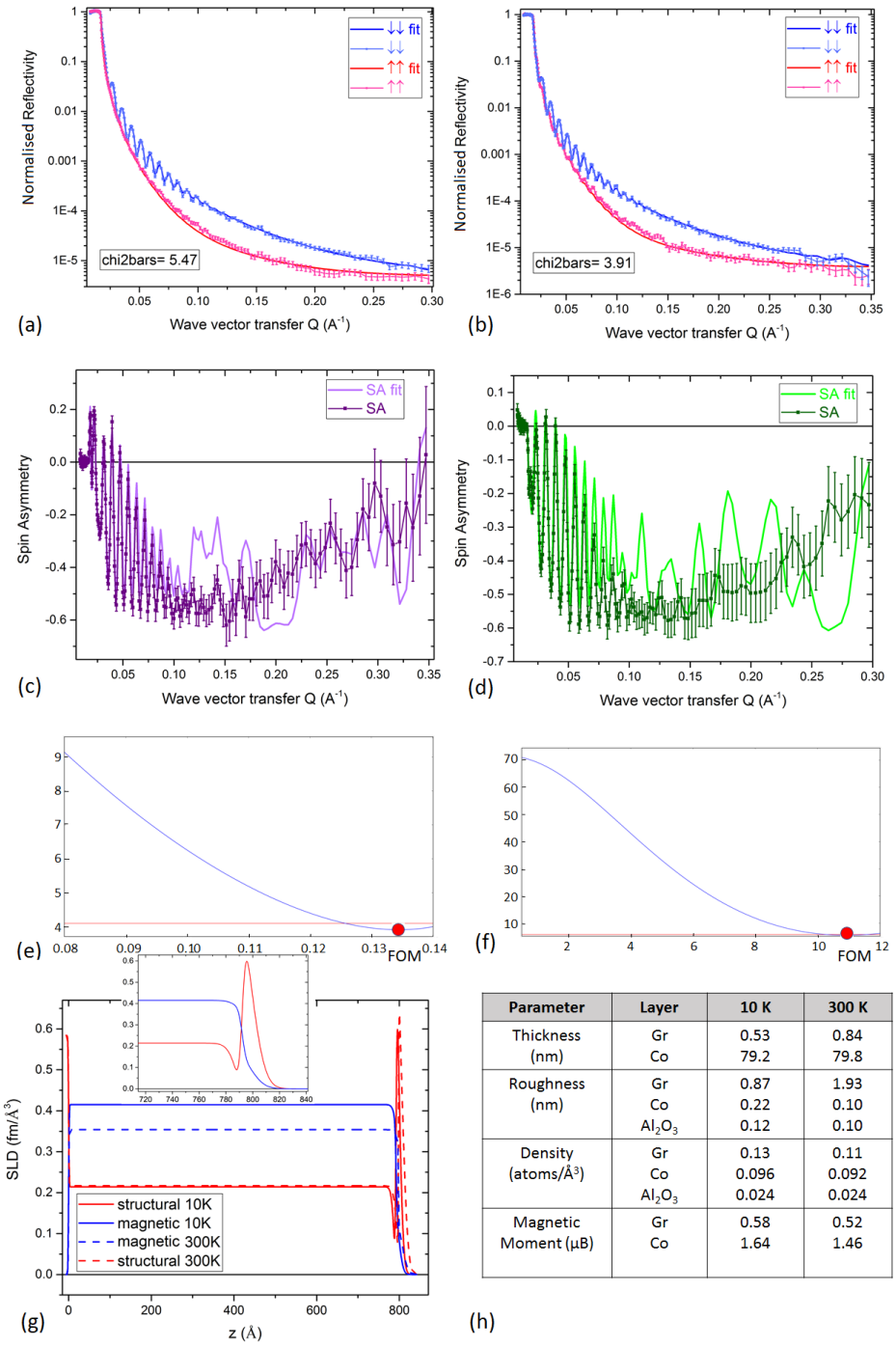

Parameter	Layer	10 K	300 K
Thickness (nm)	Gr Co	0.53 79.2	0.84 79.8
Roughness (nm)	Gr Co Al_2O_3	0.87 0.22 0.12	1.93 0.10 0.10
Density (atoms/Å^3)	Gr Co Al_2O_3	0.13 0.096 0.024	0.11 0.092 0.024
Magnetic Moment (μB)	Gr Co	0.58 1.64	0.52 1.46

Fig. 5.15 : PNR results of rotated domains graphene grown on a Co(111) film measured at 10 K and 300 K. (a) PNR 10 K, (b) PNR 300 K, (c) spin asymmetry 10 K, (d) spin asymmetry 300 K, (e) FOM 10 K, (f) FOM 300 K, (g) SLD 10 K and 300 K. The inset shows a magnified area of the graphene/air interface for the 10 K fit and h) results summary and comparison between the 10 K and 300 K measurements.

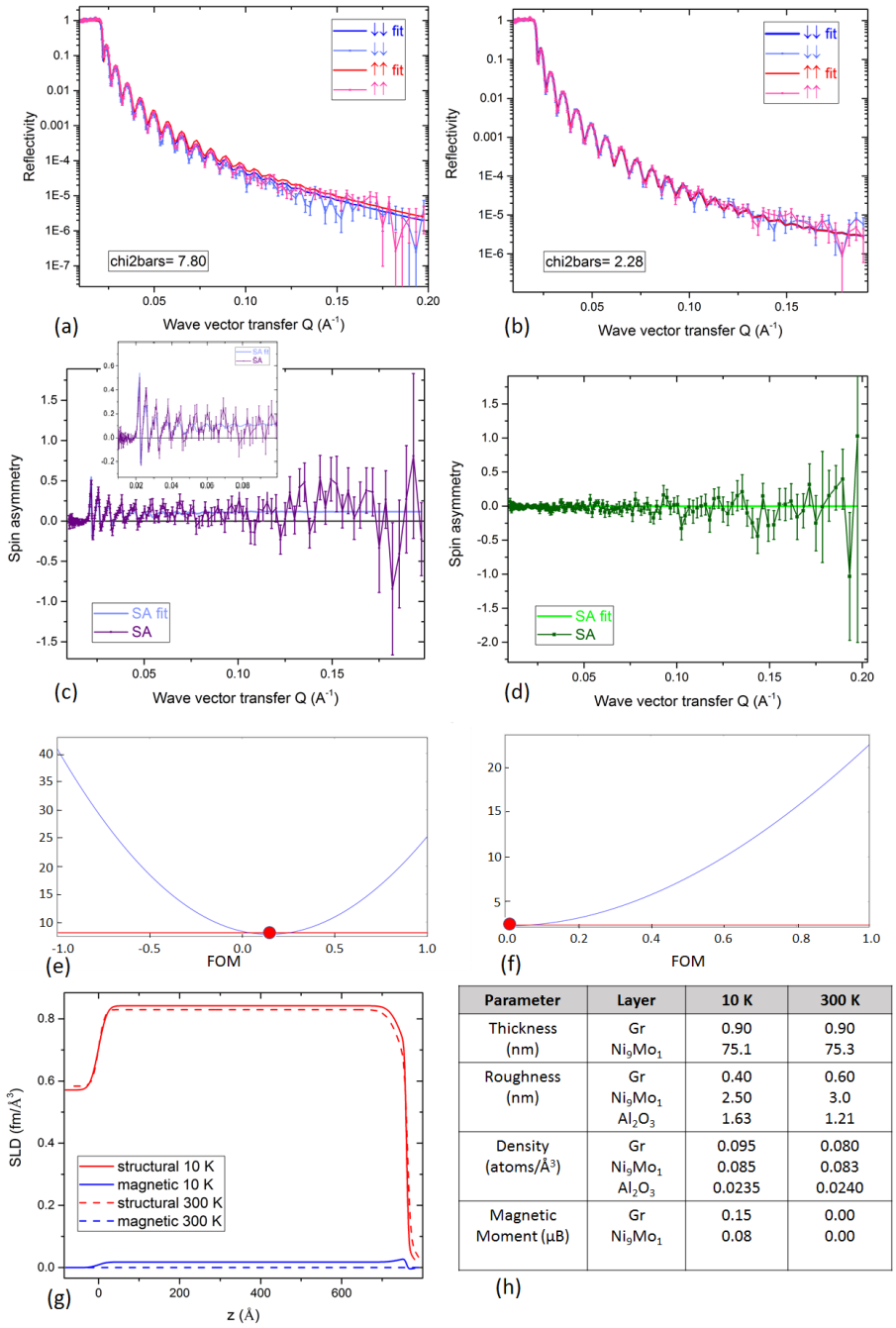

(h)

Parameter	Layer	10 K	300 K
Thickness (nm)	Gr Ni_9Mo_1	0.90 75.1	0.90 75.3
Roughness (nm)	Gr Ni_9Mo_1 Al_2O_3	0.40 2.50 1.63	0.60 3.0 1.21
Density (atoms/Å^3)	Gr Ni_9Mo_1 Al_2O_3	0.095 0.085 0.0235	0.080 0.083 0.0240
Magnetic Moment (μB)	Gr Ni_9Mo_1	0.15 0.08	0.00 0.00

Fig. 5.16 : PNR results of rotated domains graphene grown on a $Ni_9Mo_1(111)$ film measured at 10 K and 300 K. (a) PNR 10 K, (b) PNR 300 K, (c) spin asymmetry 10 K, (d) spin asymmetry 300 K, (e) FOM 10 K, (f) FOM 300 K, (g) SLD 10 K and 300 K and h) results summary and comparison between the 10 K and 300 K measurements.

even at low temperature (10 K), the measurements were repeated using a non-magnetic TM, Cu(001).

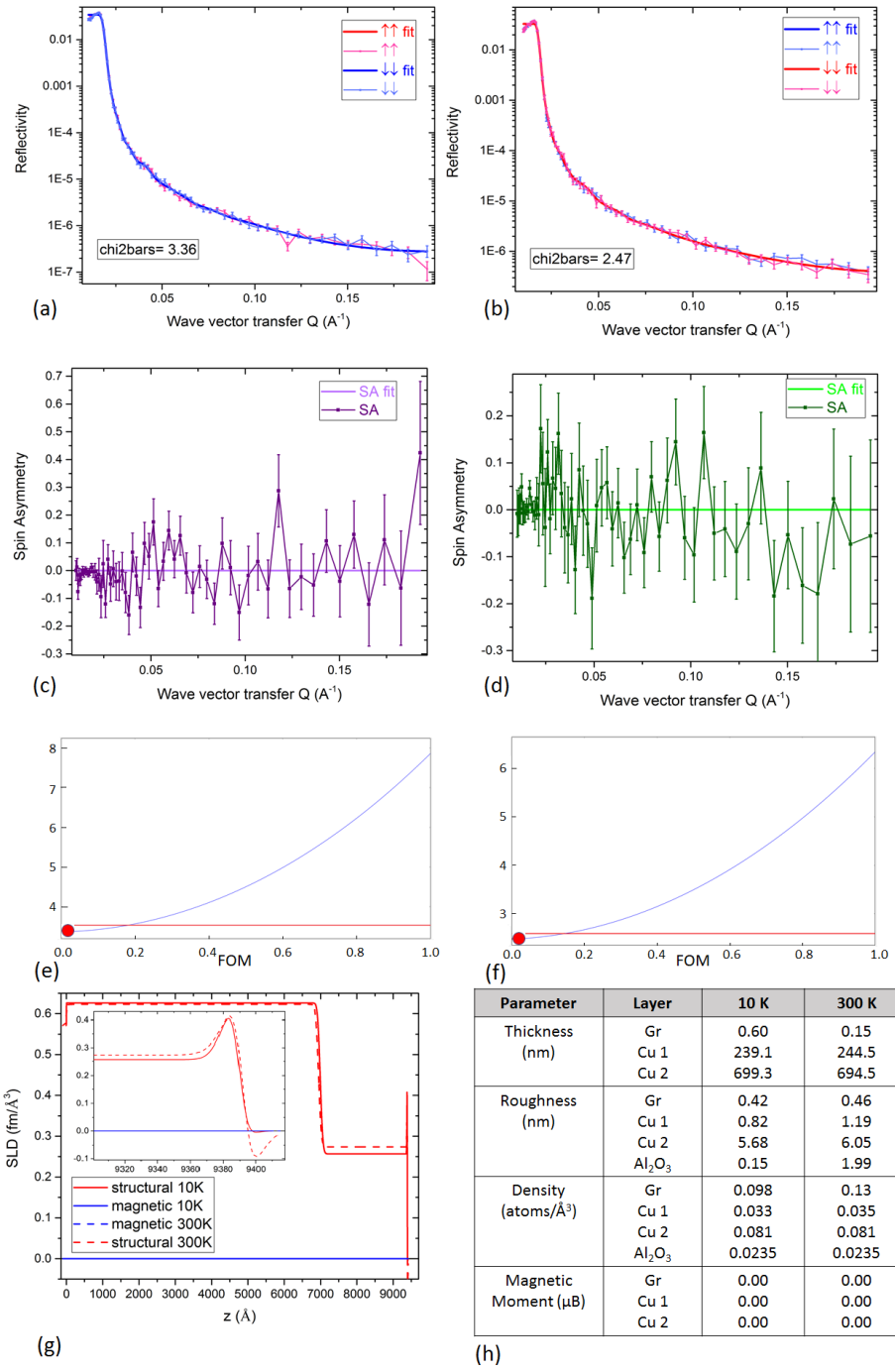

Parameter	Layer	10 K	300 K
Thickness (nm)	Gr Cu 1 Cu 2	0.60 239.1 699.3	0.15 244.5 694.5
Roughness (nm)	Gr Cu 1 Cu 2 Al_2O_3	0.42 0.82 5.68 0.15	0.46 1.19 6.05 1.99
Density (atoms/Å^3)	Gr Cu 1 Cu 2 Al_2O_3	0.098 0.033 0.081 0.0235	0.13 0.035 0.081 0.0235
Magnetic Moment (μB)	Gr Cu 1 Cu 2	0.00 0.00 0.00	0.00 0.00 0.00

(h)

Fig. 5.17 : PNR results of rotated domains graphene grown on a Cu(001) film measured at 10 K and 300 K. (a) PNR 10 K, (b) PNR 300 K, (c) spin asymmetry 10 K, (d) spin asymmetry 300 K, (e) FOM 10 K, (f) FOM 300 K, (g) SLD 10 K and 300 K (the inset enlarges the area at the interface between the graphene and the Cu film) and (h) results summary and comparison between the 10 K and 300 K measurements.

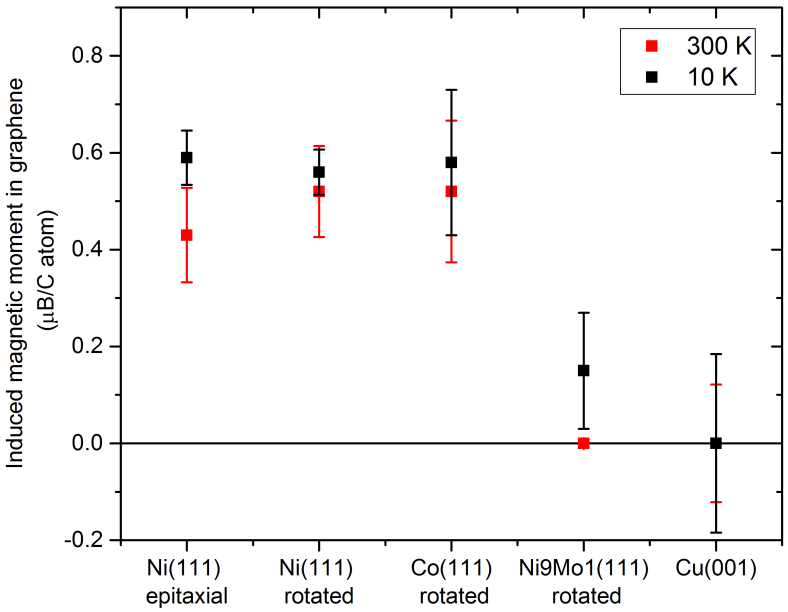

Fig. 5.18 : A summary of the induced magnetic moment in graphene measured by PNR in all the samples at 10 K and 300 K.

The results for the Cu(001)/graphene structure are shown in Figure 5.17. The inconsistent estimation of the graphene's thickness and roughness could be a result of the bendiness effect of the thin sapphire substrate or due to the absence of the spin splitting in the reflectivity curves which increases the inaccuracy of determining the graphene's z and σ. As expected, no induced magnetic moment is detected in graphene, firstly, because Cu is a non-magnetic TM and secondly because the weak interaction between the graphene and the Cu surface atoms will not open up the graphene's Dirac cones. The PNR results of all the samples are summarised in Figure 5.18.

Although the theoretical PNR accuracy is $\sim$99.5%, the complexity in fitting the data for graphene can be attributed to two main reasons: firstly, the significant drop in the SLD profile at the transition between the graphene capping layer and air which leads to an increase in the roughness of graphene. This drawback can be overcome by growing a multilayer system of $[\text{TM/graphene}]_x$. The second reason is the fact that the Q range covered in our measurements, due to the limited beamtime available, is less than 20% of the graphene's full reflectivity which occurs at Q $\approx$ 2.55 Å^{-1}. Therefore measurements up to a higher Q value ($\sim$ 0.45Å^{-1}), well above the instrument background noise, should provide a more accurate estimation of the induced magnetic moment in graphene [53].

Bayesian analysis

Dr Timothy Charlton carried out Bayesian uncertainty analysis of the Ni/graphene and Co/graphene PNR measurements to understand our fits better, test the validity of the fitting models and hence the reliability of our results. The simulations shown in Figure 5.19 to 5.23 were achieved using Refl1D and Bumps software [108, 256]. Three scenarios were tested to simulate the PNR fits for epitaxial Gr/Ni. The first model (Figure 5.19 (a)) was achieved

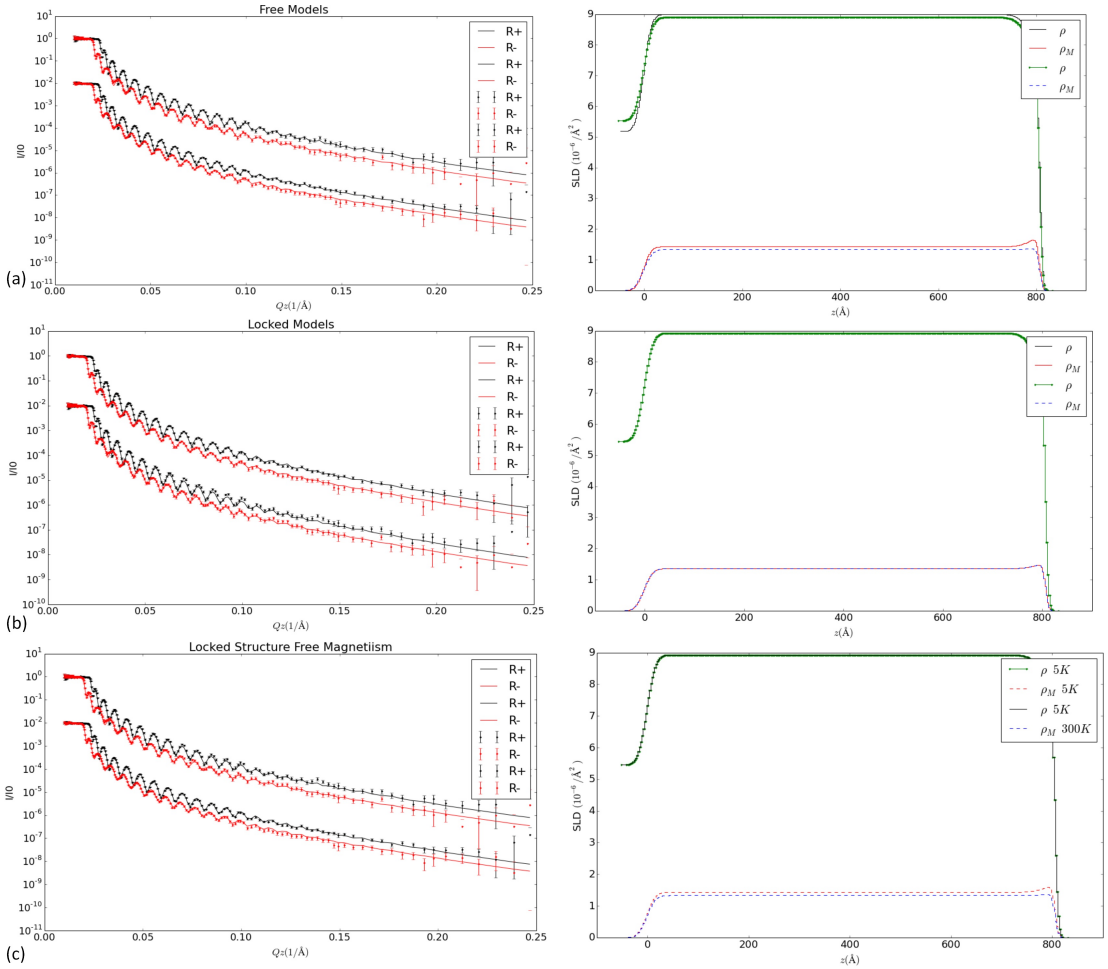

Fig. 5.19 : The model scenarios used to obtain a Bayesian simulation for epitaxial graphene grown on Ni for the 5 K and 300 K measurements. (a) Model 1: fitting the structural and magnetic SLD for 5K and 300 K independently from each other. (b) The reflectivity curves for the 5 K and 300 K obtained when the structural and magnetic SLD of both measurements is locked together and the corresponding SLD profile. (c) The reflectivity curve and the fit produced when the structural SLD of both measurements is locked together, while fitting their magnetic SLD independently. The 300 K reflectivity curves shown in (a), (b) and (c) are shifted down by a factor of 100.

using the same approach used as for fitting our PNR measurement, in which the 5 K data was fitted first, independently from the 300 K, and then the results were used as a starting model for the 300 K data. Also, several attempts were run through the Bumps software to check the robustness of the model. This method resulted in a consistent SLD profile, especially for the spin-up curve. However, running both the magnetic and structural parameters for the two datasets, independently from each other, led to an unrealistic variation in the density of the sapphire substrate. The spin splitting observed in the 5 K fit is an indication of an enhanced magnetic moment at the Ni/Gr interface, but the SLD for the 300 K shows no indication of induced magnetic moment at the interface. The second approach adopted was to lock both, the structural and magnetic SLDs and fit the 5 K and 300 K together (Figure 5.19 (b)). This method forced the fitting engine to average the fits of the two datasets. Therefore, poorer fits are obtained, especially for the 300 K, with a high χ^2 value and the induced magnetic moments are observed in the magnetic SLD profiles. Figure 5.19 (c) shows the results obtained when the film structure is locked for the 5 K and 300 K data while fitting their magnetic SLD independently. This scenario improved the fits, but slightly missed the magnitude for the spin-up graph at Q$\sim$ 0.07 Å^{-1} for the 300 K data. It shows that this scenario underestimates the magnetisation of the sample.

To investigate the sensitivity of the fitted line to the SLD magnetic profile a parameter analysis on the third model was then carried out. For this purpose, Dr Charlton noted any changes in the reflectivity curve and the χ^2 value when the values of the fitted parameters were chosen to be different to their best values. Three behaviours were observed: forcing the magnetic moments of graphene and Ni to be the same yielded a 17% increase in χ^2 from the lowest value and generally a poorer fit over a larger Q range for the spin-up curve for the 300 K data. Also, allowing for different magnetic moments in the Ni film at 5 K and 300 K, while locking the moment in graphene to that of Ni, increased the value of χ^2 by only 2% from the lowest results. However, removing the magnetic moments of graphene while forcing the dead layer to be at the surface of the sample increased the χ^2 value by a factor of 3, while reducing the spin splitting for the 5 K and 300 K in the medium-to-high Q values.

The automated parameter analysis generated for the fitted parameters is presented in the top frame of Figure 5.20, where the histogram series shows the probability distribution for each parameter (bottom frame). The shaded yellow region represents the 68% confidence interval [1], while the green line is the highest probability provided that the parameter is fixed at the maximum likelihood value. The histogram and the probability distribution should have a similar shape for all the parameters of a model to be fully converged. Hence, all the fitted parameters shown in Figure 5.20 (top frame) converge, except for the thicknesses of

[1] 68% confidence level= mean $\pm$ (1.0) x (standard deviation).

the Ni and graphene, and the density of the latter. The abnormality in these parameters can be investigated using the parameter-parameter correlation simulation shown in Figure 5.20 (bottom frame). An oval shape is expected for a well-fitted parameter as it proves that it is independent of the other parameters (see Section 2.4.2.4). However, this is not the case for the Ni film and graphene as the graph shows that they are strongly correlated. The oddities observed in Figure 5.20 in the Ni and graphene thicknesses and the density of graphene can be attributed to the low sensitivity of the PNR to the film thickness, but also to the thinness of the graphene layer and the narrow Q-range covered. Although the Bayesian simulations were

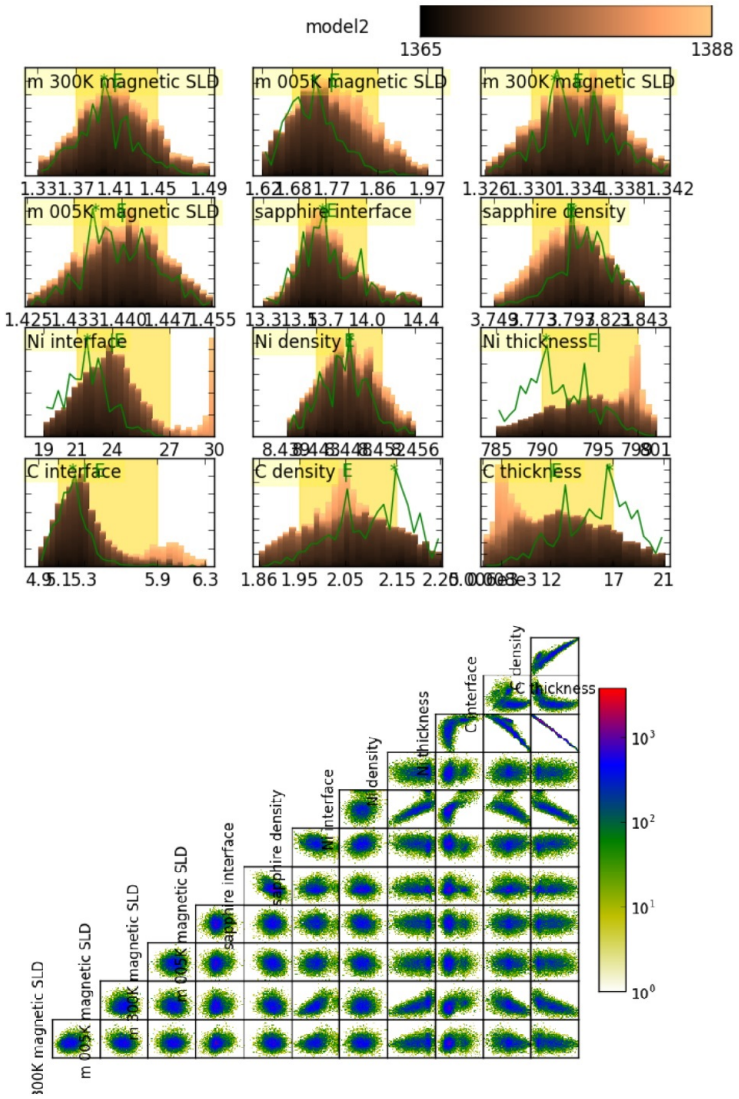

Fig. 5.20 : Top panel: the probability distribution of the fitted parameters for epitaxial graphene grown on Ni at 5 K and 300 K. Bottom panel: the parameter-parameter simulation.

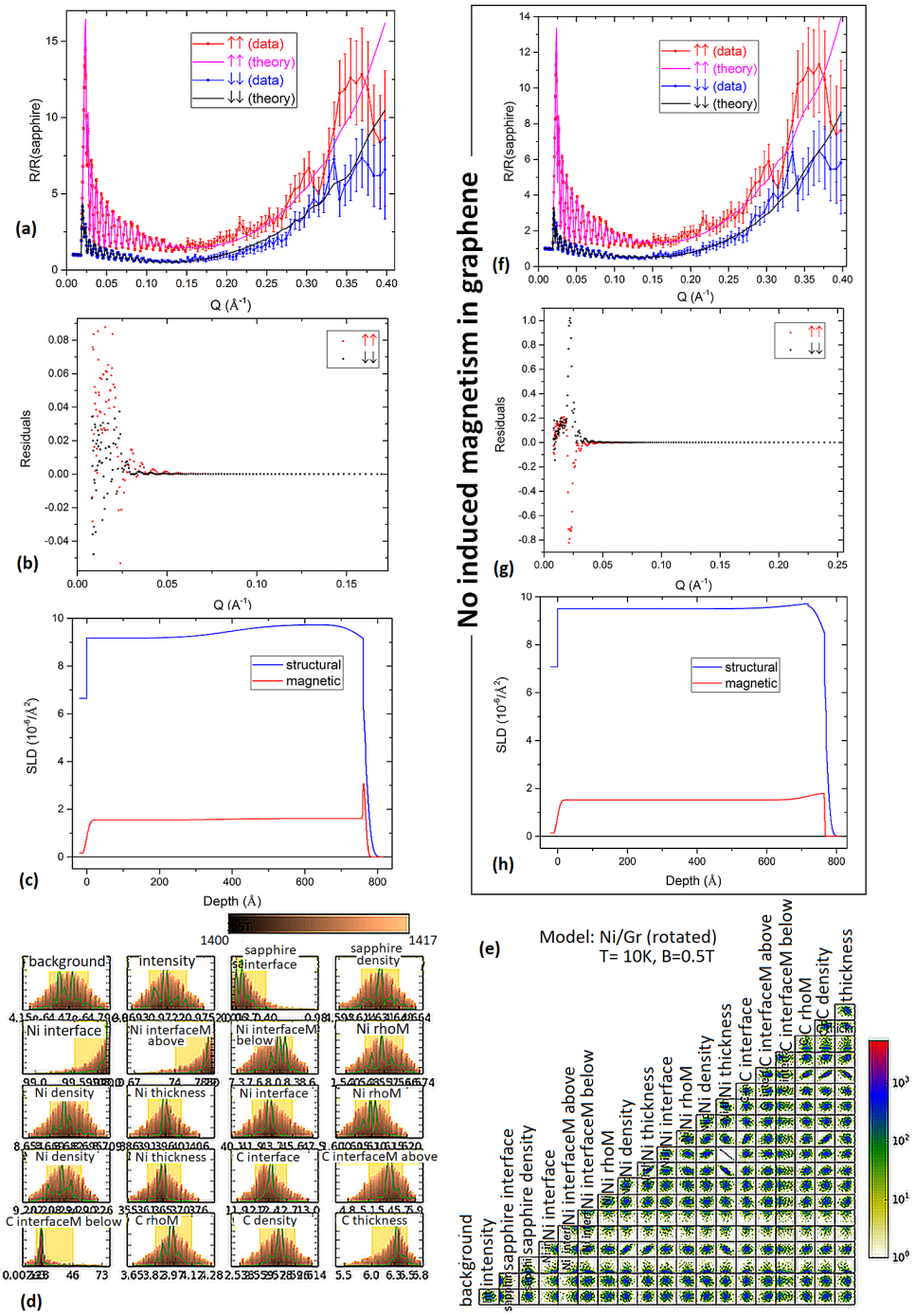

Fig. 5.21 : Bayesian simulations for rotated domains graphene grown on Ni measured at 10 K using two scenarios: with and without induced magnetic moment in graphene; (a,f). The normalised PNR reflectivity curves and their corresponding residuals in (b) and (g) and the resultant SLD profiles in (c) and (h). (d) The parameter analysis of the fitted parameters and their correlation simulation in (e).

carried out for 5 K instead of 10 K, the comparison between our 10 K measured PNR and the 5 K simulation is valid as we do not expect many changes between the two temperatures.

Similar simulations were carried out for the rotated-domain graphene on the Ni(111) film, but for a 10 K measurement instead of 5 K. The two cases investigated for this sample, with and without magnetic moment induced in graphene, are shown in Figure 5.21. The presented reflectivity curves were normalised to that of the sapphire, to eliminate the substrate contribution, thus easily highlight any features associated with the thin films. The residual graphs presented in Figure 5.21 (b) and (g) illustrate the difference between the theoretical model and the measured data. Better fits were obtained when the magnetic moment of graphene was unconstrained rather than with the graphene's magnetisation pinned to zero. This can be deduced from the residuals in Figure 5.21 (g) as it has a broader spread of data in comparison to those shown in Figure 5.21 (b). On the other hand, the population histogram shown in Figure 5.21 (d) proves that the model and the simulation are fully converged as the shape of the histogram matches that of the green line. An even better behaviour for the Ni and graphene thicknesses and the graphene density is observed in the correlation analysis.

The Bayesian analysis for the rotated domains graphene on Co(111) is shown in Figure 5.22. The reflectivity curves and their corresponding SLD profiles are shown in the top frame, where the fits were achieved when the structural SLD of both temperatures is locked together, while fitting their magnetic SLD independently. The simulations were run for a few iterations only, and therefore the models are not yet converged. This is because the aim for these simulations was to study the effect of the graphene magnetisation on the quality of the fit while keeping all the other parameters the same. Turning off the magnetisation of graphene yielded a poorer fit quality with higher residuals as shown in Figure 5.23 (a) and (b). However, these Bayesian analyses prove that our simple model is robust and that the amount of induced magnetic moment in graphene obtained from our PNR fits is reliable.

5.4 XMCD measurements

XMCD measurements were carried out at the SIM-end station at PSI to study the magnetic interactions between the graphene and the metallic substrate and to confirm that the magnetic moment detected by PNR originated indeed from the graphene and not from a diffuse interface. Rotated and epitaxial Gr/Ni(111) and rotated Gr/Co(111) were mounted on a copper holder and the chamber was then pumped down using an ion pump to $2.3\text{x}10^{-7}$ mbar. A maximum field of 0.11 T was applied for 30 seconds in-plane to the sample surface to saturate the samples, but it was then reduced to 0.085 T during the collection of XAS and XMCD measurements. Angle dependent XAS measurements on C *K*-edge of the rotated

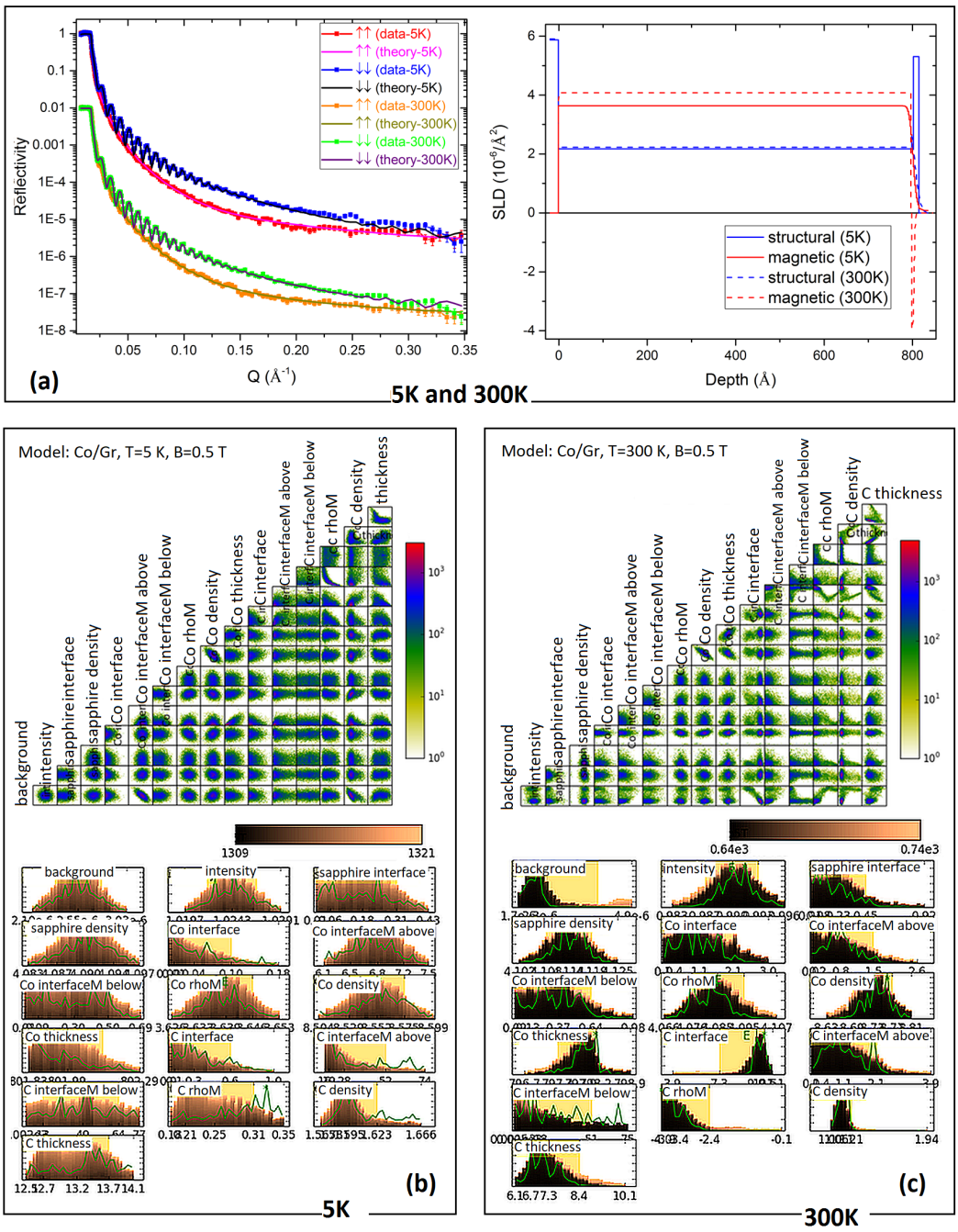

Fig. 5.22 : (a) Bayesian simulation for the rotated domains graphene grown on Co for 5 K and 300 K measurements. The top frame shows the reflectivity curves of the data with the theoretical fitted lines and the corresponding SLD profile, where the 300 K is scaled down by a factor of 100. The bottom frame presents the parameter analysis and correlation simulation for the 5 K (b) and 300 K (c).

and epitaxial Gr/Ni(111) were carried out by fixing the magnet angle to 40° to the incoming

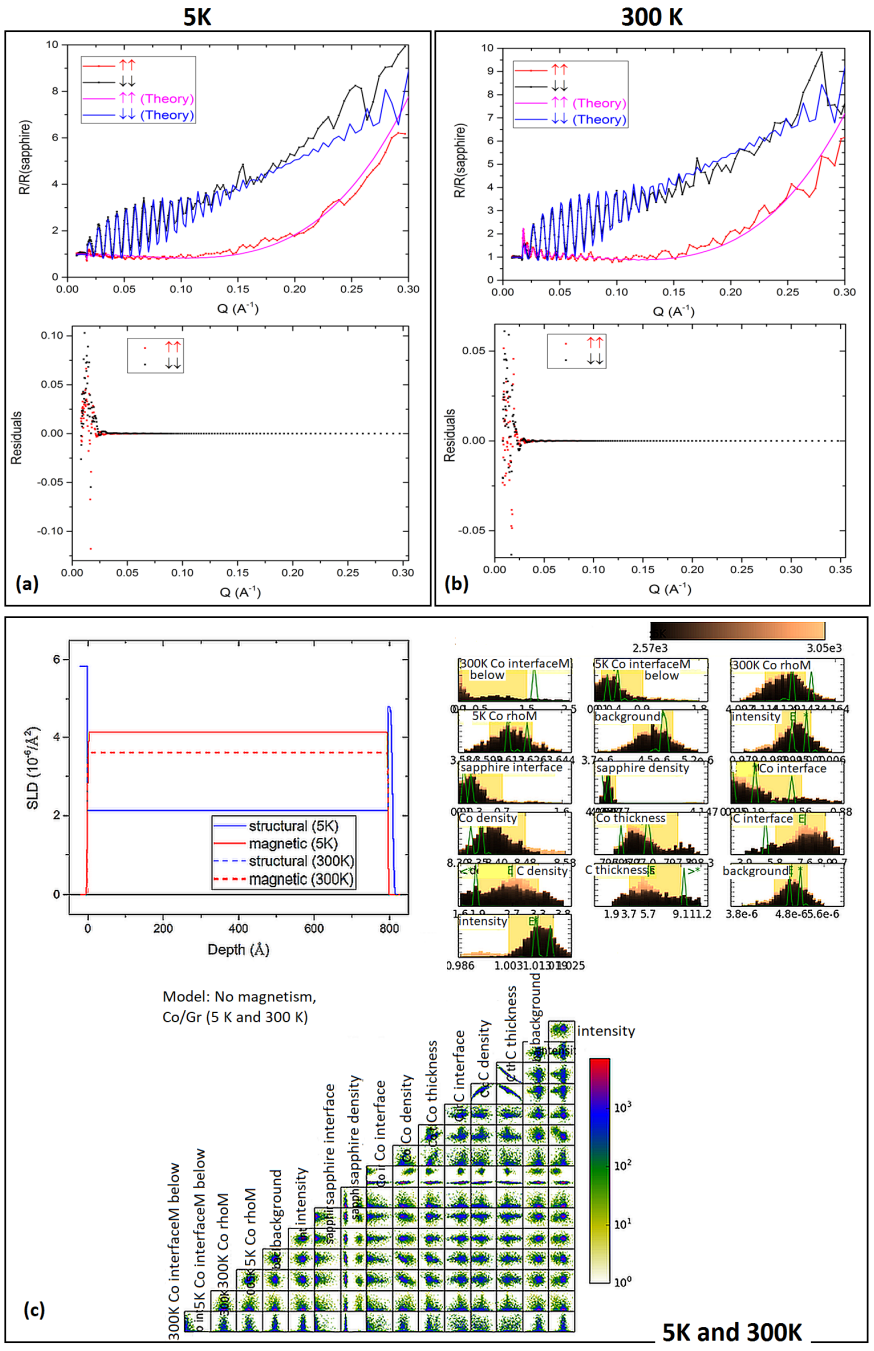

Fig. 5.23 : Bayesian simulations for the rotated domains graphene grown on Co for the 5 K and 300 K measurements when the graphene's induced magnetic moment is locked to zero, while keeping the other fitted parameters the same. (a,b) The normalised reflectivity curves and the corresponding residuals at 5 K and 300 K, respectively. The bottom panel (c) illustrates the corresponding SLD profile, the population histograms of the fitted parameters and their correlation behaviours.

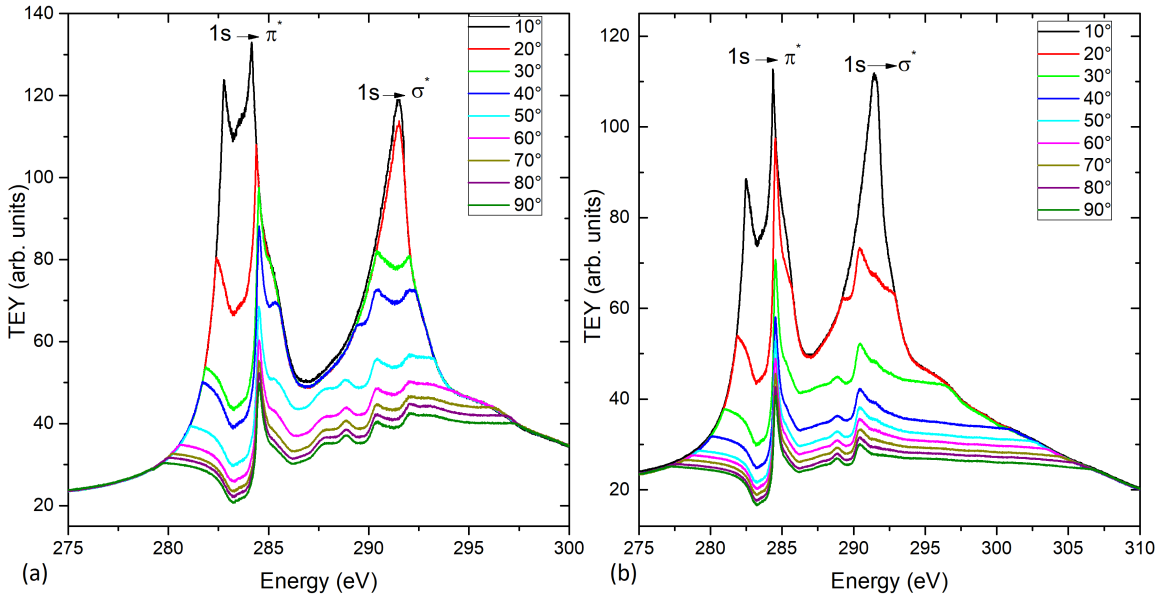

Fig. 5.24 : Angle-dependent TEY on (a) rotated Gr/Ni(111) and (b) epitaxial Gr/Ni(111) at 300 K.

beam while turning the sample holder from 10° to 90° in steps of 10°. The incident angle is measured between the incoming X-ray and the sample surface. These measurements were obtained using TEY mode with a 100% polarised light at 300 K. The results of the normalised XAS data are shown in Figure 5.24. Spectral features for both samples are observed in the ranges 280→285 eV and 287 →297 eV which are attributed to the C 1s→ π^* and C 1s→ σ^* transitions, respectively [11]. The resonance in the region of the lower energy range possesses a double-peak feature. By considering the *top-fcc* configuration, the first peak reflects the transitions of the C 1s core electrons into the empty interface states (which results from the opening of the Dirac cone, around the K-point) as a result from the C_{top} p_z-$Ni_{surface}$ 3d hybridisation [229, 257]. The second peak is due to the excitation of the C 1s core electrons into the empty interface states at around the M point, which arises from the in-plane bonding between C_{top} and C_{fcc} through the $Ni_{surface}$ forming C p_z-Ni $p_{x,y}$ and 3d hybridisation [11, 257]. Surprisingly, epitaxial and rotated graphene are found to behave differently in the higher energy range, around the σ^* transition. This behaviour can be explained as follows: since the σ peak represents the in-plane hybridisation between adjacent C atoms, C_{top} and C_{fcc}, these bonds are expected to vary due to the presence of occasional multilayered graphene in the rotated structure leading to multiple C 1s→ σ^* transitions peaks. The number of split σ^* peaks decreases with the incident angle as the measurements become more surface sensitive and thus fewer of the graphene's multilayers are detected. However, this assumption can only be ruled out using the surface PEY mode.

An incident angle of 30° was used for the XMCD experiments to enhance the magnetic contrast at the C π^* resonance and also to reduce the background contribution coming from the sample holder. Figure 5.25 shows the 300 K μ_{XAS} and μ_{XMCD} spectra for the Gr/Co(111) sample measured at the C K-edge and Co $L_{2,3}$-edge after they have been processed using the method described in Chapter 2.4.1.3. μ_{XAS} and μ_{XMCD} integrated areas are labelled in Figure 5.25 (a) and (b), respectively. ΔA_3 is taken to be at the position shown in 5.25 (a) because the region between the L_3 and L_2 with a constant negative intensity is known as the diffuse magnetism region, μ_{diff}. This effect has been observed and reported for Co, Ni and Fe XMCD spectra [258]. μ_{diff} is expected to arise as a result of the opposite spin directions for the 4s and 3d electrons, interstitial and sp-projected magnetic moments, and the fact that it couples antiferromagnetically to the sample's total magnetic moment in 3d elements, except for Mn [258, 259]. Although μ_{diff} has been reported to contribute to about -4% and -7% to the total magnetic moment in Co and Ni, respectively [60, 258], since the sum rule does not account for μ_{diff}, it was excluded from the m_o and m_s calculations. On the other hand, the main L_3 peak and the shoulder, $\mu_{shoulder}$, are due to multiple initial-states configuration, $3d^8$ and $3d^9$, respectively, and therefore they were included in the sum rule calculations [258]. Figure 5.25 (b) shows μ_{XAS}, μ_{step} and μ_{XAS} after the subtraction of the white line. A ratio of 2.8:1 for L_3:L_2 was used to place the step just at the foot of L_3 and L_2 peaks. The data was also corrected for the light degree of polarisation and the incident angle, but no correction for the saturation effect was required as this effect is more significant in thicker films, as mentioned in Section 2.4.1.2.

Taking into account the points discussed earlier, the calculated m_o and m_s of the Co(111) layer obtained by the application of the sum rules to μ_{XMCD} and μ_{XAS} are -0.186 μ_B and 0.08 μ_B, respectively. Therefore, the total magnetic moment is $\sim 16\%$ of that extracted from the PNR measurement and does not agree with the previously reported values in Ref. [77, 260] for bulk Co. Since the Co spectra show no sign of oxidation, this indicates that the reduction in the magnetic moment is not due to the oxidation of the Co film and proves that graphene acts as a good passivation layer against oxidation. Therefore, the reduced calculated values can be attributed to the fact that the measurements were taken on the hard magnetic axis of the Co film, instead of the easy axis.

Although the dichroism contrast and thus the magnetic moment for the Co film are significantly reduced, the XMCD signal of the C K-edge gives a clear indication that a magnetic moment has been induced in the graphene. Unexpectedly, the peak which corresponds to the $1s \rightarrow \sigma^*$ transition shows a magnetic dichroism response as well as the $1s \rightarrow \pi^*$ transition. However, only the latter was expected to be spin polarised as a result of the C p_z-Co 3d hybridisation. This measured effect may be due to the normalisation of the μ_+ and μ_- as

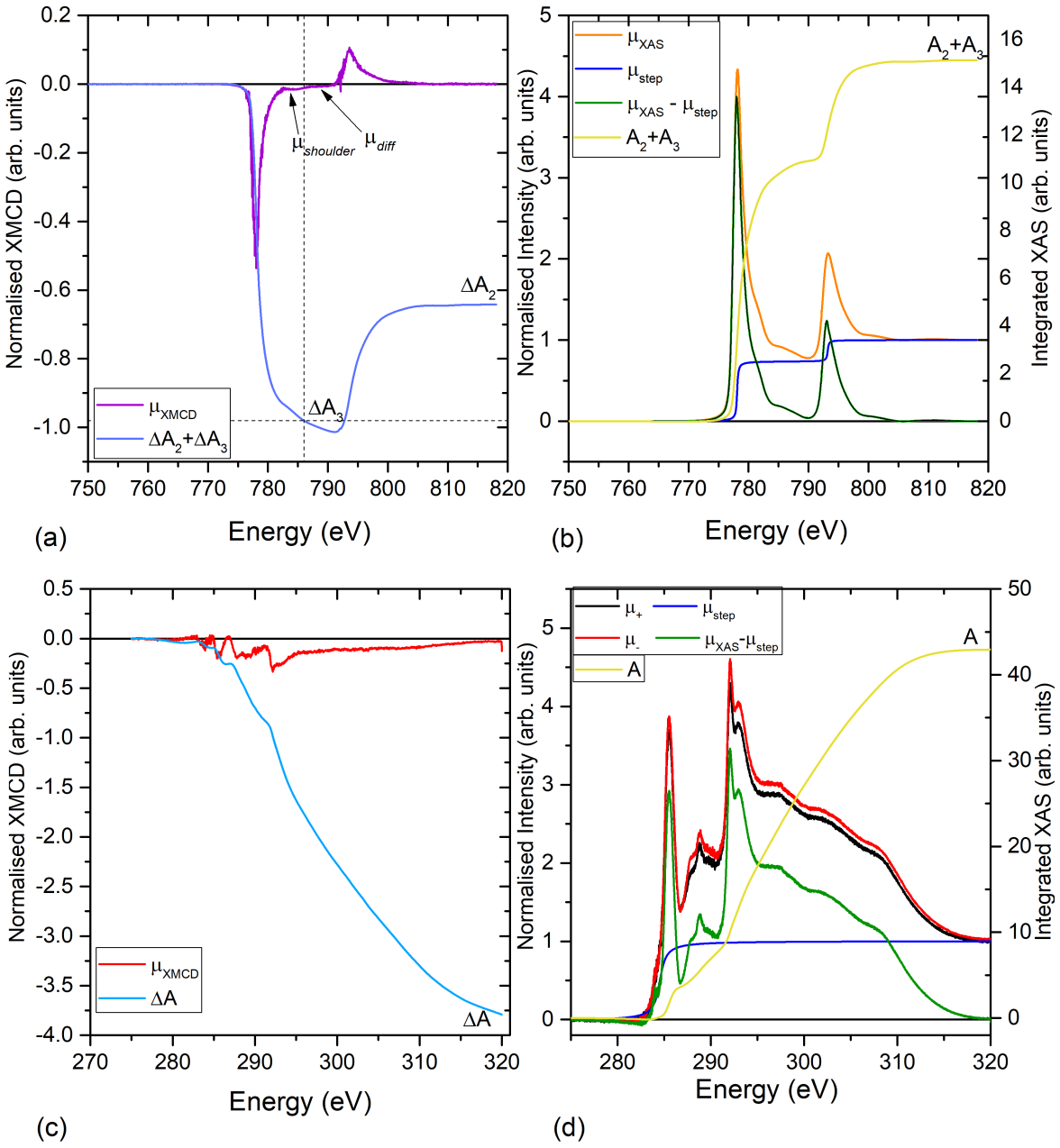

Fig. 5.25 : Absorption spectra for circular polarised light and the areas used to apply the sum rules for the graphene/Co(111) sample measured at 300 K: (a) and (b) XMCD and XAS spectra for Co $L_{2,3}$-edge. (c) and (d) XMCD and XAS spectra for the graphene layer.

the spectra presented in Figure 5.25 (d) were achieved by normalising the C π orbital peak to unity instead of the post-edge. Normalisation of the post-edge produced an additional mismatch between the two helicities, 285 eV $> E >$ 310 eV, which overestimates μ_{XMCD} and thus the calculated m_o. However, since a stronger dichroism is expected from the C p_z in

the C-Ni hybridisation the adapted method is believed to lead to a more accurate estimation of the m_o value for graphene.

For C K-edge, $m_s = 0$ since $1s \rightarrow \pi^*$ is a non-spin-split coupling. However, m_o is calculated as -0.27 μ_B/atom using $n_h = 4$. Therefore, the total magnetic moment induced in graphene measured by XMCD is $\sim 52\%$ of that extracted from PNR (Section 5.3). This discrepancy can be attributed to the difficulty of applying the sum rules to the C K-edge spectra in comparison with that for Co and Ni $L_{2,3}$-edge. For instance, various studies have been reported for Co and Ni [11, 60, 76, 77, 229, 260–263] which can be used as references for our measurements, but the application of the sum rules has not been reported for graphene before. Also, n_h has not been measured for C previously. Therefore, higher sources of errors are expected in the XMCD estimation than in PNR.

The μ_{XMCD} and μ_{XAS} of the Ni $L_{2,3}$-edge in the Gr/Ni(111) sample and its corresponding top graphene are shown in Figure 5.26. It is clear from the spectra that $\mu_{shoulder}$ is more pronounced in Ni than in Co due to the extra electrons occupied in the d band. Furthermore, although the non-resonant contribution was subtracted from the μ_+ and μ_- spectra, a higher background is measured at the post-edge ($E > 880$ eV). This tail has been excluded from the sum rules as it is considered part of the non-resonant contribution. The calculated m_o and m_s are -0.38 μ_B/C atom and -0.05 μ_B/C atom, respectively, and thus the total magnetic moment is 0.43 μ_B/C atom. This reduced magnetic moment of the Ni film may also be due to an insufficient field applied to saturate the Ni magnetisation as the spectra show no indication of oxidation. Considering the 5% accuracy of the XMCD technique in estimating the magnetic moments of materials, the results obtained for both Co and Ni are much lower than the values reported in literature. Therefore, magnetic measurements using the SQUID were performed on the samples to investigate further the magnetic properties of the TM films (see below).

The C K-edge spectra for the graphene/Ni(111) sample were treated differently from that of the graphene/Co(111) sample. The spectra were normalised to the post-edge and the resultant μ_{XMCD} and μ_{XAS} are shown in Figure 5.26 (c) and (d). The spectra show a positive linear shoulder at high energies ($E > 310$ eV) which makes it difficult to estimate the integrated area required for the sum rule. Therefore a hyperbolic tangent *tanh(x)* was fitted to the $\int \mu_{XAS}$ to deduce A and calculate m_o for graphene as -0.44 μ_B.

The additional SQUID measurements were taken for the samples to investigate further the magnetic properties of the Co(111) and Ni(111) films. The 300 K hysteresis loops of the samples shown in Figure 5.27 were measured with the field applied parallel (0°) and perpendicular (90°) to the surface of the samples. The shape of the hystereses and the size of the coercivities of both measurements show that the in-plane is the easy axis for both films, whereas the reduced sample moments measured by the SQUID may be due to the error arising

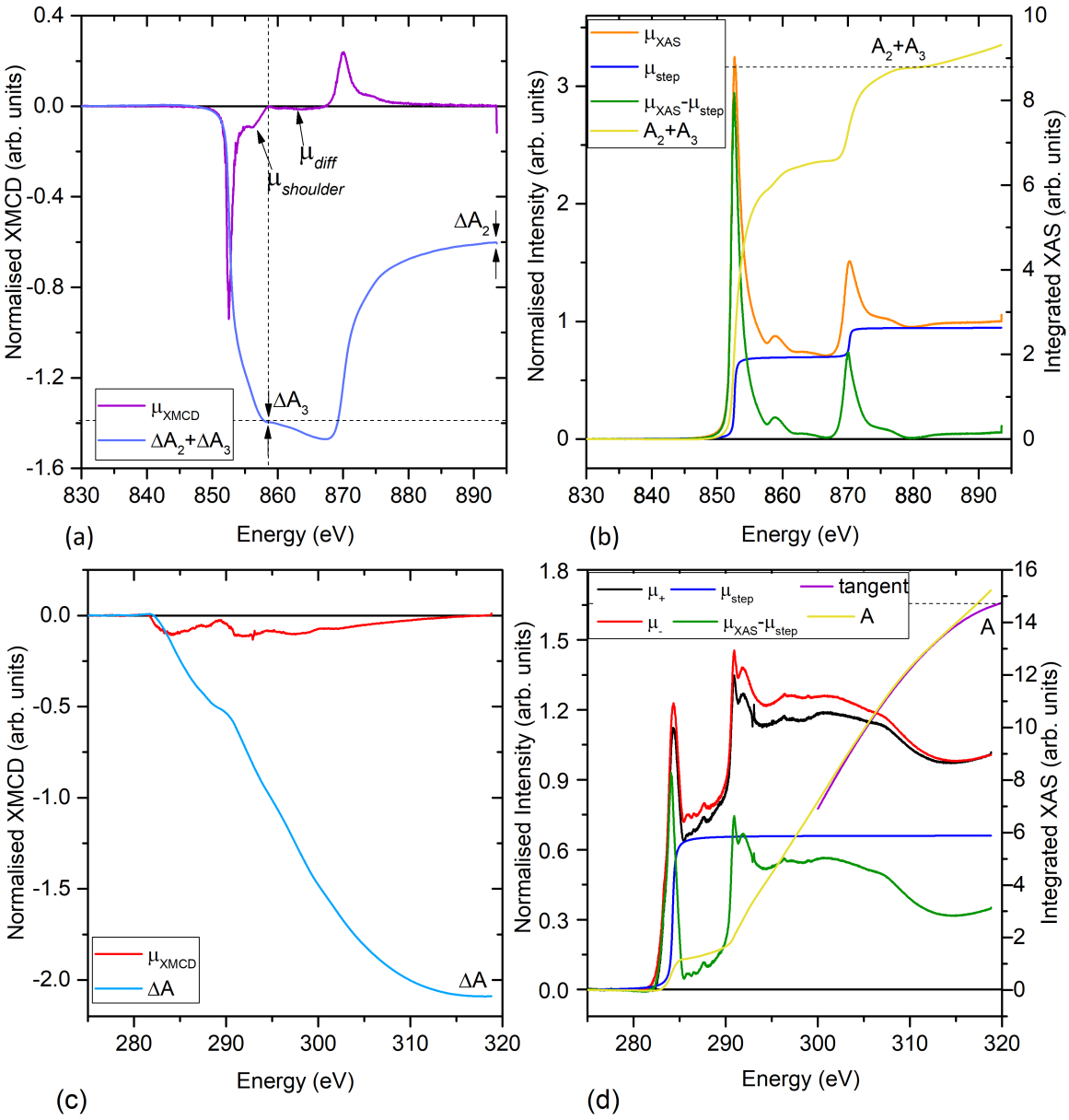

Fig. 5.26 : Absorption spectra for circular polarised light and the areas used to apply the sum rules for the graphene/Ni(111) sample measured at 300 K: (a) and (b) XMCD and XAS spectra for Ni $L_{2,3}$-edge. (c) and (d) XMCD and XAS spectra for the graphene layer.

from measuring the samples' dimensions accurately. Mounting the samples at 30° in our SQUID magnetometer is very challenging as the system is not designed for angle-dependent measurements. Nonetheless, the 30° measurement is expected to lay between the two loops. Figure 5.27 (a) shows that 0.11 T measures a magnetic moment of 0.7 μ_B/Co atom and 0.25 μ_B/Co atom when the sample is mounted parallel and perpendicular to the applied field,

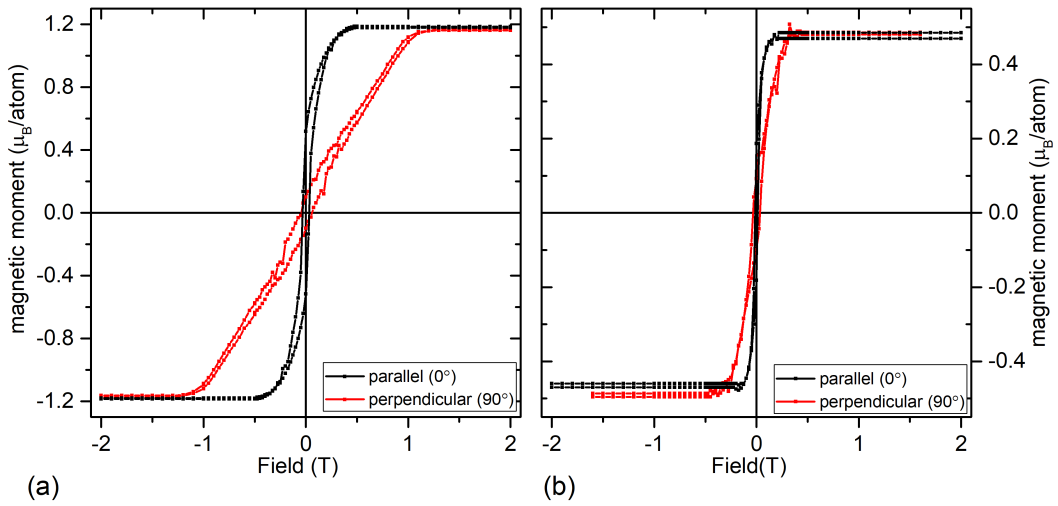

Fig. 5.27 SQUID measurements showing the hysteresis loops obtained with the field applied parallel (0°) and perpendicular (90°) to (a) graphene/Co(111) and (b) graphene/Ni(111) samples.

respectively, which are about 59% and 21% of the saturated magnetic moment of the Co(111) film. On the other hand, a field of 0.11 T applied to the graphene/Ni(111) sample yield to a magnetic moment of 0.45 μ_B/Ni atom and 0.28 μ_B/Ni atom when the field was applied parallel and perpendicular to the Ni(111) film. Therefore, the Ni(111) film was at 58-93% of its saturation only, and thus a higher moment was measured with XMCD in rotated graphene on Ni(111) than that on Co(111). Therefore, the SQUID results are consistent with those of the XMCD and explain the reduced magnetic moment measured with the XMCD. A field of 1 T was required to ensure both samples are saturated.

5.5 Conclusion and outlook

The results presented in this chapter have shown that we have successfully grown graphene on TM substrates. The samples were then used to carry out PNR and XMCD experiments to measure the induced magnetic moment in graphene in the vicinity of an FM substrate as a result of the opening of the graphene's Dirac cones due to the strong C *p*-Ni 3*d* hybridisation.

PNR fits have shown that Co(111) and Ni(111) films have induced a magnetic moment of $\sim 0.57\ \mu_B$. These results indicate larger moments induced in the graphene than the value previously predicted by Weser *et al.* who suggested that the induced magnetic moment for a graphene monolayer grown on a Ni(111) film would be between 0.05-0.1 μ_B per C atom [11]. His assumption was based on comparing the graphene/Ni system with other C/3*d* TM structures, such as C/Fe multilayer [264], carbon nanotubes on a Co film [265], where a

magnetic moment of 0.05 μ_B and 0.1 μ_B per C atom was measured, respectively. However, the PNR results show an induced magnetic moment of about 5x this range. The induced magnetic moment in graphene is expected to be higher than that reported in Ref. [264] and Ref. [265] as the measured values in these systems are averaged over many layers of carbon. Therefore, the comparison between graphene and other C allotropes/TM systems may not lead to an accurate estimation of the graphene's moment. We have validated the models used to fit the PNR results with a Bayesian uncertainty analysis and the corroborated XMCD measurements. Although the TM films were not saturated during the XMCD experiments, the spectra prove that the additional magnetic moment deduced from the PNR measurements are indeed in the top graphene layer and that it does not correspond to diffusion of the carbon atoms into the TM forming an alloy at the interface.

The presented data can be improved in various ways. For examples, the measured samples can be modified by growing a multilayer system of [TM(>100 nm)/graphene]$_x$. The advantage of such a sample is that it reduces the significant contrast in the neutron SLD profile between that of graphene and the air, and the thicker TM films will provide a better separation between the graphene layers. Therefore, a better estimation of the graphene magnetic moment and the average values of each layer can be obtained. Also, the accuracy of the PNR measurements can be improved by measuring the samples to higher Q ranges, as discussed in Section 3.4. Furthermore, applying a higher field to saturate the TM films and acquiring the XMCD data using the PEY mode will enhance the surface sensitivity of the XMCD estimation.

6

Conclusions and Future Work

Magnetic thin-film heterostructures have attracted great attention for various technological applications such as giant magnetoresistance and spin valves due to their useful properties, especially at the interface. They were found to exhibit new features at the interface while leaving the bulk properties of the films unchanged. This thesis explored the interfaces of EuO(001)/LAO(001), EuO/NiO(111) and graphene/metal interfaces using various structural and magnetic characterisation techniques such as XRD, XRR, SQUID magnetometer, PNR, XMCD and μSR.

The integration of both ferromagnetic and semiconducting properties at a nanoscopic level has been a long-pursued goal. Therefore, EuO, which is a ferromagnetic semiconductor that has a high magnetic moment of 7 μ_B/Eu atom is considered as an ideal material. However, the disadvantage of using EuO is its low T_C of 69 K. Therefore, many attempts have been reported to increase its T_C by electron doping. DFT calculations published by Lee *et al.* and Wang *et al.* predicted the formation of spin-polarised 2DEG in the EuO film at $\sim$1.5 nm from the EuO(001)/LAO(001) interface which would also increase its T_C by $\sim$ 35 K as a result of the polar catastrophe at the interface [9, 10].

The magnetic depth profile of the interfaces of EuO(001) with LaO^+- and mixed-terminated LAO(001) substrate was investigated experimentally using PNR, μSR and other structural and magnetic characterisation techniques. The termination of the substrate was confirmed from the AFM topography showing regular terraces with a step height of ∼0.4 nm for the LaO^+-terminated LAO and terraces with random step height for the mixed-terminated substrate. These terminations were achieved by wet etching using NaOH for the LaO^+-termination and HCl for the mixed-termination, followed by O_2 annealing at 1000 °C for 4 and 6 hours, respectively. The XRD scan showed a highly textured EuO(001) film grown on the LAO(001) substrate with no sign of other Eu-oxide phases. The epitaxial growth of the EuO(001) on the LAO(001) substrate was also confirmed by the X-ray ϕ-scans of the LAO(211) and EuO(113) planes as the latter adapted a similar pattern to that of the twinned LAO(211) plane. The twinned peaks were separated by 36.8° and the repetition of the pattern every 90° confirmed the cubic crystal structure of the LAO and EuO. A reduction of ∼2.6 K in the T_C of the EuO film was detected by the SQUID magnetometer, which was attributed to the lateral strain induced in the EuO film as a result of the 4.1% lattice mismatch between the EuO film and the substrate. This result agrees with that measured by Caspers of a similar, but slightly thinner, heterostructure [169]. However, it contradicts the prediction of the published DFT calculations. Furthermore, the grown EuO films were found to follow the mean-field theory rather than the 3D Heisenberg model as the critical exponents, β and γ were found to be 0.479 ± 0.09 and 0.96 ± 0.29, respectively for the LaO^+-terminated sample, and 0.455 ± 0.04 and 0.95 ± 0.057, respectively, for the mixed-terminated sample.

The results of the ZF and wTF μSR measurements provide no unambiguous proof of the formation of a spin-polarised 2DEG at the interface. Comparing the obtained results with those reported for stoichiometric EuO and EuO_{1-x} shows that EuO(001) on a LAO(001) substrate behaves differently, but no hint of an increase in the T_C is observed. However, the PNR experiments performed on both samples at different temperatures below, around and above the theoretical value of the EuO T_C showed that a small magnetic moment persisted in the structures at 72 K, but the detected magnetic moment is within the resolution limit of the instrument. Therefore, it is difficult to deduce whether or not the measured magnetic moment is real. An inhomogeneity in the grown EuO films was suggested by a five-layer of EuO model, and an enhanced magnetic moment of 3.58 μ_B/Eu atom was detected in the EuO layer of the LaO^+-terminated sample at 20 nm from the interface. Although this value is consistent with that reported for a 9% oxygen-deficient EuO film [184], it is much thicker than the thickness predicted by the DFT calculation. Although no clear indication of the formation of a spin-polarised 2DEG at the EuO(001)/LAO(001) interface was obtained from the performed experiments, the results showed that the magnetic behaviour of EuO

was modified by the LAO substrate. However, further investigation is needed to provide a quantitative understanding of the EuO(001)/LAO(001) interface. Therefore, transport measurements, although difficult to perform on EuO films as they readily oxidise to the most stable oxide phase (Eu_2O_3), would provide a better interpretation of the obtained results.

Another interface effect on EuO-based heterostructure was also reported in this thesis. The EB and the magnetisation depth profile of the EuO with the polar interface of the antiferromagnet NiO(111) were investigated, and the results were compared with those of the uncoupled EuO(001) grown on a MgO(001) substrate. The structural XRD scans show that amorphous EuO and Au layers were grown on the NiO(111)/MgO(111) sample due to the large mismatch between the EuO and NiO(111). However, highly oriented EuO(001) peaks with no presence of other Eu-oxides phases were observed in the XRD scan which agrees with the literature reporting the growth of epitaxial EuO(001) on a MgO(001) substrate. The bulk magnetic properties of the samples were measured by the SQUID magnetometer. A square-shaped hysteresis loop with H_c= 61 Oe was detected for the non-polar structure, whereas a small double-shifted hysteresis loop with an enhanced coercivity of H_c= 85 Oe was measured for the polar sample which arose from the competition between the random NiO(111) *S*-domains at the interface. Furthermore, a smaller spin-splitting was observed in the PNR curves of the polar sample compared to that of the non-polar structure, EuO(001)/MgO(001). This behaviour was attributed to the pinning of the EuO magnetisation by the randomised NiO(111) *S*-domains at the interface, which would prevent the EuO spins aligning completely with the applied magnetic field. This hypothesis was investigated by performing further PNR measurements on a FC EuO/NiO(111) sample.

The FC sample was measured by the PNR SF and NSF channels, with the field applied along and perpendicular to the initial FC direction to explore the contributions of the pinned and unpinned NiO(111) *S*-domains separately. Unfortunately, the low intensity and the poor statistics of the PNR curves detected by the SF channels made it very challenging to fit the data. Furthermore, the unknown crystallographic direction of the applied field made it difficult to obtain a reasonable fit for the NSF channels. The preliminary results show equal probability for the presence of compensated and uncompensated NiO(111) spins at the interface. Therefore, a more complicated model which takes into consideration all the 16 runs was proposed to refine the PNR fits further.

Additional PNR measurements will be carried out at the OFFSPEC beamline at ISIS to investigate the in-plane distribution at the polar interface and provide a quantitative understanding of the NiO(111)/EuO interface. Also, an optical system with linearly polarised light will be set up to observe the NiO(111) *S*-domains and to obtain a better insight into the arrangements of the domains.

Another heterostructure, graphene/metal interfaces, were explored in this thesis. Graphene is another potential material for technological applications due to its unique properties. However, it is very challenging to manipulate spin directly in a monolayer of graphene due to its negligible spin-orbit coupling. However, this challenge can be overcome by the proximity effect which uses the exchange interaction of local moments between graphene and a ferromagnetic material. Therefore, experimental work measuring the induced magnetic moment in graphene in the vicinity of a ferromagnetic layer was carried out. The growth of epitaxial and rotated domain graphene structure on Co(111) and Ni(111) films was confirmed by LEED diffraction and SEM scans, respectively. The high-quality of the grown graphene was proved by examining the position and width of the characteristic graphene peaks in the Raman spectroscopy (G and $2D$).

The fits of the PNR measurements showed that the ferromagnetic films Co(111) and Ni(111) induced a magnetic moment of $\sim$0.57 μ_B in the graphene layer which is $\sim 5\times$ higher than the value predicted by Weser *et al.* [11]. His assumption was based on a reported study of C/Fe multilayer and carbon nanotubes grown on a Co film where the magnetic moments in these structures are averaged over many layers of carbon. Therefore, the comparison of the magnetic moment induced in a monolayer of graphene with other carbon allotropes of thicknesses equivalent to many layers of graphene leads to an inaccurate estimation of the magnetic moment. Further PNR measurements on graphene grown on a non-magnetic Ni_9Mo_1 substrate confirmed that the origin of the induced magnetic moment is a result of the opening of the graphene's Dirac cones due to the strong C_p-$3d$ hybridisation. The fitted PNR models were then validated with Bayesian uncertainty analysis. XMCD measurements performed on the samples proved that the additional magnetic moment detected by the PNR arises from a top graphene layer and that it is not caused by carbon alloy formed at the interface as a result of carbon diffusion into the metal layer.

Other measurements were suggested to improve the reported graphene/metal experiments. For instance, a stronger FM layer such as EuO can be used instead of Ni and Co films. Also, a multilayer system of [graphene/TM(>100 nm)]$_x$ terminated with a TM layer can be used instead of the bilayer system to reduce the contrast in the neutron SLD profile, especially between the air and graphene. A thicker metal film is suggested to provide a wider separation between the graphene layer which would give a better estimation of the graphene's magnetic moment. PNR measurements up to high Q ranges such as 2.55 Å^{-1} to accurately estimate the induced magnetic moment in graphene. This is because a full reflectivity fringe will take place at $Q = \dfrac{2\pi}{z}$, where z is the thickness of graphene (2.46 Å) [53].

References

[1] S. A. Wolf, D. D. Awschalom, R. A. Buhrman, J. M. Daughton, S. von Molnar, M. L. Roukes, A. Y. Chtchelkanova, and D. M. Treger. Spintronics: A Spin-Based Electronics Vision for the Future. *Science*, 294(5546):1488–1495, 2001.

[2] A. Fert. Origin, Development, and Future of Spintronics (Nobel Lecture). *Angewandte Chemie International Edition*, 47(32):5956–5967, 2008.

[3] A. Fert. Nobel Lecture: Origin, development, and future of spintronics. *Reviews of Modern Physics*, 80:1517, 2008.

[4] N. J. Steinke. *Structure and Magnetic Properties of Anisotropic Ferromagnetic Thin-film Heterostructures*. PhD thesis, University of Cambridge, 2011.

[5] I. Zutic, J. Fabian, and S. D. Sarma. Spintronics: Fundamentals and applications. *Reviews of Modern Physics*, 76(2):323–410, may 2004.

[6] M. Bibes and A. Barthélémy. Oxide spintronics. *IEEE Transactions on Electron Devices*, 54(5):1003–1023, 2007.

[7] F. Pulizzi. Oxidized spintronics. *Nature Materials*, 11(7):564–564, 2012.

[8] J. Mannhart. The Interface Is Still the Device. *Nature Materials*, 11:91, 2012.

[9] J. Lee, N. Sai, and A. A. Demkov. Spin-polarized Two-dimensional Electron Gas Through Electrostatic Doping in LaAlO3/EuO Heterostructures. *Physical Review B*, 82(23):235305, dec 2010.

[10] Y. Wang, M. K. Niranjan, J. D. Burton, J. M. An, K. D. Belashchenko, and E. Y. Tsymbal. Prediction Of a Spin-polarized Two-dimensional Electron Gas at the LaAlO3/EuO(001) Interface. *Physical Review B*, 79(21):212408, 2009.

[11] M. Weser, Y. Rehder, K. Horn, M. Sicot, M. Fonin, A. B. Preobrajenski, E. N. Voloshina, E. Goering, and Y. S. Dedkov. Induced Magnetism Of Carbon Atoms at the Graphene/Ni(111) Interface. *Applied Physics Letters*, 96(1):012504, 2010.

[12] https://www.tfm.phy.cam.ac.uk/facilities.

[13] J. G. Han. Magnetron Sputtering Technology. *www.micromagnetics.com*.

[14] S. Swann. Magnetron Sputtering. *Physics in Technology*, 19(2):67–75, 1988.

[15] G. Biasiol and L. Sorba. Molecular Beam Epitaxy: Principles and Applications. *Energy Production and Energy-Saving Applications*, pages 66–83, 2001.

[16] J. R. Creighton and P. Ho. Introduction to Chemical Vapour Deposition. In *Chemical Vapor Deposition*, pages 1–28. 2010.

[17] P. Schönherr. *Growth and Characterisation Of Quantum Materials Nanostructures*. PhD thesis, University of Oxford, 2016.

[18] R. Carpenter. *Exchange Bias in Nanostructures*. PhD thesis, University of York, 2015.

[19] J. Alexander and T. Barker. *Muon Studies of Unconventional Superconductors*. PhD thesis, University of Warwick, 2016.

[20] V. Holý, U. Pietsch, and T. Baumbach. *High-Resolution X-Ray Scattering From Thin Films and Multilayers*, volume 149 of *Springer Tracts in Modern Physics*. Springer Berlin Heidelberg, Berlin, Heidelberg, 1999.

[21] J. Als-Nielsen and D. McMorrow. *Elements of Modern X-ray Physics*. Wiley, 2011.

[22] D. K. Bowen and B. K. Tanner. *High Resolution X-Ray Diffractometry and Topography*. CRC Press, 2005.

[23] P. M. S. Monteiro. *A Close Study of a Ferromagnetic Semiconductor: Doping Effects in EuO Thin Films*. PhD thesis, University of Cambridge, 2015.

[24] M. Tokac. *Investigation of Interfacial Effects in Ferromagnetic Thin-Films*. PhD thesis, Durham University, 2016.

[25] F. Moreno-Herrero and J. Gomez-Herrero. AFM: Basic Concepts. In *Atomic Force Microscopy in Liquid*, pages 1–34. Wiley-VCH Verlag GmbH & Co. KGaA, Weinheim, Germany, 2012.

[26] P. Eaton and P. West. *Atomic Force Microscopy*. Oxford University Press, 2010.

[27] E. Meyer. Atomic Force Microscopy. *Progress in Surface Science*, 41(1):3–49, 1992.

[28] S. Morita, R. Wiesendanger, and E. Meyer. *Noncontact Atomic Force Microscopy*. Number v. 1 in Advanced Texts in Physics. Springer Berlin Heidelberg, 2002.

[29] A. Mukhopadhyay. Measurement of Magnetic Hysteresis Loops in Continuous and Patterned Ferromagnetic Nanostructures by Static Magneto-optical Kerr Effect Magnetometer. Technical Report August, Indian Institute of Technology, Guwahati, 2015.

[30] W. Zhou, R. P. Apkarian, and Z. L. Wang. Fundamentals of Scanning Electron Microscopy. In *Scanning Microscopy for Nanotechnology*, pages 1–40. 2007.

[31] B. Hafner. Scanning Electron Microscopy Primer. Technical report, 2007.

[32] E. Kim, E. Iroaga, and B. Murmann. Brief Introduction to Scanning Electron Microscopy (SEM). Technical Report i, 2004.

[33] Australian Microscopy & Microanalysis Research Facility. Scanning Electron Microscope Training module, 2014.

[34] B. Cheney. Introduction to Scanning Electron Microscopy. *San Jose State University*.

[35] JEOL. Scanning Electron Microscope A To Z. Technical report, 2006.

[36] L. Jacob. An Introduction to Electron Microscopy. *FEI*, page 58.

[37] S. J. B. Reed. Scanning Electron Microscopy. In *Electron Microprobe Analysis and Scanning Electron Microscopy in Geology*, pages 41–75. Cambridge University Press, Cambridge, 2005.

[38] O. C. Wells. *Scanning Electron Microscopy*. Mcgraw-Hill, New York ; London, 1974.

[39] Y. Y. Wang, Z. H. Ni, Z. X. Shen, H. M. Wang, and Y. H. Wu. Interference Enhancement of Raman Signal of Graphene. *Applied Physics Letters*, 92(4), 2008.

[40] I. Chilres, L. A. Jauregui, W. Park, H. Cao, and Y. P. Chen. Raman Spectroscopy of Viruses and Viral Proteins. In J. I Jang, editor, *New Developments in Photon and Materials Research*, chapter 19, pages 553–595. Nova Science Publishers, Incorporated, 2013.

[41] A. Dahal and M. Batzill. Graphene–nickel interfaces: a review. *Nanoscale*, 6(5):2548, 2014.

[42] A. C. Ferrari and D. M. Basko. Raman Spectroscopy as a Versatile Tool for Studying the Properties of Graphene. *Nature Nanotechnology*, 8(4):235–246, 2013.

[43] G. S. Bumbrah and R. M. Sharma. Raman spectroscopy – Basic Principle, Instrumentation and Selected Applications for the Characterization of Drugs of Abuse. *Egyptian Journal of Forensic Sciences*, 6(3):209–215, 2016.

[44] Princeton Instruments. Raman Spectroscopy Basics. Technical report, 2012.

[45] Thermo Electron Corporation. Introduction to Raman Spectroscopy. Technical report, 2003.

[46] G. Held. Low-Energy Electron Diffraction Crystallography of Surfaces and Interfaces, 2010.

[47] P. Laukkanen, J. Sadowski, and M. Guina. Surface Studies by Low-Energy Electron Diffraction and Reflection High-Energy-Electron Diffraction. In *Semiconductor Research*, volume 182, chapter 1, pages 1–21. Springer, Berlin, Heidelberg, 2012.

[48] Vallance Group University of Oxford. Low Energy Electron Diffraction (LEED).

[49] J. Henk. Theory of Low-energy Electron Diffraction and Photoelectron Spectroscopy from Ultra-thin Films. In *Handbook of Thin Films Materials (vol. 2)*, pages 479–526. 2001.

[50] http://www.chem.qmul.ac.uk/surfaces/scc/scat6_2.html.

[51] J. M. D. Coey. Experimental methods. In *Magnetism and Magnetic Materials*, number 1, pages 333–373. Cambridge University Press, Cambridge, 2010.

[52] H. Weinstock. *SQUID Sensors: Fundamentals, Fabrication and Applications*. Springer Netherlands, Dordrecht, 1996.

[53] D. M. Love. *Functional Design of Magnetic Nanostructures: A Study of Patterened Elements, Thin Films Interfaces & Self-Assembled Systems*. PhD thesis, University of Cambridge, 2015.

[54] J. Clarke and A. I. Braginski. *The SQUID Handbook*, volume 1. 2005.

[55] O. Mathon, F. Baudelet, J. P. Itié, S. Pasternak, A. Pollan, and S. Pascarelli. XMCD Under Pressure at the Fe K Edge on the Energy-dispersive Beamline of the ESRF. *Journal of Synchrotron Radiation*, 11(5):423–427, 2004.

[56] A. Scherz. *Spin-dependent X-ray Absorption Spectroscopy of 3d Transition Metals : Systematics and Applications*. PhD thesis, University of Berlin, 2003.

[57] J. Chaboy, L. M. Garcia, F. Bartolomé, H. Maruyama, S. Uemura, N. Kawamura, and A. S. Markosayan. Fe K-edge X-ray Magnetic Circular Dichroism Study in R6Fe23 (R=Ho and Y) Compounds Near Compensation Temperature. *Journal of Applied Physics*, 88:336–338, 2000.

[58] D. Rioux, B. Allen, H. Höchst, D. Zhao, and D. L. Huber. Birefringence-induced Interference Effects in Thin-film Magnetic-circular-dichroism Spectra. *Physical Review B*, 56(2):753–758, 1997.

[59] Z. Sun, Y. Zhan, S. Shi, and M. Fahlman. Energy level Alignment and Interactive Spin Polarization at Organic/Ferromagnetic Metal Interfaces for Organic Spintronics. *Organic Electronics: physics, materials, applications*, 15(9):1951–1957, 2014.

[60] W. L. O'Brien, B. P. Tonner, G. R. Harp, and S. S. P. Parkin. Experimental Investigation of Dichroism Sum Rules for V, Cr, Mn, Fe, Co, and Ni: Influence of Diffuse Magnetism. *Journal of Applied Physics*, 76(10):6462–6464, 1994.

[61] J. Stöhr, H. A. Padmore, S. Anders, T. Stammler, and M. R. Scheinfein. Principles of X-Ray Magnetic Dichroism Spectromicroscopy. *Surface Review and Letters*, 05(06):1297–1308, 1998.

[62] Z. Y. Guo, C. H. Hong, H. Y. Xing, K. Tang, L. Zheng, W. Xui, D. L. Chen, M. Q. Cui, and Y. D. Zhao. A New Soft X-ray Magnetic Circular Dichroism Facility at the BSRF Beamline 4B7B. *Chinese Physics C*, 39(4):048003, 2015.

[63] Y. U. Idzerda, C. T. Chen, H. J. Lin, H. Tjeng, and G. Meigs. Application of Magnetic Circular Dichroism to Magnetic Thin-films. *Physics B*, 208-209(1-4):746–750, 1995.

[64] R. Wu and A. J. Freeman. Limitation of the Magnetic-circular-dichroism Spin Sum Rule for Transition Metals and Importance of the Magnetic Dipole Term. *Physical Review Letters*, 73(14):1994–1997, 1994.

[65] J. Stöhr. X-ray Magnetic Circular Dichroism Spectroscopy of Transition Metal Thin films. *Journal of Electron Spectroscopy and Related Phenomena*, 75(C):253–272, 1995.

[66] J. Lee, G. Lauhoff, C. Fermon, S. Hope, J. A. C. Bland, J. P. Schille, G. VanderLaan, C. Chappert, and P. Beauvillain. A Direct Test of x-ray Magnetic Circular Dichroism Sum Rules for Strained Ni Films using Polarized Neutron Reflection. *Journal of Physics-Condensed Matter*, 1997.

[67] J. Stöhr. Exploring the Microscopic Origin of Magnetic Anisotropies with X-ray Magnetic Circular Dichroism (XMCD) Spectroscopy. *Journal of Magnetism and Magnetic Materials*, 200(1-3):470–497, 1999.

[68] S. Pizzini. X-ray Magnetic Circular Dichroism (XMCD): Basic Concepts and Theory for Rare Earths and 3d Metals. Technical report, Magnetism of Nanostructured Systems and Hybrid Structures, Brasov, 2003.

[69] H. Ebert. Magneto-optical Effects in Transition Metal Systems. *Reports on Progress in Physics*, 59(12):1665, 1996.

[70] P. R. Stone, M. A. Scarpulla, R. Farshchi, I. D. Sharp, J. W. Beeman, K. M. Yu, E. Arenholz, J. Denlinger, E. E. Haller, and O. D. Dubon. Mn L3,2 X-ray absorption spectroscopy and magnetic circular dichroism in ferromagnetic Ga1-xMnxP. *AIP Conference Proceedings*, 893:1177–1178, 2007.

[71] K. Amemiya, T. Yokoyama, Y. Yonamoto, D. Matsumura, and T. Ohta. O K-edge X-ray Magnetic Circular Dichroism of Atomic O Adsorbed on an Ultrathin Co/Cu(100) Film: Comparison with Molecular CO on Co/Cu(100). *Physical Review B*, 64(13):132405, 2001.

[72] T. Funk, A. Deb, S. J. George, H. Wang, and S. P. Cramer. X-ray Magnetic Circular Dichroism—A High Energy Probe of Magnetic Properties. *Coordination Chemistry Reviews*, 249(1-2):3–30, 2005.

[73] https://www.psi.ch/sls/sim/sim.

[74] M. Altarelli. Sum Rules for X-ray Magnetic Circular Dichroism. *Il Nuovo Cimento D*, 20(7-8):1067–1073, 1998.

[75] D. J. Huang, H. T. Jeng, C. F. Chang, G. Y. Guo, J. Chen, W. P. Wu, S. C. Chung, S. G. Shyu, C. C. Wu, H. J. Lin, and C. T. Chen. Orbital Magnetic Moments of Oxygen and Chromium in CrO2. *Physical Review B*, 66(17):174440, 2002.

[76] R. Nakajima, J. Stöhr, and Y. U. Idzerda. Electron-yield Saturation Effects in L-edge X-ray Magnetic Circular Dichroism Spectra of Fe, Co, and Ni. *Physical Review B*, 59(9):6421–6429, 1999.

[77] C. T. Chen, Y. U. Idzerda, H.-J. Lin, N. V. Smith, G. Meigs, E. Chaban, G. H. Ho, E. Pellegrin, and F. Sette. Experimental Confirmation of the X-ray Magnetic Circular Dichroism Sum Rules for Iron and Cobalt. *Physical Review Letters*, 75(1):152–155, 1995.

[78] V. Corradini, F. Moro, R. Biagi, U. del Pennino, V. De Renzi, S. Carretta, P. Santini, M. Affronte, J. C. Cezar, G. Timco, and R. E. P. Winpenny. X-ray magnetic circular dichroism investigation of spin and orbital moments in Cr8 and Cr7Ni antiferromagnetic rings. *Physical Review B*, 77(1):014402, 2008.

[79] A. Thompson, D. Attwood, E. Gullikson, M. Howells, K. Je Kim, J. Kirz, J. Kortright, I. Lindau, Y. Liu, P. Pianetta, A. Robinson, J. Scofield, G. Williams, and H. Winick. *X-ray data booklet*, volume 8. 2009.

[80] H. Hashizume, K. Ishiji, J. C. Lang, D. Haskel, G. Srajer, J. Minár, and H. Ebert. Observation of X-ray Magnetic Circular Dichroism at the Ru K Edge in Co-Ru Alloys. *Physical Review B - Condensed Matter and Materials Physics*, 73(22):1–5, 2006.

[81] C. Sorg. *Magnetic Properties of 3 d and 4 f Ferromagnets Studied by X-ray Absorption Spectroscopy*. PhD thesis, Freie Universität Berlin, 2005.

[82] J. Schwitalla and H. Ebert. Electron Core-Hole Interaction in the X-ray Absorption Spectroscopy of 3d Transition Metals. *Physical Review Letters*, 80(20):4586–4589, 1998.

[83] H. Ebert. Magneto-optical Effects in Transition Metal Systems. *Reports on Progress in Physics*, 59:1665–1735, 1996.

[84] J. Daillant and A. Gibaud. *X-ray and Neutron Reflectivity*. 2009.

[85] T. Chatterji. *Neutron Scattering from Magnetic Materials*. Elsevier Science, 2005.

[86] International Atomic Energy Agency. Neutron Reflectometry: A Probe for Materials Surfaces. Proceedings of a Technical Meeting. page 208, Vienna, 2006. IAEA.

[87] F. H. Allen, O. Kennard, D. G. Watson, L. Brammer, A. G. Orpen, and R. Taylor. *Tables of Bond Lengths Determined by X-ray and Neutron Diffraction. Part 1. Bond Lengths in Organic Compounds*. Number 12. 1987.

[88] H. Fritzsche, Z. Yamani, R. Cowley, and R.C.C. Ward. Polarised Neutron Reflectometry As a Unique Tool in Magnetisation Reversal Studies of Thin Films and Multilayers. *Physics in Canada*, 62(5):265–271, 2006.

[89] H. Zabel. Neutron Reflectivity of Spintronic Materials. *Materials Today*, 9(1-2):42–49, 2006.

[90] V. O. De Haan and A. A. Van Well. Comparison Between a Time-of-flight and a Monochromatic Neutron Reflectometer at a Continuous Neutron Source. *Journal of Neutron Research*, 3(2):63–68, 1996.

[91] http://www.isis.stfc.ac.uk/about-isis/how-isis-works—in-depth4371.html.

[92] http://www.isis.stfc.ac.uk/instruments/polref/technical/polref-technical-information7280.html.

[93] University of London School of Crystallography, Birkbeck College. Advanced Certificate in Powder Diffraction on the Web.

[94] https://www.ill.eu/instruments-support/instruments-groups/instruments/d17/characteristics/.

[95] R. Cubitt and G. Fragneto. D17: The New Reflectometer at The ILL. *Applied Physics A: Materials Science & Processing*, 74:s329–s331, 2002.

[96] O. Arnold, J. C. Bilheux, J. M. Borreguero, A. Buts, S. I. Campbell, L. Chapon, M. Doucet, N. Draper, R. Ferraz Leal, M. A. Gigg, V. E. Lynch, A. Markvardsen, D. J. Mikkelson, R. L. Mikkelson, R. Miller, K. Palmen, P. Parker, G. Passos, T. G. Perring, P. F. Peterson, S. Ren, M. A. Reuter, A. T. Savici, J. W. Taylor, R. J. Taylor, R. Tolchenov, W. Zhou, and J. Zikovsky. Mantid - Data Analysis and Visualization Package for Neutron Scattering and μSR Experiments. *Nuclear Instruments and Methods in Physics Research A*, 764:156–166, 2014.

[97] the Large Array Manipulation Program LAMP. http://www.ill.eu/data_treat/lamp/the-lamp-book/.

[98] D. Richard, M. Ferrand, and G. J. Kearley. Analysis and Visualisation of Neutron-scattering Data. *Journal of Neutron Research*, 4(1):33–39, 1996.

[99] Mantid (2013): Manipulation Project. and Analysis Toolkit for Instrument Data.; Mantid. http://dx.doi.org/10.5286/SOFTWARE/MANTID.

[100] M. Björck and G. Andersson. GenX: An Extensible X-ray Reflectivity Refinement Program Utilizing Differential Evolution. *Journal of Applied Crystallography*, 40(6):1174–1178, 2007.

[101] Https://uk.mathworks.com/discovery/genetic-algorithm.html. Matlab-Genetic Algorithm.

[102] https://www.ncnr.nist.gov/resources/n-lengths/list.html.

[103] D. Sivia and J. Skilling. *Data Analysis: A Bayesian Tutorial*. Oxford science publications. Oxford University Press, illustrate edition, 2006.

[104] R. Van de Schoot, D. Kaplan, J. Denissen, J. B. Asendorpf, F. J. Neyer, and M. A.G. van Aken. A Gentle Introduction to Bayesian Analysis: Applications to Developmental Research. *Child Development*, 85:842–860, 2014.

[105] J. VanderPlas. Frequentism and Bayesianism: A Python-driven Primer. In *Proceedings of the 13th Python in Science Conference*, pages 91–99, 2014.

[106] A. B. Downey. *Think Bayes: Bayesian Statistics Made Simple*. O'Reilly Media, 2013.

[107] T. Eguchi. An Introduction to Bayesian Statistics Without Using Equations.

[108] P. A. Kienzle, J. Krycka, N. Patel, and I. Sahin. Refl1D, 2016.

[109] S. J. Blundell. Spin-polarized Muons in Condensed Matter Physics. *Contemporary Physics*, 40(3):175–192, 1999.

[110] S. Cox. Introduction to muSR: What, How, Where? In *Summer School on Muon Spin Rotation/Relaxation/Resonance*, page 16, 1994.

[111] A. Yaouanc and P. Réotier. A Short Survey of μSR Research. In *Muon Spin Rotation, Relaxation and Resonance Applications to Condensed Matter*, number 1956, page 486. OUP Oxford, illustrate edition, 2011.

[112] D. Andreica. Muon Spin Rotation. *Babeş-Bolyai University*, page 10, 2005.

[113] J. E. Sonier. Muon Spin Rotation Studies of Electronic Excitations and Magnetism in The Vortex Cores of Superconductors. *Reports on Progress in Physics*, 70(11):1717–1755, 2007.

[114] A. J. Steele. *Quantum Magnetism Probed with Muon-Spin Relaxation*. PhD thesis, University of Oxford, 2011.

[115] L. Nuccio, L. Schulz, and A. J. Drew. Muon Spin Spectroscopy: Magnetism, Soft Matter and The Bridge Between The Two. *Journal of Physics D: Applied Physics*, 47(47):473001, 2014.

[116] F. Bert. Local Probes of Magnetism, NMR and μSR: A Short Introduction. *École thématique de la Société Française de la Neutronique*, 13:03001, 2014.

[117] K. Nagamine. Muon Spin Rotation/Relaxation/Resonance: Basic Principles. In *Introductory Muon Science*, pages 100–125. Cambridge University Press, Cambridge, 2011.

[118] J. E. Sonier. Muon Spin Rotation/Relaxation/Resonane (μSR). Technical report, Simon Fraser University, 2002.

[119] A. Berlie. *A Study of Magnetic Materials Based Upon the Organic Acceptor 7,7,8,8-Tetracyanoquinodimethane*. PhD thesis, Durham University, 2013.

[120] E. Morenzoni, H. Glückler, T. Prokscha, R. Khasanov, H. Luetkens, M. Birke, E. M. Forgan, C. Niedermayer, and M. Pleines. Implantation Studies of keV Positive Muons in Thin Metallic Layers. *Nuclear Instruments and Methods in Physics Research Section B: Beam Interactions with Materials and Atoms*, 192(3):254–266, 2002.

[121] P. Dalmas De Réotier and A. Yaouanc. Muon Spin Rotation and Relaxation in Magnetic Materials. *Journal of Physics Condensed Matter*, 9(43):9113–9166, 1997.

[122] Low-Energy Muons: Overview of the Experimental Setup. Https://www.psi.ch/low-energy-muons/experimental-setup.

[123] https://www.psi.ch/low-energy-muons/lem-low-energy-muons-group.

[124] F. L. Pratt. WIMDA: A Muon Data Analysis Program for The Windows PC. *Physica B: Condensed Matter*, 289-290:710–714, 2000.

[125] M. S. Dresselhaus. Two Dimensional Electron Gas, Quantum Wells & Semiconductor Superlattices. In *Solid State Properties From Bulk to Nano*, chapter 9, page 521. Springer, Berlin, Heidelberg, 2018.

[126] A. Savoia, D. Paparo, P. Perna, Z. Ristic, M. Salluzzo, F. M. Granozio, U. Scotti di Uccio, C. Richter, S. Thiel, J. Mannhart, and L. Marrucci. Polar Catastrophe and Electronic Reconstructions at The LaAlO3 / SrTiO3 Interface: Evidence from Optical Second Harmonic Generation. *Physical Review B - Condensed Matter and Materials Physics*, 80(7):2–7, 2009.

[127] S. W. Lee. Two-Dimensional Electron Gas at SrTiO 3 -Based Oxide Heterostructures via Atomic Layer Deposition. *Journal of Nanomaterials*, 2016:1–9, 2016.

[128] J. F. Gregg. Spintronics: A Growing Science. *Nature Materials*, 6(11):798–799, 2007.

[129] A. Schmehl, V. Vaithyanathan, A. Herrnberger, S. Thiel, C. Richter, M. Liberati, T. Heeg, M. Röckerath, L. F. Kourkoutis, S. Mühlbauer, P. Böni, D. A. Muller, Y. Barash, J. Schubert, Y. Idzerda, J. Mannhart, and D. G. Schlom. Epitaxial Integration Of The Highly Spin-polarized Ferromagnetic Semiconductor EuO with Silicon and GaN. *Nature Materials*, 6(11):882–887, 2007.

[130] P. M. S. Monteiro, P. J. Baker, A. Ionescu, C. H. W. Barnes, Z. Salman, A. Suter, T. Prokscha, and S. Langridge. Spatially Homogeneous Ferromagnetism Below The Enhanced Curie Temperature in EuO1-x Thin Films. *Physical Review Letters*, 110(21):1–5, 2013.

[131] S. J. Blundell, T. Lancaster, F. L. Pratt, P. J. Baker, W. Hayes, J. P. Ansermet, and A. Comment. Phase Transition in The localized Ferromagnet EuO Probed by uSR. *Physical Review B - Condensed Matter and Materials Physics*, 81(9):1–4, 2010.

[132] T. S. Santos, J. S. Moodera, K. V. Raman, E. Negusse, J. Holroyd, J. Dvorak, M. Liberati, Y. U. Idzerda, and E. Arenholz. Determining Exchange Splitting in a Magnetic Semiconductor by Spin-filter Tunneling. *Physical Review Letters*, 101(14):1–4, 2008.

[133] T. Santos. *Europium Oxide as a Perfect Electron Spin Filter*. PhD thesis, Massachusetts Institute of Technology, 2007.

[134] T. Stollenwerk. *Ferromagnetic Semiconductor-Metal Transition in Heterostructures of Electron Doped Europium Monoxide*. PhD thesis, University of Bonn, 2013.

[135] J. M. An and K. D. Belashchenko. Electronic Structure and Magnetic Properties of Gd-doped and Eu-rich EuO. *Physical Review B - Condensed Matter and Materials Physics*, 88(5):1–14, 2013.

[136] A. Mauger and C. Godart. The Magnetic, Optical, and Transport Properties of Representatives of a Class of Magnetic Semiconductors: The Europium Chalcogenides. *Physics Reports*, 141(2-3):51–176, 1986.

[137] L. Passell, O. W. Dietrich, and J. Als-Nielsen. Neutron Scattering from The Heisenberg Ferromagnets EuO and EuS. I. The Exchange Interactions. *Physical Review B*, 14(11), 1976.

[138] P. Liu, J. A C. Santana, Q. Dai, X. Wang, P. A. Dowben, and J. Tang. Sign of the Superexchange Coupling Between Next-nearest Neighbors in EuO. *Physical Review B - Condensed Matter and Materials Physics*, 86(22):1–6, 2012.

[139] M. Barbagallo, T. Stollenwerk, J. Kroha, N. J. Steinke, N. D. M. Hine, J. F. K. Cooper, C. H. W. Barnes, A. Ionescu, P. M. D. S. Monteiro, J. Y. Kim, K. R. A. Ziebeck, C. J. Kinane, R. M. Dalgliesh, T. R. Charlton, and S. Langridge. Thickness-dependent Magnetic Properties of Oxygen-deficient EuO. *Physical Review B - Condensed Matter and Materials Physics*, 84(7):1–5, 2011.

[140] S. Kimura, T. Ito, H. Miyazaki, T. Mizuno, T. Iizuka, and T. Takahashi. Electronic Inhomogeneity EuO: Possibility of Magnetic Polaron States. *Physical Review B*, 78(5):052409, 2008.

[141] M. M. Abd-Elmeguid and R. D. Taylor. Onset of Valence and Magnetic Instabilities in the Ferromagnetic Semiconductor EuO at High Pressures. *Physical Review B*, 42(1):1048–1051, 1990.

[142] P. G. Steeneken, L. H. Tjeng, I. Elfimov, G. A. Sawatzky, G. Ghiringhelli, N. B. Brookes, and D. J. Huang. Exchange Splitting and Charge Carrier Spin Polarization In Euo. *Physical review letters*, 88:047201, 2002.

[143] M. A. Carpenter, S. V. Sinogeikin, J. D. Bass, D. L. Lakshtanov, and S. D. Jacobsen. Elastic Relaxations Associated with the Pm3m-R3c Transition in LaAlO3: l. Single crystal Elastic Moduli at Room Temperature. *Journal of Physics: Condensed Matter*, 22(3):035403, 2010.

[144] J. Yao, P. B. Merrill, S. S. Perry, D. Marton, and J. W. Rabalais. Thermal Stimulation of the Surface Termination of LaAlO3(100). *The Journal of Chemical Physics*, 108(January):1645–1652, 1998.

[145] T. Q. Ngo, A. Posadas, M. D. McDaniel, D. A. Ferrer, J. Bruley, C. Breslin, A. A. Demkov, and J. G. Ekerdt. Epitaxial Growth of LaAlO3 on SrTiO3-buffered Si (001) Substrates by Atomic Layer Deposition. *Journal of Crystal Growth*, 363:150–157, 2013.

[146] M. Salluzzo. Electronic Reconstruction at the Interface Between Band Insulating Oxides: The LaAlO3/SrTiO3 System. In *Oxide Thin Films, Multilayers, and Nanocomposites*, pages 181–211. Springer International Publishing, 2015.

[147] J. Q. Chen, X. Wang, Y. H. Lu, A. R. Barman, G. J. You, G. C. Xing, T. C. Sum, S. Dhar, Y. P. Feng, Ariando, Q. H. Xu, and T. Venkatesan. Defect Dynamics and Spectral Observation of Twinning in Single Crystalline LaAlO3 under Subbandgap Excitation. *Applied Physics Letters*, 98(4):1–4, 2011.

[148] H. Lehnert, H. Boysen, P. Dreier, and Y. Yu. Room Temperature Structure of LaAlO3. *Z. Kristallogr*, 215:145–147, 2000.

[149] M. R. Levy. *Chapter 3: Perovskite Perfect Lattice*. PhD thesis, Imperial College London, 2005.

[150] J. L. Blok. *Experimental Design of Oxide Materials*. PhD thesis, University of Twente, 2015.

[151] K. Krishnaswamy, C. E. Dreyer, A. Janotti, and C. G. Van de Walle. First-principles Study of Surface Charging in LaAlO3/SrTiO3 Heterostructures. *Physical Review B - Condensed Matter and Materials Physics*, 92(8):1–15, 2015.

[152] K. Krishnaswamy, C. E. Dreyer, A. Janotti, and C. G. Van De Walle. Structure and Energetics of LaAlO3 (001) Surfaces. *Physical Review B - Condensed Matter and Materials Physics*, 90(23):1–6, 2014.

[153] Z. Huang, X. R. Wang, Z. Q. Liu, W. M. Lu, S. W. Zeng, A. Annadi, W. L. Tan, X. P. Qiu, Y. L. Zhao, M. Salluzzo, J. M. D. Coey, T. Venkatesan, and Ariando. Conducting Channel at the LaAlO3/SrTiO3 Interface. *Physical Review B - Condensed Matter and Materials Physics*, 88(16):1–5, 2013.

[154] M. L. Reinle-Schmitt, C. Cancellieri, D. Li, D. Fontaine, M. Medarde, E. Pomjakushina, C. W. Schneider, S. Gariglio, P. Ghosez, J. M. Triscone, and P. R. Willmott. Tunable Conductivity Threshold at Polar Oxide Interfaces. *Nature Communications*, 3(May):932, 2012.

[155] A. Janotti, L. Bjaalie, L. Gordon, and C. G. Van de Walle. Controlling the Density of the Two-dimensional Electron Gas at the SrTiO3/LaAlO3 Interface. *Physical Review B - Condensed Matter and Materials Physics*, 86(24), 2012.

[156] Z. Q. Liu, C. J. Li, W. M. Lü, X. H. Huang, Z. Huang, S. W. Zeng, X. P. Qiu, L. S. Huang, A. Annadi, J. S. Chen, J. M. D. Coey, T. Venkatesan, and Ariando. Origin of the Two-Dimensional Electron Gas at LaAlO3/SrTiO3 Interfaces: The Role of Oxygen Vacancies and Electronic Reconstruction. *Physical Review X*, 3(2):1–9, 2013.

[157] G. Herranz, M. Basletić, M. Bibes, C. Carrétéro, E. Tafra, E. Jacquet, K. Bouzehouane, C. Deranlot, A. Hamzić, J. M. Broto, A. Barthélémy, and A. Fert. High Mobility in LaAlO3/SrTiO3 Heterostructures: Origin, Dimensionality, and Perspectives. *Physical Review Letters*, 98(21):3–6, 2007.

[158] A. Kalabukhov, R. Gunnarsson, J. Börjesson, E. Olsson, T. Claeson, and D. Winkler. Effect of Oxygen Vacancies in the SrTiO3 Substrate on the Electrical Properties of the LaAlO3 SrTiO3 Interface. *Physical Review B - Condensed Matter and Materials Physics*, 75(12):2–5, 2007.

[159] K. Janicka. *Two Dimensional Electron Gas at Oxide Interfaces*. PhD thesis, University of Nebraska - Lincoln, 2011.

[160] W. Siemons, G. Koster, H. Yamamoto, W. A. Harrison, G. Lucovsky, T. H. Geballe, D. H.A. Blank, and M. R. Beasley. Origin of Charge Density at LaAlO3 on SrTiO3 Heterointerfaces: Possibility of Intrinsic Doping. *Physical Review Letters*, 98(19):3–6, 2007.

[161] S. Thiel. Tunable Quasi-Two-Dimensional Electron Gases in Oxide Heterostructures. *Science*, 313(5795):1942–1945, 2006.

[162] J. E. Kleibeuker, G. Koster, W. Siemons, D. Dubbink, B. Kuiper, J. L. Blok, C. Yang, J. Ravichandran, R. Ramesh, J. E. ten Elshof, D. H. A. Blank, and G. Rijnders. Atomically Defined Rare-earth Scandate Crystal Surfaces. *Advanced Functional Materials*, 20(20):3490–3496, 2010.

[163] X. Wan. *Growth and Characterization of CaTiO3 Thin Films with (111) Orientation*. PhD thesis, University of Twente, 2008.

[164] A. Biswas, C. Yang, R. Ramesh, and Y. H. Jeong. Atomically Flat Single Terminated Oxide Substrate Surfaces. *Progress in Surface Science*, 92(2):117–141, 2017.

[165] R. Gunnarsson, A. S. Kalabukhov, and D. Winkler. Evaluation of Recipes for Obtaining Single Terminated Perovskite Oxide Substrates. *Surface Science*, 603(1):151–157, 2009.

[166] T. Ohnishi, K. Takahashi, M. Nakamura, M. Kawasaki, M. Yoshimoto, and H. Koinuma. A-site Layer Terminated Perovskite Substrate: NdGaO3. *Applied Physics Letters*, 74(17):2531–2533, 1999.

[167] Z. L. Wang and A. J. Shapiro. Studies of LaAlO3(100) Surfaces Using RHEED and REM. II: 5 × 5 Surface Reconstruction. *Surface Science*, 328(1-2):159–169, 1995.

[168] Z. Q. Liu, Z. Huang, W. M. Lu, K. Gopinadhan, X. Wang, A. Annadi, T. Venkatesan, and Ariando. Atomically Flat Interface Between a Single-terminated LaAlO3 Substrate and SrTiO3 Thin Film is Insulating. *AIP Advances*, 2(1):0–5, 2012.

[169] C. Caspers. *Magnetic Oxide Heterostructures : EuO on Cubic Oxides and on Silicon*. PhD thesis, University of Duisburg-Essen, 2013.

[170] R. A. Marshall. *Critical Behaviour and Quantum Properties in (Ga, Mn) As*. PhD thesis, The University of Nottingham, 2012.

[171] S. Bustingorry, F. Pomiro, G. Aurelio, and J. Curiale. Second-order Magnetic Critical Points at Finite Magnetic Fields: Revisiting Arrott Plots. *Physical Review B*, 93(22):1–12, 2016.

[172] M. Wang, R. A. Marshall, K. W. Edmonds, A. W. Rushforth, R. P. Campion, and B. L. Gallagher. Three-dimensional Heisenberg Critical Behavior in the Highly Disordered Dilute Ferromagnetic Semiconductor (Ga,Mn)As. *Physical Review B*, 93(18):1–16, 2016.

[173] M. Müller, G. Miao, and J. S. Moodera. Thickness Dependence of Ferromagnetic- and Metal-insulator Transition in Thin EuO Films. *Journal of Applied Physics*, 105(7):07C917, 2009.

[174] E. Wolfgang. *Computer Simulation of Ion-Solid Interactions*. Spinger-Verlag, 1991.

[175] H. Saadaoui, Z. Salman, T. Prokscha, A. Suter, B. M. Wojek, and E. Morenzoni. Zero-field Spin Depolarization of Low-Energy Muons in Ferromagnetic Nickel and Silver Metal. *Physics Procedia*, 30:164–167, 2012.

[176] J. A. Krieger, C. Z. Chang, M.-A. Husanu, D. Sostina, A. Ernst, M. M. Otrokov, T. Prokscha, T. Schmitt, A. Suter, M. G. Vergniory, E. V. Chulkov, J. S. Moodera, V. N. Strocov, and Z. Salman. Spectroscopic Perspective on the Interplay Between Electronic and Magnetic Properties of Magnetically Doped Topological Insulators. *Physical Review B*, 96(18):184402, 2017.

[177] P. M. S. Monteiro, P. J. Baker, N. D. M. Hine, N. J. Steinke, A. Ionescu, J. F. K. Cooper, C. H. W. Barnes, C. J. Kinane, Z. Salman, A. R. Wildes, T. Prokscha, and S. Langridge. The Elevated Curie Temperature and Half-metallicity in the Ferromagnetic Semiconductor LaxEu$_{1-x}$O. *Physical Review B*, 92(4):045202, 2015.

[178] B. Cywinski. Muon Spin Relaxation Functions. *University of Leeds*, pages 1 – 33, 2005.

[179] S. J. Blundell. Muon Relaxation Functions. *University of Oxford*, pages 1–9, 2010.

[180] M. R. Crook and R. Cywinski. Voigtian Kubo - Toyabe Muon Spin Relaxation. *Journal of Physics: Condensed Matter*, 9(5):1149–1158, 1997.

[181] G. Solt. A Generalized Kubo-Toyabe Formula for Muon Spin Relaxation in Crystals with Uniaxial Symmetry. *Hyperfine Interactions*, 96(1):167–175, 1995.

[182] Z. Salman, T. Prokscha, A. Amato, E. Morenzoni, R. Scheuermann, K. Sedlak, and A. Suter. Direct Spectroscopic Observation of a Shallow Hydrogen-like Donor State in Insulating SrTiO$_{3}$. *Physical Review Letters*, 113(15):156801, 2014.

[183] J. E. Lynn. The Energy Dependence of the Neutron Coherent Scattering Length of Europium. *Journal of Applied Crystallography*, pages 476–482, 1989.

[184] M. Barbagallo, N. D. M. Hine, J. F. K. Cooper, N.-J. Steinke, A. Ionescu, C. H. W. Barnes, C. J. Kinane, R. M. Dalgliesh, T. R. Charlton, and S. Langridge. Experimental and Theoretical Analysis of Magnetic Moment Enhancement in Oxygen-deficient EuO. *Physical Review B*, 81(23):235216, 2010.

[185] J. Nogués and I. K. Schuller. Exchange Bias. *Journal of Magnetism and Magnetic Materials*, 192(2):203–232, 1999.

[186] R. L. Stamps. Review-Mechanisms for Exchange Bias. *Journal of Physics D: Applied Physics*, 33:R–247–R–268, 2000.

[187] K. Arai, T. Okuda, A. Tanaka, M. Kotsugi, K. Fukumoto, T. Ohkochi, T. Nakamura, T. Matsushita, T. Muro, M. Oura, Y. Senba, H. Ohashi, A. Kakizaki, C. Mitsumata, and T. Kinoshita. Three-dimensional Spin Orientation in Antiferromagnetic Domain Walls of NiO Studied by X-ray Magnetic Linear Dichroism Photoemission Electron Microscopy. *Physical Review B - Condensed Matter and Materials Physics*, 85(10):1–12, 2012.

[188] K. Arai, T. Okuda, A. Tanaka, M. Kotsugi, K. Fukumoto, T. Ohkochi, F. Guo, T. Nakamura, T. Matsushita, T. Muro, M. Oura, Y. Senba, H. Ohashi, A. Kakizaki, and T. Kinoshita. Direct Observation of Twin Domains of NiO(100) by X-ray Linear Dichroism at the O K Edge Using Photoemission Electron Microscopy. *Physical Review B - Condensed Matter and Materials Physics*, 85(17):1–6, 2012.

[189] J. Baruchel, M. Schlenker, K. Kurosawa, and S. Saito. Antiferromagnetic S-domains in NiO I. Neutron Magnetic Topographic Investigation. *Philosophical Magazine B: Physics of Condensed Matter; Statistical Mechanics, Electronic, Optical and Magnetic Properties*, 43(5):853–860, 1981.

[190] O. Madelung, U. Rössler, and M. Schulz. NiO: Lattice Parameter, Thermal Expansion. In O. Madelung, U. Rössler, and M. Schulz, editors, *Non-Tetrahedrally Bonded Binary Compounds II*, pages 1–4. Springer-Verlag, Berlin/Heidelberg, 1991.

[191] W. L. Roth. Neutron and Optical Studies of Domains in NiO. *Journal of Applied Physics*, 31(11):2000–2011, 1960.

[192] I. Sänger, V. V. Pavlov, M. Bayer, and M. Fiebig. Distribution of Antiferromagnetic Spin and Twin Domains in NiO. *Physical Review B - Condensed Matter and Materials Physics*, 74(14):1–9, 2006.

[193] S. Saito, M. Miura, and K. Kurosawa. Optical Observations of Antiferromagnetic S Domains in NiO (111) Platelets. *Journal of Physics C: Solid State Physics*, 13(8):1513–1520, 1980.

[194] K. Kurosawa, S. Saito, and S. Takemoto. Antiferromagnetic Domain Structures in Vapour-Grown NiO (111) Platelets Containing Growth Twins. *Japanese Journal of Applied Physics*, 13(5):804–811, 1974.

[195] H. A. E. Hagelin-Weaver, J. F. Weaver, G. B. Hoflund, and G. N. Salaita. Electron Energy Loss Spectroscopic Investigation of Ni Metal and NiO Before and After Surface Reduction by Ar+ Bombardment. *Journal of Electron Spectroscopy and Related Phenomena*, 134(2-3):139–171, 2004.

[196] A. Venter and J. R. Botha. Optical and Electrical Properties of NiO for Possible Dielectric Applicatons. *South African Journal of Science*, 107(1-2):1–6, 2011.

[197] M. Ghougali, O. Belahssen, and A. Chala. Structural, Optical and Electrical Properties of NiO Nanostructure Thin Film. *Journal of Nano- and Electronic Physics*, 8(4(2)):04059–1–04059–4, 2016.

[198] G. A. Niklasson and C. G. Granqvist. Electrochromics for Smart Windows: Thin Films of Tungsten Oxide and Nickel Oxide, and Devices Based on These. *Journal of Materials Chemistry*, 17(2):127–156, 2007.

[199] M. Kiwi. Exchange Bias Theory. *Journal of Magnetism and Magnetic Materials*, 234(3):584–595, 2001.

[200] J. Nogués, J. Sort, V. Langlais, V. Skumryev, S. Suriñach, J. S. Muñoz, and M. D. Baró. Exchange Bias in Nanostructures. *Physics Reports*, 422(3):65–117, 2005.

[201] H. J. Hug, I. Schmid, P. Kappenberger, O. Hellwig, and E. E. Fullerton. The Role of Uncompensated Spins in Exchange Biasing. In *INTERMAG 2006 - IEEE International Magnetics Conference*, pages 581–581. University of Basel, IEEE, 2006.

[202] F. Radu and H. Zabel. Exchange Bias Effect of Ferro-/Antiferromagnetic Heterostructures. In *Magnetic Heterostructures*, volume 227, pages 97–184. Springer Berlin Heidelberg, Berlin, Heidelberg, 2007.

[203] A. E. Berkowitz and K. Takano. Exchange Anisotropy. *Journal of Magnetism and Magnetic Materials*, 200(1-3):552, 1999.

[204] A. P. Malozemoff. Mechanisms of Exchange Anisotropy (invited). *Journal of Applied Physics*, 63(8):3874–3879, 1988.

[205] Z. W. Jiao, P. Z. Si, W. D. Jiang, Q. Wu, and G. X. Ye. Anomalous Exchange Bias in Gd/Cr Bilayer and Cr/Gd/Cr Trilayers. *Journal of Alloys and Compounds*, 458(1-2):1–4, 2008.

[206] K. D. Sossmeier, L. G. Pereira, J. E. Schmidt, and J. Geshev. Exchange Bias in a Ferromagnet/Antiferromagnet System with TCTN. *Journal of Applied Physics*, 109(8), 2011.

[207] A. G. Swartz, J. J. I. Wong, I. V. Pinchuk, and R. K. Kawakami. TiO2 as an Electrostatic Template for Epitaxial Growth of EuO on MgO(001) by Reactive Molecular Beam Epitaxy. *Journal of Applied Physics*, 111(8):083912, 2012.

[208] N. Iwata, G. Pindoria, T. Morishita, and K. Kohn. Preparation and Magnetic Properties of EuO Thin Films Epitaxially Grown on MgO and SrTiO3 Substrates. *Journal of the Physical Society of Japan*, 69(1):230–236, 2000.

[209] C. Lee, X. Wei, J. W. Kysar, and J. Hone. Measurement of the Elastic Properties and Intrinsic Strength of Monolayer Graphene. *Science*, 321(5887):385–8, 2008.

[210] E. W. Hill, A. K. Geim, K. Novoselov, F. Schedin, and P. Blake. Graphene Spin Valve Devices. *IEEE Transactions on Magnetics*, 42(10):2694–2696, 2006.

[211] J. S. Bunch, S. S. Verbridge, J. S. Alden, A. M. van der Zande, J. M. Parpia, H. G. Craighead, and P. L. McEuen. Impermeable Atomic Membranes from Graphene Sheets. *Nano Letters*, 8(8):2458–2462, 2008.

[212] F. Bonaccorso, Z. Sun, T. Hasan, and A. C. Ferrari. Graphene Photonics and Optoelectronics. *Nature Photonics*, 4(9):611–622, 2010.

[213] P. Blake, E. W. Hill, A. H. C. Neto, K. S. Novoselov, D. Jiang, R. Yang, T. J. Booth, and A. K. Geim. Making Graphene Visible. *Applied Physics Letters*, 91(6):063124, 2007.

[214] V. M. Karpan, G. Giovannetti, P. A. Khomyakov, M. Talanana, A. A. Starikov, M. Zwierzycki, J. van den Brink, G. Brocks, and P. J. Kelly. Graphite and Graphene as Perfect Spin Filters. *Physical Review Letters*, 99(17), 2007.

[215] M. Weser, E. N. Voloshina, K. Horn, and Y. S. Dedkov. Electronic Structure and Magnetic Properties of the Graphene/Fe/Ni(111) Intercalation-like System. *Physical Chemistry Chemical Physics*, 13(16):7534, 2011.

[216] Y. G. Semenov, K. W. Kim, and J. M. Zavada. Spin Field Effect Transistor with a Graphene Channel. *Applied Physics Letters*, 91(15):153105, 2007.

[217] M. S. Fuhrer, C. N. Lau, and A. H. MacDonald. Graphene: Materially Better Carbon. *MRS Bulletin*, 35(04):289–295, 2010.

[218] K. Pi, W. Han, K. M. McCreary, A. G. Swartz, Y. Li, and R. K. Kawakami. Manipulation of Spin Transport in Graphene by Surface Chemical Doping. *Physical Review Letters*, 104(18):187201, 2010.

[219] J. C. Leutenantsmeyer, A. A. Kaverzin, M. Wojtaszek, and B. J. van Wees. Proximity Induced Room Temperature Ferromagnetism in Graphene Probed with Spin Currents. *2D Materials*, 4(1):014001, 2016.

[220] Z. Wang, C. Tang, R. Sachs, Y. Barlas, and J. Shi. Proximity-Induced Ferromagnetism in Graphene Revealed by the Anomalous Hall Effect. *Physical Review Letters*, 114(1):016603, 2015.

[221] H. Haugen, D. Huertas-Hernando, and A. Brataas. Spin Transport in Proximity-induced Ferromagnetic Graphene. *Physical Review B*, 77(11):115406, 2008.

[222] D. V. Tuan and S. Roche. Spin Manipulation in Graphene by Chemically Induced Pseudospin Polarization. *Physical Review Letters*, 116(10):106601, 2016.

[223] A. H. Castro Neto, F. Guinea, N. M. R. Peres, K. S. Novoselov, and A. K. Geim. The Electronic Properties of Graphene. *Reviews of Modern Physics*, 81(1):109–162, 2009.

[224] B. Pollard. *Growing Graphene via Chemical Vapor Deposition*. PhD thesis, Pomona College, 2011.

[225] M. Weser. *Electronic and Magnetic Properties of Graphene-Based Systems*. PhD thesis, University of Berlin, 2013.

[226] Y. Dedkov and E. Voloshina. Graphene Growth and Properties on Metal Substrates. *Journal of Physics: Condensed Matter*, 27(30):303002, 2015.

[227] J. N. Fuchs and M. O. Goerbigmark. Introduction to the Physical Properties of Graphene, 2008.

[228] Y. E. Eva, G. Li, and X. Du. Electronic Properties of Graphene: a Perspective from Scanning Tunneling Microscopy and Magnetotransport. *Reports on Progress in Physics*, 75(5):56501, 2012.

[229] Y. S. Dedkov and M. Fonin. Electronic and Magnetic Properties of the Graphene–ferromagnet Interface. *New Journal of Physics*, 12(12):125004, 2010.

[230] M. O. Goerbig. Electronic Properties of Graphene in a Strong Magnetic Field. *Reviews of Modern Physics*, 83(4):1193–1243, 2011.

[231] X. Liu, C. Z. Wang, M. Hupalo, Y. X. Yao, M. C. Tringides, W. C. Lu, and K. M. Ho. Adsorption and Growth Morphology of Rare-earth Metals on Graphene Studied by Ab Initio Calculations and Scanning Tunneling Microscopy. *Physical Review B*, 82(24):245408, 2010.

[232] Elena Voloshina and Yuriy Dedkov. Electronic and Magnetic Properties of the Graphene- Ferromagnet Interfaces: Theory vs. Experiment. In *Physics and Applications of Graphene - Experiments*, volume 499, pages 75–78. InTech, apr 2011.

[233] H. Raza. *Graphene Nanoelectronics*. NanoScience and Technology. Springer Berlin Heidelberg, Berlin, Heidelberg, 2012.

[234] V. Fal'ko. Quantum Information on Chicken Wire. *Nature Physics*, 3(3):151–152, 2007.

[235] C. W. J. Beenakker. Colloquium: Andreev Reflection and Klein Tunneling in Graphene. *Reviews of Modern Physics*, 80(4):1337–1354, 2008.

[236] E. Voloshina and Y. Dedkov. Graphene on Metallic Surfaces: Problems and Perspectives. *Physical Chemistry Chemical Physics*, 14(39):13502, 2012.

[237] C. Gong, G. Lee, B. Shan, E. M. Vogel, R. M. Wallace, and K. Cho. First-principles Study of Metal-graphene Interfaces. *Journal of Applied Physics*, 108(12), 2010.

[238] D. Jiang, M. H. Du, and S. Dai. First Principles Study of the Graphene/Ru(0001) Interface. *The Journal of Chemical Physics*, 130(7):074705, 2009.

[239] Y. Gamo, A. Nagashima, M. Wakabayashi, M. Terai, and C. Oshima. Atomic Structure of Monolayer Graphite Formed on Ni(111). *Surface Science*, 374(1-3):61–64, 1997.

[240] G. Bertoni, L. Calmels, A. Altibelli, and V. Serin. First-principles Calculation of the Electronic Structure and EELS Spectra at the Graphene/Ni(111) Interface. *Physical Review B*, 71(7):075402, 2005.

[241] E. N. Voloshina and Y. S. Dedkov. General Approach to the Understanding the Electronic Structure of Graphene on Metals. 2014.

[242] A. Allard and L. Wirtz. Graphene on Metallic Substrates: Suppression of the Kohn Anomalies in the Phonon Dispersion. *Nano Letters*, 10(11):4335–4340, 2010.

[243] L. M. Malard, M. A. Pimenta, G. Dresselhaus, and M. S. Dresselhaus. Raman Spectroscopy in Graphene. *Physics Reports*, 473(5-6):51–87, 2009.

[244] S. Reichardt and L. Wirtz. Raman Spectroscopy of Graphene. In *Optical Properties of Graphene*, pages 85–132. WORLD SCIENTIFIC, 2017.

[245] J. C. W. Swart, E. van Steen, I. M. Ciobica, and R. A. van Santen. Interaction of Graphene with FCC-Co(111). *Physical Chemistry Chemical Physics*, 11(5):803–807, 2009.

[246] V. M. Karpan, P. A. Khomyakov, A. A. Starikov, G. Giovannetti, M. Zwierzycki, M. Talanana, G. Brocks, J. van den Brink, and P. J. Kelly. Theoretical Prediction of Perfect Spin Filtering at Interfaces Between Close-packed Surfaces of Ni or Co and Graphite or Graphene. *Physical Review B*, 78(19):195419, 2008.

[247] L. L. Patera, C. Africh, R. S. Weatherup, R. Blume, S. Bhardwaj, C. Castellarin-Cudia, A. Knop-Gericke, R. Schloegl, G. Comelli, S. Hofmann, and C. Cepek. In Situ Observations of the Atomistic Mechanisms of Ni Catalyzed Low Temperature Graphene Growth. *ACS nano*, (9):7901–7912, 2013.

[248] P. Braeuninger-Weimer, B. Brennan, A. J. Pollard, and S. Hofmann. Understanding and Controlling Cu-Catalyzed Graphene Nucleation: The Role of Impurities, Roughness, and Oxygen Scavenging. *Chemistry of Materials*, 28(24):8905–8915, 2016.

[249] A. Reina, H. Son, L. Jiao, B. Fan, M. S. Dresselhaus, Z. Liu, and J. Kong. Transferring and Identification of Single- and Few-Layer Graphene on Arbitrary Substrates. *The Journal of Physical Chemistry C*, 112(46):17741–17744, 2008.

[250] I. Shlimak, A. Haran, E. Zion, T. Havdala, Y. Kaganovskii, A. V. Butenko, L. Wolfson, V. Richter, D. Naveh, A. Sharoni, E. Kogan, and M. Kaveh. Raman Scattering and Electrical Resistance of Highly Disordered Graphene. *Physical Review B*, 91(4):045414, 2015.

[251] A. C. Ferrari and D. M. Basko. Raman Spectroscopy as a Versatile Tool for Studying the Properties of Graphene. *Nature Nanotechnology*, 8(4):235–246, 2013.

[252] A. Cabrero-Vilatela, R. S. Weatherup, P. Braeuninger-Weimer, S. Caneva, and S. Hofmann. Towards a General Growth Model for Graphene CVD on Transition Metal Catalysts. *Nanoscale*, 8(4):2149–2158, 2016.

[253] A. C. Ferrari, J. C. Meyer, V. Scardaci, C. Casiraghi, M. Lazzeri, F. Mauri, S. Piscanec, D. Jiang, K. S. Novoselov, S. Roth, and A. K. Geim. Raman Spectrum of Graphene and Graphene Layers. *Physical Review Letters*, 97(18):187401, 2006.

[254] F. A. Ma'Mari, T. Moorsom, G. Teobaldi, W. Deacon, T. Prokscha, H. Luetkens, S. Lee, G. E. Sterbinsky, D. A. Arena, D. A. MacLaren, M. Flokstra, M. Ali, M. C. Wheeler, G. Burnell, B. J. Hickey, and O. Cespedes. Beating the Stoner Criterion Using Molecular Interfaces. *Nature*, 524(7563):69–73, 2015.

[255] M. Hansen, R. P. Elliott, and F. A. Shunk. *Constitution of Binary Alloys*. McGraw-Hill, New York, 1958.

[256] J. F. Ankner and C. F. Majkrzak. Subsurface Profile Refinement for Neutron Specular Reflectivity. In Charles F. Majkrzak and James L. Wood, editors, *Subsurface profile refinement for neutron specular reflectivity*, volume 1738, pages 260–269, 1992.

[257] E. N. Voloshina, A. Generalov, M. Weser, S. Böttcher, K. Horn, and Y. S. Dedkov. Structural and Electronic Properties of the Graphene/Al/Ni(111) Intercalation System. *New Journal of Physics*, 13(0001), 2011.

[258] W. L. O'Brien and B. P. Tonner. Orbital and Spin Sum Rules in X-ray Magnetic Circular Dichroism. *Physical Review B*, 50(17):12672–12681, 1994.

[259] O. Eriksson, A. M. Boring, R. C. Albers, G. W. Fernando, and B. R. Cooper. Spin and Orbital Contributions to Surface Magnetism in 3d Elements. *Physical review. B, Condensed matter*, 45(6):2868–2875, 1992.

[260] O. Eriksson, B. Johansson, R. C. Albers, A. M. Boring, and M. S. S. Brooks. Orbital Magnetism in Fe, Co, and Ni. *Physical Review B*, 42(4):2707–2710, 1990.

[261] C. T. Chen, F. Sette, Y. Ma, and S. Modesti. Soft-x-ray Magnetic Circular Dichroism at the L2,3 Edges of Nickel. *Physical Review B*, 42(11):7262–7265, 1990.

[262] C. Chacon, O. Isnard, L. Chioncel, C. Giorgetti, F. Baudelet, and E. Dartyge. XMCD Measurements and Calculations at the Co K Edge in YCo4B. *Journal of Magnetism and Magnetic Materials*, 242-245:861–863, 2002.

[263] P. Söderlind, O. Eriksson, B. Johansson, R. C. Albers, and A. M. Boring. Spin and Orbital Magnetism in Fe-Co and Co-Ni Alloys. *Physical Review B*, 45(22):12911–12916, 1992.

[264] H.-Ch Mertins, S. Valencia, W. Gudat, P. M. Oppeneer, O. Zaharko, and H. Grimmer. Direct Observation of Local Ferromagnetism on Carbon in C/Fe Multilayers. *Europhysics Letters (EPL)*, 66(5):743–748, 2004.

[265] O. Céspedes, M. S. Ferreira, S. Sanvito, M. Kociak, and J. M. D. Coey. Contact Induced Magnetism in Carbon Nanotubes. *Journal of Physics: Condensed Matter*, 16(10):L155–L161, 2004.